Magnetoreception

Dissertation zur Erlangung des akademischen Grades eines
Doktors der Naturwissenschaften (Dr. rer. nat.)

vorgelegt von

MARKUS BELAU

an der UNIVERSITÄT KONSTANZ
Mathematisch-Naturwissenschaftliche Sektion
Fachbereich Physik

Tag der mündlichen Prüfung: 09.12.2015
1. Referent: Prof. Dr. Georg Maret
2. Referent: Prof. Dr. Martin Wikelski

Contents

1 Introduction

1.1 Historic observations / uses

First archeological indications for the use of pigeons by humans go back about 10000 years[1]. Back then they were used as food source. But already more than 2000 years ago they were used to carry messages by ancient Egyptians. The impressive homing behavior led to an extensive use of pigeons particularly for military purposes. It was not until about 20 years ago that the Swiss army exempted the use of their military pigeons. References to the use of the magnetic field by migrant birds as navigation cue have already been mentioned by von Middendorff in 1855:

> "... so liegt der Gedanke nahe, es möge die erstaunliche Unbeirrbarkeit der Zugvögel - trotz Wind und Wetter, trotz Nacht und Nebel - eben darauf beruhen, dass das Geflügel immerwährend der Richtung des Magnetpoles sich bewusst ist, und demzufolge auch seine Zugrichtung genau einzuhalten weiss. Was dem Schiffe die Magnetnadel ist, wäre dann diesen 'Seglern der Lüfte' das innere magnetische Gefühl, welches im Zusammenhang mit den galvanisch-magnetischen Strömungen stehen mag, die im Innern des Körpers dieser Tiere, zumal in ihren Bewegungsapparaten, erwiesener Maassen kreisen." [2]

But it was not until 1947 that this was investigated in greater detail from Yeagley and Whitemore by attaching magnets to the wings and the head of homing pigeons[3] which however gave inconclusive results. More elaborate experiments were not performed before the 1960s where Wiltschko and Merkel demonstrated avian magnetoreception in european robin[4–7]. The disruption of the homing behavior of pigeons was shown by Keeton in 1971[8] by gluing magnets to their backs and by Walcatt and Green[9] by inducing small magnetic fields with coils around the pigeons head.

1.2 Many animals sense the magnetic field

When people realized that some animals can perceive the magnetic field, it has particularly fascinated them due to the fact that it is a sense that we do not experience on our own. Therefore they started to look for evidence for magnetic behavior in a variety of species and indeed have found some. Although some evidence may be weak (e.g. defecation of dogs with a preferred alignment along the magnetic field[10]) and controversial for many species there is convincing evidence, indicating that magnetoreception may not be an exotic feature which can only be found in a small number of specialized animals but seems to be a rather general feature which can be found in all kind of taxa. Some selected examples are given below:

Bacteria	Magnetotactic bacteria[11–16]
Reptiles	Turtle[17–24]
Fish	Salmon[25]
Invertebrates	Honeybee[26]
	Beetle[27–29]
	Crustacean[30]
	Mullusk[31,32]
	Frogs[33–35]
	Salamander[36]
	Drosophila[37,38]
	C. Elegans[39]
	Butterfly[40]
Birds[41]	European robin[7]
	Australian Silvereye[42–46]
	Garden warbler[47–50]
	Homing pigeon[9]
	Pied flycatcher[51]
Mammals[52]	Mole rat[53]
	Bat[54,55]
	Cattle[56,57]
	Red foxe[58]
	Dog[10]
	Dolphin[59]

And even experiments with humans have been performed, which however gave inconclusive results[60–66].

The mechanism of perception is however less clear. The only exception are some basic animals, such as magnetotactic bacteria, where long chains of magnetite (Fe_3O_4), greigite (Fe_3S_4) (and pyrite (FeS_2)) or combinations thereof are repeatedly found, which result in a macroscopic torque and thereby to an orientation of the whole organism in the earth field.

For birds two mechanism are currently discussed:
one relies on small magnetic particles (magnetite and maghemite) which are located either in the beak or the inner ear and somehow couple to nerves to perceive

the magnetic field. The other is based on cryptochrome, a blue light receptor protein found in the retina of birds, which forms a radical pair by light-activated electron transfer between a donor and acceptor molecule. The radical pair can either convert between singlet and triplet state or decay into products. The singlet-triplet conversion, and therefore also the end products, are modulated by the magnetic field. It is supposed that the end products modulate the vision of the birds and therefore they can literally “see” the magnetic field.

1.3 Motivation

Despite more than 50 years of research in the area of magnetoreception the mechanism is still not fully resolved. One of the reasons for this is that most of the experiments performed so far were behavioral studies which are influenced by many factors which can not be completely controlled in the wild. Furthermore conclusions can only be obtained by statistical means which require a large number of individuals, limiting the number of hypothesis which can be tested in a given time. Quite recently new approaches have appeared which also tried to investigate magnetoreception in the more controlled laboratory environment.

The approach in this thesis is to apply novel functional neuroimaging techniques which rely on the detection of changes in neuronal hemodynamics which are associated with neural activity. Furthermore, it has the advantage that it can be applied in a laboratory environment where all factors can be controlled, and ideally, conclusions can already be drawn from single individuals allowing new insights in this fascinating topic.

The thesis is arranged in the following way:
First the currently discussed theories of magnetoreception are presented. In addition the literature is thoroughly reviewed and the results of key experiments are presented. Reproducibility and contradictory results are a particular problem in this field. Therefore an extended discussion of both supporting and opposing evidence is given.
In the following chapter anesthesia and analgesia of pigeons is described in detail. Anesthesia is necessary for functional ultrasound measurements, a new neuroimaging technique, which requires the thinning of the skull and the implementation of a chronic window. It has additionally been found that narcosis is a key factor in obtaining reproducible data with a high signal to noise ratio. Furthermore, neurovascular coupling, which is the basis for the neuroimaging techniques applied in this study, as well as the effect of anesthesia to the coupling, will be discussed in some detail.
In the experimental section, the theory and signal processing of diffusing wave spec-

troscopy, the optical neuroimaging technique, will be presented. This is followed by a number of findings showing the effect of changes in the isoflurane concentration, temperature and arrhythmia to cerebral blood flow. Then results from functional measurements with visual and magnetic stimulation will be shown.

Furthermore the intervention which is required for functional ultrasound measurements as well as first results will be described.

In addition a second approach which tries to non-invasively detect the presence or absence of magnetic particles in the head of the pigeons with magnetic resonance imaging and computed tomography will be presented.

Finally the results are summarized and future steps are discussed.

2 Literature

The extraordinary ability of homing pigeons to return from unfamiliar sites have fascinated people even back to the ancient Egyptians. The homing ability is so impressive that homing pigeons have been used in the military up to the 20th century. It is well known that pigeons use many senses for orientation, which will be shortly summarized. The focus of this chapter will however be set on the use of the magnetic field for orientation. First, key facts of the earth's magnetic field will be stated. Then the models of magnetoreception, which are currently discussed, will be presented together with key experiments, which help to understand certain parts of the magnetoreception process. In this field of research there has been a particular problem with the reproducibility of experiments. It is therefore particularly important to have a good overview about the research conducted so far in order to evaluate the evidence for the different theories. Furthermore it should provide a starting point for the search of the magnetoreceptor in this work.

2.1 Orientation

It was postulated by Kramer that navigation is based on a two step process: First it requires the determination of the current position (map step) and then to set and maintain the direction (compass step)[67,68]. Numerous cues are well known to be used by birds for the process to find their way back home. These cues are particularly important in behavioral flight experiments where it is usually not possible to control all of these factors. They are however also important in laboratory experiments where the presence or absence of certain factors might influence the neural processing of presented stimuli. Therefore they should shortly be presented but without an extensive discussion on the evidence and to what extend they are used (for a more thorough review see e.g.[69]):

- Sun compass[70,71]: Birds need to compensate for the change of the sun position over time by their internal clock. It has been observed that birds that experienced a day/night cycle that was shifted by 6 hours showed an initial orientation shifted by 90°[72–74].

- Celestial cues: Emlen showed that indigo buntings which were prevented to view the night sky before migration season could not orient under planetarium sky. However birds that were exposed to the normal rotating planetarium when they were juvenile oriented to the normal southerly direction. In contrast birds which were exposed to a planetarium sky that was rotated by an incorrect artificial axis oriented towards a migration direction which corresponds to the new rotation axis[75].

- Infrasound[76–78]: Pigeons can hear infrasound down to 0.05Hz[77]. It is known that infrasound can travel hundreds to thousand kilometers. It has been postulated that pigeons might use an acoustic map which consists of infrasonic cues radiated from steep-sided topographic features. The source of these signals are mircoseisms continuously generated by interfering oceanic waves.[76,77]. A correlation with atmospheric processes affecting infrasound cues and homing ability have been shown[78].
- Landmarks (e.g. streets)[71,79]: it is well known that birds use prominent landmarks, such as streets for navigation.
- Olfactory navigation[80–86]: There is a hypothesis that birds can use gradients in atmospheric gases to navigate. Even though the odors which are used are not known it has been shown that there are volatile organic compounds in the atmosphere that are distributed as fairly stable gradients which might allow for odor based navigation. An alternative hypothesis postulates odors rather as activational effects for navigation than for navigation itself[87,88].
- Gravity[89–91]: Gravity anomalies are suggested to affect homing behavior.

One particular fascinating cue is however the magnetic field. Behavioral evidence for responses to artificial changes to the earth's magnetic field have first been obtained in European robins[4,7], but is now well established in a large number of bird species[92]. Much has been done to identify the mechanism of reception and the routes of neural processing. The theoretical models and the evidence from the literature will be discussed in the following section.

2.2 Theoretical models

In this section the theoretical models for the perception of magnetic fields, which are currently the most promising for birds, will be described. Namely, an iron mineral based mechanism where the mineral is most likely either in the beak or the ear and a chemical compass based on the formation of a radical pair in the retina. Other models which can be excluded for birds, such as induction, will not be discussed. Furthermore the experiments supporting these models will be described in the next sections.

In addition a short introduction of the earth's magnetic field and the relevant parameters for magnetoreception will be given.

2.2.1 Earth's magnetic field

For a discussion about the mechanism of animal magnetoreception first a detailed knowledge about the earth's magnetic field is important. The earth's magnetic field is generated by a self-sustained geo-dynamo, where electrically conducting material in the outer liquid core is moved across the existing magnetic field[2]. At the surface and farther away the magnetic field has a mainly dipolar character, where the magnetic north pole is located close to the axis of rotation (see figure 2.1).

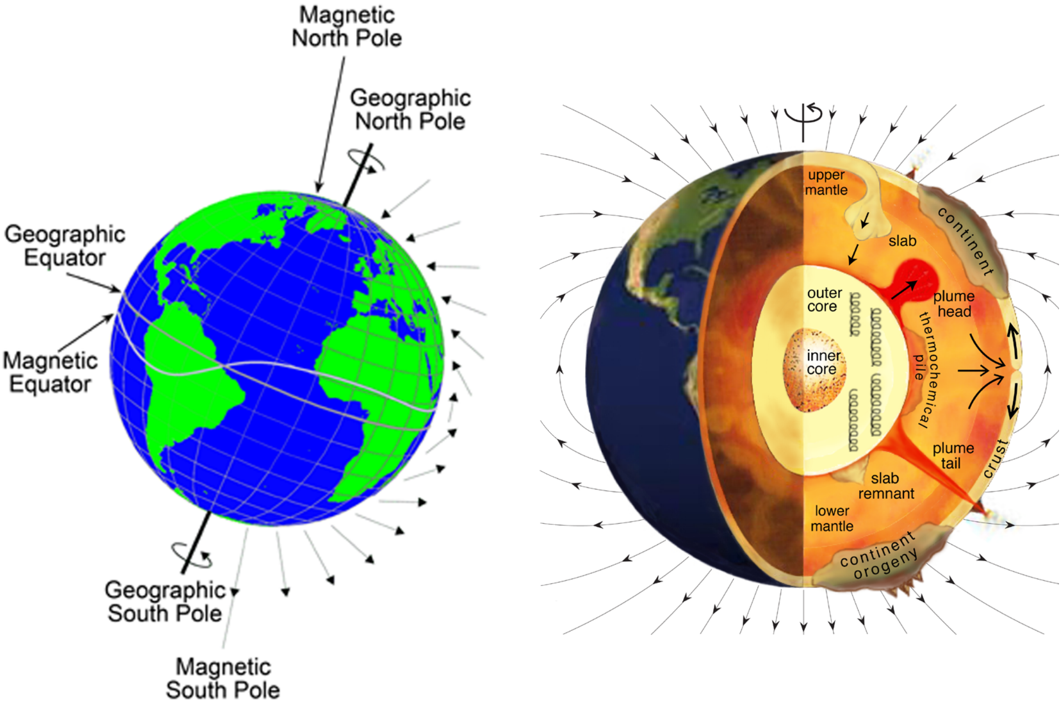

Figure 2.1: Left: Schematic depicting the earth magnetic field. The arrows show the direction of magnetic field lines with its length drawn proportional to magnetic field intensity at different latitudes. The inclination angle is given by the angle between the magnetic field lines relative to the surface of the earth, with a maximum angle of ±90° at the magnetic poles and a minimum angle of 0° at the equator. The field intensity varies between 68µT at the poles and 23µT at the equator. Text closely follows[2]. Figure copied from[2].
Right: The fluid motion of the outer core generate the Earth's magnetic field. Convection currents of magma in the Earth's outer core, driven by heat flow from the inner core, are organized in helical rolls. The flow of electrically conducting iron create circulating currents, which generate the magnetic field. Figure from Kay Lancaster, University of Liverpool. Use with permission.

The magnetic north pole is not fixed but is wandering about 10-15 km per year.

Currently the location of the geomagnetic north pole[1] is at approximately 80.30 N latitude - 72.62 E longitude (calculated by `http://www.ngdc.noaa.gov/geomag/geom_util/gmpole.shtml` for the 01.01.2015). Figure 2.2 shows the wandering of the magnetic and geomagnetic poles over time.

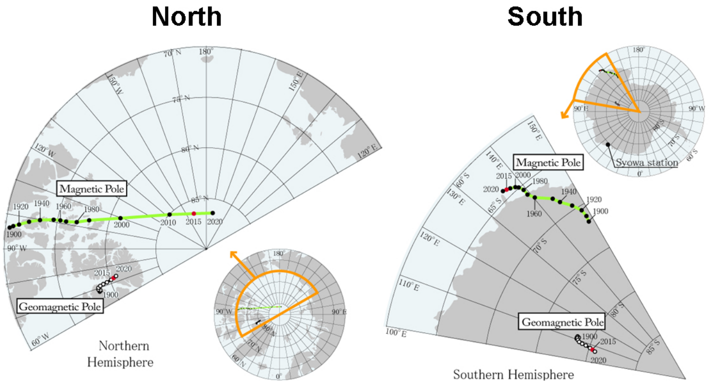

Figure 2.2: Locations of the magnetic and geomagnetic poles for the years 1900 to 2020. The red point show the current location of the poles. Figures from `http://wdc.kugi.kyoto-u.ac.jp/poles/polesexp.html`.

The intensity varies between about 68 µT at the magnetic pole, where the field lines stand vertically to the earth surface (inclination 90°) and about 23 µT close to the magnetic equator, where the field lines are parallel to the earth surface (inclination 0°). The magnetic field is however not a perfectly dipole, but shows some variations. Current maps of the intensity and the inclination from the world magnetic model 2015[93] are showns in figure 2.3 and 2.4, respectively. The field in Konstanz, where the experiments are performed, has a strength of approximately 48 µT and an inclination of about 64°.

The field is not constant but is changing up to 100nT/year and up to 25 arc-minute/year (secular variation). Furthermore solar electromagnetic radiation also produces large time varying magnetic fields which are usually in the order of 10 to 30nT but can reach up to 500nT during magnetic storms (diurnal changes). In addition there are local variations in the magnetic field due to magnetic sources near the surface (e.g. iron material close to the earth surface as often found in mountains and volcanic rocks) as well as modern electric buildings, such as power lines, which lead to disturbance of the magnetic field in their close vicinity.
As a comparison, the intensity and inclination vary only about 3nT/km and 0.01°/km, respectively[94]. This makes it even more impressive that birds can use

---

[1] Note that since the earth's magnetic field is in reality more complicated than a bar magnet one distinguishes the magnetic poles (points at which magnetic needles become vertical) and the geomagnetic poles (intersections of the Earth's surface and the axis of a bar magnet hypothetically placed at the center of the Earth)

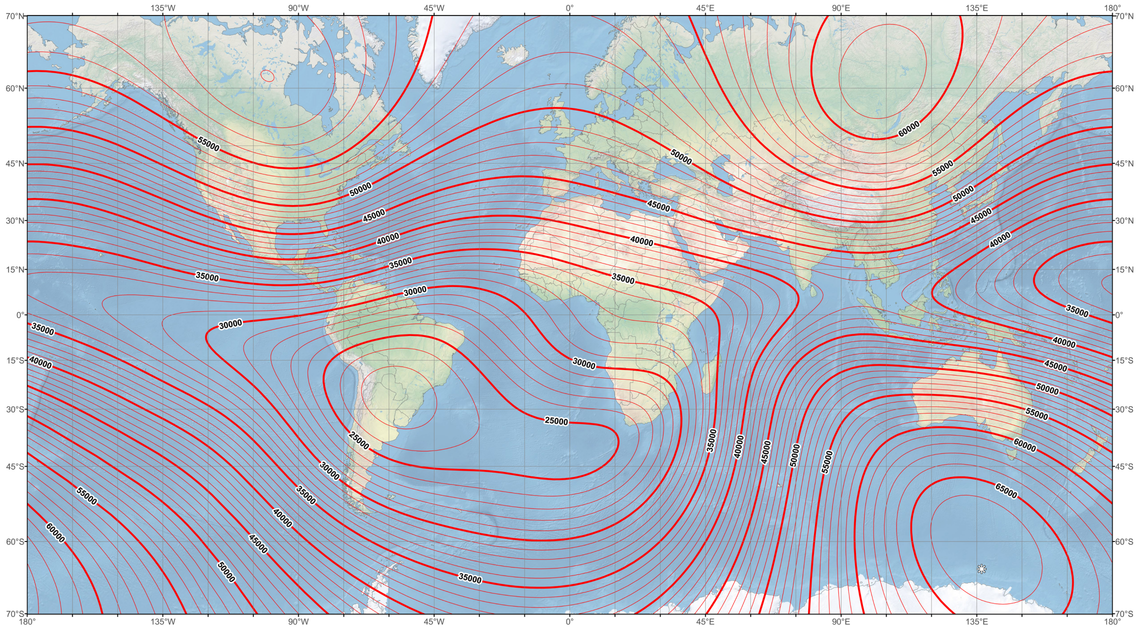

Figure 2.3: World magnetic model of the total intensity for the year 2015. Image from [93].

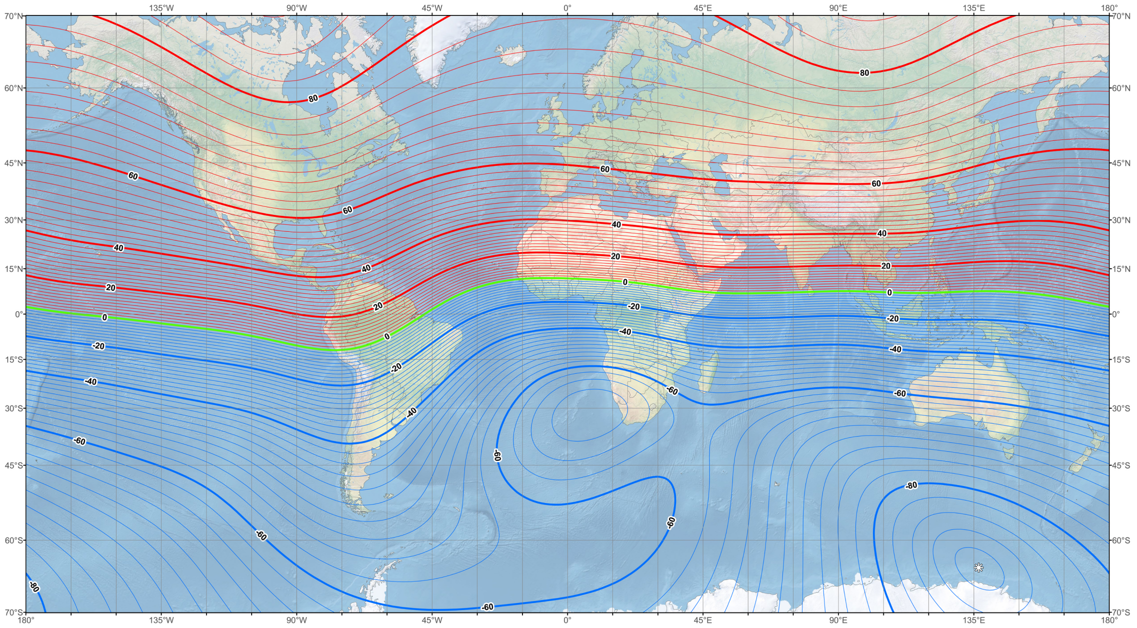

Figure 2.4: World magnetic model of the inclination angle for the year 2015. Image from [93].

such small changes for accurate navigation.

One can distinguish between two types of magnetic compasses: a polarity compass and an inclination compass. The first one is similar to our technical compass which uses the polarity to distinguish between north and south. In contrast, the inclination compass ignores the polarity and instead relies on the axial course of the field lines. It obtains directional information by interpreting the inclination of the field in respect to up and down (which may be determined by gravity or landscape)[2]. Figure 2.5 shows the principle of the compasses. Inversion of either the vertical, horizontal or both components can be used to distinguish between the two types of compasses. It was first shown by Wiltschko et al.[7] in robins (Erithacus rubecula) by inversion of the horizontal component, inversion of the vertical component and inversion of both components of the magnetic field that birds show the behavior which is expected for an inclination compass (see figure 2.5). In addition they applied a field with only a horizontal component and found a disoriented behavior[7] showing that European robins don't use a polarity compass. The inclination compass was later also demonstrated in homing pigeons[9] by applying magnetic fields with a small coil system during flight and have been found in all avian species tested so far[92,95].

As a consequence of the inclination compass inclination angles of 0° and 90° should

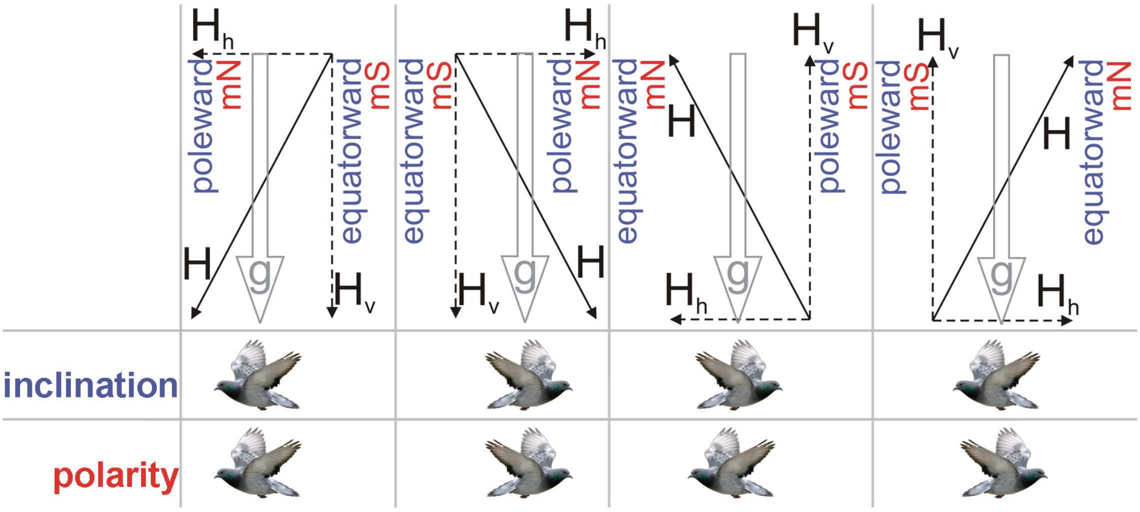

Figure 2.5: Figure shows the principle of the polarity and inclination compass. The vertical and horizontal component of the magnetic field is denoted H_v and H_h, respectively. g is the gravity vector and H is the vector of the magnetic field lines. Inversion of the vertical, horizontal or both components of the magnetic field can be used as a tool to discriminate between the two types of compass. Figure is based on[2,7,95,96].

offer no utilizable information on where to find north or south. In order to investigate what are the smallest deviations from horizontal or vertical inclination which are required for orientation, the steepest angle where birds are still oriented were determined. This has been found to be between 85°(oriented) and 88°(disoriented) in Eurasian blackcap[97] at 49.3μT and even between 88.6°(oriented) (58.099μT) and 89.7°(disoriented) (57.266μT) for Gambel's white-crowned sparrows in the wild[98]. This correspond to horizontal components as small as 4.3µT and 1.4µT for oriented behavior.

2.2.2 Magnetic particles

Since the discovery of magnetic particles in bacteria[11] they are an evident candidate for magnetoreception. The first report of magnetite in birds was published by Walcott et al.[99] who measured the remanence in the head of pigeons with a SQUID magnetometer and found permanent magnetic material, presumably single domain magnetite. A first model based on a magnetite magnetoreceptor was developed by Kirschvink et al.[100]. Now there are a large number of models describing the magnetic field perception based on iron containing particles. Mostly they rely on mechanical coupling of magnetic particles to membrane proteins and thereby influencing the membrane potential. The detailed mechanism should however not be discussed in detail and the reader is referred to some good reviews[101–107].
Magnetic particles could in principle be located anywhere in the bird because of the ability of magnetic fields to permeate biological tissue, but current evidence only suggests two regions, namely the beak and the ear. For both regions there is still a controversy in literature, both with supporting and opposing evidence. In the next two sections the literature for both receptor positions will be shortly reviewed with a particular focus on the particle properties, locations and the suggested brain regions which are innervated from those positions.

2.2.2.1 Beak

It is suggested that one magnetoreceptor is based on magnetite which is located in the upper beak of the pigeon and is innervated by the Ramus ophthalmicus, a branch of the trigeminal nerve. The findings both in favor and against this hypothesis will be thoroughly reviewed. First, key experiments will be presented, which based on the nerves which are involved in the perception, hint at the beak as position for the magnetoreceptor. Then a particular focus will be set on the location, size and properties of the magnetic particles. The summary largely relies on[107–109].

Involvement of the ophthalmic nerve:
Figure 2.6 schematically shows the ophthalmic branch of the trigeminal nerve which by its median branch (Ramus ophthalmicus medialis) gives rise to the entire somatosensory innervation of the tip of the upper beak[110]. The left rectangle (a) in figure 2.6 highlights the area where magnetic particles have been found. Both the

N. ophthalicus (V_1) and the N. trigeminus are repeatedly discussed to be involved in the perception of the magnetic field. In addition an enlarged view with positions from electrophysiological measurements of Semm and Beason[111] which showed a magnetic field dependent activation in the N. trigeminus are shown (Figure 2.6 b).

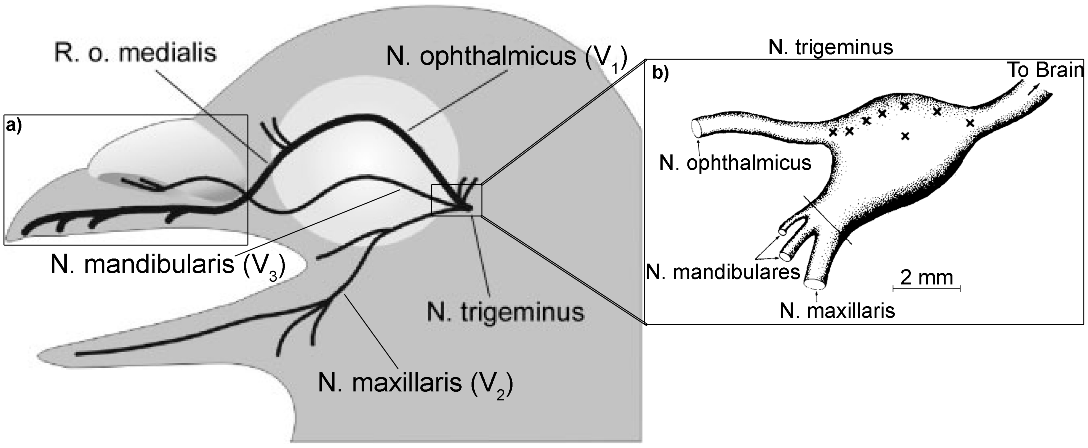

Figure 2.6: Localization of the putative magnetoreceptor in the beak of homing pigeons. Schematic drawing of the skull of the pigeon with the peripheral course of the ophthalmic branch of the trigeminal nerve. The entire somatosensory innervation of the upper tip is by the median branch (R.o. medialis) of the ophthalmic nerve. a) highlights the area where magnetic particles have been found in the beak. b) Measuring positions of the electrophysiological study of Semm and Beason[111]. Left modified image from[2,110], right modified image from[111]. Reprints with permission.

Electrophysiology:

The pioneering work of Semm and Beason recorded electrophysiological responses from the ophthalmic nerve and the trigeminal ganglion in Bobolink during magnetic stimulation[112,113]. Stimulation was performed with one Helmholz coil oriented in the vertical direction (in some cases also parallel to the ambient magnetic field) and applied either rectangular or sine magnetic stimulation on top of the ambient magnetic field of 52µT[113][2]. Changes in the firing rate have been reported for magnetic field changes as small as 200nT up to 100µT in the vertical component (see figure 2.7). The data can be fitted with a saturating(exponential) and/or logarithmic[102] dependency.

Due to the remarkable similarity data from another magnetoresponsive brain region, the vestibular brainstem, measured by Wu et al.[114] is shown for compari-

---

[2] Experiments were performed at the State University of New York in Geneseo, NY. Approximate coordinates were determined by google maps to latitude: 42.79739° N and longitude: 77.81979° W. Magnetic field were determined by the IRGF12 model for 1990 to be about Declination: -10.804°; Inclination: 71.168°; Horizontal Field: 18.209µT; Vertical Field: 53.392µT; Total field: 56.441µT

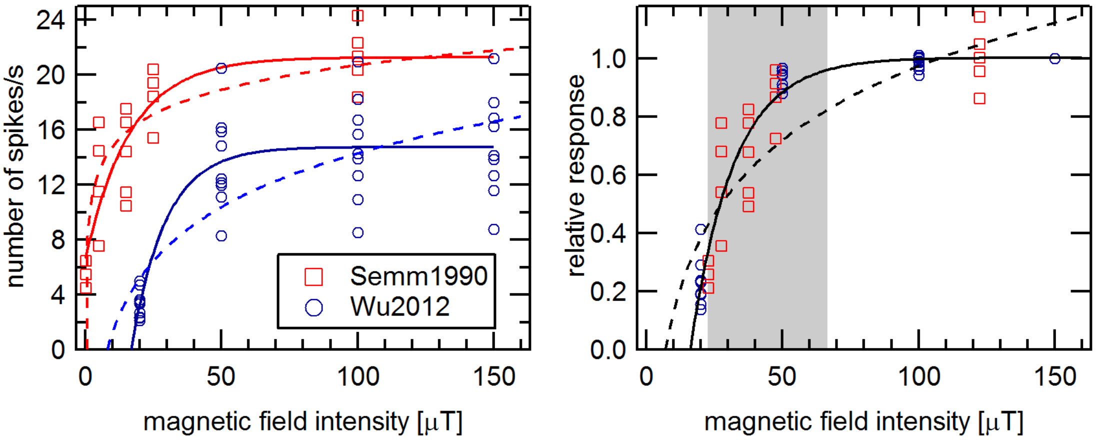

Figure 2.7: The figure shows the response of magneto-responsive neurons as a function of magnetic field intensity. Data were taken from figures in Semm and Beason[113] (open red square) and Wu and Dickman[114] (open blue circle) where the former measurement was performed in the ophthalmic branch and the trigeminal ganglion (local magnetic field 52µT (inclination approx 71°); vertical component was stimulated with rectangular change with intensities ranging from 0.2-100μT) and the later measurement in the vestibular brainstem (compensated external field, 3D rotating field (along 4 great planes - see below) with intensities from 20-150µT). Solid lines show the fit with saturating behavior (exponential: $y = y_0 + A\exp(-Bx)$) and dashed lines the fit with a logarithmic behavior ($y = A + B\log(x)$).
Right: Spiking rate normalized to the saturation value of each neuron (Wu2012) and average saturation (Semm1990). A somehow arbitrary X offset value of 22.515µT is added to data of Semm. No clear physical explanation could be found for the offset (see text for details). It is nevertheless interesting that the data can be fitted by some kind of "uniform" curve. The light gray area highlights the magnetic field found on earth. The steep slope in this range would be consistent with a use for navigation.

son. Here the ambient magnetic field was actively canceled to zero and magnetic stimulation was applied by rotating the magnetic field along four great planes and the firing rate (Sensitivity) was determined from a 3d cosine fit of the modulated spiking rate (see section 2.2.2.2 for details). By applying a somehow arbitrary X offset value of 22.515µT to the data of Semm and normalizing the data to the saturation value of each neuron (Wu2012) and average saturation (Semm1990) the data fall on top of each other. No clear physical explanation could be found for the applied offset. There are however some parameters which are in the same range such as e.g. the horizontal component or the projection of magnetic field vector onto the preferred direction vector (elevation 33.7°) from Wu, but no plausible explanation why this would result in the offset could be found. It is nevertheless interesting that the data can be fitted by some kind of "uniform" curve. The steepest part of this "uniform" curve falls in the range of the magnetic field observed on earth which would be consistent with the use for navigation.

The measurements of Semm et al.[111] suggests that the ophthamic branch of the trigeminal nerve is involved in magnetoreception (see figure 2.6).
Note that other researches however failed to replicate the results of Semm et al.[115]. In fact it was shown that the input V_1 is neither necessary nor sufficient for compass orientation in European robins[116].

Behavior:
Evidence in favor of the involvement of the trigeminal nerve is given by a behavioral study of the group of Semm and Beason where the injection of an anesthetic (lidocain) in the ophthamic nerve suppressed the change in direction which have been observed after the application of a short, strong magnetic pulse in the case without anesthetic[117]. It is noteworthy that the birds were still able to orient to the original migratory direction before the pulse treatment.
Kishkinev et al.[118] reported that Eurasian reed warblers are unable to compensate for a 1000km east-west displacement if V_1 is cut. In contrast, Gagliardo et al.[119–121] found no effect of the homing behavior during flight experiments in V_1 sectioned pigeons compared to control.
In addition Zapka et al.[116] showed that European robins where still able to orient in Emlen funnels when V_1 was cut and therefore they concluded that the connection is not necessary for magnetoreception.

Conditioning:
Mora et al.[122] showed that conditioned pigeons can discriminate between the presence and absence of a magnetic anomaly. In addition they found that the discrimination could be impaired by adjusting a magnet to the cere, local anesthesia (lignocaine) of the upper beak or bilateral sectioning of the ophthalmic branch of the trigeminal nerve[122]. Mora et al. also showed that pigeons could be conditioned to discriminate between intensity gradients where they could even differentiate between increasing and decreasing intensity values[123]. In a follow up study they also demonstrated that they can be conditioned to discriminate differences in magnetic inclination[124].
Thalau et al.[125] conditioned a group of pigeons to associate food with a magnetic anomaly. The conditioned group was more successful than the control group in finding food, which was additionally marked with a bar magnet, hidden below sand.
Note that the number of conditioning experiments which found negative results with magnetic stimuli by far outnumbers the experiments with positive results (see[125–127] for a more detailed discussion).

ZENK:

Heyers et al.[128] used the neuronal activity-dependent marker ZENK in European robins. They found magnetic activation[3] in the principal (PrV) and spinal tract (SpV) (in particular in the medial part of SpV) nuclei of the trigeminal brainstem complex, which is known to be innervated by the trigeminal nerve. A significant reduction in this region could be observed in both zero magnetic field and in changing magnetic field with prior sectioning of V_1, whereas no changes have been observed in the optic tectum.
The same result was found in pigeons by Lefeldt et al.[129], albeit with a smaller number of ZENK activated neurons compared to the study with European robins.

Anatomical structures:
Permanently magnetic material, presumably magnetite, was found by Walcott[99] in the head of the pigeon between the head and skull. Based on histological studies with Prussian blue(PB) Beason et al.[130,131] identified iron rich structures in the nasal region of bobolinks. In addition Williams et al.[132] found PB-positive cells bilaterally in an oval, sac-like structure embedded in the bone caudo-ventral to the concha of pigeons. The sacs measure approximately 0.5mm in diameter and are surrounded by relatively large diameter (2-8µm) ramifying nerve fibers. Based on remanence measurements Tian et al.[133] suggested the presence of magnetite, predominantly in a superparamagnetic state. A chain arrangement as found in magnetic bacteria is not supported by their measurements[4]. In histological sections stained with Prussian blue they found some tiny, dotted, dark-blue aggregates with sizes of about 1-4µm which were located directly beneath the subcutics. The particles were within strands of connective tissue close to the border of a region which was full of red nuclei[133]. No particular arrangement of these iron clusters is shown in the images nor mentioned in the text.
The most comprehensive work about magnetic particles in the upper beak however has been performed by the group of Fleissner et al.[94,108–110,134–138]. Hanzlik et al.[135] first found iron rich areas in the subcutis in the upper beak of homing pigeons which they identified by transmission electron microscopy (TEM) as aggregates of magnetite nanocrystals (with sizes of about 1-5nm (superparamagnetic)) arranged in clusters of about 1-3µm which form elongated structures. More detailed histological and electron microscopy studies revealed the fine structure and indicated that the clusters of nanocrystals are adjacent to or within dendrites of the ophthalmic nerve[108,110,136].

The detailed analysis of the size, location and composition revealed that the structures are located bilaterally at six positions with a specific 3 dimensional ori-

---

[3] The magnetic stimulation consisted of 3 hours changing magnetic fields, where the magnetic field was changed every 30s switching every 5 minutes between a change of 90° in the horizontal component and a random assignment of field strength between -70 and +70µT to the three axis of the magnetic field.

[4] Delta ratio of less than 2 from thermal demagnetization curves of SIRM5 K. See[133] for details.

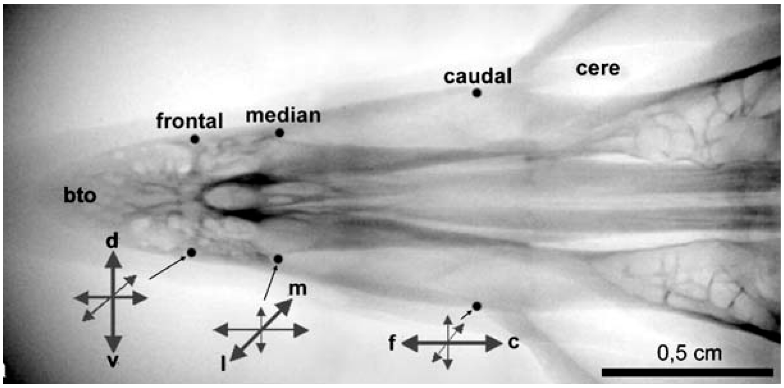

Figure 2.8: The figure shows the position of the six elongated iron rich structures (about 350µm x 200µm) described by Fleissner et al.[108] to be bilaterally located in the upper beak of homing pigeons. The predominant orientation of the dendrites in the frontal, middle and caudal parts are perpendicular to each other with a dorsal(d) to ventral(v), median(m) to lateral(l) and caudal(c) to frontal(f) orientation, respectively. Figure copied from[108]. Reprint with permission.

entation, where the most caudal patches are aligned caudal to rostral, the middle patches in a median to lateral and the frontal patches in a dorsal to ventral orientation[110](see figure 2.8). Each of this six locations is about 350µm long and about 200µm in diameter and varies only slightly in shape and size.

These structures are located in dendrites which are mediated by the ophthalmic branch of the trigeminal nerve. The dendrites themselves form a regular pattern where several are aligned side by side with a nearly uniform minimum distance of about 100µm.

Each dendrite contains two types of iron in three subcellular compartments:

1. 10-15 iron bullets (≈1µm) composed of superparamagnetic magnetite nanocrystals (size 2-4nm) adhering to the cell membrane.
2. One vesicle with a diameter of 3-5µm and a spherical or elongated shape. This vesicle is covered with non-magnetic iron crust (about 0.1µm[94]) and contacts the cell membrane.
3. Several bands (each about 10µm long) of maghemite platelets (each platelet is about 0.5µm[110]-1µm[108] wide and long and less than 0.1µm thin).

A model based on the description is shown in figure 2.9.

The type of receptor is not so clear. It is shown that the iron bullets exclusively occur in “naked” (unmyelinated) nervous endings[108]. However they do not contain nuclei nor are they nerve cell somata (no staining to nuclear red and no diffraction patterns of DNA). Also they are negative on antibody staining which is specific for synaptic transduction. Therefore they are neither receptor cells with efferent output nor afferent input.

The quantitative composition was accessed by micro-synchrotron x-ray absorption-

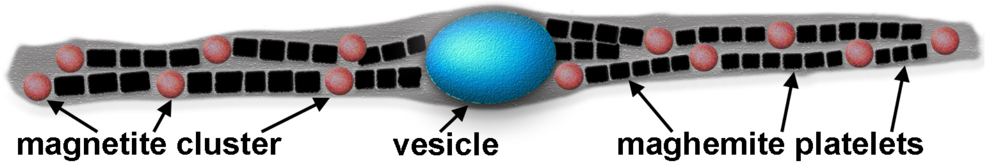

Figure 2.9: Model of iron rich structure in a single dendrite following the drawing of Fleissner et al.[108,109]. The structure contains three subcellular components: 1) superparamagnetic magnetite (about 2-4nm) is accumulated in 10-15 clusters with an diameter of about 1µm (shown in red). 2) one round or elongated vesicle (shown in blue) with a diameter of about 3-5µm which is covered by a crust of non-magnetite iron mineral and contacts the cell membrane. 3) Several bands of maghemite platelets (shown in black) with dimensions of 0.5-1µm long and wide with a maximum thickness of about 0.1µm[108,110]. The total amount of iron is about $4 \cdot 10^{11}$ atoms corresponding to about 35pg[108]. The ratio of iron is about 15:85 for magnetite to maghemite[108]. The dimensions of the structure is about 20-40µm long and 5µm wide[109].

near-edge-structure spectroscopy (μ-XANES) and found that the predominant iron is maghemite with a ratio of about 85:15 in respect to magnetite[5]. The amount of iron within one dendrite was found to be about $4 \cdot 10^{11}$ Fe atoms with an equivalent mass of 35pg[108]. Several dendrites are located in parallel (minimum distance of about 100µm) with an estimate of about $1.5 \cdot 10^{14}$ Fe (14ng) in the entire dendritic field (one of the six locations). Histological studies with Prussian blue (PB Fe^{3+}) and Turnbull's blue (TB Fe^{2+})) confirm the presence of both iron forms and is in agreement with the presence of magnetite ($Fe^{2+}\,(Fe^{3+})_2\,O_4$).

Similar dentritic structures were also found in a number of avian species including domestic chicken (resident), European robins (short to middle distance migrant) and garden warbler (long distance migrant)[109]. It is however notable that the authors in this study did not investigate the arrangement of these structures in the beak[6] which have previously been described in pigeons as bilateral at six specific positions[110].

There are however a number of studies which challenge the view presented above. In particular the work of Treiber et al.[140] raises doubt about particles found at six specific locations which are innervated by nerves.

Treiber et al. performed a systematic analysis of these cells (in total more than 200 birds from 7 different lofts were dissected). They sectioned the upper beak of pigeons with ceramic-coated microtome blades and stained serial sections (10µm) from the caudal respiratory concha to the tip of the beak with Prussian blue (PB) (labels ferric (Fe^{3+}) iron) and nuclear fast red (NFR) (identify nuclei). They

---

[5] Note that the assignment to magnetite and in particular to maghemite is not unambiguous (see e.g.[139])

[6] at least it is not mentioned and they state in the discussion: "A precise measurement of the natural variation of the dendritic alignment and bilateral symmetry will be essential for an estimation of the physiological range and dynamics of the sensory system."[109]

consistently found PB positive cells in three specific regions: 1) the stratum laxum of the dorsal and/or the ventral subepidermis, 2) the buds of feather follicles and 3) the basal region of the respiratory epithelium. These regions were characterized by the presence of multiple dark blue spherules (0.25-5.0µm) and/or by light blue cytoplasmic staining with a notable nucleus[140].
The PB positive cells show a large variation both in distribution and in the total number (from 200 up to 108800 PB positive cells in the subepidermis) and in particular they did not find them at six specific, bilateral locations but rather distributed all over the beak[140,141]. Furthermore it was investigated if the PB positive cells are neurons. Therefore they stained the tissue with PB, NFR and antibodies that label neuronal structures (neurofilament, TUBB3, MAP1B) and only found a very small amount of co-localization (0.6% at the most)[140]. The small amount of co-localization was explained by two cells (one PB positive and one neuronal marker positive) lying in the same vertical plane, but are not the same cell[140] and/or the nature of Prussian blue itself which sometimes stains diffuse[141].
A detailed analysis with transmission electron microscopy (TEM) of the ultrastructure of the PB-positive cells revealed the presence of ferritin-like granules (6-9nm) throughout the cytoplasm and in some instances haemosiderin and membrane bound electron dense organelles known as siderosomes (about 300nm)[140]. It was confirmed by energy filtered transmission electron microscopy (EFTEM) that the electron dense granules consists of iron, but no magnetite could be observed by selected area electron diffraction (SAED) in any cellular structure[140]. Instead they found that the haemosiderin masses in the feather follicle contain goethite like material and the siderosomes in the respiratory epithelium consists of ferrihydrite. On the cellular level the PB-positive cells in the respiratory epithelium were characterized by the presence of osmophilic lipid vacuoles, whereas the cells originating from the feather follicles and the subepidermal region had notable dendritic extensions that resemble filopodia. In some instances these cytoplasmic tentacles appeared to engulf neighboring cells suggesting that the PB positive cells may be phagocytic macrophages. To verify this hypothesis they used a stain (major histocompatibility complex class II (MHC II)) which labels antigen-presenting cells including macrophages and found a large co-localization with PB positive cells (98,8%, 95%, 94,4% for respiratory epithelium, subepidermis and feather follicles, respectively). In a followup study they also showed co-localization with CD44 ($>$ 97%), which is a transmembrane glycoprotein expressed on T-cells, B-cells and macrophages. The fact that they did not observe 100% co-localization was conjectured to be due to the fact that the antibody did not fully penetrate the tissue when immunostaining were performed[141].

In summary Treiber et al. suggests that the iron rich cells are rather macrophages than magnetosensitive neurons. In detail they find that[140–142]:

1. The iron containing cells are not located at six specific bilateral locations, but are rather diffusely distributed through the whole body.
2. The dark blue particles are ferritin containing siderosomes instead of magnetite spherules.
3. The diffuse staining is due to ferritin granules rather than maghemite platelets.
4. The large round structure is a nucleus instead of a vesicle.

It is now interesting to ask whence the difference in the findings of the two groups arise. One critical point is that the Fleissner group did not publish any quantitative data supporting their claim that the magnetic sensor is located at six specific positions, that are arranged bilaterally with dendrites, which are oriented perpendicular to each other. In addition Treiber et al. describe a plausible explanation that the large iron rich structures are environmental contamination which are due to the way how Fleissner et al. have performed the preparation of the slices (re-embedding semithin slices before ultrathin sections are prepared)[141]. Contamination have been a common problem in identifying magnetite in animals.
However, in the discussion of the phd thesis of Nießner[143] it is stated that although she did not find the structures at six specific locations she did find dendritic structures such as the one described by Fleissner et al. and that these structures have most likely not been detected by the automatic analysis of Treiber et al. It is currently not possible to decide definitively who is correct, but there seems to be increasing evidence to doubt the six specific locations.
One should however note the previous described evidence of the involvement of the trigeminal nerve effect as well as magnetic measurements suggesting the existence of magnetic material in the beak.

2.2.2.2 Vestibular system

The vestibular system was suggested as an alternative place for the detection of geomagnetic fields[144]. In particular the lagena, which is found in fish, amphibians and birds but not in mammals has been suggested[144,145]. With synchrothron x-ray fluorescence analysis it was shown by Harada et al.[144,146] that lagenal otoliths exist as a large number of crystals varying in size from 0.25µm-20µm and contain more iron than saccular and utricular otoliths. In contrast Zhao et al.[147] used inductively coupled plasma mass spectroscopy and found that the lagenal otholits only consists of less than 0.7% (normalized to Calcium) ferromagnetic material (Fe, Co, Ni). In addition they found that saccular and utricular otoliths contain ferromagnetic material in the same order of magnitude as those in lagenal otoliths[147].
Lauwers et. al[148] also found iron-rich organelle in the cuticular plate of cochlear and vestibular hair cells in pigeon. They found positive Prussian blue (PB - labeling ferric iron Fe^{3+}) hair cells in the basilar papilla (28%), the lagena (1.8%), the

saccule (2.9%) and the utricle (5.7%) where more than 99% of those PB positive cells contained only a single iron rich structure which was mostly located apically. This structure had an approximately spherical shape with a diameter of about 545 ± 32 nm in the cochlear hair cells and 365 ± 27 nm in the vestibular hair cells. Each of these structures contains hundreds of ferritin-like granules with diameters of about 6.75 ± 0.06 nm and 6.48 ± 0.06 nm for the basilar papilla and the vestibular hair cells, respectively. It was shown with selected area electron diffraction analysis (SAED) that the dominant iron species in each organelle is ferrihydrite which is inconsistent with current models of a torque-based magnetoreceptor constructed of single domain magnetite[148]. In addition in a later study[149] they used spinning magnetic fields to identify magnetic materials[150]. However they only found very few (14 spinning cells out of more than 6.6 million cells screened in 10 pigeons which had magnetic moments between $8 - 106\text{fAm}^2$). A systematic investigation of the properties led to the conclusion that the particles they found were most likely contaminants from the environment[149]. Since the method can only detect cells with a magnetic moment above 2fAm^2 they cannot exclude the presence of magnetic material with a smaller magnetic moment, however no clear candidate for a primary magnetoreceptor in the ear has yet been identified.

Nonetheless Wu et. al. used an early release gene marker for neural activation (c-Fos transcription factor) to identify brain regions in pigeons which are activated during magnetic stimulation with a rotating field with an intensity of three times the earth's magnetic field[145]. Figure 2.10 shows results from the stimulation where

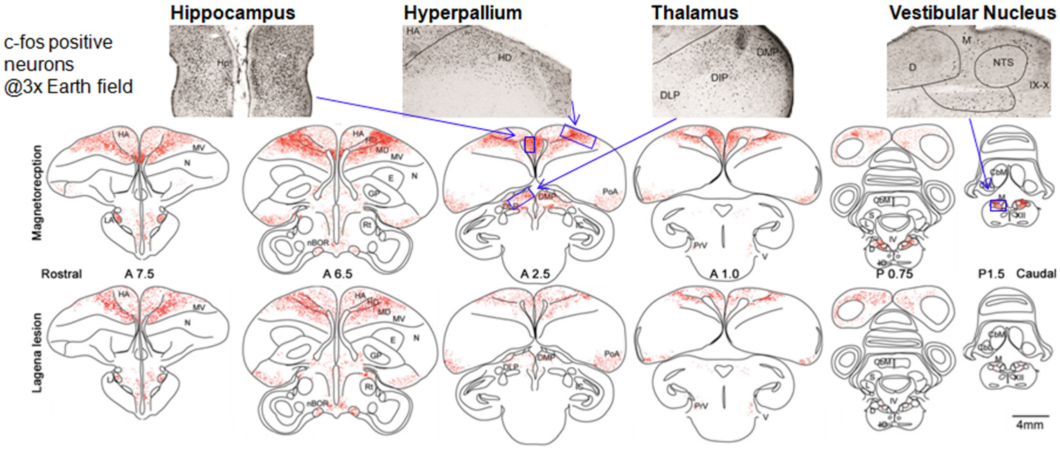

Figure 2.10: Transverse sections after magnetic stimulation showing c-Fos activated cells (red dots) at three times the magnetic field (magnetoreception) and the same stimulation in lagena lesioned pigeons. Slices are arranged from rostral to caudal where distances are given in mm relative to the interaural axis (AP0). For a better visualization of the brain regions for non experts the approximate location of the four main magnetoreceptor regions are highlighted in blue. Modified figures from[145]. Reprint with permission.

four main magnetoreception brain regions can be identified: lateral hyperpallium, hippocampus, dorsal thalamus, and caudal vestibular nuclei, which are all known to be involved in spatial orientation and navigation functions[145]. Lesion of the inner ear lagena eliminated magnetic activation in some regions, including the vestibular nuclei where lagena afferents terminate[114,151]. Therefore they hypothesized that the vestibular brainstem serves as primary magnetoreception center. This was further investigated by recording extracellular single-cell responses from the vestibular system in awake pigeons[114]. Experiments were performed in total darkness with the head of the pigeon fixated. Magnetic stimulation were generated with a coil system which rotated the magnetic field vector in 10° steps (100ms/step) along four great planes (horizontal, sagittal, and 45°) both in increasing (CW) and decreasing (CCW) inclination angle (see figure 2.11). 53 vestibular brainstem neurons showed significant activation during stimulation, 276 cells were unresponsive. The activation (mean firing rate) was not affected by the direction of rotation and showed a cosine angular dependence with the magnetic field vector with the maximal activation at a direction of about 85.2° azimuth and –33.7° elevation and a minimal activation in the orthogonal plane. This indicates that the cells encode both the elevation (inclination), azimuth as well as the polarity (cosine tuning)[114]. In addition the sensitivity of these cells were determined by stimulation with magnetic field intensities of 20, 50, 100 and 150µT. The firing rate were dependent on the intensity and showed a significant increase between 20 and 50µT and a slight increase between 50 and 100μT. Saturation was reached between 70 and 120µT[114] (see figure 2.7). Therefore the cells seems to be tuned to intensities of the earth's magnetic field.

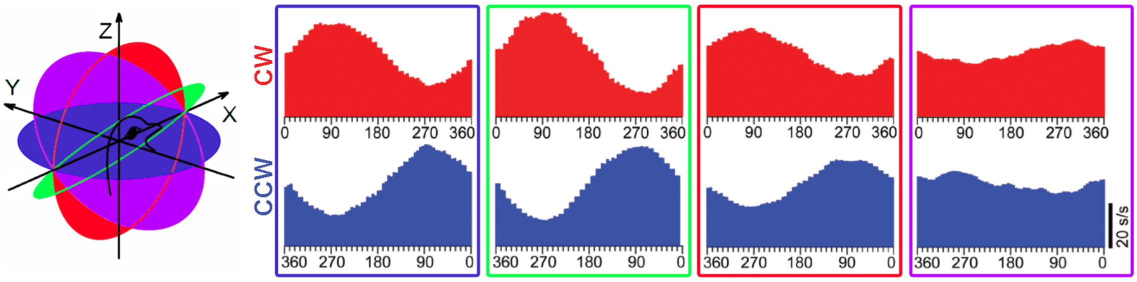

Figure 2.11: The 4 great planes of the rotation of the magnetic field are shown (left). On the right the mean firing rate from single cell extracellular recording during the rotation along those great planes in clock wise (CW) and counter clock wise (CCW) rotation are shown (see text for details). Figures modified from[114]. Reprint with permission.

The cells which are responsible for the reception and thereby for the tuning of neurons in the verstibular brainstem with the magnetic stimulation still needs to be determined.

Note that there is also a MRI study that detects field strength dependent activation of the vestibular system[152], albeit with an about 100 times higher field strength. Where the activation is postulated to be due to the Lorentz force resulting from the magnetic field and naturally occurring ionic currents which pushes on the semicircular cupula.

2.2.3 Radical pair

In the late 70th an alternative mechanism was suggested by Klaus Schulten[153] which is based on the formation of a radical pair. This so called radical pair mechanism has been described in more detail in 2000 by Ritz et al.[154]. The mechanism is schematically depicted in figure 2.12, where first a radical pair is formed by light-activated electron transfer between a donor (D) and acceptor (A). The spin coherent radical pair can then either convert between singlet and triplet state or can decay into products due to e.g. loss of spin coherence, recombination or separation of radicals in solution[155]. The conversion between singlet and triplet state depends on the magnetic field (both internal (e.g. hydrogen, nitrogen) and external (geomagnetic) due to hyperfine coupling (strength see[156]) and Zeeman interaction)[157]. Therefore the reaction yields of the singlet and triplet state are also B-field dependent. In order to act as a compass the radical pair reaction must respond to the direction of the field not only its intensity. Therefore the radicals must be at least partially immobilized, oriented and posses appropriate anisotropic

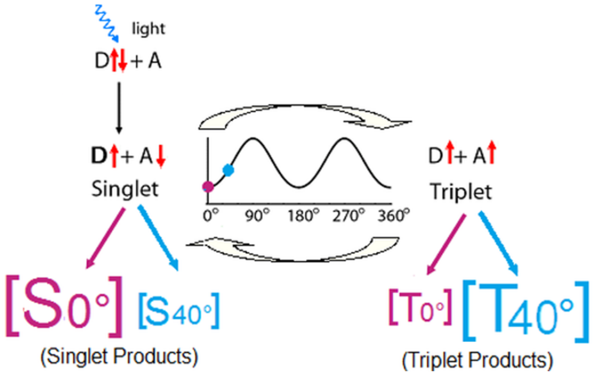

Figure 2.12: The basic mechanism of the radical pair model: A photon excites a donor-acceptor molecule. One of the electrons from the donor is transferred to the acceptor to form a spatially separated electron pair in a singlet state. The singlet-triplet conversion is induced due to anisotropic hyperfine interaction between the electron and the nucleus. The conversion can be modulated by the direction and strength of the geomagnetic field with respect to the radical pair and thus the ratio of singlet and triplet products is modulated by the earth's magnetic field (here exemplary shown for 0° and 40°). These changes in the products can then possibly modulate the vision so that the bird literally "sees" the magnetic field. Note that the conversion has a periodicity of 180° so that no difference between e.g. 0° and 180° can be detected. Image copied from[95].

interactions[157]. The most likely source of such an anisotropy is the hyperfine interaction like for example the dependence of the electron-nuclear coupling on the orientation of the molecule in an external magnetic field[157].

It was suggested that the molecules are located in the eye in some ordered fashion. Therefore cells at different positions have different angles with the earth's magnetic field vector (see figure 2.13) and thus respond differently. It is further suggested that the reaction yields influence the vision and therefore the pigeons literally can "see" the magnetic field. Note that the ordering of the molecules do not have to be perfect but that they can have a small portion of disorder. The amount of disorder which can be tolerated depends on the model assumptions and is discussed in various theoretical papers[158–160]. In these papers it was assumed that the light absorption is isotropic. If this condition is relaxed, it is reported in Lau et al.[161] "that even a totally disordered array of static receptor cells molecules could give rise to a signal that varies with both the location of the cell in the retina and the orientation of the bird's eye with respect to the geomagnetic vector". However the signal is considerable larger for an ordered alignment.

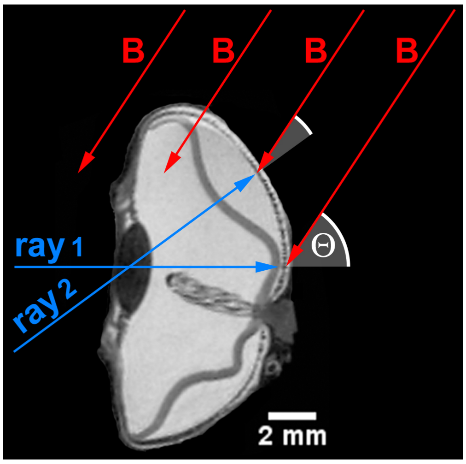

Figure 2.13: Figure shows an MRI scan with the anatomical structures (retina, pecten oculi, optic nerve,...) of the left eye of a dead pigeon (for details see section 4.3). The principal of how the pigeon can "see" the magnetic field is schematically depicted. Assuming normal orientation of the receptor cells relative to the surface or an anisotropic absorption of light that leads to the formation of the radical pair (photoselection see[161]) the radical pair forms different angles with the magnetic field B at different positions of the retina. Thus leading to a change in the singlet, triplet reaction yields. Figure follows[154].

As a candidate for the radical pair cryptochrome (Cry), a blue light photoreceptor has been suggested by Ritz et al.[154]. Indeed four different types of the cryptochrome multigen family have been found in the birds eye: Cry 1a[162–166] (located at the discs in the outer segment of the ultraviolet/violet cones), Cry 1b[163], Cry 2[162], Cry 4[167] (for a more general review of cryptochrome see[167–170]).

Cryptochrome contains two noncovalently bound chromophores: a redox active flavin adenine dinucleotide (FAD) and a light-harvesting factor[157]. The supposed activation is shown in figure 2.14. In the first step photoreduction by UV and blue light (up to about 500nm[166]) of the fully oxidized state of flavin adenine dinucleotide (FADox) occurs by electron transfer along a conserved triad of tryptophan (Trp) residues to give a radical pair $FADH^{\bullet}/Trp^{\bullet}$ consisting of a flavosemiquinone radical and a radical derived from the terminal residue of Trp-triad[115,171,172]. This radical pair can be re-oxidized either directly in a light-independent reaction, or by the absorption of UV-green light (up to about 570nm[166]) to form the fully reduced form $FADH^{-}$. It is suggested that the fully reduced form is re-oxidized in a light-independent reaction to form a second radical pair, possibly $FADH^{\bullet}/O_2^{\bullet -}$ [166,169].

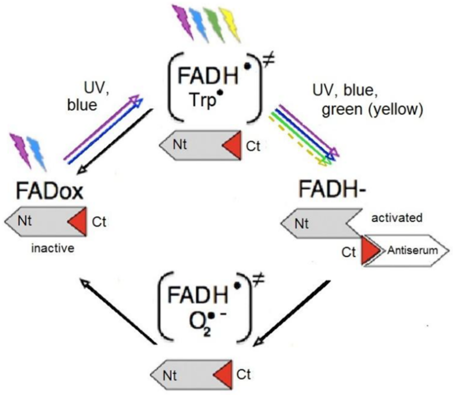

Figure 2.14: Redox cycle of flavin. Oxidized flavin (FADox) is photoreduced by UV and blue light to form the radical pair $FADH^{\bullet}/Trp^{\bullet}$. This radical pair can be re-oxidized either directly in a light-independent reaction to FADox, or by the absorption of UV-green light to form the fully reduced form $FADH^{-}$. It is suggested that the fully reduced form is re-oxidized in a light-independent reaction to form a second radical pair, possibly $FADH^{\bullet}/O_2^{\bullet -}$. Abbreviations: Nt: nitrogen-terminus, Ct: carboxy-terminus of the Cry1a, with the antiserum-binding epitope in red. Black arrows indicate light-independent reactions. Image copied from[95] which follows the image from[165,169].

For a compass the radical pair reaction must not only by influenced by the intensity but must also respond to the direction[157]. This is unlikely to occur in a solution. Therefore the radicals must be at least partially immobilized and oriented to show an anisotropic response (but see[161]). Ritz et al.[154] suggested that the cells responsible for the light dependent magnetoreception are distributed around and aligned with the retina in the manner of visual rod and cone cells. In European robins cryptochrome was indeed detected in the retina[162–164] aligned with ultraviolet/violet cone cells.

From the model several predictions can be made: cryptochrome should be found in the eye of the bird and the orientation should be wavelength dependent since the initial photon absorption requires a high enough energy to form a radical pair. The oriented behavior should be destroyed by the emission of a rf-field in the MHz range because they would interfere with the singlet-triplet conversion[173,174]. Furthermore this effect should show an angular dependence on the orientation of the rf-field relative to the static magnetic field. In addition, magnetoreception based on a radical pair would correspond to an inclination compass.

Evidence for the predictions will be given in the following[95,115,167].

Inclination compass:

Wiltschko et al.[7] performed orientation experiments with European robins during spring migration. Figure 2.15 shows results from these experiments showing oriented behavior in all test conditions, but with opposite orientation if only the horizontal or only the vertical component is reversed. This is in agreement with an inclination compass (compare figure 2.5). In addition they observed an disoriented behavior if the vertical component is set to zero and only the horizontal component is available.

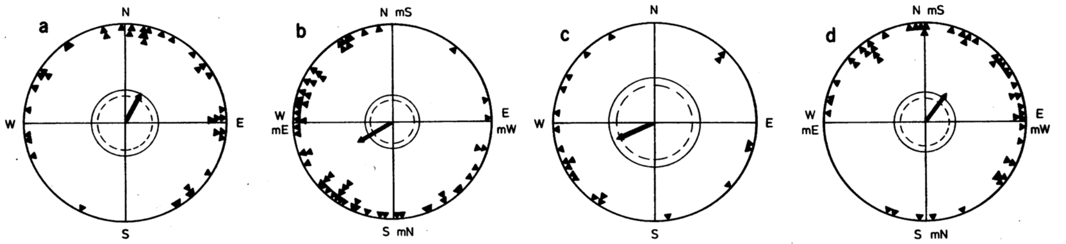

0.46 gauss, 360°, +66° inclination   0.46 gauss, 180°, +62° inclination   0.46 gauss, 360°, −65° inclination   0.46 gauss, 180°, −65° inclination

Figure 2.15: Results from orientation experiments performed by Wiltschko et al.[7] in European robins. a) Test in local magnetic field, b) horizontal component reversed, c) vertical component reversed, d) both horizontal and vertical components reversed. The observed behavior is in agreement with an inclination compass. Figure copied from[7]. Reprint with permission.

Wavelength dependence:

It was shown by Wiltschko et al. that the avian magnetic compass shows a strong light dependency where an oriented behavior is observed in birds illuminated with short wavelength light up to a wavelength of about 565nm, while a disoriented behavior is found if only wavelength larger than 590nm are used[42,48,92,175–179]. In these experiments low intensity light ($7 \cdot 10^{15}$ quanta/s m^2) as found about 45min

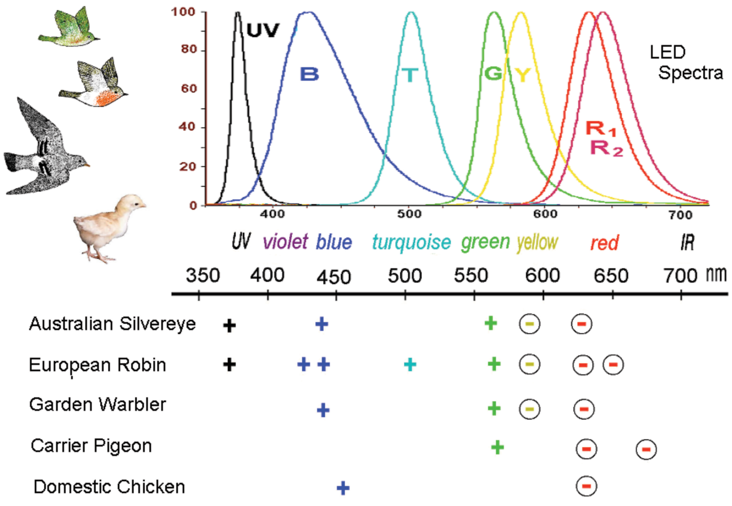

Figure 2.16: Wavelength dependence of the magnetic compass of birds. Top: Spectrum of LEDs used in the experiments. Bottom: orientation behavior of the birds during test. + indicats oriented behavior and Θ disoriented behavior. A clear transition from oriented to disoriented behavior can be seen between about 565nm and 590nm. Figure copied from[175]. Reprint with permission.

before sun rise was used (except UV where the intensity was about one-tenth). Note that also an disoriented behavior was found under higher intensities of monochromatic light and bichromatic light, but not under high intensities of white light[179].

rf-field:

Ritz et al[180] showed that oscillating magnetic fields disrupt the magnetic

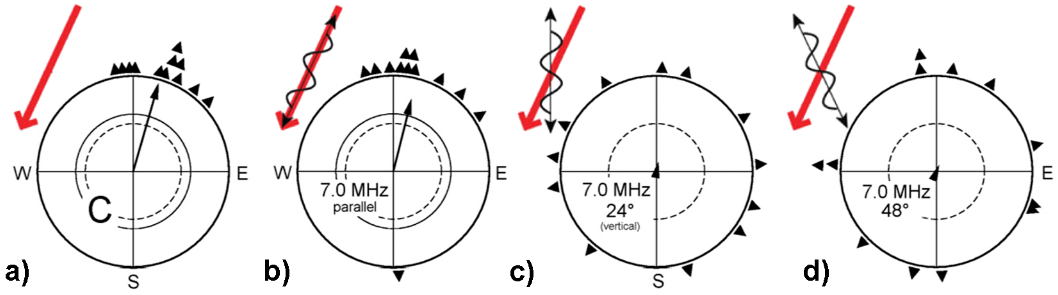

Figure 2.17: Orientation of European robin when exposed to an oscillating magnetic field of 7 MHz at a strength of 470nT. a) shows the control group with only the geomagnetic field, b) with an orientation of the oscillating magnetic field parallel, c) with an angle of 24° and d) 48°relative to the geomagnetic field[180]. Modified figure from[180]. Reprint with permission.

orientation of European robins. Disoriented behavior was found when the birds were exposed to a vertical aligned broadband (0.1-10MHz, 85nT) rf-field or a single frequency (7MHz, 470nT) oscillating field which is tilted 24° or 48° relative to the geomagnetic field[180] (see figure 2.17). This behavior was also shown by the same group for 1.315MHz and strength of 480nT[183]. Spectroscopic measurements at a strength of 480nT showed oriented behavior for 0.01MHz and 0.03MHz, bidirectional behavior for 0.10MHz and 0.50MHz, and disoriented behavior for frequencies between 0.65-7.0 MHz[181]. An particular high sensitivity to the rf-fields was found at the lamor frequency (1.315 MHz at 46μT and 2.63 MHz at 92 μT), where disoriented behavior is already found at field strengths as small as 15nT, whereas the same frequencies did not disrupt orientation when the static magnetic field was changed so that the frequencies no longer correspond to the lamor frequency[181]. Conditioned directional response in domestic chicken[178] and zebra finches[182] was also disrupted by radio frequency fields. Furthermore it is shown that birds cannot adjust to radio-frequency fields like they can for static

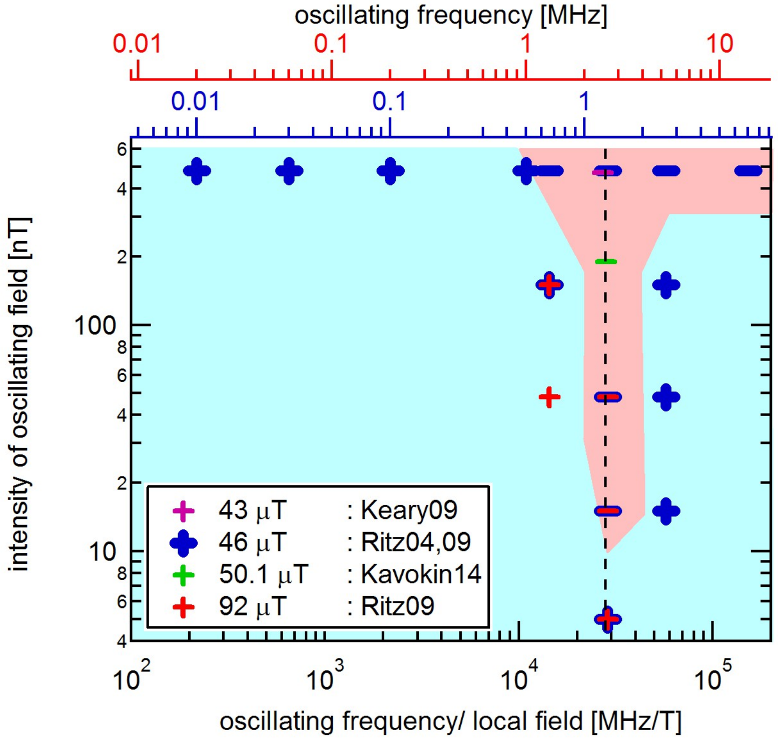

Figure 2.18: Effect of radio frequency magnetic fields on the orientation of birds. The black dashed line represents the lamor frequency of a free electron. As a guide to the eye oriented (light blue) and disoriented (light red) behavior are colored by linear interpolation between data points assuming monotonicity. The top axis shows the frequencies of the oscillating field for the experiments at 46μT (blue) and 92μT(red). The transition of oriented to disoriented behavior at small frequencies can be used to estimate the lifetime of the radical pair. Data was taken from[50,180–182].

magnetic fields[184]. This suggests that the rf-fields directly interfere with the primary process of magnetoreception[184].
An independent replication with garden warblers (Sylvia borin) at a radiofrequency of 1.4MHz and strength of 190nT at static field of 50100nT was shown by Kavokin et al.[50][7]. A summary of the experimental results is shown in figure 2.18.
The disorientation under broadband magnetic signal in the MHz range is confirmed by a recent finding of Engels et al.[185] that European robins could not orient under anthropogenic electromagnetic noise in the frequency range from 0-5 MHz at strength of 10nT and below. It is somehow surprising how birds can still use their magnetic compass if these extreme high sensitivities are true.
The disruption of orientation due to radio frequency fields close to free electron lamor frequency suggests that internal fields are small. This means that the reaction partner should be devoid of internal magnetic fields, i.e. without hydrogens or nitrogens[186]. Therefore superoxid and peroxid are suggested as partner[181].

Field dependence:
Experimental data (for robins) of the intensity range in which the magnetic compass is working is summarized in figure 2.19. Is is shown that the compass works in a rather narrow intensity range where a change of more than about 25-30% leads to disorientation[190]. However it has been shown that the compass can adjust to other intensities rather quickly (1h for 92µT and 17h for 4µT)[187–190]. It is somehow surprising that the compass seems to always work on the intensity of the local geomagnetic field regardless of adjustments to other functional intensities (e.g. see 150µT data).
The observed effects can be understood theoretically[191]. Xu et al.[191] investigated the requirements for the hyperfine coupling. They assumed that a monotonic behavior of the reaction yield is a prerequisite for oriented behavior. They found that only strong and weak hyperfine coupling is compatible with this assumption. Furthermore they show that weak coupling can also be excluded because this would result in a singlet yield which is independent of field intensity and rf-fields and therefore incompatible with experimental data. In the case of strong hyperfine coupling the directions distinguishability is almost unchanged if the intensity is changed and only the singlet yield is changed which may explain the transient disorientation. The agreement with experimental findings suggests a strong hyperfine coupling. The coupling constant has been estimated to be in the range of $10^{-7} - 10^{-6}$meV[156].
From this calculations they predict that birds can adjust to fields from almost zero

---

[7] Note that the study has some weaknesses: Only 8 birds out of 19 planned were analyzed. The analysis was not double blind. In addition they tested each bird 3-5 times and only took the mean direction of the oriented cases which results in a bias.

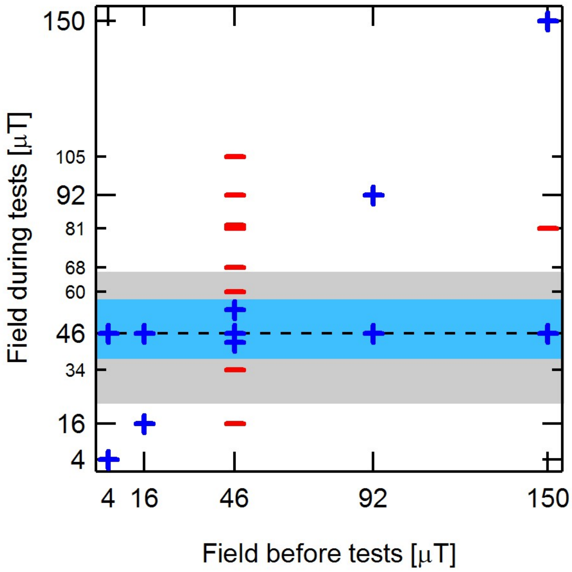

Figure 2.19: The figure shows the functional window of birds (robins) magnetic compass orientation. + size indicates oriented, - disoriented behavior. The light blue area highlights the approximate intensities where oriented behavior is observed [187], the light Grey area indicated the geomagnetic field intensities on earth. The dashed black line is the geomagnetic field at the test site (46µT). Figure following [95]. Data from [187–189].

up to a field B_{max} where γB_{max}[8] is on the order of the hyperfine coupling strength and therefore can be used for its estimation [191].
It is further shown that the decay constant k should be on the order of γB_{rf}, therefore for $B_{rf} = 150\text{nT}$ the lifetime $1/k$ can be estimated to about 10^{-4}s [191–194] (however check [195,196] who find lifetimes in the microsecond range). Additionally rf-fields parallel to the external field should have no influence on the reaction yield [191] which is also compatible with experimental data.

Cryptochrome:
Nießner et al. [164] showed that Cry1a is located at the discs in the outer segment of the UV/violet cones (see figure 2.20). In Nießner et al. [165] it was further shown that the antiserum against Cry1a only labeled the light-activated form of Cry1a. They showed that activated Cry1a was found under all wavelength where the birds showed magnetic orientation (373nm, 424nm, 502nm and 565nm), but not under red (635nm) light.
Under UV to turquoise light the full cycle can run, but in contrast for green light the first step cannot be initiated. In their 2014 study [166] they tested chickens

---

[8] $\gamma = \frac{1}{2}\mu_B g_s$ is the gyromagnetic ratio with μ_B being the Bohr magneton and g_s the g factor of the electron

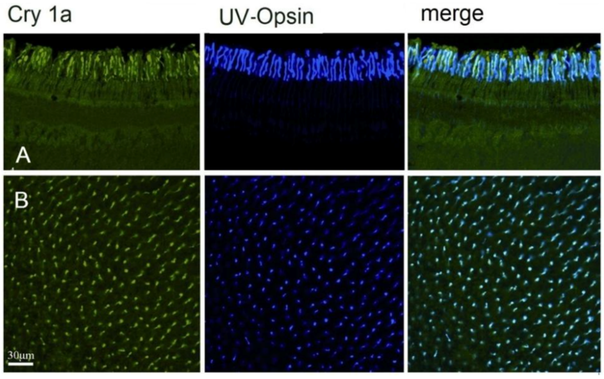

Figure 2.20: Localization of immuno-labeled cryptochrom 1a and UV cones and their co-localization in the retina of robins[95,164]. A) shows a vertical section through the outer part of the retina and B) the whole mount of the retina. Figure from[95].

under three conditions (a) exposure for 30min, after daylight; (b) for 30min, after 30min total darkness and (c) for 1h after daylight. Under green light a small amount of activated Cry1a was found in the first condition (a) suggesting that when semiquione FADH$^\bullet$ is still available photoreduction to the activated form can occur. No activation were found for conditions (b) and (c). Therefore it is suggested that the depletion of FADH$^\bullet$ to FADox takes between 30-60min. These findings were further verified by accompanying behavioral experiments with European robins[190]. They showed that robins were oriented under green light when they were kept under white light before the test, but showed disoriented behavior when kept for 1h in total darkness or 1h under green light before the test. Therefore confirming the predicted reaction scheme (Figure 2.14).
It is shown by Wiltschko et al.[184] that exposure to a radio-frequency field of 1.315 MHz with 480nT has no disruptive effect on the photoreduction of the Cry1a chromophore from FADH$^\bullet$ to the fully reduced form FADH$^-$ (identical labeling with antiserum to Cry1a).

Supporting evidence for cryptochrome comes from optical spectroscopy measurements which found lifetimes of milliseconds in photochemically formed FAD and Trp radicals from plants[197] and garden warblers[198]. In addition “measurements, with a higher time resolution, on Escherichia coli photolyase (photolyases are DNA-repair enzymes with extensive similarities to cryptochromes) revealed an earlier FAD Trp radical pair with a microsecond lifetime which responded weakly to a magnetic field considerably stronger than that of the Earth[199,200]”[115].
Biskup et al. observed by time resolved electron paramagnetic resonance that frog cryptochrome form spin correlated radical pairs[171,172]. They also showed that FAD-Trp radical pairs have long lived spin polarization in the microsecond range which are necessary for a magnetic compass[171,201].

The principal of a chemical compass has been shown in an ex vivo experiment with a structurally unrelated carotenoid–porphyrin–fullerene model system where changes in the concentration of reaction products have been observed at magnetic fields of earth strength as well as a directional sensitivity at stronger fields (3.1mT) which was invariant to inversion of the field[202]. Furthermore they find in the model system that the effect of varying the angle between the static and oscillating field is crucially dependent on the magnitude of the hyperfine coupling relative to the static field strength[203].

Maeda et al.[204] also found changes in the reaction yield at magnetic fields in the mT range in photo-induced radical pairs in cryptochrome from Arabidopsis thaliana. Ahmed at al.[205] found that magnetic intensity affected cryptochrome dependent responses in Arabidopsis thaliana which however could not be independently replication by Harris et al.[206].

Gegear et al.[37] show in a binary choice behavioral experiment that cryptochrome is necessary for light dependent magnetosensitive responses in Drosophila. They also find that light with wavelength smaller than 420nm is necessary for a magnetosensitive response which is not in agreement with tryptophan triad-generated radical pairs mediating the ability to sense magnetic fields[38]. Note however that in birds oriented behavior at wavelength larger than 420nm are repeatedly observed.

Electrophysiology

Semm and Demaine also investigated the lateral and superior vestibular nuclei, the vestibular-cerebellum and the nucleus of the basal optic root (nBOR) in pigeons on magnetic sensitivity[207]. Responses to magnetic fields in the vestibular system were only found if the animal was tilted out of the horizontal plane. About 70% of the cells in the nBOR, which showed directional sensitivity to dynamic photic stimulation, were influenced by gradual inversion of the magnetic field. No response to artificial magnetic fields were found in total darkness[207,208].

However repeated measurements in both, anesthetized and awake pigeons, by Ramirez et al.[209] did not find any indication of magneto-sensitive cells.

2.3 Key experiments

This section should provide the reader with additional key experiments, where a stronger focus has been set on the different approaches which have been used to investigate magnetoreception.

2.3.1 Flight experiments

Many of the early experiments were based on release experiments of birds where their vanishing bearing and the time they needed for homing have been deduced as an indicator of their homing ability. Newer approaches use GPS tracking in order to cover the whole flight path and allow for more sophisticated analysis of the flight tracks (e.g.[210]). However even though some sensory functions can be manipulated during the flight not all inputs can be controlled and therefore disturbances (e.g. birds of prey) as well as the use of other navigation cues (sun, odor, ...) might influence the homing process. Therefore large group numbers are required to draw trustworthy conclusions which makes studies quite time consuming.

2.3.2 Funnel

A widely used approach in migratory birds is to test them in Emlen funnels[211]. It has been observed that during the migration seasons birds held in small cages exhibit a nocturnal restlessness which has been termed “Zugunruhe” [211]. Furthermore it was noticed that the birds tend to orient towards their migration direction. Therefore birds where placed in a funnel shaped test unit which has an ink pad at the bottom and the pattern due to footprints is analyzed. In newer approaches scratch paper is often used instead of ink. The big advantage of these experiments is that orientation behavior can be investigated under controlled laboratory environment, however birds can only be tested during migratory season. Furthermore if analysis is not performed double blind or even better with an automated computer analysis[9] this method is prone to wishful thinking.

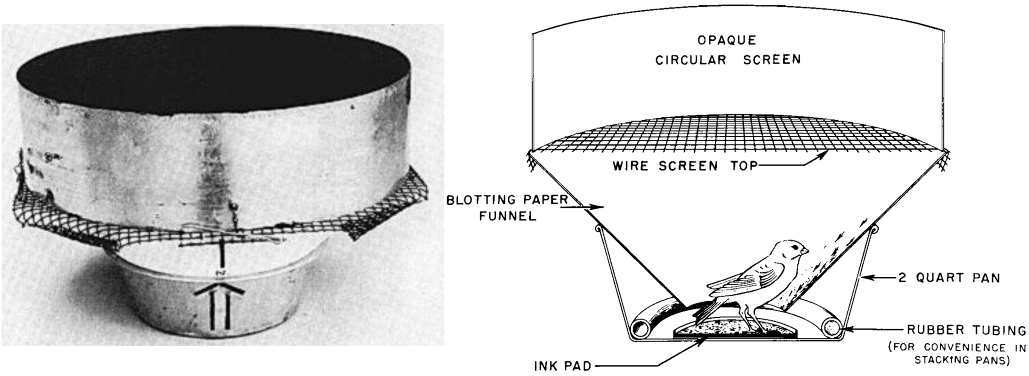

Figure 2.21: Schematic drawing of an emlen funnel. Either the shown inc pad at the bottom is used or the inclined surface is covered with scratch paper. Figure copied from[211].

Nevertheless many of the key experiments have been performed with this experimental design: inclination compass[7], light dependency[42], rf-fields[180] and identification of brain regions involved in magnetoreception[116].

---

[9] To the best of the authors knowledge automated image processing is still not used in the field

2.3.3 Electrophysiology

Electrophysiological measurements are commonly used in the investigation of functional studies. However based on induction effects due to changing magnetic fields they are particularly prone to artifacts in the investigation of magnetoreception. If artifacts can be avoided this is however a very direct method which allows for testing in laboratory environment but also during flight[212,213].
Key findings of Semm and Beason[113,207], which found changes in the firing rate associated with magnetic field changes in the trigeminal nerve, have been described in detail (see section 2.2.2.1 Electrophysiology).
Wu and Dickman[114] performed measurements in the vestibular brainstem and found a correlation with a rotating magnetic field as well as a tuning with the field strength (see section 2.2.2.2 for details).
Vargas et al.[214] measured extracellular recordings in the hippocampal formation in pigeons. In a small number of neurons they found an increase in firing rate with an onset latency between 20-40ms and duration of 25-40ms, followed by a decrease in firing rate below baseline for about 80-120ms. It is noteworthy that only fast-firing neuron ($>$ 17 spikes/s) showed a response, but no slow-firing neurons. However the small number of responsive cells (3 neurons responsive from 7 fast-firing, from a total of 44 neurons measured) prevents clear-cut conclusions.
Semm and Demaine[208] reported a high prevalence of magneto-sensitive neurons in the optic tectum. But repeated measurements in both, anesthetized and awake pigeons, by Ramirez et al.[209] did not find any indication of magneto-sensitive cells.

2.3.4 Conditioning

In 2004 Mora et al. showed that pigeons can discriminate between the presence and absence of a magnetic anomaly in a conditioned choice experiment[122](intensity and inclination varied from 44 µT to 189 µT and 60° to 80°, respectively). Furthermore they showed that this discrimination is impaired by attachment of a magnet to the cere, local anesthesia of the upper beak area, and bilateral section of the ophthalmic branch of the trigeminal nerve, but not of the olfactory nerve[122]. Suggesting that magnetoreception occurs in the upper beak area of the pigeon.
In a newer work Mora et al. has shown that pigeons can also detect an intensity gradient[123] and the inclination of the magnetic field[124].
However replication of this work has been extremely difficult. Even though positive results of conditioning birds to magnetic stimuli have been reported (e.g., homing pigeons[122,215,216], chicken[217,218], zebra finch[219], Peking Duck[220,221]) replication of the conditioning paradigms in other laboratories by other research groups often failed “e.g., the data of Carman and Mahowald reported in the study by Carman et al.[222]-a failure to replicate Bookman[215]; A. van Hettinga and H. Mouritsen (reported in Liedvogel and Mouritsen 2010[167])-a unsuccessful attempt to repli-

cate Freire et al. (2005)[217]" [127]. Also Kishkinev[127] reports that they could not replicate the results of Mora et al.[122] for a songbird.

2.3.5 Morphological studies

Histological studies have been used to identify iron containing particles and to characterize these and their surrounding[94,108–110,134–138,140,141,148]. In addition a number of physiochemical methods have also been applied. The evidence in favor and against magnetic particles has already been discussed in detail in section 2.2.2. In addition, neuromarker such as ZENK and c-fos have been used to identify brain regions which showed neural activity before the animal was killed.

By using the ZENK marker Mouritsen et al.[223] identified a forebrain region in night migratory birds that is only highly active during night vision. This so called Cluster N is part of the ascending visual processing stream, the thalamofugal pathway (for details on the thalamofugal pathway see section 2.4.2 and[224,225])[226]. Furthermore, they showed in a day and night migratory species that Cluster N is active during night and under dim light conditions, but not under full room-light conditions during day[227] (no magnetic stimulation applied). It is suggested that Cluster N may be a general feature in birds (European robin[223], garden warbler[223], zebra finch[223], canary[223], Sardinian warbler[228], meadow pipit[227]). Zapka et al.[116] showed that European robins with bilateral lesion of Cluster N are unable to orient by the magnetic field. In contrast bilateral sectioning of V_1 did not influence orientation. Therefore, they concluded that Cluster N is necessary for the processing of magnetic compass information, but V_1 is neither necessary nor sufficient for magnetoreception[116].

In contrast, Lefeldt et al.[129] analyzed the ZENK expression after exposing pigeons to a constantly changing magnetic field, a zero magnetic field and a changing magnetic field after bilaterally sectioning of V_1. They found an activation in the trigeminal brainstem, which receives input from V_1, under changing magnetic field which vanished if either the magnetic stimulation was removed or V_1 was cut. Therefore, they conclude that the trigeminal system is involved in the processing of magnetic field information. This is consistent with findings in European robins by Heyers et al.[128] who found a higher number of ZENK activation near the principal and spinal tract nuclei of the trigeminal brainstem complex after a changing magnetic stimulation in comparison to a zero magnetic field. The number of activated neurons was also reduced after section of V_1.

Liedvogel et al.[228] demonstrated ZENK expression during dim light conditions, but they found that the level of ZENK during magnetic stimulation, zero magnetic field and different lighting conditions (monochromatic light with peak wavelength 650nm) was not significantly different from the control (normal magnetic field). Cluster N activation is not affected by season nor by migratory behavior[228].

By analyzing the c-fos activity Wu et al.[145] also found a significant activation in four brain regions: lateral hyperpallium, hippocampus, dorsal thalamus, and caudal vestibular nuclei (see figure 2.10 and section 2.2.2.2 for details). Keary et al.[229] found a similar, but fainter activation of c-fos in zebra finches. Significant activation was found in the dorsomedial part of the rostral hippocampus and a nearly significant activation was found in the hyperpallium.

2.4 Anatomical/ physiological facts

This chapter should function as a reference of the anatomical and physiological data known for pigeons. This should especially help non specialists to orient in the brain and summarize the important neurophysiological processing steps of magnetic and visual information. For the processing of olfactory and acoustic data the reader is referred to[224,225].
A stereotaxic atlas of the pigeon has been developed by Karten and Hodos[230]. A 3-dimensional brain atlas which gives a comprehensive overview of the anatomical structures with a mapping of different brain regions can be found in[231]. A general description of anatomical structures, in particular the positions of brain regions and nerves can be found in[232]. The nomenclature and organization of the avian brain can be found in[233–237]. Also see `http://avianbrain.org/` for brain atlas and nomenclature.

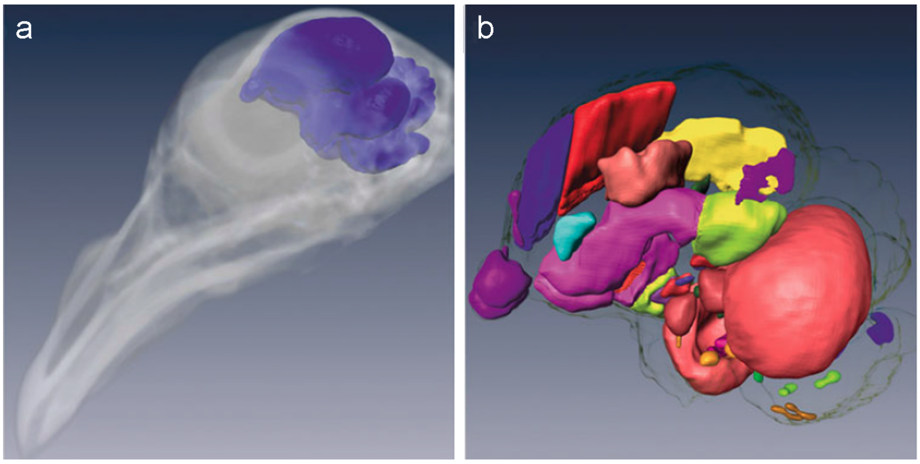

Figure 2.22: 3-dimensional atlas of the pigeon brain from an overlap of magnetic resonance imaging and computed tomography data[231]. a) the orientation of the brain with respect to the bony structure is shown. b) subdivisions of the brain. For a detailed description of the subdivision see[231]. Figure copied from[231]. Reprint with permission.

2.4.1 Magnetoreception

The distribution of brain areas which are involved in magnetoreception is far from being clear. In order to get a good starting point for the search in the functional neuroimaging study the most likely candidates from literature should be presented:
Cluster N:[223,226,228,238]
It has been suggested that Cluster N, which is located at the dorsal surface of the brain[223] close to (or in) the visual Wulst[226] and has dimensions of about 1mm x 1.5mm x 1.5mm[223] might be involved in magnetoreception. By using neuronal activity dependent immediate-early gene markers (ZENK, c-Fos) it has been shown, that Cluster N is activated under night and dim light conditions in night-migratory birds (European robin, garden warbler[223]), compared to a significantly lower ZENK expression during day[223,227]. In contrast, no difference between day and night is found in day migratory birds (zebra finch, canary[223]). Day and night migratory birds (meadow pipit[227]) show the same activation as night migratory birds[227] and even fairly sedentary birds (Sardinian warbler[228]) show activation during night. It is therefore suggested that Cluster N may be a general feature in migratory songbirds[227].

Heyers et al.[226] demonstrated an anatomical connection between the retina and Cluster N through the thalamus. They suggest that Cluster N is at least partly

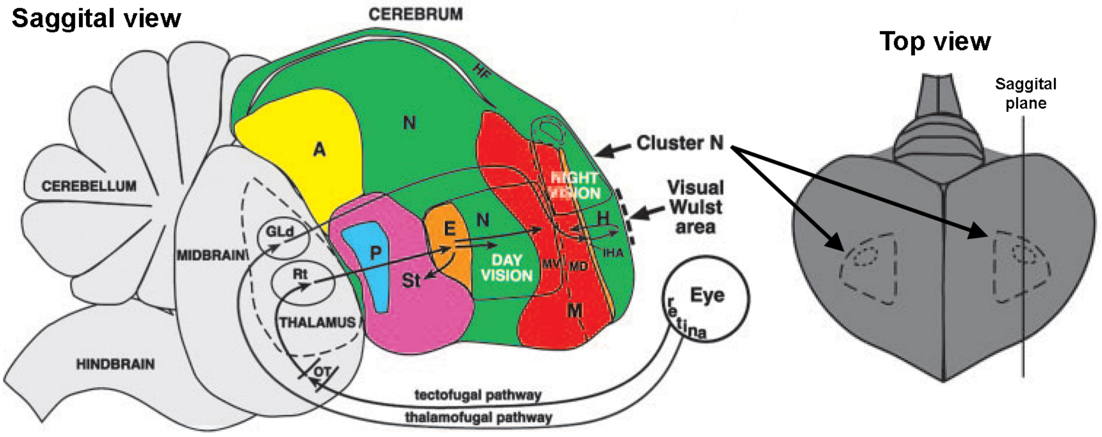

Figure 2.23: Schematic drawing of a brain showing the location of Cluster N which is active during night vision and has been suggested to be involved in magnetoreception. Left image shows the saggital view of the slice indicated by the line of the top view shown on the right which indicates the medial-lateral and frontal-caudal extent of Cluster N. In addition the thalamofugal and tectofugal pathways are shown. A: arcopallium; N: nidopallium; HF: hippocampal formation; P: pallidum; St: striatum; E: entopallium; M: mesopallium; MD: dorsal mesopallium; MV: mesopallium ventrale; H: hyperpallium; IHA: interstitial region of the hyperpallium apicale; OT: optic tectum; Rt: nucleus rotundus; GLd: lateral geniculate nucleus, dorsal part. Modified figure from[223].

located in the visual Wulst since it receives sensory input from the eyes. Therefore Cluster N is part of the ascending visual processing stream via the thalamofugal pathway[10].

Even though Cluster N has repeatedly been discussed to be involved in magnetoreception, experimental evidence is sparse or contradictory.

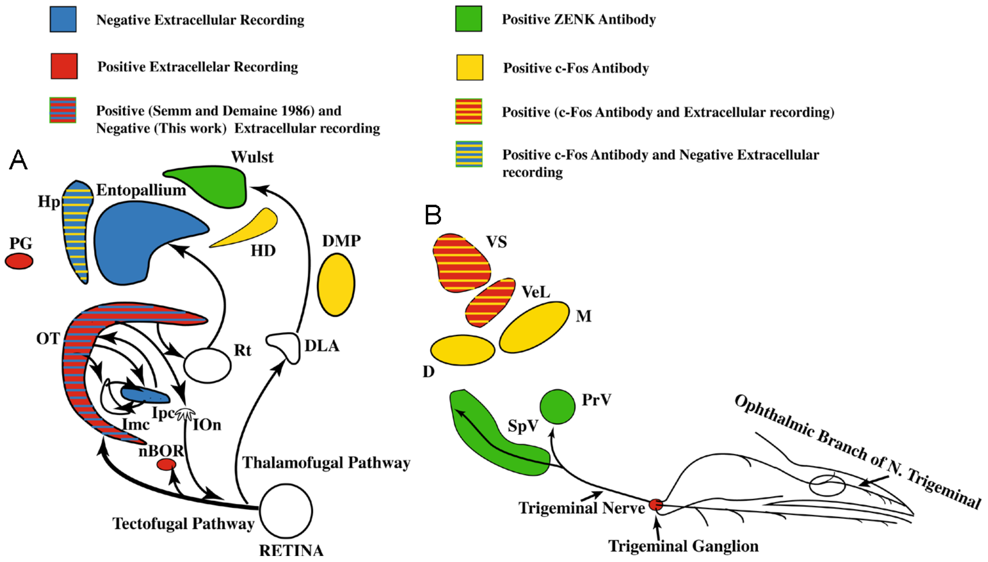

Figure 2.24: The figure summarizes results from avian magnetoreception research using extracellular recordings and activity markers (cfos, ZENK).
Positive electrophysiological results have been reported in: the pineal gland (PG) (Semm 1983[239]), the trigeminal ganglion (Semm and Beason 1990[111,113]), the superior (VS) and lateral (VeL) vestibular nuclei (Wu and Dickman 2012[114]), the nucleus of the basal optic root (nBOR) and the optic tectum (Semm and Demaine 1986[208]).
Negative electrophysiological results have been reported in the optic tectum, the nucleus isthmi pars parvocellularis (Ipc), the entopallium and the hippocampus (Hp) (data from Rose 2005[240] and Ramirez 2011[241]).
Positive evidence derived from activity markers has been found in the Wulst, and subdivisions of the hyperpallium (HD, DMP) (Mouritsen et al. 2005[242]; Heyers et al. 2007, 2010[128,226]; Mouritsen and Hore 2012[115]; Mouritsen 2013[243]). Also subdivisions of the trigeminal nucleus labeling (PrV: Principal sensory nucleus of the trigeminal nerve, SpV: Spinal trigeminal nucleus) (data from Heyers et al. 2010[128]; Wu and Dickman 2011[145]). Some important nuclei, because of their physiology and position in the visual pathways, have not been explored: the nucleus rotundus (Rt), the nucleus of the dorsal thalamus (DLA) and the isthmo optic nucleus (IOn). Text and figure copied from[209]. Reprint with permission.

Liedvogel et al.[228] also demonstrated ZENK expression during dim light conditions, but they found that the level of ZENK during magnetic stimulation, zero magnetic field and different lighting conditions (monochromatic light with

---

[10] for details on the thalamofugal pathway see for example Sturkies Avian Physiology[224,225]

peak wavelength 650nm) was not significantly different from the control (normal magnetic field). They also found that Cluster N activation is not affected by season nor by migratory behavior[228]. Even though, as they state in the discussion, this does not exclude Cluster N to be involved in magnetoreception, but it certainly does not support this finding.
Evidence in favor of Cluster N is given by Zapka et al.[116] who showed that lesion (focal injection of ibotenic acid) of Cluster N disrupted magnetic orientation. However it is not evident from the study if only Cluster N was lesioned or if neighboring structures might also be partly damaged or only the visual processing pathway is strongly disturbed so that orientation behavior is not observed.
In summary, the fact that Cluster N is not activated in day migratory birds and that the rate of neural activity (measured by ZENK expression) is at least not strongly affected by magnetic stimulation make it unlikely to find responses to magnetic field in homing pigeons in this brain area.

Other brain areas including the vestibular brainstem[114,145], parts of the hippocaompus, hyperpallium and thalamus[145] have already be shown in section 2.2.2.2 figure 2.10. Also activation of the principal (PrV) and spinal tract (SpV) nuclei of the trigeminal brainstem complex[128,129], which is innervated by V_1, has already be discussed in some detail in section 2.2.2.1.

A summary of the findings from extracellular recordings and activity marker (ZENK, c-fos) has been constructed by Ramirez et al.[209] and is shown in figure 2.24.

2.4.2 Visual system

In this section the processing of visual stimuli should be shortly reviewed with a particular focus on the location of the different parts of the brain which are involved in the processing. This closely follows[244]. The pigeon is a highly visual bird which is routinely used for studying higher processes of avian visual cognition[245] and is routinely used in psychology studies. They show an extensive array of visual abilities, which include “detection of static and dynamic stimuli in noise[246], detection of biological motion[247] and other complex motion[248,249], color and UV vision[250–252] and stereopsis[253]”[244]. In particular the tectofugal system, whose division of function is reminiscent of the visual streams in the cortex of primates[254], has been studied extensively in pigeons.

In general there are three major visual pathways in birds (see figure 2.25 A)[244]:

- Tectofugal pathway: Optic nerve axons decussate in the chiasma opticum and end in the optic tectum (TeO)[224]. The tectum projects to the nucleus

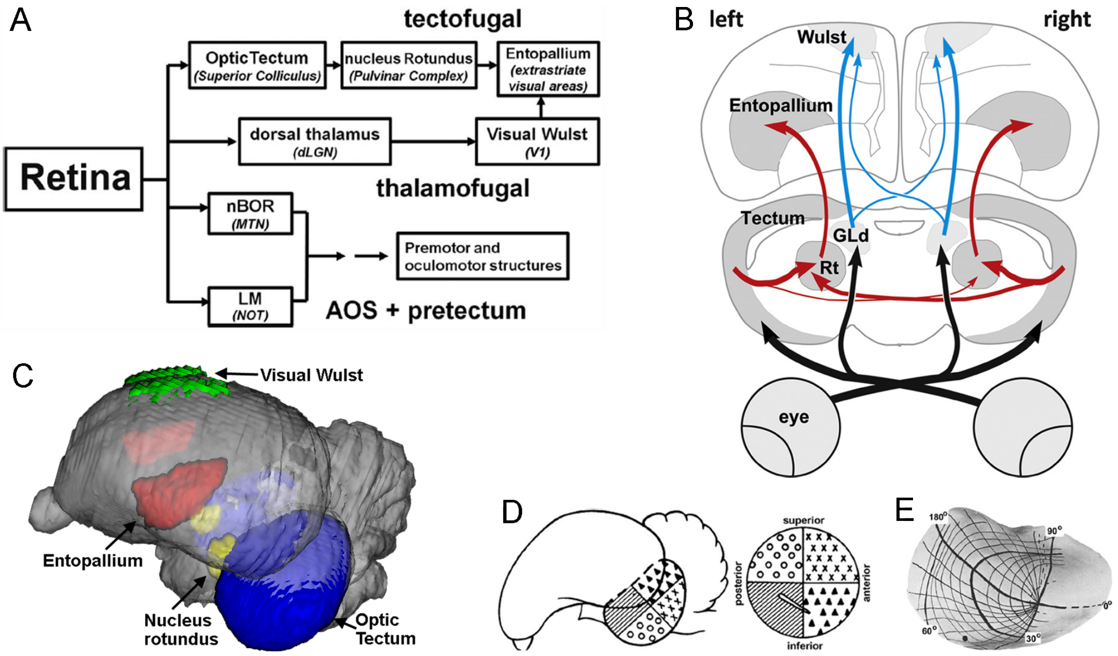

Figure 2.25: A: Schematic showing the three major visual pathways in birds. In parentheses, the equivalent mammalian structures are shown. Figure copied from [244].
B: "Schematic diagram of the ascending visual pathways of pigeons. The thalamofugal pathway is depicted in blue, the tectofugal system in red. Note that the tectorotundal pathway is asymmetrically organized such that the projection from the right tectum to the left rotundus is larger than that from the left tectum to the right rotundus. As a result, the left sided tectofugal structures integrate information from both eyes to a larger extent." [255]. Figure and text copied from [255].
C: 3-dimensional image of a pigeon brain from MRI data and mapping of brain regions showing the the main regions of the visual processing pathway. MRI data and mapping of brain regions from [231]. Image generated with Image J.
D: Illustrates the retinotopic map in the optic tectum of birds. A lateral view of pigeon brain shows the optic tectum, indicating the gross topography of the retina (right from McGill et al. 1966 [256]).
E: A detailed map of the visual field projected on the tectum (from Clarke and Whitteridge 1976 [257]). Figure D and E copied from [244].
Abbreviations: dLGN: dorsal lateral geniculate nucleus; V_1: primary visual cortex; nBOR: nucleus of the basal optic root; MTN: medial terminal nucleus; LM: nucleus lentiformis mesencephali; NOT: nucleus of the optic tract; AOS: accessory optic system; GLd: nucleus geniculatus lateralis pars dorsalis; Rt: nucleau rotundus. Reprints with permission.

rotundus (nRt) of the thalamus to the entopallium in the telencephalon [258]. Note that the tectofugal pathway shows a lateralization where "projections from the right optic tectum to the contralateral nucleus rotundus are stronger than the projections of the left tectum to the right rotundus" [259]. Due to the fact that the number of ipsilaterally ascending fibers does not differ between sides and due to the asymmetry in contralateral projections the effective input of the left rotundus is increased[260]. Therefore the left hemisphere receives a more complete representation of information from both hemispheres[259].

- Thalamofugal pathway: Retinal projection onto the nucleus geniculatus lateralis pars dorsalis (GLd) and from there a bilateral projection to the visual Wulst[224]. The visual Wulst is organized from dorsal to ventral in four layers (old and new names are given): hyperstriatum accesorium/ hyperpallium apicale (HA), intercalated nucleus of the hyperstriatum/ nucleus interstitialis hyperpallii apicale (IHA), hypertriatium intercalatus superior/ hyperpallium intercalatum (HIS), and hyperstriatum dorsale/ hyperpallium densocellulare (HD). No lateralization is found in the thalamofugal pathway in pigeons[259,261].
- Nuclei in the accessory optic system (AOS) and pretectum: There are connections to numerous brain areas[262,263], however most studies have focused on the connection to the cerebellum[264–266]. The AOS and pretectum are important for the analysis of optic flow and the generation of the optokinetic response to control posture and stabilizing eye movements.

Generally speaking the tectofugal pathway would be described as the major pathway in birds. The optic tectum is quite large compared to other vertebrates and the tectofugal pathway is generally regarded as the primary route of visual information to the telencephalon[267]. About 75-95% of ganglion cells have axons leading to the tectum[224]. In contrast GLd in the thalamofugal pathway does not receive input from the complete retinal field, but e.g. for pigeons results in a frontal blindness due to a paucity of ganglion cells in the “red field” of superiotemporal retina[224,268]. For pigeons the left hemisphere dominates visual processing thereby preferentially encoding local cues whereas the right hemisphere prefers global encoding[259].

There have been a number of anatomical, immunohistological, developmental, and electrophysiological studies investigating the avian tectum in more detail[269–274]. It is responsible for the generation of orienting movements to stimuli of interest and consists of a laminated structure with 15 layers. It is retinotopically organized with the nasal-temporal dimension of the retina represented along the rostro-cauda axis of the contralateral optic tectum. Of the connections where retinotopy is maintained the isthmal nuclei, including magnocellular nucleus isthmi (Imc), parvocellular nucleus isthmi (Ipc) and the nucleus semilunaris (SLu), is the most studied[244]. Electrophysiological studies have shown that the tectal cells are center-surround organized and best respond to a spot moving through an excitatory center as the background is moving in the opposite direction[244]. In addition, inactivation of Imc and Ipc by injection of lidocain abolished the excitatory center and inhibitory surrounding[244]. In general Imc and Ipc neurons have receptive fields consisting of a central vertically oriented excitatory strip surrounded by inhibitory regions[244,275]. Simultaneaously, Imc neurons, which are GABAergic, project heterotopically to the tectum, SLu and Ipc, effectively inhibiting activity throughout the tectum, except at the one locus[244,274,276].

It is shown by single cell electrophysiology that the nucleus rotundus can be divided in several functionally distinct subdivisions, including luminance, color, two dimensional motion and motion in depth (3d)[277]. The regions consists of excitatory and inhibitory cells, e.g. for luminance 68 out of 109 cells responded to a change in luminance where 38 showed an excitatory and 30 an inhibitory response[277].

Such a behavior with about equal contribution of both inhibitory and excitatory cells may be problematic for neurovascular imaging where spatial resolution can not resolve such fine structures therefore averaging over both responses and thereby reducing the total response.

3 Anesthesia

For any surgery (which is necessary for the preparation for ultrasound measurements) as well as any painful manipulation on the pigeon it is necessary to induce an adequate anesthesia and analgesia. Furthermore anesthesia can be used to minimize motion artifacts which is of utmost importance both for diffusing wave spectroscopy (DWS) as well as functional ultrasound (fUS) measurements. Introducing a stable narcosis in pigeons over a time of up to several hours has not been implemented at this university before. Furthermore it is well known that birds are high risk patients with a high number of critical incidents and there is no consent about the best narcotic setting in the literature. In addition for the DWS and fUS experiments not only a stable narcosis but also minimal variation of physiological parameters and an as much as possible unchanged neural activity and coupling of this activity to blood flow (neurovascular coupling) is desired.

Thus a brief introduction in general anesthesia and the required equipment with a specific focus on birds is given. The different possibilities of anesthesia in birds are briefly reviewed. In addition an extended discussion about the effect of anesthetic drugs with a focus on the effects on neurovascular coupling as well as on blood flow and physiology will be given. It has to be noted that in contrast to human anesthesia there is no general consent on how to perform anesthesia in pigeons and one gets contradictory advices by different experts[278,279]. In particular the effect of anesthesia on neurovascular coupling in pigeons has not been described in literature. This is however a very crucial point for the experiments in this study which might need further optimization.
Finally results from injection and different inhalation anesthesia will be given with a detailed description of the current setting and future optimizations.

3.1 Literature

Anesthesia is a reversible progress that renders a patient unconscious, provides muscle relaxation, amnesia and freedom of pain (analgesia)[280]. Even though anesthetics have been used for more than 160 years the full mechanism of action of anesthetics is still not known. A complete review of the state of research is beyond the scope of this thesis (for selected reviews see[281–287]), however some of the major sites of action should be shortly described because they have been the starting point for a combined drug therapy with the aim to reduce the amount of isoflurane needed for anesthesia. The description follows[281].

It is generally accepted that there is not one universal principle of general anesthesia for all anesthetics but rather different molecular mechanisms that effect various structures in the nervous system and lead to the state of narcosis[281,289]. Anesthetics influence both voltage gated as well as ligand gated ion channels (see table 3.1). Ligand gated ion channels are responsible for the synaptic signal transmission. The most important excitatory neurotransmitter in the nervous system is glutamate which opens ion channels by binding to glutamate receptors (e.g. AMPA, NMDA, Kainat). This leads to a depolarization of the cell membrane and if the threshold potential is exceeded to an action potential. The inhibitory neurotransmitter (e.g.

Table 3.1: Physiological and pharmacological role for ion channel targets of anesthetics. Modified after[281,288]. Abbreviations: GABA: γ-aminobutyric acid; NMDA: N-methyl-D-aspartate; NMDA: N-methyl-D-aspartate; AMPA: α-amino-3-hydroxy-5-methyl-4-isoxazolepropionic acid; HCN: hyperpolarization-activated cyclic nucleotide-gated

	Ion channel	Cellular function	Physiological and pharmacological effect
ligand gated	**GABA$_A$ receptor**	Increased Cl^- permeability, membrane hyperpolarization, inhibition of excitability	Anxiolysis, sedation, amnesia, anticonvulsive action, muscle relaxation
	Glycine receptor	Increased Cl^- permeability, membrane hyperpolarization, inhibition of excitability	Spinal reflexes, startle impulse, major inhibitory receptor in spinal cord
	Nicotinic acetylcholine receptors	Increased permeability of monovalent cations and calcium, release of neurotransmitters	Memory, nociception, autonomic functions
	Serotonin receptors	nonspecific cation conductance leading to membrane depolarization	Alertness, nausea, nociception, neural excitation
	Glutamate receptors (NMDA, AMPA, Kainat)	Fast excitatory neurotransmission, increased permeability of calcium, sodium and magnesium	Perception, learning and memory, nociception (NMDA)
voltage gated	**Potassium-2P-Channels**	Modulation of resting potential and excitability membrane repolarization	Mood regulation, alertness, nociception
	Sodium channel	Generation and propagation of action potentials	neural oscillation in thalamus, nerve conduction
	HCN channel	activation by hyperpolarization, control by cyclic nucleotide, accelerated depolarization	neural pacemaker, generation of thalmic oscillations

Table 3.2: Effect of anesthetics on ion channels. ↑: enhancement, ↓: reduction, o: no effect, -: no data, ↑↑/↓↓: secure data for enhancement/reduction at clinical relevant doses. Modified from[281].

Ion channel	GABA$_A$ receptor	Glycine receptor	Nicotinic acetylcholine receptors	NMDA receptor	AMPA receptor	Kainat recpetor	Serotin (5HT$_3$) receptor	T-type calcium channel	Potassium-2P channel	HCN channel
Isoflurane	↑↑	↑↑	↓↓	↓	↓↓	↑↑	↑↑	↓	↑	↓
Ketanest	↑/o	o	↓↓	↓↓	o	o	o	↓	-	↓

GABA) lead to a hyperpolarization and reduces the cellular excitability. Voltage gated ion channels are opened if the voltage over the cell membrane is changed and thereby regulate cellular activity and excitability[281].

The GABA$_A$ receptors with β_3 subunit are responsible for the hypnotic component of isoflurane, while immobility is produced by modulation of NMDA- , Glycine-, GABA$_A$ receptors and Potassium-2P-Channels[289]. In contrast the GABA receptor is irrelevant for ketanest[290]. The effect of isoflurane and ketanest on ion channels is shown in table 3.2.

3.1.1 Stages of anesthesia

In general one discriminates 4 stages of anesthesia (Guedel's classification)[291], which however have only limited applicability for birds. Therefore a modified scheme differentiating between light, medium and deep anesthesia[292,293] is used.

However it is quite difficult to discriminate the different stages in birds. For a quantitative assessment a reflex score developed by Korbel et al.[294] is used (see Korbel Reflex score on page 169). Note however that the eye is not always a reliable indicator. In some cases, even in deep anesthesia, a reaction of the eye has been observed.

The extend of the stages greatly differs between different anesthesia schemes, but also between individuals. For example a pronounced excitement is mostly observed with ketanest/xylazine whereas with isoflurane as a single agent this is usually not very pronounced and only lasts for a short time. In contrast this stage is already more often observed in awakening when isoflurane was used in combination with midazolam.

One can discriminate three schemes of anesthesia: injection anesthesia where the anesthetics are applied i.m or i.v., inhalation anesthesia where the anesthetics are vaporized and delivered via inhalation and air sac perfusion anesthesia where

Table 3.3: Stages of avian anesthesia. Table copied from [293].

Anesthetic Plane	Reflexes Present	Reflexes Absent	Expected Physiological Parameters	Comments
I. Induction	All	None	Sedate, lethargic, eyelid droop. Breathing deep or shallow, rapid and irregular based on patient excitement	
II.	All	None, eyes closed	Feathers ruffled, head hangs down, arousable but does not resist handling. Increased third eyelid movement	Excitatory phase may occur here
III. Light	Palpebral, pedal and cere present but slow. Corneal, withdrawal, pain on feather pluck	Lack of voluntary movement, no response to postural changes	Rapid, regular, deep respirations, no response to sound. Some jaw tone present	Preferred plane for minor non-painful procedures
IV. Medium Surgical	Corneal present but sluggish	Palpebral, pedal, cere withdrawal, pain of feather pluck	Good muscular relaxation, slow, deep, regular respiration. Little jaw tone	Preferred plane for surgery
V. Deep	None, lack of corneal	All	Respiration is slow and shallow to intermittent. Pupillary dilation	Death ensues, emergency pending

a special air sac catheter is introduced into the left caudal thoracic air sac and anesthesia is induced by retrograde perfusion of the air sac with an inhalation anesthetic. Only the first two have been used in this study and will be described in detail. For details on air sac perfusion anesthesia see [293,295,296].

3.1.2 Injection anesthesia

The method of choice with the least complexity of instruments needed to induce anesthesia is by administering an injection anesthetic. Drugs can in principle be applied i.m., i.v. , i.o., i.n. or i.p. (not common in birds). However only the first method will be described because all the others require additional preparation and have not been performed during this work.

Mostly ketamine is used in combination with either an α_2-agoniste (e.g. xylazine, medetomidine) or with a benzodiazepine (e.g. midazolam, diazepam[297,298]). As an alternative a completely antagonizable injectable anesthesia[299] with medetomidine (0.35mg/KG) + midazolam (4.5mg/kg BW) + fentanyl (0.006mg/kg BW) which may be antagonized by atipamezole (2mg/kg BW) + sarmazenil (0.6 mg/kg BW) or flumazenil + naloxone (0.16μg/kg BW) may be used. Other possibilities can be found in[293,296].

For the i.m. application the puncture is performed in the M. supracoracoideus paramedian of the keel (carina) at the cranial third of the sternum[296]. Then one tries to aspirate blood and if none can be aspirated the drug is administered. After administration the area is shortly massaged to accelerate the uptake of the drug and the pigeon is put back to the cage until loss of consciousness is induced.

Propofol, urethane and α-chloralose which have often been used in neuroimaging studies are not commonly used in birds.

The main advantage of the injection anesthesia is the small amount of equipment which is needed, but the effect of the drugs varies strongly between individuals and at least for i.m. application the narcotic depth can not be controlled precisely. Also, for ketanest/xylazine, a pronounced excitation stage is observed during induction and recovery with a long reconvalescence. Furthermore the duration of the narcosis can not easily be adjusted because the effect of repeated drug doses depends on individual pharmacokinetics and can not easily be predicted. This results in stronger variations in baseline physiological parameters.

3.1.3 Inhalation anesthesia

Inhalation anesthesia uses inhaled gases which induce general anesthesia. There are several inhalation anesthetics available: isoflurane, sevoflurane, desflurane, enflurane, methoxyflurane, halothane (historic diethyl ether, chlororphorm) and relative new xenon. Nowadays usually isoflurane or sevoflurane are used for birds[294].

The partial pressure difference of the gases between different compartments (e.g residual volume/blood or blood/tissue) is the driving force of diffusion, not the concentration. The wash-in time is determined by the partial pressure of the inhalation anesthetic in the breathing air. The absorption in the blood is determined by the perfusion of the lung and the blood/gas partition coefficient. If the solubility of the gas in the blood is high, more gas can be dissolved in the blood until it is saturated. Therefore a high blood/gas partition coefficient leads to a slow increase of partial pressure in the blood which results in a bad controllability of the inhalation anesthetic and a slow induction of anesthesia. A high tissue/blood partition coefficient results in a slow concentration increase in the tissue. A high fat/blood partition coefficient is based on an accumulation in lipids which results in a cumulation in fatty tissue during long narcosis which leads

Table 3.4: Physical and pharmacological properties of inhalation anesthetics. Table copied and translated from[300].

Substance	partition coefficient[1]			MAC[2] (Vol%)	boiling point[3] (°C)	vapor pressure[4] (mmHg)	rate of metabolization %
	Blood/ Gas	Tissue/Blood					
		Brain	Fat				
Halothane	2.3	2.9	51	0.8	50.2	243	20
Enflurane	1.8	1.4	36	1.6	56.5	175	2.5-8.5
Isoflurane	1.4	2.6	45	1.2	48.2	250	< 0.2
Desflurane	0.45	1.3	27	6.0	22.8	664	0.02
Sevoflurane	0.65	1.7	48	2.0	58.5	160	3-5
Nitrous oxide	0.47	1.1	2.3	104.0	-88.5	gas	0.004
Xenon	0.12	-	-	70.0	-107.1	gas	0

[1]: at 37°C
[2]: MAC minimal alveolar concentration for an adult in pure oxygen
[3]: at 760mmHg
[4]: at 20°C

to a slower recovery[300].

In inhalation anesthetics the narcotic depth directly correlates with the partial pressure of the anesthetic at the brain. Changes in the partial pressure leads to a flattening or deepening of the narcosis. During the wash-in phase the partial pressure of the anesthetic is higher in the inhalation air than in the blood and tissue. During maintenance phase the partial pressure in the tissue approaches the partial pressure of the inhaled air. During wash-out the relation reverses and the partial pressure in tissue is higher than in the inhaled air.

The potency of an inhalation anesthetic is given by the MAC (minimal alveolar concentration). It describes the concentration where 50% of the patients do not react on a specific pain stimulus (pull away the arm on skin incision)[301][1]. The important point for the elimination of the motor reaction is the concentration at the spinal cord but the narcotic depth depends on the concentration at the brain[2]. Even though the MAC value is a parameter for the elimination of spinal cord reflexes it is usually (wrongly) used as a parameter of anesthetic power. Therefore one has to be careful generalizing the results from MAC to the effect on other tissues, but for most practical applications they are reasonable well coupled.

---

[1] there are other MAC definitions such as MAC-awake, MAC-E$_{95}$, MAC-BAR$_{95}$ which have more practical relevance however since even the normal MAC is only imperfectly known for pigeon, only the dependence of MAC on various factors is discussed.

[2] GABA$_A$ receptors with β_3 subunit are important for the hypnotic effect but motionlessness is produced by proportionate modulation of NMDA, Glycin, GABA$_A$ receptors and potassium-$_{\text{2P}}$-channels[281]

The MAC varies between substances and species. The literature values for the $\text{MAC}_{\text{Isoflurane}}$ of homing pigeons shows a considerable variability: Smith et al.[302] reported a value of 1.45%, Fitzgerald et al.[303] found a minimal anesthetic dose of $1.51 \pm 0.15\%$ whereas a concentration of 2.7% is reported in[296].
Furthermore it is well known that the MAC can be influenced by a number of other factors which are summarized in table 3.5:

Table 3.5: Factores influcening the MAC value in inhalation anesthetics. Translated from[301].

reduction	increase
opiods	
sedatives, hypnotics, anesthetics	
increased age	
hypothermia	hyperthermia
gravidity	
acute alcohol abusus	chronical alcohol abusus
drugs that decrease catecholamine concentration in the central nervous system	drugs that increase catecholamine concentration in the central nervous system
Lidocaine	

It is known that many anesthetic agents, including isoflurane, influence the coupling between neural activity and vascular response (for details see 3.1.6). It is therefore desirable to reduce the $\text{MAC}_{\text{Isoflurane}}$ in neuroimaging experiments as much as possible to minimize anesthetic side effects.
In human anesthesia this is mostly achieved by a balanced anesthesia with a combination of opiods, benzodiazepines and muscle relaxants where a reduction of up to 90% is reported[301]. Furthermore a combination with N_2O can also reduce the MAC in humans[301]. The effect is less studied in birds and there is not yet a reference protocol which can be followed and only a very limited number of publications are available:
Smith et al. reported a profound sedation and reduced isoflurane MAC of approximately 38%[302] (30-70%[304]) with midazolame (15mg/kg i.m.) in pigeons. Benzodiazipine seem to be a good choice due to the modulation of GABA-A receptor[305].
After personal communication[306] a first attempt to reduce the required isoflurane concentration is made with 5mg/kg BW midazolame (see experiments 3.2.2).

All inhalation anesthetics cause vasodilation, hypotension, myocardial and respiratory depression to some degree[280]. Other side effects which are observed are nausea, vomiting, ilius and cardiac arrhythmias. In particular cardiac arrhythmia, vasodilation and hypotension may have negative effects for functional hemodynamic imaging.

3.1.4 Drugs

A short description of the drugs used throughout this work. The doses which were used in this work are also given as a reference.

Isoflurane is a halogenated ether which is used for inhalation anesthesia. The effect on various ion channels have already previously been described (see table 3.2). [Dose 1.0.-3.5%]

Ketamine is used to start and maintain anesthesia as well as an analgesic. It has hypnotic effects by blocking the ligand gated NMDA receptor by binding to the phencyclidine binding site and binding to the HCN1 receptor. The analgesia and sedation is modulated by the cholinergic, aminergic, and opioid systems. Ketanest does not result in muscle relaxation and the bird can be very excitable during recovery. It should therefore not be used as a single agent, but may be used in combination with α_2-agonist or benzodiazepine. The half life is about 15min (alpha phase) to 2.5 hours (beta phase). [Dose: 25mg/kg]

Xylazine is a α_2-agonist which is used for sedation, anesthesia, muscle relaxation and analgesia. It is often used in combination with ketanest. A pronounced bradycardia is triggered by the α_2-agonistic effect. [Dose: 5mg/kg]

Midazolame is a short acting central nervous system depressant of the benzodiazepine class. It possesses anxiolytic, sedative, hypnotic, anticonvulsant and skeletal muscle relaxant properties and is mostly used as a premedication for sedation in general anesthesia. Midazolame modulate GABA effects by binding to a specific, high-affinity site (distinct from the GABA-binding site of isoflurane) located at the interface of the α and γ subunit of the GABA_A receptor. This increases the frequency of channel openings produced by GABA. Thereby the effect of GABA is enhancing which results in a neural inhibition. In humans it has a half-life of one to four hours. [Dose 5mg/kg]

Flumazenil is a GABA receptor antagonist that can rapidly reverse the effects of benzodiazepines by competitively inhibiting the activity at the benzodiazepine recognition site of the GABA/benzodiazepine receptor complex. The half-life is about 1 hour. [Dose 0.1mg/kg]

Meloxicam is a nonsteroidal anti-inflammatory drug (NSAID) with analgesic effects due to blocking of the cyclooxygenase (COX) with a higher inhibition of COX-2 than COX-1. [Dose 0.5mg/kg]

Buprenorphine is a long acting partial opioid agonist at the μ-opiod-receptor. It has also antagonistic effects at the δ- and κ-opioid-receptors[3] and agonistic effects on the nociceptin (ORL-1) receptor. The analgesic effect is about 6-8h. Note that buprenorphine has a bell shaped dose effect curve which results in a smaller analgesic effect if the dose is further increased at the maximum of effect. The analgesic potency is about 30 times that of morphine. [Dose 0.5mg/kg]

---

[3] Note that other authors also found agonistic effects at the δ- and κ-opioid-receptors (see[307] for details)

Butorphanol is a synthetic opioid analgesic with partial agonist and antagonist activity at the μ-receptor, as well as competitive antagonist activity and partial agonist activity at the κ-receptor. The analgesic potency is about 5 times that of morphine and the analgesic effect has a duration of about 2-4h. The plasma elimination half-life time is about 2.4 hours for pigeons. [Dose 1mg/kg]

3.1.5 Physiological parameters of a pigeon

Reference physiological parameters of the pigeon can be found in table 3.6. Data about pigeon blood can be found in the appendix 8.2.

Table 3.6: Physiological parameters of a pigeon (Table copied and translated from [299] with some modifications based on additional literature).

Parameter	Unit	Reference value	Literature
Body temperature	°C	39.8-43.3 (cloacal)	[308–310]
Breathing frequency	bpm	20-35	[310–313]
Heart rate	bpm	160-250	[310,314,315]
Blood volume	ml/g	0.1-0.01	[310]
mean arterial pressure	mmHg	106 (local anesthesia)	[315]
arterial O_2 partial pressure	mmHg	95	[316]
arterial CO_2 partial pressure	mmHg	34	[316]
arterial pH	pH	7.46	[316]

3.1.6 Neurovascular coupling

> "Although it is widely appreciated amongst scientific communities that the relationships between activity within heterogeneous neural population and neuroimaging are complex, rather indirect, and incompletely understood, many research papers continue to report neuroimaging signals as 'measures of neural activity', which they are not." [317]
> "Neuroimaging signals arise because of a coupling between changes in neural activity, metabolism, and hemodynamics (blood flow, oxygenation, and volume) in the brain, termed neurovascular coupling" [317].

Neurovascular coupling describes the relationship between neuronal activity and the vascular/hemodynamic response which is measured by most of functional neuroimaging techniques[318,319] and all techniques applied throughout this work. The relationship between the two is very complex and incompletely understood[317]. A detailed review about the current knowledge is beyond the scope of the work. For some excellent recent reviews see e.g.[317,320].

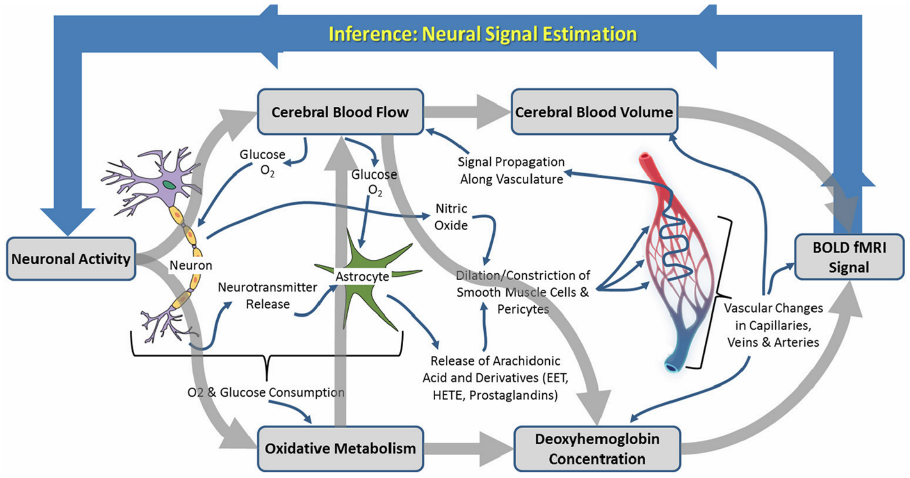

Figure 3.1: Schematic showing neurophysiological processes underpinning hemodynamic neuroimaging signals. The outer gray boxes represents components of the "parametric neurovascular coupling" which are usually used in functional studies to measure changes associated with neural activity. The inner processes detail the physiological factors involved in the coupling ("physiological neurovascular coupling"). The relationship between the depicted biophysical and physiological components, as well as baseline conditions upon which changes are superimposed, may be mediated by a number of factors[317]. This is shown in more detail in figure 3.2. Text follows[317]. Figure copied from[317].

Nevertheless some details which are particular important for this work should be discussed. This description closely follows[317]. Neuroimaging signals arise because of the coupling of neural activity, metabolism and hemodynamics (blood flow, oxygenation and volume)[317] [320–323]. Some of these factors are summarized in figure 3.1. The biomedical or physiological mechanisms are reviewed in greater detail in[320,324–326]. The gray boxes represent components of interest which can be measured with different neuroimaging methods (for a summary see[317] table 1). In addition the interplay between the physiological and biophysical factors are influenced by a number of factors, such as anesthesia, baseline blood flow, brain regions, subject, patient groups and time points which are shown in figure 3.2. This illustrates that the neuroimaging signal in two targets, which may be 1) different brain regions, 2) the same region in different subjects, 3) the same region in the same subject at different times, or 4) the same region before and after an experimental manipulation[317] might result in different results even though the stimulation was the same. Particularly in hemodynamic measurements there is a high degree of inter-trial and inter-subject variability[317]. One should keep this in mind when interpreting the results of any neuroimaging signal.

Nevertheless the validity of e.g. fMRI signal changes as an indicator of altered neural activity in healthy cortical structure has been clearly shown[317] and mathematical models that estimate the hemodynamic response to a single

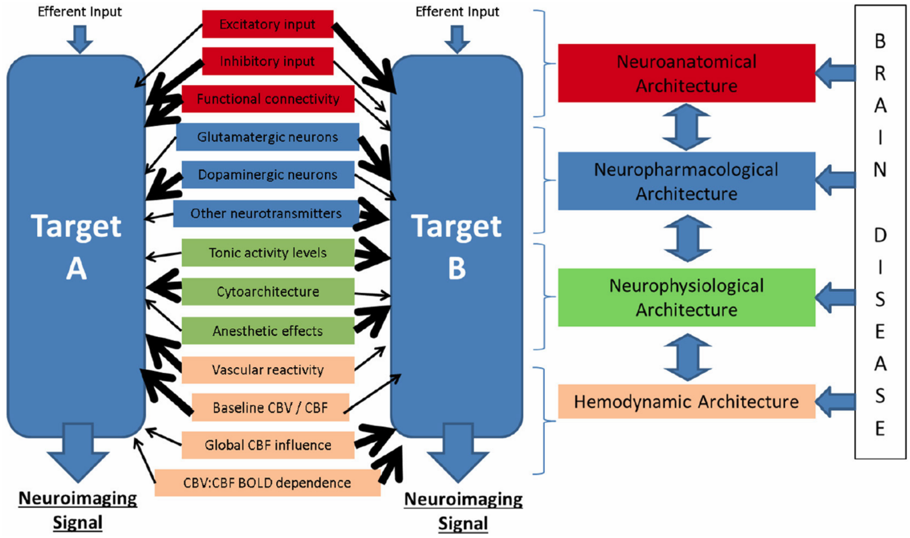

Figure 3.2: The image shows potential modulators of neuronal-neuroimaging signal relationships shown in figure 3.1. If two targets, such as a) different brain regions, b) the same region in different subjects, c) the same region in the same subject at different times or d) the same region before and after experimental manipulations is measured it is important to consider the many possible differences between these targets that might affect the relationship between measured hemodynamic signal and the inferred neuronal events. Text follows[317]. Figure copied from[317].

neuronal event, the so called hemodynamic response function (HIRF), have been developed[327]. Although this is best established for blood oxygenation level dependent (BOLD) fMRI, it is demonstrated by arterial spin labeling (ASL) MRI that there is a tight coupling between BOLD response and cerebral blood flow (CBF)[328]. Note however that Hirano et al.[329] found a discrepancy between BOLD HIRF and CBF HIRF in longer stimulation. For new imaging methods or other species the response function is not very well established and can only be inferred from results of other methods such as fMRI. In addition the HIRF is affected by brain regions, health and disease status, as well as pharmacological and physiological manipulations[330,331]. Also the spatial structure of the HIRF is less well understood[317].

One question is, how to interpret functional brain imaging signals in respect to neuronal activity. Neuronal activity is usually classified in two types: local field potentials (LFPs) and spiking activity. The relative contribution of these two types to the BOLD signal has been extensively discussed where it is generally recognized that neuroimaging signals correlate best with LFPs[332,333], but also correlate with spiking activity in many[332,334], but not all contexts[335–337] [317]. In addition it is important to ask whether the hemodynamic response is linearly or non-linearly related to changes in neural activity. It has been shown by simultaneous measurement of both neuronal and hemodynamic signal that both linear and non-linear patterns of coupling are found[334,338–345] [317].

In the following, spatiotemporal characteristics which add in the complexity of interpreting the results, should be presented:
Although not much research has been performed whether the neurovascular coupling is brain region dependent, the research which has been conducted suggests that it differs between regions[317,346,347]. By studying the positive BOLD response Goense et al.[348] found that the depth profile of BOLD, cerebral blood volume (CBV) and cerebral blood flow (CBF) varied, with a maximum BOLD response at the cortical surface, while CBF was maximal at about layer IV. and CBV increased uniformly throughout the cortical layers. Negative BOLD signals occurred in regions where CBV increased and CBF decreased. Maximal negative responses occurred in the middle cortical layers whereas CBF response was maximal at the surface, and CBV response were largest around layer IV.. They conclude that there are differing neurovascular coupling mechanism operating at different cortical layers and underlying positive and negative BOLD signals[317]. Therefore quantitative comparison between brain regions may be problematic.
In some cases a focal increase in blood flow with an inverted response in the surrounding has been observed[349–352]. This type of response is due to a localized change in blood oxygenation resulting from a mismatch of changes in cerebral blood flow, volume and metabolic rate of oxygen[353] consumption which generate a positive BOLD signal. This is often accompanied by a sustained negative change which is usually, but not exclusively, found in surrounding cortical regions[354]. Boorman et al.[350] found in a rat that the negative BOLD signal occurred in deeper (1-2mm) cortical layers than the positive BOLD signal (0-1mm). These findings have been confirmed by Kennerley et al.[355] who studied whisker stimulation with both high resolution fMRI and concurrent 2D optical imaging spectroscopy quantifying the effect in more detail.
Furthermore Martin et al.[352] suggest that the temporal response has additional complexity in unanesthetized animals with a more dynamic, oscillatory response in the cortex. Both the negative response in the surrounding as well as temporal signal oscillations are supported by a recent theoretical work[356].

Theses findings are further complicated by anesthesia which has effects on various levels: interference with neural processing, alter neurovascular coupling and change physiological baseline[357]. It has been shown that anesthesia disrupts neurovascular coupling in a number of ways[341,351,358–365], including via alterations in baseline hemodynamic parameters[366,367]. Schroeter et al.[357] showed in mice that the temporal characteristics of the BOLD response depends on the anesthetic used and varies across brain regions. In addition they found that the first stimulus always yields the largest response[357,365]. The differences in the response can be largely attributed to differing systemic effects of the stimulation under the four anesthetic conditions that were used in the study[357]. Under normal conditions CBF is maintained at a relatively constant level over a broad range of mean arterial blood pressures (MAP) by adjusting the cerebrovascular resistance (CVR) via constriction and dilation of blood vessels[357]. It is known that this autoregulation mechanism is affected by anesthetics where CBF is becoming increasingly dependent on peripheral blood pressure. This is particularly found in inhalation anesthetics with a dose dependent impairment of autoregulation[368–370] which is presumably related to their vasodilatory effect[371,372] [357].

One consistent finding is that the hemodynamic response is delayed in anesthesia compared to awake animals[341,365,373,374] (also see figure 3.3). This can be nicely seen in a study of Pisauro et al.[365] who used optical imaging in mouse primary visual cortex (V_1) to study the response of mice, both awake and anesthetized (isoflurane (1-2%) and urethane (1g/kg i.p.)), to visual stimulation with moving and flashing bars. They found that the response was twice as fast and four times larger in wakefulness compared to anesthesia. This is in agreement with laser Doppler flowmetry measurements of cerebral blood flow in the somatosensory cortex of mice during whisker stimulation in an awake and anesthetized (1% isoflurane) state. It was furthermore shown by Pisauro et al.[365] with electrode recordings that these changes reflect changes in neurovascular coupling, not neural activity.
A further complication is that different anesthetics disrupt neurovascular coupling in different ways[317].

There is only a limited number of studies systematically comparing the effect of different anesthetic settings on neural response. One particular interesting study has been performed by Franceschini et al.[374] who investigated by EEG and diffuse optical imaging the response to electrical forepaw stimulation with six different maintaining anesthetic (α-chloralose, pentobarbitat, ketamine, fentanyl, isoflurane, propofol) in Sparque-Dawley rats. Strongest changes in the concentration of oxy- and deoxyhemoglobin (ΔHbO and ΔHbR, respectively) have been observed for α-chloralose with a nearly equal response in isoflurane (1.2%). Isoflurane becomes a strong vasodilator at higher concentrations and by either preventing further vasodilation or by saturating cortical tissue with oxygen it may reduce hemodynamic changes in response to stimulation. Smaller hemodynamic responses have been observed for the other anesthetics used. Furthermore they found that the somatosensory evoked potentials (SEP) could be decomposed in four components. Neural input affects secondary and late activity and different anesthetics differently affect neural input and secondary late response[374]. By linear regression analysis they found that the hemodynamic response better correlates with the secondary and late activity than with neural input. In addition they found that baseline blood flow positively affects hemodynamic evoked responses and that neurovascular cou-

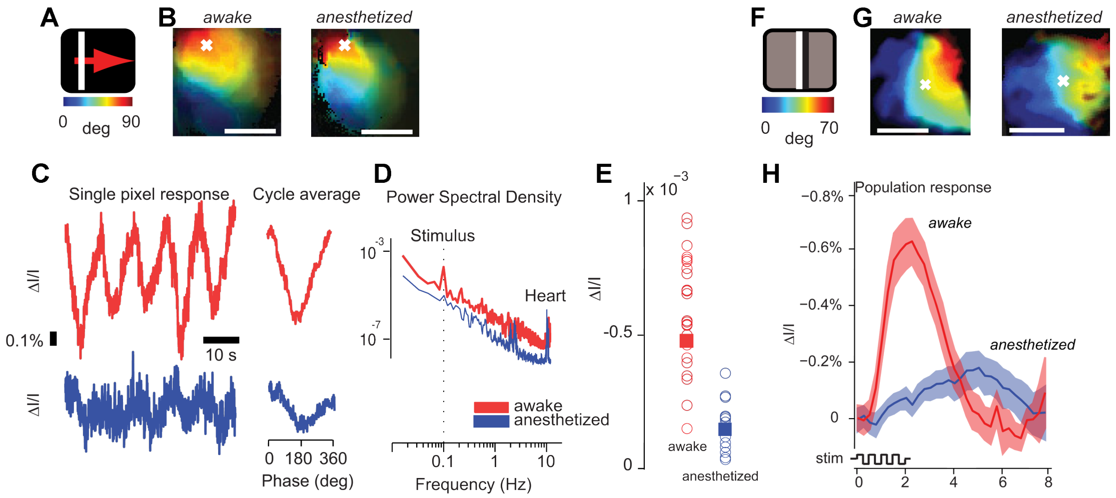

Figure 3.3: Hemodynamic response to periodically moving bars (A-E) and flashing bars (F-H) in mouse V_1 in wakefulness and anesthesia. A) Moving bar stimulus (4° wide drifting at 0.1 Hz for 5 cycles) and color bar mapping degrees of visual field to the position of the bar on the screen. B) Lowpass filtered maps of retinotopy for a mouse in awake (left) and anesthetized (right) conditions. Colors map degrees of visual field on the azimuth. Brightness indicates signal amplitude. Scale bar: 1 mm. C) Time courses of activity for the pixel marked with a white cross in B) for the whole stimulus (left) and averaged across cycles (right), awake (red trace), and anesthetized (blue trace). D) Examples of power spectral density in awake and anesthetized conditions. A peak at frequencies of $\approx$ 10 Hz was present in both responses and reflected the heart rate. Dotted line indicates the frequency of the stimulus. E) Summary of amplitudes for all experiments, 23 awake (red circles) and 19 anesthetized (blue circles). Squares indicate mean amplitudes for each condition.
F: Flickering bar stimulus (15° wide, reversing in contrast at 2 Hz for 2 s) Color bars map degrees of visual field to the position of the bar on the screen. G) Maps of retinotopy for one example animal in awake (top) and anesthetized (bottom) conditions. H) Time courses of average activity for ROI in wakefulness (top, red trace), and under anesthesia (bottom, blue trace). Shaded regions represent ±1 SE. Bottom: Schematic of the luminance change of the stimulus flickering at 2 Hz.
Text and modified figures copied from[365]. Reprint with permission.

pling is constant across anesthetics[374]. Note that this is in contrast to Pisauro et al.[365] who reported an unchanged neural activity in anesthesia and wakefullness, but a much smaller hemodynamic response indicating a change in neurovascular coupling. These smaller changes in anesthesia compared to awake conditions have generally been observed[341,375].

Masamoto et al.[376] investigated the dose dependent effect of isoflurane. They found that the response varied with stimulus frequency, with a dose-dependent increase for low frequency stimulation and a dose-dependent decrease for high frequency stimulation. An increase in CBF response from 7% to 17% have been observed for isoflurane levels of 1.1% and 2.1% while the local field potential was not affected

by the change. In addition a significant decrease in mean arterial blood pressure has been observed while no changes in the baseline CBF have been detected.
A good review summarizing quantitative effects of anesthesia on neurovascular coupling can be found in[377]. They review the effect of anesthetics which particularly highlight the spatial, temporal and quantitative changes due to anesthesia.

Not only neurovascular coupling but also the neural (electrical) activity is changed by the anesthetic. The description is far from being complete but some facts which might be relevant for the forthcoming studies should be noted. Land et al.[378] investigated the effect of visual and auditory stimulation during increasing and decreasing isoflurane level (0.7% to 2.5% and reverse) in the mouse visual cortex V_1 and the subiculum (figure 3.4). They found that auditory evoked burst activity occurred in visual cortex after transition to deep anesthesia while for visual stimuli only the shape of response changed slightly but with nearly unchanged onset and amplitude. The auditory response showed up about 200ms after stimulation in comparison to about 70ms for visual response. It is suggested that this activation is due to cortical spreading which freely propagates across and beyond the typical functional areal orders in deep anesthesia. This view is supported by the finding that both visual as well as auditory evoked bursts occurred in the subiculum during deep anesthesia whereas the subiculum was unresponsive in both stimuli during light anesthesia. Note that this delocalized response has both advantages and disadvantages. On the one hand it may allow for the detection of the response to stimuli even if one doesn't measure over the correct brain regions, which might prove beneficial for detecting changes associated with magnetic stimuli. On the other hand the response is smaller and delayed and functional brain mapping becomes more cumbersome.

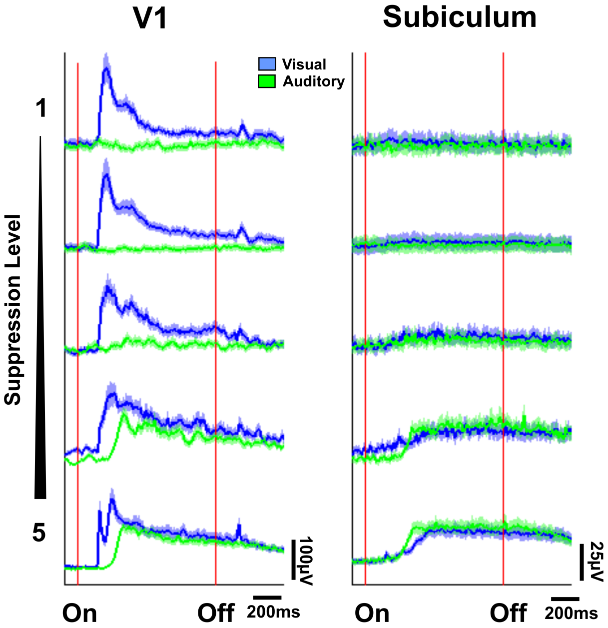

Figure 3.4: Evoked local field potential response for visual (blue) and auditory (green) stimulation in V_1 (left) and subiculum (right) during increasing levels of anesthesia. Figure copied from[378].

Supp et al.[379] studied stepwise drug induced (propofol) loss of consciousness with EEG in healthy humans. They found that the stimulus related response to median nerve stimulation consists of an early and midlatency component in

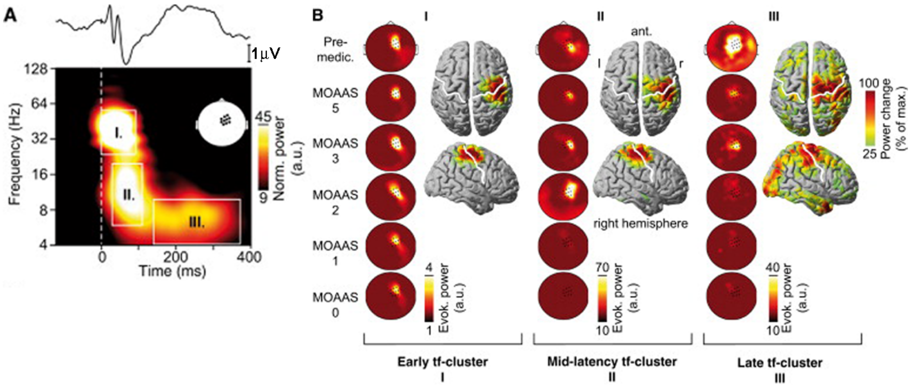

Figure 3.5: The figure shows somatosensory evoked EEG responses during shifts in the state of sedation which was induced by propofol anesthesia. A) Shows a time-frequency representation of evoked responses during premedication. The somatosensory response has three components: early (24–56 Hz, 0–90 ms), midlatency (6–20 Hz, 30–110 ms), and late (4–10 Hz, 140–370 ms). The time trace with the grand average evoked response is displayed above. B) Topographic distributions and source reconstructions of each component (I.,II. and III.) are displayed. The source reconstruction during premedication revealed that the early and midlatency components are largely confined to the contralateral primary somatosensory cortex (S1). Whereas the late response also involved right temporal and parietal brain areas. The topographies display the modulation of each component with increasing sedation, showing a persistent early response across all sedation levels but a breakdown for both, the mid- and late latency component. Text closely follows[379]. Image copied from[379]. Reprint with permission.

the contralateral primary somatosensory cortex (S1) and a late component also involving temporal and parietal regions[379] (figure 3.5). The data shows that during progressive sedation the midlatency and late response are reduced and eventually vanish while the early responses, though modulated, persist during anesthesia. Note that Franceschini et al.[374] found that in particular those late components are predictive for the hemodynamic response.

These effects show that appropriate anesthesia and adjusting its dosage is crucial in obtaining stable and reproducible experimental conditions as well as for the interpretation of the results.

For birds these effects have hardly been studied. Mottin et al.[380] used spectral picosecond optical tomography in zebra finches to study the disruption of the coupling of perfusion and oxidative metabolism which is observed in the first minute after the onset of a sudden functional challenge. They used an anesthesia with 2% isoflurane and measured auditory stimulation in the telencephalon. They found significant changes in the auditory forebrain areas with a short initial dip in Hb and HbO_2 in the first 2-3s after onset of stimulation with non significant results in the rest of the stimulation. A significant increase has been found after stimulation, which is more pronounced in Hb than in HbO_2. The transmittance shows an opposite behavior with an increase after onset of stimulation and a decrease after stimulation.

3.2 Experiments

3.2.1 Injection anesthesia

The pigeon is fasted at the evening before the narcosis. In the morning of the experiment a mixture of 25mg/kg BW ketamine (10%) and 5mg/kg BW xylazine (2%) (after[381]) was injected i.m. into the M. supracoracoideus. The pigeon is then brought back to the cage. Usually about 5-10 minutes after the injection the pigeon was lying flat in the cage in a somnolent state. To prevent a too strong decrease in body temperature the pigeon is placed on a heating blanket and covered with a rescue blanket. The eyes were regularly covered with Thilo Tears® gel (Alcan API:3mg Carbomer /g) to prevent drying.

A great variability both in depth and duration of the narcosis has been observed (from no loss of consciousness up to about an hour of narcosis). Furthermore a pronounced excitation stage both in induction and reconvalescence has been observed in some pigeons. All pigeons took quite a while to fully recover to an awake state (about 1-4h). Nevertheless all pigeons fully recovered from narcosis.

In addition a markedly bradycardia (about 60bpm) and bradycapnie from the α_2-agonist xylazine have been observed.

Figure 3.6 left and middle show one of the first measurements with the same pigeon measured in an awake condition and on the next day with a ketanest/xylazine narcosis as well as an inhalation anesthesia with isoflurane and midazolam in a different bird. It can be nicely seen that the countrate is strongly increased which is due to the better adjustment of the laser and detector on the non-moving pigeon. For the inhalation anesthesia the system was further developed where the countrate can be adjusted to the optimal level. This results in a better signal to noise ratio in the dynamic signal (relative cerebral blood flow (rCBF) - see section 4.1 for details). Furthermore it can be seen that no motion artifacts, which can be seen as positive spikes in the awake case, are observed in the case of narcosis. Finally the pronounced bradycardia observed for ketanest/xylazine can be nicely seen whereas a physiological heart rate is observed for isoflurane.

Thus the injection anesthesia allows for a better adjustment of the measurement equipment with a higher signal to noise ratio, but with changed physiological parameters and a great variability of the narcosis. With i.m. application no titration to effect is possible and also re-injection for an extended measurement time is problematic. Therefore no controlled and stable narcosis for prolonged neuroimaging is possible with this anesthesia scheme.

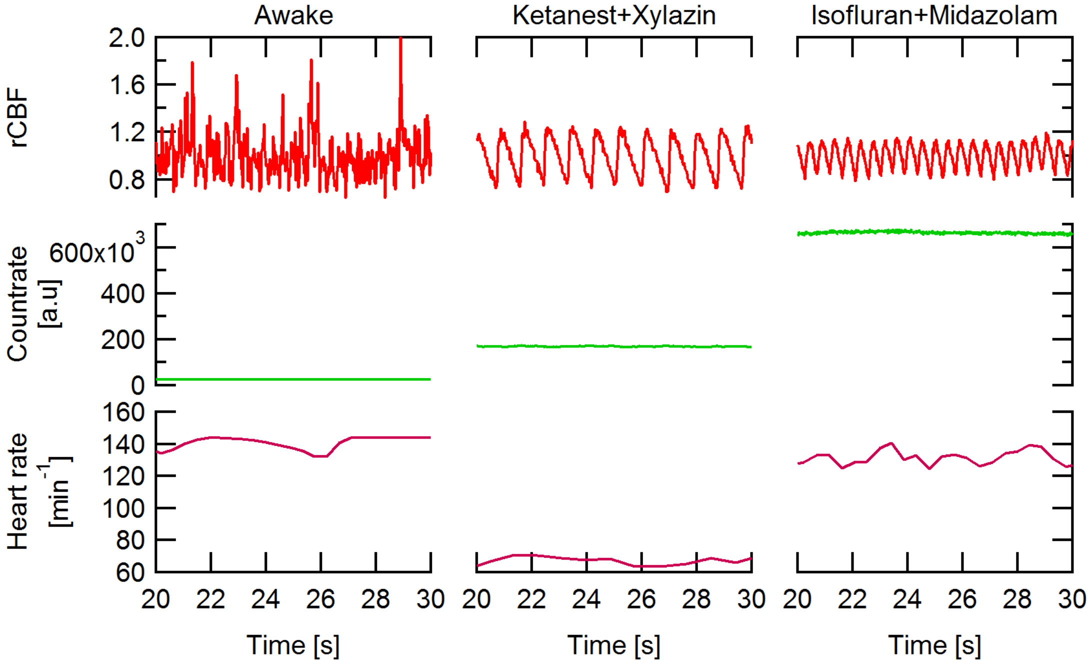

Figure 3.6: Comparison of the optical measurement with diffusing wave spectroscopy with an awake measurement (left), an injection anesthesia with ketamin/xylazine (middle) and an inhalation anesthesia with isoflurane and midazolam in a pigeon. Top shows the normalized diffusion coefficient which is approximately proportional to cerebral blood flow; Middle: Countrate; Bottom: heart rate (extracted from diffusion coefficient). See section 4.1 for details.

3.2.2 Inhalation anesthesia

Three different schemes of inhalation anesthesia have been performed: first a scheme optimized to perform the surgery of thinning the skull of the pigeon, which is necessary for functional ultrasound measurements, was developed with a focus on a general anesthesia (analgesie, amnesia, unconsciousness, immobility) with an adequate analgesia.

In the experiments where only neuroimaging was performed the focus was more on the immobility and it is not necessarily intended to reach the surgical plane. Here the same scheme as for the surgery have been used first. Later experiments were performed with isoflurane as a single agent and in the latest experiments midazolam (5 mg/kg BW i.m.) was used to reduce the isoflurane concentration in order to optimize the neurovascular coupling.

First the general procedure will be discussed. In the later part the additional steps which are necessary for the specific experiment are described.

The pigeon is fasted for about 6-12h before narcosis (usually from late evening over night). Anesthesia is performed with an anesthetic apparatus from Eickemeyer for labratory animals with a custom build gas wash bottle to moisten the gas in order to minimize heat loss. The anesthesia system is half open where waste gases are removed by a custom build suction system. The respirator mask is a small animal mask (size 1) from Eickemeyer. For the anesthesia the animal is placed on a water perfused heat blanket. Anesthesia is induced with 5% isoflurane for about 150-180s and then reduced to the maintenance dose. As an initial guess for the maintenance dose usually 2.5% is used if no experience from previous narcosis is available for the pigeon. The concentration is then further reduced or increased dependent on drug effect. The heartbeat and oxygen saturation is measured by a pulse oximeter (SurgiVet V90041) on the distal end of the M. gastrocnemius or the heel[4] (see figure 3.7). The temperature is measured rectally with a digital thermometer (Voltcraft Multi-Thermometer DT-300). The pigeon is then fixated in a stereotaxic device which has been modified for pigeons.

Figure 3.7: Positioning of the pulse oximeter sensor roughly at the heel or the distal end of the M. gastrocnemius turned out to give the best signal quality.

Anesthesia for surgery:

The pigeon is fasted for about 12h prior to the procedure. At least 30 minutes prior the surgical operation the pigeon is injected with 0.5mg/kg BW buprenorphine (Temgesic 0.3mg/ml) i.m. in the M. supracoracoideus as a preemptive analgesic. The pigeon is placed on a water perfused heat blanket. Anesthesia is induced with 5% isoflurane for about 150-180s and then reduced to the maintenance dose (typically about 2.5-3.5%). When the surgical plane is reached (intended reflex score: 3 after Korbel et al.[294]). The pigeon is fixated in a stereotactic device. The heartbeat and oxygen saturation is measured by a pulse oximeter (SurgiVet V90041) on the M. gastrocnemius. The temperature is measured rectally with a digital thermometer. The eyes are regularly moistened with Thilo Tears®.

---

[4] Literature suggests to position the pulse oxymeter on the M. gastrocnemius of the pigeon. However repeated signal loss with unreliable SpO_2 readings, especially during low perfusion, occurred at this position requiring adjustment. It turned out that it is easier to get a good, stable and reliable signal if the sensor is positioned at the heel of the pigeon

For postoperative analgesia 0.5mg/kg BW buprenorphine i.m. is administered every 12h for at least 3 days as well as three injections of meloxicam (Metacam® 2mg/ml) 0.5mg/kg BW every 4h. In addition one can supply the pigeon once daily with 20-30ml/kg BW s.c. of a mix of Ringer's- and 5% glucose solution (50:50)[382].

Anesthesia for neuroimaging:
First experiments were performed with operated pigeons with buprenorphine 0.5mg/kg BW administered about 30 minutes before induction of anesthesia. After full recovery of the operated pigeons and with non-operated pigeons anesthesia was performed with isoflurane as a single agent.
In later experiments midazolam 5mg/kg BW was administered in addition. In the first experiments midazolam was administered directly before induction of anesthesia. In later experiments midazolam was administered 20-30min before induction of anesthesia to allow the drug to reach full effect. The dose of midazolam is not high enough to induce anesthesia directly.
In some cases an agitation could be observed when isoflurane was turned on which was not observed with isoflurane as a single agent.
Both the time from turning off isoflurane to the first response as well as total recovery was significantly delayed. It takes about 3-4 hours after injection of midazolam till full recovery which is in agreement with the elimination time of midazolam found in humans.

A summary of the maintenance doses which were used in the different anesthetic settings is shown in figure 3.8. The average maintenance dose for isoflurane as a single agent and for isoflurane in combination with 0.5mg/kg buprenorphine is about 3%. The variability to higher doses in the later case results from the need to reach the surgical plane which for some pigeons required very high concentration of isoflurane. For the combination of 5mg/kg midazolam and isoflurane a reduction of about one third with an average maintenance dose of 2% could be achieved, where in some pigeons the maintenance dose could even be reduced as low as 1%. This reduction is in agreement with findings of Smith et al. who reported a reduction of 38%[302] (30-70%[304]).

For all applied inhalation anesthesia schemes the physiological parameters such as heart rate and breathing rate are within the normal physiological range of pigeons (see figure 3.6). The stable anesthesia allows for the optimal placement of the measurement equipment which allows to adjust the measurement parameters such that an optimal signal to noise ratio is achieved.

However some problems with narcosis have also been observed:

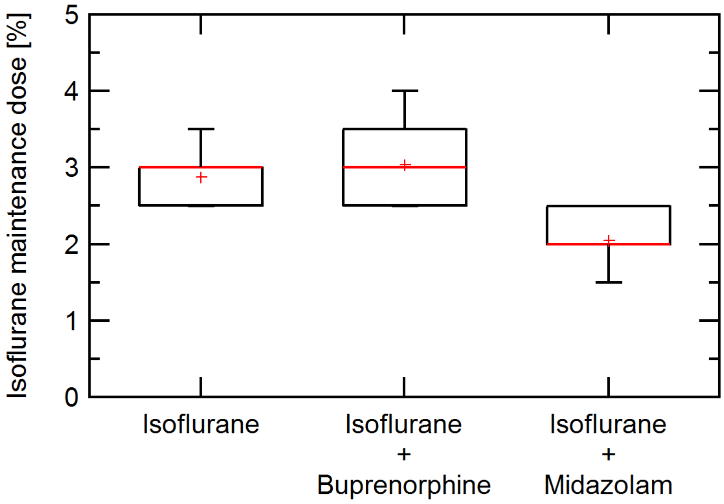

Figure 3.8: Summary of maintenance dose of isoflurane in anesthesia with isoflurane as a single agent (N=39), in combination with buprenorphine (N=14) and in combination with midazolam (N=22). The averge is shown by a red cross, the median by a red horizontal line, the box shows the 25% and 75% quantiles and whiskers 10% and 90%. A reduction in the average maintenance dose from 3% (isoflurane, isoflurane + buprenorphine) to 2% (isoflurane + midazolam) has been observed.

- Initial temperature drop:
  An initial drop in temperature after induction of anesthesia is observed. This is commonly observed with isoflurane[383,384] and is mostly due to a mixing of the colder blood from the periphery and the central blood due to a vasodilation[301,384]. However it has to be noted that while the temperature drop is repeatedly observed in summer times in contrast in winter times one rather has to take care not to get too high temperatures.
  The change in temperature in an inhalation anesthesia is particularly important because the blood/gas partition coefficient is temperature dependent[385,386] and therefore the narcotic depth is also influenced by the temperature. This effect might explain the high dose of isoflurane which is necessary for anesthesia in pigeons. The effect will be discussed in some more detail in section 4.1.5.

- Increased heart rate:
  A slight increase in heart rate over time has often been observed. In some cases a more pronounced increase in heart rate occurred which led to the abortion of the narcosis. The increase in heart rate with isoflurane is also reported in the literature[384].

- Arrhythmia:
  A number of arrhythmia have been observed with isoflurane anesthesia. This

is discussed in more detail in section 4.1.6. A case report of strange, yet not understood behavior is reported in the appendix 8.5. An increase in arrhythmia is well known for isoflurane (see package insert). Also the effect of arrhythmia can be compensated to some extend by advanced signal processing it adds a significant source of noise which makes functional imaging more cumbersome.

- Vasodilation:
  It is well known that higher concentrations of isoflurane lead to vasodilation and a reduction in the mean arterial blood pressure[384]. The blood pressure could not be measured directly in our measurements, but blood flow changes after concentration changes in isoflurane indicate that this is also observed in our experiments (see section 4.1.4 for details). Pronounced vasodilation might be problematic for functional neuroimaging since if the vessels are already fully dilated, the diameter can not be further increased to increase blood flow in response to a stimulus. Furthermore the amount of oxygen might already be sufficient and no increase in blood flow is necessary.

- Strong excitations:
  In some pigeons a very pronounced excitation has been observed which in a few cases could not be overcome and the narcosis had to be stopped. In a few pigeons this was observed in each attempt of anesthesia and the pigeons had to be excluded from future experiments. It is not known if genetic factors such as the one that lead to malignant hyperthermia are responsible for this behavior. Nevertheless all pigeons fully recovered.

- Post narcotic vomiting:
  Vomiting of the pigeons after anesthesia is often observed with a slightly higher occurrence in the case of isoflurane with midazolam compared to isoflurane alone. Post narcotic vomiting after inhalation anesthesia is well known in humans. A slightly longer reconvalescence has been observed but no prolonged adverse effects have been seen.

- Problems in spring:
  In spring it has been repeatedly observed that for about 1-2 weeks a higher number of narcosis problems, such as a more pronounce excitation, strong arrhythmia and unstable physiological baseline values occurred. To the best of the authors knowledge no such effect is reported in literature. However a recent finding which showed a seasonal modulation of GABA[387,388] might give a hint for a possible explanation.

Despite these problems the inhalation anesthesia with isoflurane allows for a stable narcosis which can be maintained even for long imaging sessions with relative stable physiological parameters. In order to further improve the anesthesia it might prove beneficial to intubate and artificially ventilate the pigeon where in particular the end-expiratory CO_2 concentration can be measured and maintained in its physiological range. Also a continuous measurement of the arterial blood pressure and ecg might be helpful for a more detailed analysis of the results.

4 Experiments

4.1 Diffusing Wave Spectroscopy

Diffusing wave spectroscopy is the extension of quasi-elastic light scattering to the multiple scattering regime. Since the development of DWS[389,390] many applications such as particle sizing, microrheology, aging of foams[391,392] and many more have been developed. The principles of multiple scattering was also applied to other waves such as acoustic and seismic waves. About 20 years ago it was realized that DWS can not only be used to characterize average values but also as an imaging tool to measure dynamic heterogeneities[393–395]. Shortly after this discovery the principle was applied to biomedical applications, such as the non-invasive measurement of blood flow e.g. during cuff occlusion[396]. The non-invasive measurement of blood flow is particularly interesting for functional neuroimaging where changes in the cerebral blood flow can be used as diagnostic if certain brain areas are involved in the processing of a presented stimulus.

4.1.1 Motivation

In order to understand the process of magnetoreception it is important to identify the brain regions which are involved in the neuronal processing of magnetic information and how they are altered dependent on the input signal. Considering only non-invasive methods there are in principal two possibilities to do this.

On the one hand direct methods that measure either the electric field (electroencephalography (EEG)) or magnetic field (magnetoencephalography (MEG)) which are strongly affected by interferences of the input field due to induction or directly by the magnetic field itself and therefore makes the use very challenging.

On the other hand one can measure changes which are somehow modulated by neuronal activity. In our case we use the hemodynamic response, in particular the cerebral blood flow (CBF) .

The standard method for functional neuroimaging studies, functional magnetic resonance imaging, is prohibitive due to the large magnetic fields necessary for imaging. Positron emission tomography (PET) and single photon emission computed tomography (SPECT) might work in principal but have low spatial as well as temporal resolution, require costly equipment and require the injection of tracer molecules. An emerging class of experiments uses near infrared light to either probe changes in absorption (blood volume) known as near infrared spectroscopy and/or use the intensity fluctuations of the near infrared light to probe tissue dynamics (blood flow). The later is called diffusing wave spectroscopy (DWS) also known as diffuse correlation spectroscopy (DCS). There is also the frequency domain equivalent of DWS, Laser Doppler flowmetry as well as an emerging technique called laser speckle contrast analysis (LASCA), which uses the contrast of the speckle pattern at specific exposure times. However, with current technology, both techniques are only sensitive to superficial layers. In addition Doppler optical coherence tomography (OCT) and calcium imaging might be used, but they are also limited to superficial structures and therefore require a craniotomy for imaging.

Furthermore ultrasound technology such as functional ultrasound imaging as well as photoacoustic imaging might be used. This will be discussed in a later chapter (see section 4.2).

We decided to use DWS because it was already well established in our group, is non-invasive, has a high temporal and a sufficient spatial resolution for low resolution tomography and is not effected by the low magnetic fields used in this study.

I start with a brief description of the basic theoretical concepts of DWS. This will cover the derivation of the relevant equations (section 4.1.2), which might be skipped for non experts, and a more qualitative discussion (section 4.1.2.3) which is sufficient for a rough understanding of the method. This is followed by a review of validation studies which demonstrate the correlation between blood flow and the signal measured by DWS. For a more detailed view which also covers the progress of recent years the reader is referred to some current reviews[397–402].

Then the experimental set-up in its current stage is described. Furthermore the signal processing and analysis is discussed in greater detail. In addition accidental findings such as the effect of isoflurane concentration, temperature and arrhythmia on cerebral blood are reported. These results are particularly interesting for clinical monitoring during general anesthesia and suggest DWS as a new tool for routine continuous monitoring of cerebral blood flow during anesthesia. Results from functional studies showing validation experiments with visual stimulation as well as measurements during magnetic stimulation are presented. Last a discussion of the results with future prospects will be given.

4.1.2 Theory

4.1.2.1 Light Transport in Turbid Media

In general there are mainly three effects that affect light propagation in biological tissue: refraction, scattering and absorption[403].

4.1.2.1.1 Refraction

One of the fundamental properties of a material is its index of refraction. For a homogeneous medium it is given by:

$$\tilde{n}\left(\lambda\right) = n\left(\lambda\right) - i\alpha\left(\lambda\right) \tag{4.1}$$

where α is the attenuation and encompasses the absorption (and scattering for heterogeneous media) and λ is the wavelength of light in vacuum. The real part

$$\mathrm{Re}\left[\tilde{n}\left(\lambda\right)\right] = n\left(\lambda\right) \tag{4.2}$$

will be referred to as the refractive index. The wavelength in the medium is then given by

$$\lambda_{\mathrm{m}} = \frac{\lambda}{n\left(\lambda\right)} \tag{4.3}$$

The effect of light transmitted or reflected by the boundary depends on the refractive indices, the incident angle and the polarization of the incoming wave. This effect is particularly important on layered tissue like skin (e.g. epidermis, dermis, subcutis) and thereby influences the boundary conditions of the light transport at the border of the medium.

4.1.2.1.2 Scattering

Fluctuations of the refractive index on length scales comparable with the wavelength of light lead to light scattering. Scattering can be quantified by the scattering cross section and for a monochromatic plane wave is given by

$$\sigma\left(\hat{s}\right) = \frac{P_{\mathrm{scatt}}}{I_0} \tag{4.4}$$

where I_0 is the intensity of the incident wave, P_{scatt} is the amount of power which gets spatially redirected and $\hat{s}$ is the direction of the incident wave[403] (see figure 4.2). The angular distribution of the scattered radiation is given by the differential cross section:

$$\frac{d\sigma_{\mathrm{s}}}{d\Omega}\left(\hat{s}, \hat{s'}\right) \tag{4.5}$$

where $\hat{s'}$ defines the axis of a cone of solid angle $d\Omega$ originating at the scatterer. At first we will assume that the particle is spherically symmetric, so that the scattering cross section does not depend on the relative orientation of the incident light and the orientation of scatterer. A medium with a uniform distribution of identical scatterers can be described by the scattering coefficient

$$\mu_{\mathrm{s}} = \rho\sigma_{\mathrm{s}} \tag{4.6}$$

where ρ is the number density of scatterers. The scattering mean free path

$$l_\mathrm{s} = \frac{1}{\mu_\mathrm{s}} \tag{4.7}$$

is the average distance a photon travels between consecutive scattering events. The transport mean free path l^* is the length scale over which the direction of light propagation is randomized and is related to the mean free path by:

$$l^* = \frac{l_\mathrm{s}}{1 - \langle \cos(\vartheta) \rangle} \tag{4.8}$$

where ϑ is the scattering angle and $\langle\rangle$ is the ensemble average over many scattering events.

In biological tissue scattering is the dominant mechanism affecting light propagation. It can be characterized by three regimes determined by the relative ratio of the size of scatterer compared to the wavelength:
(i) the Rayleigh limit, where the size of the scatterer is small compared to the wavelength, (ii) the Mie regime, where the size of the scatterer is comparable to the wavelength and (iii) the geometric limit (Fraunhofer diffraction), where the size of the scatterer is much larger than the wavelength. The first two regions are the most important in biological tissue.

Rayleigh limit The Rayleigh limit involves scattering of light by structures much smaller than the wavelength, like membranes, cellular subcompartments and extracellular components such as the banded ultrastructure of collagen fibrils[403]. In this case, the scatterer “sees” a uniform electric field and therefore can be assumed to be point-like, thus emitting dipole radiation. In the Rayleigh limit the differential cross section for a spherical particle with radius a illuminated with unpolarized light is given by

$$\frac{d\sigma_\mathrm{s}}{d\Omega} = 8\pi^4 n_\mathrm{m}^4 \left(\frac{n_\mathrm{s}^2 - n_\mathrm{m}^2}{n_\mathrm{s}^2 + 2n_\mathrm{m}^2}\right)^2 \frac{a^6}{\lambda^4}\left(1 + \cos^2\vartheta\right) \tag{4.9}$$

where n_m and n_s are the refractive indexes of the medium and the scatterer, respectively and ϑ is the angle between the incoming light and the outgoing wavevector. The differential scattering cross-section is symmetric about $\vartheta = \frac{\pi}{2}$ for polarizations of the incident wave parallel and perpendicular to the scattering plane. Hence backscattering has equal probability as forward scattering (“isotropic scattering”) thus $\langle \cos\vartheta = 0 \rangle$ and $l^* = l_\mathrm{s}$[404].
The Rayleigh-Debye-Gans theory extends the Rayleigh limit under certain conditions to arbitrarily shaped particles by superposing the scattered field from infinitesimal small scattering volumes. This ansatz is valid provided the phase shift

is sufficiently small during the crossing of the waves through the particle:

$$2ka\left|\frac{n_\mathrm{s}}{n_\mathrm{m}}-1\right| \ll 1 \tag{4.10}$$

For the calculation of the resulting scattered wave amplitude under an angle ϑ one has to account for the shape of the particle by multiplying an angle dependent form amplitude

$$f\left(\vartheta\right)=\frac{1}{V}\int \exp\left(i\vec{q}\vec{r}\right)dV \tag{4.11}$$

which results in an additional form factor of $\left|f\left(\vartheta\right)\right|^2$ in the intensity compared to Rayleigh scattering[405]. Therefore the scattering is not isotropic anymore and $l^* \neq l_\mathrm{s}$.

Note that the assumption of equation 4.10 is not valid for human red blood cells (RBC) with an average volume of 90fl which corresponds to a sphere with an equivalent radius of about 2.78 µm. The refractive index of a RBC is about $1.39-1.42$ and the refractive index of the surrounding serum is close to water which results in a relative refractive index of about 1.05. The laser which is used in the measurements has an wavelength of about 0.8µm. Therefore $2ka\left|\frac{n_\mathrm{s}}{n_\mathrm{m}}-1\right| \approx 2.18 > 1$. For the blood of pigeons with an average volume of the RBC with about 201fl (see appendix 8.2) an even larger value of 2.85 results. In this regime one has to apply Mie theory or approximations thereof.

Mie Scattering Scattering by arbitrarily large spherical particles can be described by Mie scattering. In practice it is applied in the medium wavelength range where the Rayleigh and geometric approximations are not valid. The theory of Mie scattering has been first derived by Gustav Mie in his article on the optical characteristics of turbid tubes, especially colloidal metal solutions in 1908[406]. He basically solves the Maxwell equations in a medium with strongly scattering spheres. In order to solve the equation he expands the electrical fields of the incident and scattered light in a power series of emitting spherical wave functions as well as the internal field in the particle as a regular spherical wave function. With the boundary conditions on the surface of the sphere one can determine the coefficients of the expansion.

The equations can only be solved analytically for highly symmetrical problems, but numerical approximations can be applied to solve the problem for other shapes.

As a result one gets a higher intensity in the forward direction which increases with increasing particle sizes[405]. Therefore the incident direction of the light is partially preserved and the scattering is not randomized after a single scattering event. Hence $l^* \geq l_\mathrm{s}$.

4.1.2.1.3 Absorption

Absorption is an important process in the biomedical photonics framework because specific transitions can be used in diagnostic and therapeutic applications. The most important mechanisms for absorption are transitions between electronic levels (UV-IR region), vibrational transitions (IR) and rotational transitions (far IR to submillimeter wavelength)[403]. While in many biomedical applications these transitions can be used for diagnostic purposes diffusing-wave spectroscopy is usually negatively affected by absorption because it limits the maximal path length in the tissue.

For a localized absorber the absorption cross section can be defined analogous to the scattering cross section:

$$\sigma_{\mathrm{a}} = \frac{P_{\mathrm{abs}}}{I_0} \tag{4.12}$$

where P_{abs} is the amount of power absorbed out of an initially uniform plane wave of intensity I_0. A medium with a uniform distribution of identical absorbing particles can be characterized by the absorption coefficient:

$$\mu_{\mathrm{a}} = \rho \sigma_{\mathrm{a}} \tag{4.13}$$

with ρ the number density of absorbers. With the absorption coefficient one can again define an absorption length:

$$l_{\mathrm{a}} = \frac{1}{\mu_{\mathrm{a}}} \tag{4.14}$$

For a homogeneous (non-scattering) medium with absorption coefficient μ_{a} the intensity I after distance s is given by the Beer-Lambert law:

$$I = I_0 \exp\left(-\mu_{\mathrm{a}} s\right) \tag{4.15}$$

For a scattering medium the modified Beer-Lambert law, which considers the longer path length of the photons due to scattering as well as the boundary conditions due to the geometry of the experiment, can be applied:

$$I = I_0 \exp\left(-\mu_{\mathrm{a}} \mathrm{DPF} \rho + G\right) \tag{4.16}$$

where DPF is the differential path length factor, ρ the geometric distance between source and detector and G a geometric factor.

In order to minimize the effect of absorption in biologic tissue DWS measures in the so called therapeutic window in the range of 600-1300nm, which is mainly given by absorption of hemoglobin below 600nm (and many more biomolecules at even shorter wavelength) and the absorption of water above 1300nm (see figure 4.1). In this wavelength range scattering is dominant over absorption and the propagation

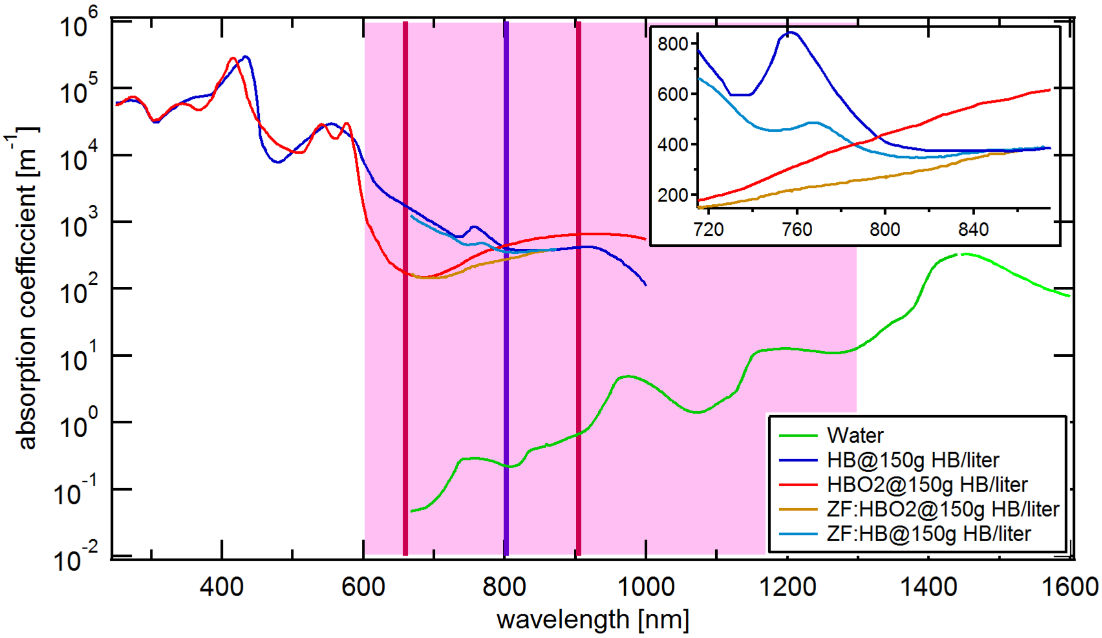

Figure 4.1: The so called therapeutic window (light pink) between 600-1300nm where absorption is relatively low is shown. It is mainly given by the absorption of water (green - data from[407]) at long wavelength and the absorption of hemoglobin (and other biomolecules) at short wavelength. Absorption data of human oxygenated (red) and deoxygenated (blue) blood (data from[408,409]) and oxygenated (orange) and deoxygenated (light blue) blood from zebra finch (data from figure 3 in[410] scaled to 150g/L HB) is shown.

The ratio of oxygenated and deoxygenated blood is used in pulse oximetry to measure oxygen saturation (vertical pink lines of 660nm and 905nm). The wavelength of the DWS measurement which is approximately at the isosbestic point of human blood is shown by purple vertical line at 802nm. In the inset it can be nicely seen that the isosbestic point in zebra finches is shifted to about 870-880nm.

of light becomes diffusive[403].

Since we are not interested in the effects of oxygenated and deoxygenated blood DWS experiments are performed at the isosbestic point of oxy- and deoxyhemoglobin at 800nm where the molar extinction coefficient is the same for both species. Note that a recent study[410] found that the absorption coefficients of blood from zebra finches are different from those found in humans and that the isosbestic point is shifted to about 870-880nm (see figure 4.1). No absorption data for the blood of pigeon is available.

4.1.2.2 Diffusing-Wave Spectroscopy: Theory

I first start with single scattering and then extend the theory to the multiple scattering regime of DWS. This mainly follows the derivation from[404]. Then I will give an alternative approach based on the transport of correlation in an optically dense system following[396,411].

4.1.2.2.1 Single Scattering

The incident light is scattered by a dilute suspension of identical scattering particles. The light scattered into an angle ϑ is detected by a photo detector. The electrical field that reaches the detector is a superposition of all the scattered electric fields:

$$\vec{E} = \vec{E}_0 f(q) \sum_{i=1}^{N} \exp\left(i\vec{k}_{\text{in}}\vec{r}_i\right) \exp\left(i\vec{k}_{\text{out}}\left(\vec{R}_{\text{d}} - \vec{r}_i\right)\right) \tag{4.17}$$

$$= \vec{E}_0 f(q) \exp\left(i\vec{k}_{\text{out}}\vec{R}_{\text{d}}\right) \sum_{i=1}^{N} \exp\left(-i\vec{q}\vec{r}_i\right) \tag{4.18}$$

where $\vec{E}$ is the electrical field at the detector position $\vec{R}_{\text{d}}$, $\vec{E}_0$ the incident electric field, $f(q)$ is the form amplitude for light to receive a momentum transfer $\vec{q} = \vec{k}_{\text{out}} - \vec{k}_{\text{in}}$, where $\vec{k}_{\text{out}}$ and $\vec{k}_{\text{in}}$ is the output and input wave vector, respectively, and $|\vec{q}| = 2k_0 \sin\left(\frac{\vartheta}{2}\right)$ with $k_0 = \left|\vec{k}_{\text{out}}\right| = \left|\vec{k}_{\text{in}}\right| = \frac{2\pi}{\lambda_{\text{m}}}$ with λ_{m} being the wavelength in the medium (see equation 4.3). In the following I will neglect polarization effects and will assume randomly oriented scatterers. Under these conditions the differential cross section only depends on the magnitude of $\vec{q}$. The summation is over the N particles at positions $\vec{r}_i$. The phase of each scattered wave depends on the momentum transfer and on the position of the particle. In a disordered system

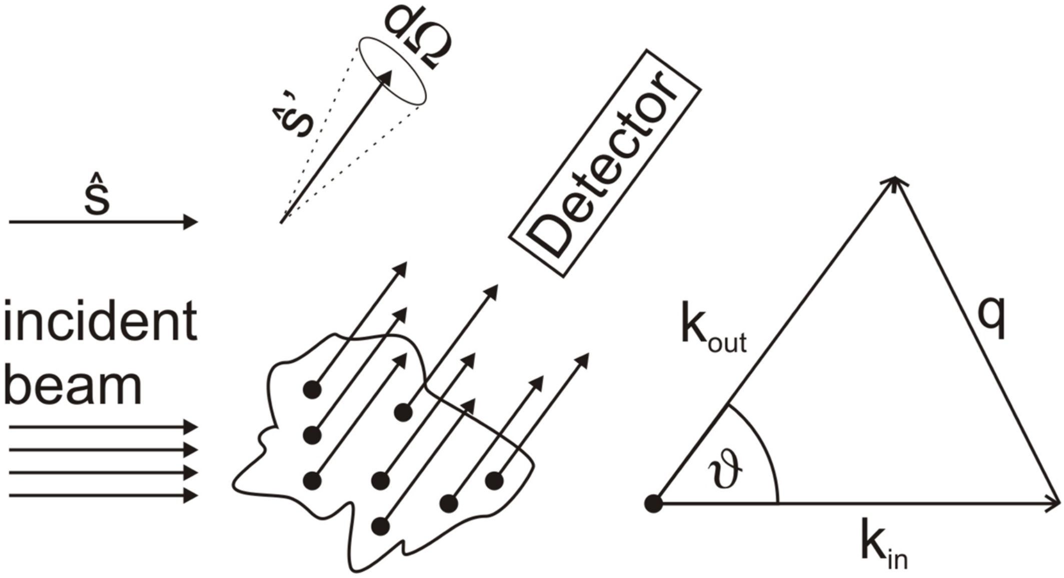

Figure 4.2: Schematic figure illustrating single light scattering in a dilute system.

the particles are randomly distributed, resulting in a random constructive and destructive interference at the detector. Displacing a single particle changes the phase and thereby the interference pattern at the detector.

For particles undergoing random relative motion (e.g. Brownian motion) the phases of individual waves are changing randomly and independently of the other scattered waves. Thus the intensity at the detector fluctuates. The time scale of these fluctuations is related to the rate at which the phase of the waves changes and therefore depends on the motion of the particles and the momentum transfer $\vec{q}$. The intensity fluctuates more rapidly for faster moving particles and larger scattering angles. By monitoring the intensity fluctuations it is possible to derive information about the motion of the particles. Usually one measures the intensity autocorrelation function in the homodyne (self-beating) configuration

$$g_2(\tau) = \frac{\langle I(t)\, I(t+\tau)\rangle}{\langle I(t)\rangle^2} \tag{4.19}$$

where $I(t)$ is the intensity at time t and $\langle\rangle$ denotes the ensemble average. For an ergodic system an ensemble average is equivalent to a time average and thus $g_2(\tau)$ can be obtained from a temporal average of the correlation function. For Gaussian processes the field autocorrelation function $g_1(\tau)$ is related to the intensity autocorrelation function by the Siegert relation[389]

$$g_2(\tau) = 1 + \beta\, |g_1(\tau)|^2 \tag{4.20}$$

where β depends on the experimental setup and is primarily determined by the collection optics. For an ideal single mode detection (one polarization) $\beta = 1$ and for two modes (two polarizations) $\beta = \frac{1}{2}$. For a detailed discussion on different modes see[412,413], finite coherence length see[414], incoherent background and detector nonlinearity (e.g. dead time) see[415,416].

For convenience the time t has been set to zero in the following derivation. For a system of Rayleigh scatterers the field autocorrelation function in the single-scattering regime is given by[404]:

$$g_1(\tau) = \frac{\sum_{k=1}^{N}\sum_{j=1}^{N}\langle \exp[i\vec{q}(\vec{r}_k(0) - \vec{r}_j(\tau))]\rangle}{\sum_{k=1}^{N}\sum_{j=1}^{N}\langle \exp[i\vec{q}(\vec{r}_k(0) - \vec{r}_j(0))]\rangle} \tag{4.21}$$

In the case of non-interacting particles, the cross-terms $k \neq j$ vanish and thus

$$g_1(\tau) = \langle \exp(-i\vec{q}\Delta\vec{r}(\tau))\rangle \tag{4.22}$$

with $\Delta\vec{r}(\tau) = \vec{r}(\tau) - \vec{r}(0)$. If $\Delta\vec{r}(\tau)$ is a Gaussian variable, then

$$g_1(\tau) = \exp\left(-\frac{q^2\langle \Delta r^2(\tau)\rangle}{6}\right) \tag{4.23}$$

with $\langle \Delta r^2 (\tau) \rangle$ being the mean square displacement. For a scatterer undergoing Brownian motion $\langle \Delta r^2 (\tau) \rangle = 6 D_{\mathrm{B}} \tau$ and for a Gaussian random flow $\langle \Delta r^2 (\tau) \rangle = \langle \Delta V^2 \rangle \tau^2$ where D_{B} is the Brownian diffusion coefficient and $\langle \Delta V^2 \rangle$ is the mean square velocity fluctuation[417,418].

4.1.2.2.2 Multiple Scattering

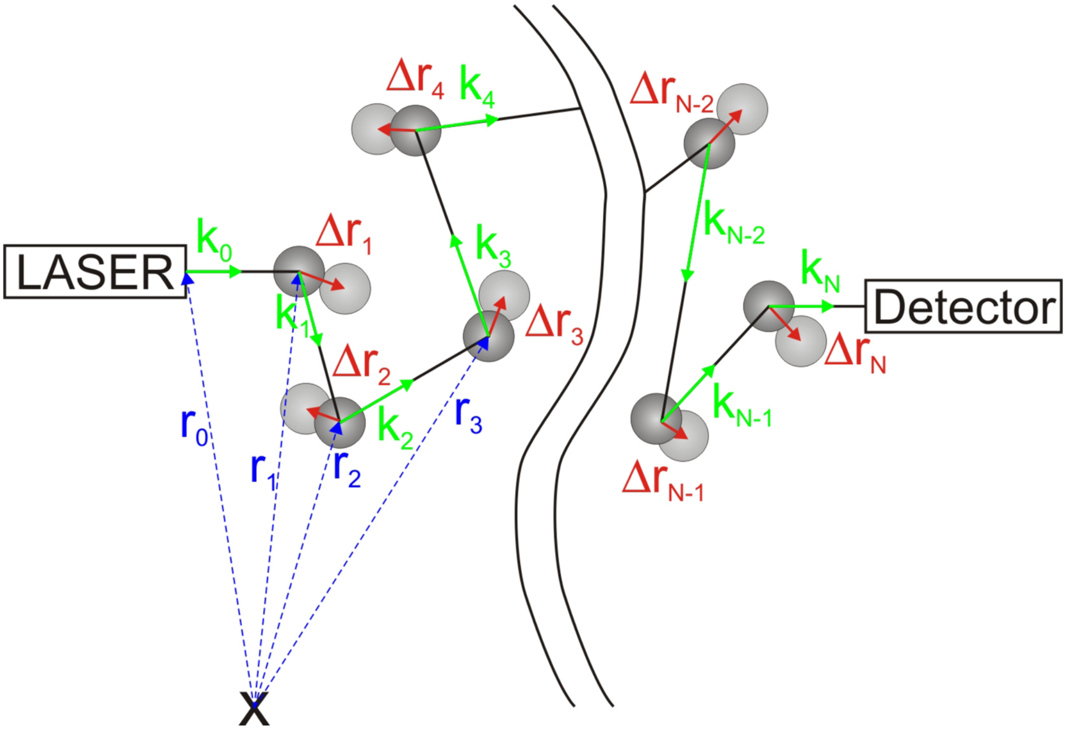

Figure 4.3: Single path through a multi scattering sample. The wave vectors k_i (green) have magnitude k_0 and point in the direction of propagation. The particle position r_i (dashed blue line) is the position of the scatter from the i-th scattering event. Δr_i (red) denotes the displacement of particle r_i in time τ. The black line is the path length s. (Modified figure after[404,405])

When the concentration of particles is increased, light is scattered many times before it reaches the detector. Photons reaching the detector have usually followed various trajectories with different path length. For a single path where the photon was scattered N times the path length is given by:

$$s = \sum_{i=0}^{N} |\vec{r}_{i+1} - \vec{r}_i| = \sum_{i=0}^{N} \left(\frac{\vec{k}_i}{k_0} \right) (\vec{r}_{i+1} - \vec{r}_i) \tag{4.24}$$

and thus gives a total phase shift

$$\phi = k_0 s = \sum_{i=0}^{N} \vec{k}_i \left(\vec{r}_{i+1} - \vec{r}_i\right) \tag{4.25}$$

The field at the detector is the superposition of the fields from all light paths:

$$E\left(\tau\right) = \sum_{\mathrm{p}} E_{\mathrm{p}} \exp\left(i\phi_{\mathrm{p}}\left(\tau\right)\right) \tag{4.26}$$

where $\sum_{\mathrm{p}}$ is the sum over paths and E_{p} is the amplitude of the field associated with the photon path p at the detector. Hence one gets for the field autocorrelation function

$$g_1\left(\tau\right) = \frac{\left\langle \left(\sum_{\mathrm{p}} E_{\mathrm{p}} \exp\left(i\phi_{\mathrm{p}}\left(0\right)\right)\right) \left(\sum_{\mathrm{p}'} E_{\mathrm{p}'} \exp\left(-i\phi_{\mathrm{p}'}\left(\tau\right)\right)\right) \right\rangle}{\left\langle \left|E\right|^2 \right\rangle} \tag{4.27}$$

For independent particles, the fields from different paths are to a very good approximation uncorrelated. Thus only terms with $\mathrm{p} = \mathrm{p}'$ contribute:

$$g_1\left(\tau\right) = \left\langle \sum_{\mathrm{p}} \frac{\left|E_{\mathrm{p}}\right|^2}{\left\langle I \right\rangle} \exp\left(i\left(\phi_{\mathrm{p}}\left(0\right) - \phi_{\mathrm{p}}\left(\tau\right)\right)\right) \right\rangle = \sum_{\mathrm{p}} \frac{\left\langle I_{\mathrm{p}} \right\rangle}{\left\langle I \right\rangle} \left\langle \exp\left(i\left(\phi_{\mathrm{p}}\left(0\right) - \phi_{\mathrm{p}}\left(\tau\right)\right)\right) \right\rangle \tag{4.28}$$

For a large N, $\Delta\phi_{\mathrm{p}}\left(\tau\right) = \phi_{\mathrm{p}}\left(\tau\right) - \phi_{\mathrm{p}}\left(0\right)$ is a Gaussian variable and thus

$$\left\langle \exp\left(-i\Delta\phi_{\mathrm{p}}\left(\tau\right)\right) \right\rangle = \exp\left(-\frac{\left\langle \Delta\phi_{\mathrm{p}}^2\left(\tau\right) \right\rangle}{2}\right). \tag{4.29}$$

With $\Delta\phi_{\mathrm{p}}\left(\tau\right) \approx \sum_{i=1}^{N} \vec{q}_i \Delta\vec{r}_i\left(\tau\right)$ and assuming that successive phase factors $\vec{q}_i \Delta\vec{r}_i\left(\tau\right)$ are independent, we obtain

$$\left\langle \Delta\phi_{\mathrm{p}}^2\left(\tau\right) \right\rangle = \sum_{i=1}^{N} \sum_{j=1}^{N} \left\langle \left(\vec{q}_i \Delta\vec{r}_i\left(\tau\right)\right) \left(\vec{q}_j \Delta\vec{r}_j\left(\tau\right)\right) \right\rangle = \sum_{i=i}^{N} \left\langle \left(\vec{q}_i \Delta\vec{r}_i\left(\tau\right)\right)^2 \right\rangle \tag{4.30}$$

If we further assume that the scattering vectors $\vec{q}_i$ and the displacement vectors $\Delta\vec{r}_i\left(\tau\right)$ are independent, we get

$$\left\langle \Delta\phi_{\mathrm{p}}^2\left(\tau\right) \right\rangle = N \left\langle \left(\vec{q}_i \Delta\vec{r}_i\left(\tau\right)\right)^2 \right\rangle = \frac{1}{3} N \left\langle q^2 \right\rangle \left\langle \Delta r^2\left(\tau\right) \right\rangle \tag{4.31}$$

The average $\langle q^2 \rangle$ is weighted by the single scattering form factor and can be expressed in terms of the mean free path

$$\left\langle q^2 \right\rangle = \left\langle \left(2k_0 \sin\left(\frac{\vartheta}{2}\right)\right)^2 \right\rangle = 2k_0^2 \left\langle 1 - \cos\vartheta \right\rangle = 2k_0^2 \frac{l_{\mathrm{s}}}{l^*} \tag{4.32}$$

with $N = \frac{s}{l_\mathrm{s}}$ we get

$$\left\langle \Delta\phi_\mathrm{p}^2(\tau)\right\rangle = \frac{2}{3}k_0^2\left\langle \Delta r^2(\tau)\right\rangle \frac{s}{l^*} \tag{4.33}$$

For light which has traveled a path length s we therefore have

$$g_1^s(\tau) = \exp\left[-\frac{1}{3}k_0^2\left\langle \Delta r^2(\tau)\right\rangle\left(\frac{s}{l^*}\right)\right] \tag{4.34}$$

If we replace the fraction of scattered intensity in path p, $\frac{\langle I_\mathrm{p}\rangle}{\langle I\rangle}$ by the weight of transmitted intensity in the path of length s, $P(s)$, we obtain

$$g_1(\tau) = \sum_s P(s)\exp\left(-\frac{1}{3}k_0^2\left\langle \Delta r^2(\tau)\right\rangle\frac{s}{l^*}\right) \tag{4.35}$$

where the sum can be replaced by an integral for large s

$$g_1(\tau) = \int_0^\infty P(s)\exp\left(-\frac{1}{3}k_0^2\left\langle \Delta r^2(\tau)\right\rangle\frac{s}{l^*}\right)ds \tag{4.36}$$

In this derivation we have neglected absorption but this can be easily corrected by multiplying the path by a factor $\exp(-\mu_\mathrm{a}s)$ (see equation 4.15), which will reduce the contribution of longer paths. This is the central equation of DWS where the path length distribution $P(s)$ depends on the geometry and the dynamics are given by the mean square displacement $\langle \Delta r^2(\tau)\rangle$. The most important contributions for $\langle \Delta r^2(\tau)\rangle$ are given by the diffusion due to Brownian motion, random flow and shear flow[1]:

$$\left\langle \Delta r^2(\tau)\right\rangle = 6D_\mathrm{B}\tau + \left\langle \Delta V^2\right\rangle\tau^2 + \frac{1}{5}\frac{\Gamma_\mathrm{eff}^2}{\mu_\mathrm{s}'^2}\tau^2 \tag{4.37}$$

4.1.2.2.3 Correlation Diffusion Equation

A different approach for calculating the field autocorrelation function of multiple scattered light uses the steady state correlation transport equation which can be derived from the Boltzmann transport equation and is given by[396,411,417,421–423]:

$$\nabla G_1(\vec{r},\hat{s},\tau)\hat{s} + \mu_\mathrm{t}G_1(\vec{r},\hat{s},\tau) = \mu_\mathrm{s}\int_{4\pi} G_1(\vec{r},\hat{s}',\tau)\, g_1^s(\hat{s},\hat{s}'\tau)\, f(\hat{s},\hat{s}')\, d\hat{s}' + S(\vec{r},\hat{s}) \tag{4.38}$$

where $G_1(\vec{r},\hat{s},\tau)$ is the unnormalized field autocorrelation function, $g_1^s(\hat{s},\hat{s}',\tau)$ is the normalized field correlation function for single scattering, $f(\hat{s},\hat{s}')$ is the phase

---

[1] The general case has been described by[419] where $\Gamma_\mathrm{eff}^2 = 2\int\sum_{i,j}\sigma_{i,j}^2(\vec{r})\,\rho_n(\vec{r})\,d\vec{r}$, with $\sigma_{i,j}$ the strain tensor and $\rho_n(\vec{r})$ the spatial distribution of diffusion paths of length s. For a homogenous shear flow with $V = (0,\dot{\varepsilon}z,0)^{-1}$ $\Gamma_\mathrm{eff}^2 = \dot{\varepsilon}^2$ and for a muscle contraction[420] $\Gamma_\mathrm{eff}^2 = 3\dot{\varepsilon}^2$ where $\dot{\varepsilon}$ is the strain rate.

function, $\mu_\mathrm{t} = \mu_\mathrm{a} + \mu_\mathrm{s}$ and $S(\vec{r}, \hat{s})$ is the light source distribution. The correlation transport equation is valid as long as localization effects are negligible and is essentially a conservation equation, where the left side basically accounts for flux, scattering and absorption and is balanced by the gain as given on the right side of the equation[417]. The equation can easily be modified to the non-steady state (e.g. a pulsed laser or a non-equilibrium system) by adding a factor $\frac{1}{v}\frac{\partial G_1(\vec{r},\hat{s},\tau,t)}{\partial t}$ to the left side of the equation.
Within the P_1 approximation[396] the correlation transport equation reduces to the following steady-state diffusion equation:

$$\left(D_\gamma \nabla^2 - v\mu_\mathrm{a} - \frac{1}{3} v \mu'_\mathrm{s} k_0^2 \left\langle \Delta r^2(\tau) \right\rangle \right) G_1(\vec{r}, \tau) = -vS(\vec{r}) \tag{4.39}$$

where $D_\gamma = \frac{v}{3\mu'_\mathrm{s}}$ is the photon diffusion coefficient and v is the speed of light in the medium. Note that G_1 no longer depends on the direction $\hat{s}$ and the reduced scattering coefficient μ'_s appears instead of μ_s[417].
We can recast this into a Helmholtz equation

$$\left(\nabla^2 + K^2(\tau)\right) G_1(\vec{r}, \tau) = -\frac{vS}{D_\gamma} \delta^3(\vec{r} - \vec{r}_\mathrm{s}) \tag{4.40}$$

where $K^2(\tau) = -3\mu'_\mathrm{s}\mu_\mathrm{a} - \mu'^2_\mathrm{s} k_0^2 \langle \Delta r^2(\tau) \rangle$ and the light source has been assumed to be a point source located at $\vec{r}_\mathrm{s}$.

For a infinite homogeneous system the solution is given by[393]:

$$G_1(\vec{r}, \tau) = vS \frac{\exp\left(-\sqrt{3\mu_\mathrm{a}\mu'_\mathrm{s} + \mu'^2_\mathrm{s} k_0^2 \langle \Delta r^2(\tau) \rangle}\, |\vec{r} - \vec{r}_\mathrm{s}|\right)}{4\pi D_\gamma |\vec{r} - \vec{r}_\mathrm{s}|} \tag{4.41}$$

In the following the solutions for the normalized field autocorrelation function derived from the correlation diffusion equation for typical experimental set-ups are stated. Depending on the dynamics in the system the corresponding formula of the mean square displacement (see equation 4.37) has to be used.

Transmission

Plane wave illumination - point detection

For a plane wave illumination and point detection geometry through a slab one gets[396,404,424]:

$$g_1(\tau) = \frac{\frac{\frac{L}{l^*} + \frac{4}{3}}{\frac{z_0}{l^*} + \frac{2}{3}} \left(\sinh\left(\frac{z_0}{l^*}\sqrt{K_D}\right) + \frac{2}{3}\sqrt{K_D}\cosh\left(\frac{z_0}{l^*}\sqrt{K_D}\right)\right)}{\left(1 + \frac{4}{9}K_D\right)\sinh\left(\frac{L}{l^*}\sqrt{K_D}\right) + \frac{4}{3}\sqrt{K_D}\cosh\left(\frac{L}{l^*}\sqrt{K_D}\right)}$$

$$g_1\left(\tau\right) \overset{K_D \ll 1}{\approx} \frac{\left(\frac{L}{l^*}+\frac{4}{3}\right)\sqrt{K_D}}{\left(1+\frac{4}{9}K_D\right)\sinh\left(\frac{L}{l^*}\sqrt{K_D}\right)+\frac{4}{3}\sqrt{K_D}\cosh\left(\frac{L}{l^*}\sqrt{K_D}\right)} \tag{4.42}$$

where L is the thickness of the slab and $K_D = k_0^2 \left\langle \Delta r^2\left(\tau\right)\right\rangle$

Point illumination - point detection

For a point illumination and a point detection geometry through a slab, where the laser and detector are on one axis, one gets[404,424]:

$$g_1\left(\tau\right) = C\int_{\frac{L}{l^*}\sqrt{K_D}}^{\infty}\left[A(s)\sinh s + \exp\left(-s\left(1-\frac{z_0}{L}\right)\right)\right]ds \tag{4.43}$$

with

$$A(s) = \frac{\left(\frac{2l^*}{L}s-1\right)\left[\frac{2l^*}{L}s\exp\left(-s\frac{z_0}{L}\right)+\left(\sinh s+\frac{2l^*}{L}s\cosh s\right)\exp\left(-s\left(1-\frac{z_0}{L}\right)\right)\right]}{\left(\sinh s+\frac{2l^*}{L}\cosh s\right)^2-\left(\frac{2l^*}{L}s\right)^2} \tag{4.44}$$

where C is a normalization constant chosen so that $g_1\left(0\right)=1$, L is the thickness of the sample, z_0 is obtained from the boundary condition and $K_D = k_0^2 \left\langle \Delta r^2\left(\tau\right)\right\rangle$.

Backscattering

For a backscattering geometry with a plane wave illumination and point detection one gets[396,404,424]:

$$g_1\left(\tau\right) = \frac{\sinh\left(\sqrt{K_D}\left(\frac{L-z_0}{l^*}\right)\right)+\frac{2}{3}\sqrt{K_D}\cosh\left(\sqrt{K_D}\left(\frac{L-z_0}{l^*}\right)\right)}{\left(1+\frac{4}{9}K_D\right)\sinh\left(\frac{L}{l^*}\sqrt{K_D}\right)+\frac{4}{3}\sqrt{K_D}\cosh\left(\frac{L}{l^*}\sqrt{K_D}\right)} \tag{4.45}$$

where $K_D = k_0^2 \left\langle \Delta r^2\left(\tau\right)\right\rangle$, z_0 is given by the boundary condition and can be taken as approximately l^* and L is the thickness of the slab. For an infinite thick slab this reduces to:

$$g_1\left(\tau\right) = \frac{\exp\left(-\sqrt{k_0^2\left\langle \Delta r^2\left(\tau\right)\right\rangle}\right)}{1+\frac{2}{3}\sqrt{k_0^2\left\langle \Delta r^2\left(\tau\right)\right\rangle}} \tag{4.46}$$

Infinite medium

For an infinite medium with a point source and point detection, the path length distribution is given by:

$$P\left(s\right) = \frac{s^{-\frac{3}{2}}\exp\left(-\frac{3\mu_{\mathrm{s}}'\rho^2}{4s}\right)\exp\left(-\mu_{\mathrm{a}}s\right)}{\sqrt{\frac{4\pi}{3\mu_{\mathrm{s}}'}}\frac{\exp\left(-\sqrt{3\mu_{\mathrm{s}}'\mu_{\mathrm{a}}}\rho\right)}{\rho}} \tag{4.47}$$

where ρ is the distance between source and detector and thus

$$g_1\left(\tau\right) = \exp\left(-\sqrt{3\mu_{\mathrm{a}}\mu_{\mathrm{s}}' + \mu_{\mathrm{s}}'^2 k_0^2\left\langle \Delta r^2\left(\tau\right)\right\rangle}\rho\right) \tag{4.48}$$

Banana geometry

For a semi-infinite geometry with a point source and point detector and source-detector separation ρ, the path length distribution is given by[396,424,425]

$$P\left(s\right)=\frac{s^{-\frac{3}{2}}\left[\exp\left(-\frac{3\mu_{\mathrm{s}}' r_1^2}{4s}\right)-\exp\left(-\frac{3\mu_{\mathrm{s}}' r_2^2}{4s}\right)\right]\exp\left(-\mu_{\mathrm{a}}s\right)}{\sqrt{\frac{4\pi}{3\mu_{\mathrm{s}}'}}\left[\frac{\exp\left(-\sqrt{3\mu_{\mathrm{s}}'\mu_{\mathrm{a}}}r_1\right)}{r_1}-\frac{\exp\left(-\sqrt{3\mu_{\mathrm{s}}'\mu_{\mathrm{a}}}r_2\right)}{r_2}\right]} \tag{4.49}$$

where $r_1=\sqrt{\rho^2+{z_0}^2}$ and $r_2=\sqrt{\rho^2+\left(z_0+2z_b\right)^2}$, with z_0 approximately l^* and z_b the extrapolation distance which accounts for the mismatch in the indices of refraction at the surface of the sample. For a detailed discussion about boundary conditions see[423]. We then get:

$$g_1\left(\tau\right)=\frac{\exp\left(-\sqrt{3\mu_{\mathrm{a}}\mu_{\mathrm{s}}'+\mu_{\mathrm{s}}'^2k_0^2\left\langle\Delta r^2\left(\tau\right)\right\rangle}r_1\right)-\exp\left(-\sqrt{3\mu_{\mathrm{a}}\mu_{\mathrm{s}}'+\mu_{\mathrm{s}}'^2k_0^2\left\langle\Delta r^2\left(\tau\right)\right\rangle}r_2\right)}{\exp\left(-\sqrt{3\mu_{\mathrm{a}}\mu_{\mathrm{s}}'}r_1\right)-\exp\left(-\sqrt{3\mu_{\mathrm{a}}\mu_{\mathrm{s}}'}r_2\right)} \tag{4.50}$$

4.1.2.3 Qualitative description of DWS

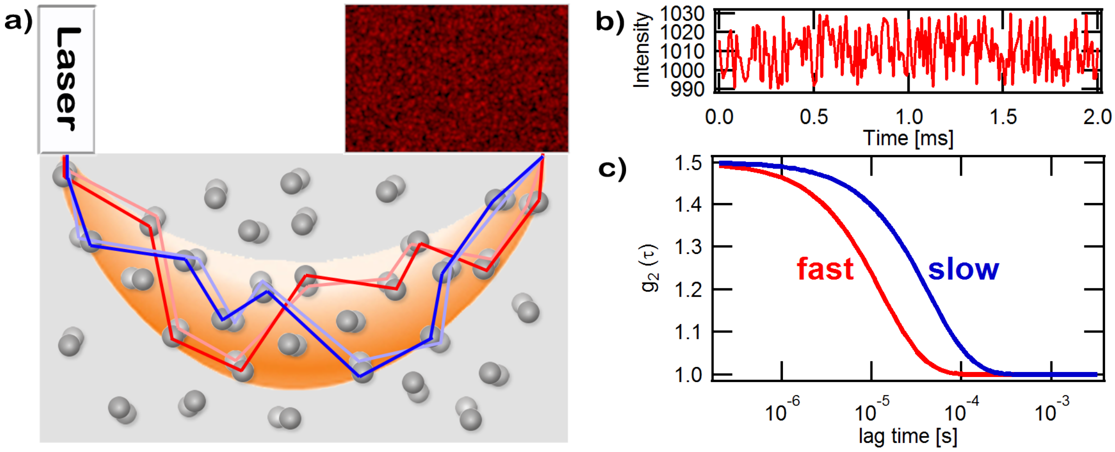

Figure 4.4: Principle of Diffusing Wave Spectroscopy. a) A laser with a long coherence length is used to illuminate the sample. The light is multiple scattered along different paths. The light from these different paths interfere constructively and destructively at the surface and build a so called speckle pattern. If the scatterers move in time the speckle pattern will also change with time. b) DWS measures the intensity fluctuations of one speckle. From the intensity fluctuations the autocorrelation function is calculated which measures how fast the intensity fluctuates in time. c) The normalized intensity autocorrelation function $g_2(\tau)$ is shown. From the timescale of the decay and the shape one gets information about the dynamics (red: fast; blue: slow) and the type of motion of the scatterers (e.g. diffusive).

Figure 4.4 schematically shows the principle of DWS in a geometry which is typically used in biomedical application. Light with a long coherence length is used to illuminate the sample and is detected at a distance ρ. The light between source and detector is multiple scattered along different paths which are on average located in a banana shaped area determining the spatial resolution and the penetration depth of DWS. The light from the different paths interfere constructively and destructively at the surface and form a so called speckle pattern. If the scatterers move in time the paths and therefore the speckle pattern will change in time. The light from one of these speckles is detected and the normalized intensity autocorrelation function $g_2(\tau)$ is calculated. The autocorrelation function can then be fitted with the analytical solution of the diffusion equation to deduce the dynamics.

4.1.2.3.1 Validation

It has been observed that the blood flow in tissue can be best fitted with a diffusive motion rather than a directed motion. Although it is not fully understood why the fit better suits the data, it has been well validated against various modalities that the fit value of the effective diffusion coefficient is approximately proportional to blood flow (see table 4.1). In particular when measuring cerebral blood flow (CBF) one can use the small changes related to a specific tasks to identify the brain regions which are involved in the processing (see neurovascular coupling 3.1.6).

These functional DWS (fDWS) studies have been used to measure the response to sensorimotor stimuli due to finger tapping[432,438,444], changes in the somatosensory cortex during passive tactile stimulation of the hand in preterm infants[445], changes during a verbal fluence stimulation task (word generation)[446], comparison of speaking and non speaking tasks in people who stutter[447] as well as visual stimulation[448,449].

Note that the cerebral blood flow changes during functional tests might be underestimated due to partial volume effects (only a small part of the brain is activated but DWS probes large portions of the tissue). Therefore one has to be careful if one compares the relative changes to other modalities. For a quantitative evaluation more anatomical data as well as multiple source detector separations to incorporate effects such as the layered structure[432,450,451] of the brain are required to come to a more accurate modeling.

Also one has to emphasize that all motions of scatterers and not only blood flow contribute to the decay of the autocorrelation function. For example Yu et al.[441] wrongly assigned the signal change during plantar flexion to blood flow. With the superior temporal resolution in our setup the author could show that the signal is due to muscle motion rather than blood flow[452].

Being aware of these limitations DWS provides a sound methods for functional brain imaging.

Table 4.1: Validation of DWS. Data is an extension of the data presented in[399]. DU: Doppler ultrasound, CEU: contrast-enhance ultrasound, LD: laser Doppler, FM: fluorescent microspheres, ALS-MRI: arterial spin labeling magnetic resonance imaging

Sample	Perturbation	Modality	Correlation coefficient	Slope DWS/Mod	Reference
Mouse tumor	Photodynamic therapy	DU	N/A	Agreement	[426]
premature infants	Absolute baseline	DU	0.91	0.9	[427]
premature neonates	Absolute baseline	DU	0.53	N/A	[428]
Mouse tumor	Photodynamic therapy	DU	N/A	0.97	[429]
Adult human	Acetazolamide	DU	N/A	Agreement	[430]
Mouse tumor	Antivascular therapy	CEU	N/A	Agreement	[431]
Rat	Hypo-/Hypercapnia	LD	0.94	1.3	[432]
Mouse	Occlusion	LD	0.94	1.4	[433]
Mouse	Femoral artery occlusion	LD	>0.8	0.96-1.07	[434]
Adult human	Vasopressor, Hyperventilation	Xenon-CT	0.73	1.1	[435]
Neonatal Piglet	Traumatic brain injury	FM	0.63	0.4	[436]
Human muscle	Cuff inflation/deflation	ASL-MRI	>0.77	1.5-1.7	[437]
Adult human	Finger tapping	ASL-MRI	N/A	1.14	[438]
Rat	Hypercapnia	ASL-MRI	0.81-0.86	0.75	[439]
Neonate	Hypercapnia	ASL-MRI	0.7	0.86	[440]
Adult human	Occlusion	Literature	N/A	Agreement	[441]
rat	Hypercapnia	Literature	N/A	Agreement	[442]
Kidney (ex vivo)	Artificial perfusion	volume flow	0.99	N/A	[443]

4.1.2.3.2 Origin of Signal

Even though, for simplicity, the signal is called cerebral blood flow throughout this thesis, the origin of the signal is still incompletely understood and, in general, diffusing wave spectroscopy only measures changes associated with changes in the optical pathlength of the different paths through the tissue. These may arise due to movement of the scatterers as well as changes in the scattering properties.

One of the main factors contributing to this signal during neuroimaging is the movement of red blood cells, which is also called slow signal (>100ms). In particular it is puzzling why the decay of the autocorrelation function shows the shape of diffusive rather than directed motion. Likely explanations for this behavior are contributions from rotation of the red blood cells which should be proportional to the shear rate as well as shear induced self-diffusion ($\propto \dot{\gamma} a^2$)[453,454] which results from the spatial hindrance that particles experience in a concentrated suspension when it is macroscopically forced to flow[455].

The second signal of interest for neuroimaging is the so called fast optical signal (10ms-100ms). It arises from optical changes which occur during an action potential traveling through the nerve. Such changes may arise due to swelling[456] as well as changes in the optical properties[457] of the nerve. The details of the fast signal are however still not fully understood. In addition there is a controversy in literature with both positive[458,459] and negative results[460,461]. One of the major obstacles in the interpretation of the fast signal is that motion artifacts can hardly be eliminated completely in in vivo experiments.

An attempt to understand both the fast signal and the shape of the autocorrelation function in blood flow has been made during several bachelor, master and diploma thesis[462–465]. A detailed discussion of the experiments and results is beyond the scope of this thesis, but the basic concepts and results should be presented.

The fast optical signal was investigated with diffusing wave spectroscopy in an ex vivo experiment with brain slices of a rat in the diploma thesis of Julian Ströbele[462]. Action potentials can be triggered by electrical or chemical stimulation and the electrical activity can be monitored by electrodes. One limitation of the brain slices is that they have to be very thin (≈ 100-200µm) in order to get enough nutrient and oxygen. These thin slices are almost transparent and only a small portion of the light is scattered. The limited number of scattering events reduces the sensitivity and the signal is superimposed by distracting unscattered light. This problem could not be overcome and the measurements stayed inconclusive. A new approach with the thicker nerve of the earthworm by Moritz Schlötter is more promising. No reproducible signal in the temporal range of the fast signal has been observed in the pigeon so far. However if a clear characteristic shape of the fast optical signal can be determined it may be worthwhile reanalyzing the data.

In order to understand the blood flow signal in more detail first the light scattering of single red blood cells in solution and in shear flow should be investigated in order to infer the behavior in concentrated suspensions. Due to challenging experiments only the first part could by realized (see[463–465] for more details). Fresh human blood samples from the author were used for these experiments. The translational and rotational diffusion coefficient was determined by Clara Engesser[465] to $D = (1.5 \pm 0.2) \cdot 10^{-13} \frac{\mathrm{m}^2}{\mathrm{s}}$ and $D_{rot} = (3.6 \pm 1.2) \cdot 10^{-3} \frac{1}{\mathrm{s}}$, respectively. This is in good agreement with theoretical calculation for an oblate ellipsoid with similar dimensions after Perrin.

Furthermore the static structure factor of the erythrocytes has been measured (see[465]). Simulations by the author using ADDA[466], an open source implementation of the discrete dipole approximation which can be used to simulate light scattering of arbitrary shaped 3-dimensional objects, showed good agreement with the measured data.

Future measurements in a rotational shear cell will show whether the diffusive shape of the autocorrelation function can be explained by the rotational diffusion coefficient or the shear induced self-diffusion is causal.

With a better theoretical understanding of the signal a more detailed modeling of the autocorrelation function can be performed which results in more detailed fits possibly contributing additional information.

4.1.3 Experiments

A homemade experimental set-up has been build which continuously is improved. Only the latest setup is described in detail. Note that some measurements did not include all equipment described below. Therefore some of the data may differ in its representation.

A diode laser (Toptica TA100) with a long coherence length (>100m) operating at a wavelength of 802nm is used as a light source. The laser beam is coupled into a graded index multimode fiber to transport the light to the skin. The fiber end is cleaved and glued in a cannula (21G) where the tip has been ground off. The detection fiber bundle consists of 32 single-mode fibers with a nominal cutoff wavelength of 780nm. A bandpass filter with a center wavelength of 800nm is used to reject stray light. Photons are detected by 8 four-channel avalanche photo diode (APD) modules (Perkin Elmer SPCM-AQ4C). Normalized intensity autocorrelation functions with integration times between 6.5 and 104.8ms are continuously calculated by a custom build 32-channel multitau correlator (correlator.com).[467]

The laser power is monitored by a power meter (Thorlabs PM100D) and the countrate is corrected for any changes occurring during measurements.

Movement of the pigeon is monitored with two cameras (Basler acA640-100gc) with a typical frame rate of 77 Hz. Any noise that might influence the measurements is monitored by a preamplified microphone. The oxygen saturation, heart rate and absorption curve is measured with a capnometer monitor (SurgiVet® V90041). Endexpiratory CO_2 concentration could not be monitored due to the fact that the pigeon was not intubated and the breathing volume was too small to measure it with the high flow rate of the capnograph.

The magnetic field is measured with a 3-axis fluxgate magnetometer (Bartington Mag03MS100 with low noise option). The analog voltage is digitized by an analog digital converter (NI PXI-4462 24-bit ADCs). Note that the fluxgate magnetometer is driven at 15 kHz which provides a small source of magnetic noise at this frequency. The magnetometer is placed about 5 cm below the head of the pigeon in the stereotaxic device. The orientation of the axis relative to the pigeon's head are shown in figure 4.5. The B_x-axis is oriented to the tail, B_y oriented to the right and B_z to the top of the pigeon.

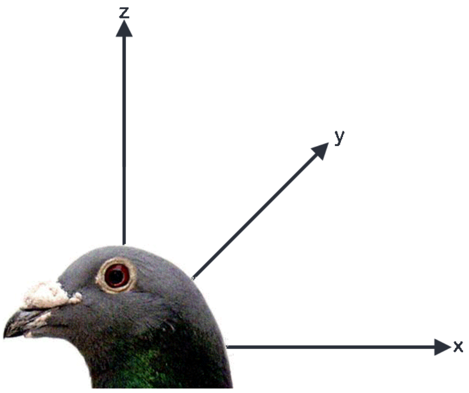

Figure 4.5: Orientation of magnetic field axis with B_x oriented to the tail, B_y oriented to the right and B_z to the top of the pigeon.

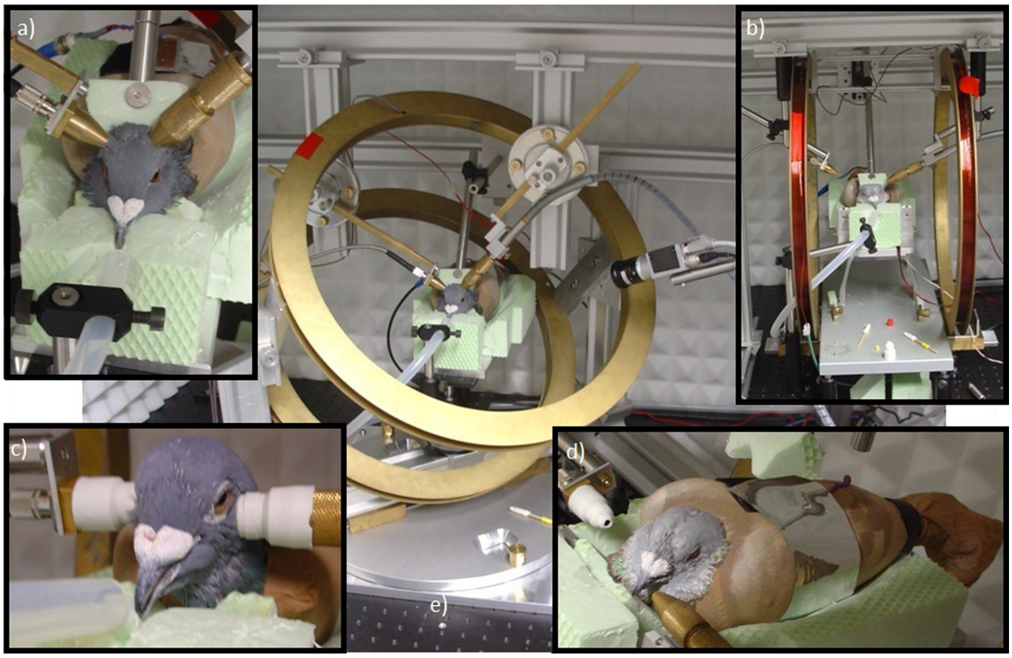

Figure 4.6: Early version of the setup for measurements in wakeful condition. a) shows the occipital-lateral orientation of the source and detector, b) magnetic field tilted by 90 degree to the head axis, c) measurement in transmission through the ears, d) rest position with piezoelectric foil and e) magnetic field tilted by 45°.

The setup at an early stage where awake measurement at varies laser-detector geometries have been performed is shown in figure 4.6. Here the pigeon was placed in tights where the tip of the toe has been cut away as opening for the head. The legs of the bird were fixated with adhesive tape (figure 4.6 d). The head was additionally fixated by foam holding the neck in position. With this set-up DWS measurements can be performed. Notwithstanding the pigeon can still move slightly. This motion often resulted in a bad coupling between laser, detector and the skin which makes measurements with awake pigeons laborious. Furthermore, a movement response to the presented stimuli has often been observed, precluding meaningful, reproducible experiments. Nevertheless, measurements during wakefulness might still be used in cases where anesthesia might proof problematic.

In the current setup (figure 4.8) the magnetic field is controlled by a custom build three dimensional Merritt 4 coil system. The advantage of the 3d Merritt four coil system compared to the previously used Helmholtz coil (see figure 4.6) is that it has a higher field homogeneity as well all as 3 independent axis which allows for an arbitrary orientation and strength of the magnetic field. Each dimension consists of four rectangular coils with identical edge length d where the outer coils have 85 windings and are positioned b/d=0.505492 from the center and the inner coils have 36 windings positioned at a/d=0.128106 from the center[468,469]. The edge sizes for the 3 dimensions are 72.5 cm, 80.5 cm and 86.5 cm for x, y and z, respectively. The system is controlled by custom written software which produces an output voltage (NI PXI-6722 output voltage ±10V with 13bit). The voltage is then converted to a current proportional to the voltage by a custom build voltage-current converter.

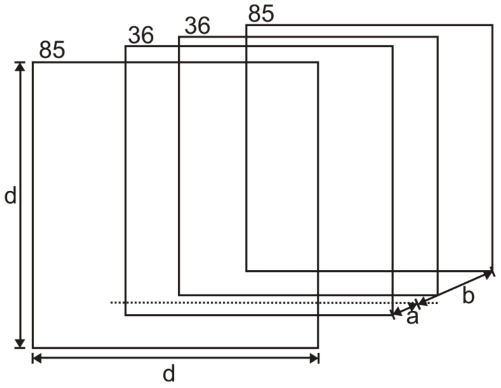

Figure 4.7: Schematic drawing of Merritt 4 coil. Four rectangular coils with diameter d and 85 and 36 windings, for the outer and inner coils respectively. The inner coils are positioned at a distance a/d and the outer coils at b/d relative to middle line.

The system shows some cross talk between the axis which is however linearly dependent on the applied voltage and therefore can be corrected by solving the equation:

$$\begin{pmatrix} B_{xx} & B_{yx} & B_{zx} \\ B_{xy} & B_{yy} & B_{zy} \\ B_{xz} & B_{yz} & B_{zz} \end{pmatrix} \begin{pmatrix} V_x \\ V_y \\ V_z \end{pmatrix} = \begin{pmatrix} B_{outx} \\ B_{outy} \\ B_{outz} \end{pmatrix} \tag{4.51}$$

where the columns in the matrix represents the magnetic field changes per volt which was applied for x, y and z component, respectively. In order to get the voltage which has to be applied to get the desired magnetic field the linear equation system has to be solved. Furthermore the magnetic field in the laboratory is not completely stable over time (changes from other labs, other positions of electrical equipment, etc.). Therefore a calibration run is performed on a regular basis. However regardless of the fact whether the magnetic field coincides with the preset field the actual magnetic field at the pigeons head is always monitored during experiments. For details on the calibration see chapter 8.4.

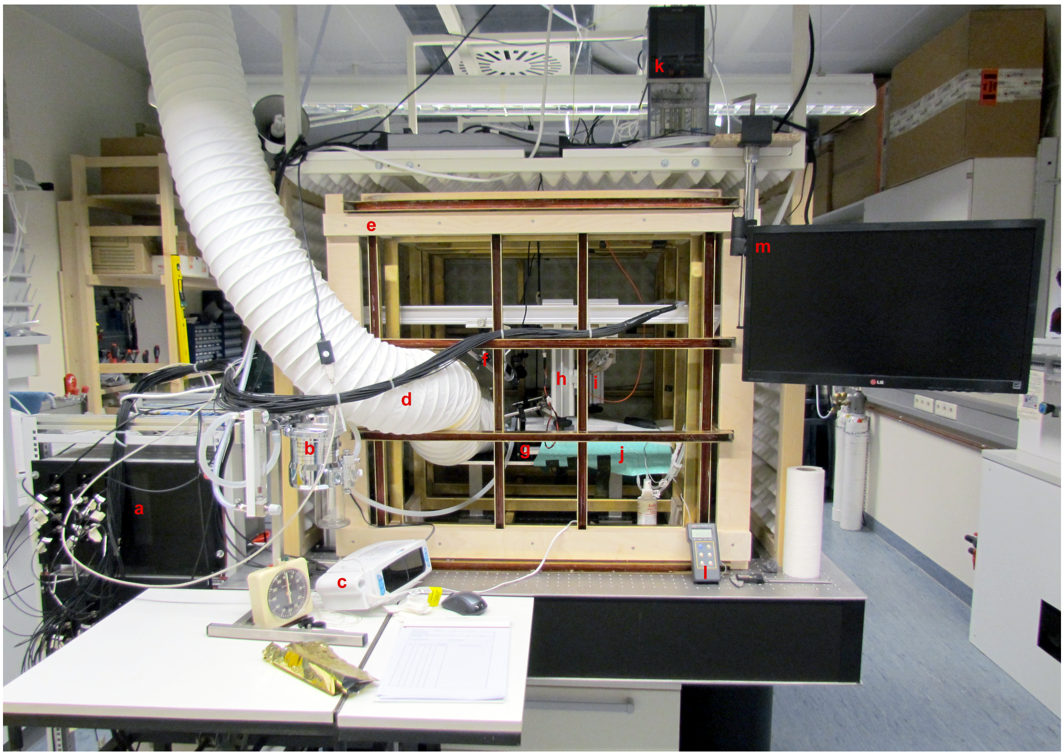

Figure 4.8: DWS Setup: a) rack with 32 avalanche photo diodes and the 32 channel autocorrelator; b) anesthetic unit with isoflurane vaporizer, flow meter and air humidifier; c) pulse oximeter and capnometer; d) suction unit for anesthetic waste gases; e) three dimensional Merritt 4-coil system for the control of the magnetic field; f) two cameras; g) stereotactic device with fluxgate magnetometer (not visible); h) laser and i) detector holder with 6 degrees of freedom; j) heating blanket; k) heating thermostat; m) monitor for real time monitoring.

The setup at its current stage as previously described is shown in figure 4.8. For the measurements the pigeon is placed on the heating blanket and narcosis is induced. After placing the monitoring equipment (pulse oximeter, thermometer) the pigeon is fixated in the stereotactic device. Finally the laser and detector can be positioned with the custom build rail system over the brain region of interest. The experiment can be remotely controlled by custom written software of Wolfgang Scheffer. It has to be noted that all experiments were performed together with Wolfgang Scheffer and also the set-up has been build together.

4.1.3.1 Signal Processing

The 32 autocorrelation functions are averaged weighted by their relative count rate $C_i(t)$:

$$g_2(\tau,t) = \frac{1}{\sum_{i=1}^{32} C_i^2(t)} \sum_{i=1}^{32} C_i^2(t)\, g_{2i}(\tau,t) \tag{4.52}$$

Even though all fibers sample the same dynamics the count rate differs between channels due to an unequal optical coupling of the fibers as well as different quantum efficiencies of the avalanche photo diodes. In order to further justify this kind of averaging the variance of the individual channels was z-transformed[470] and showed, as expected, a reciprocal behavior with the average count rate of the channels. Figure 4.9 shows exemplary data of the countrate and the standard deviation of the channels as well as the reciprocal of the variance of the diffusion coefficient of the individual channels (correlation coefficient: 0.94).

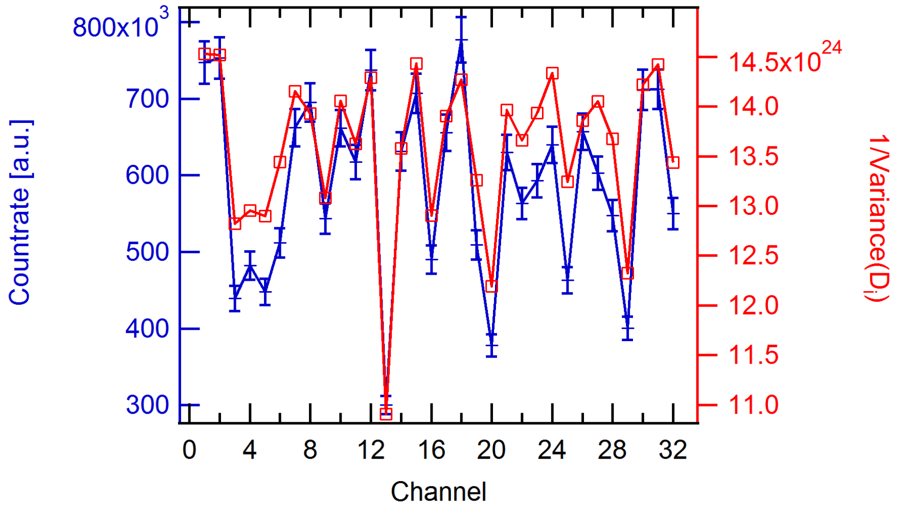

Figure 4.9: Exemplary data of the average countrate and its standard deviation of the channels is shown (left axis - blue curve) with the reciprocal of the variance of the diffusion coefficient (right axis - red) of the individual channels is shown.

The optimal analysis of the autocorrelation function is not completely obvious because the head of the pigeon is a heterogeneous multilayer object with different dynamics. Furthermore it is not fully clear if the dynamics are purely diffusive. Therefore different ways of analyzing the autocorrelation functions were applied

which rely on different assumptions.
A model independent measure of the average dynamics is the decay time:

$$\tau_d\left(t\right) = \int_{t_1}^{t_3} \tau^b \left(g_2\left(\tau, t\right) - 1\right) d\tau \tag{4.53}$$

where τ^b is a weighting factor which allows to weight the short times (long path) more strongly ($b < 1$). Except it is noted differently all times are weighted equally (b=0) and the integration is performed between $t_1 = 0.4$µs and $t_3 = 120.4$µs.

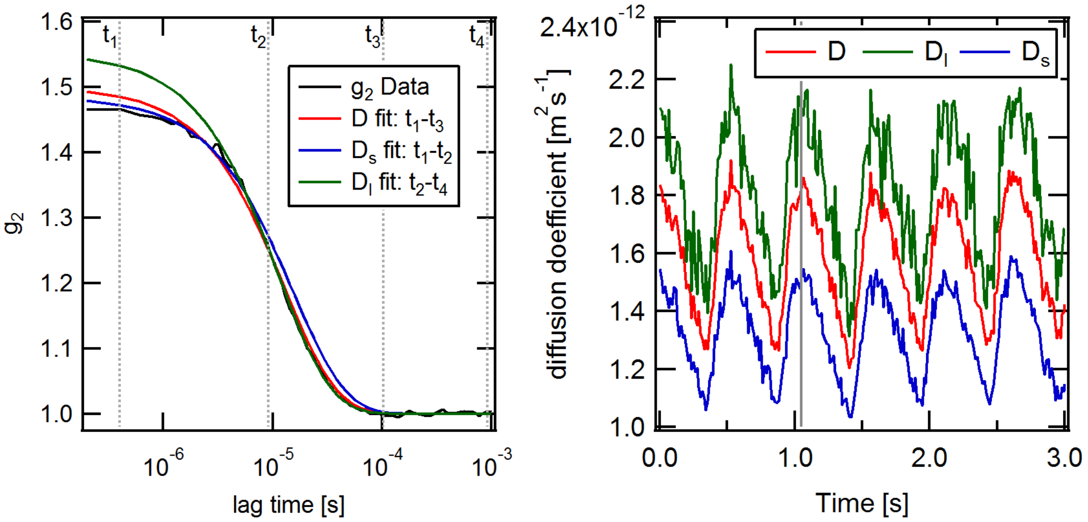

Figure 4.10: The left figure shows the averaged autocorrelation function g_2 with an integration time of 13ms (black) and the semi-infinite fit with Brownian dynamics between the times indicated in the legend. The right figure shows the time course of the data. The changes in the diffusion coefficient are due to changes is blood flow during systole and diastole. The gray line marks the position of the fit data shown in the left figure.

Furthermore the auto correlation functions g_2 are fitted with the analytical solution of semi-infinite model (equation 4.50). The different fits presented below are shown in figure 4.10.

- Diffusion coefficient: D
  Fit intercept and diffusion coefficient of the complete decay in the interval $t_1 = 0.4$µs and $t_3 = 120.4$µs. This is the standard method used.

- Short time diffusion coefficient: D_s
  The fitted autocorrelation function of the diffusion coefficient D is used to determine the time t_2 when the autocorrelation function g_2 crosses 1.25 (corresponding to $g_1 \approx 0.7$ if $\beta = 0.5$) and only the part between t_1 and this point

is used for the fit. These short times correspond to long paths and therefore should have more photons from deeper regions. See[471] for a more detailed discussion about the sensitivity. This will be denoted as D_s or short time diffusion coefficient.

- Long time diffusion coefficient: D_l
  The long time diffusion coefficient which will be denoted D_l is determined from the fit between t_2 and $t_4 = 921.6$µs. This function has a greater sensitivity to short path and therefore more to superficial structures.

- D_{ratio}
  In addition the ratio between D_s and D_l is calculated. The idea is that physiological changed should affect both D_s and D_l, but the activation of the brain area should be restricted (or at least be larger) in the short time diffusion coefficient. Therefore D_l is used to correct for physiological changes which are not associated with the activated brain area. Note that D_s and D_l are however not independent of each other and that the noise level of D_s and D_l is larger compared to D.

- Fit individual channels
  The intercept of individual channels is fitted and the fit value β is used to calculate the corrected g_2. This can either be done by using the temporal average of each channel for the fit or by fitting each autocorrelation function individually and then calculate the average. Both methods show only minor differences and it is not obvious which method is the better one.

  $$g_{2i}^{corr}(\tau, t) = \left[(g_{2i} - 1) * \frac{0.5}{\beta_i}\right] + 1 \tag{4.54}$$

  The averaged g_2 is calculated according to equation 4.52

- Two dynamics
  The autocorrelation function g_2 is fitted both with a diffusive and a directed part, which means that $\langle \Delta r(\tau) \rangle \propto \text{lin}\ \tau + \text{quad}\ \tau^2$. This approach is important if a significant part of the signal is from directed motion such e.g. muscle motion (see[420] for details). For cerebral blood flow measurements no separation of the two dynamics is possible. The fit is less stable and assigns part of the dynamics to the quadratic fit. This introduces an additional source of noise and reduces the signal of the diffusive part which results in a reduced signal to noise ratio. Under these circumstances no additional information could be gained from the fit with two dynamics.

4.1.3.1.1 Noise removal

The signals due to neuronal activation are very small. Therefore all kind of “noise”, which includes physiological noise such as heartbeat and breathing as well as non periodic physiological changes such as temperature, partial CO_2 level, “spontaneous” hemodynamics (reflecting ongoing brain activity) and other artifacts due to motion, arrhythmia, etc., have to be removed from the signal in order to reconstruct the correct hemodynamic response function (HRF) as well as to enhance the signal to noise ratio.

Different strategies to remove or at least reduce the various sources of noise have been implemented. Only the version which showed the best results for neuroimaging will be presented in more detail. This process is largely based on the procedure described in Fekete et al.[470] for NIRS imaging, however with some changes in order to adapt the procedures to DWS.

The process is divided into three steps: First, periodic physiological changes are removed from the data followed by the removal of sharp non-periodic artifacts. Finally slow varying, non-periodic changes are reduced. The procedure has been optimized for the dynamic signal (diffusion coefficient - blood flow) but is also applied to the intensity data (absorption - blood volume).

A typical example of the diffusion coefficient and the processed data with various sources of noise is shown in figure 4.11 with the power spectrum of the data in figure 4.12. A step by step description of the different strategies to remove the physiological signal is given.

Remove periodic physiological artifacts

Removal of heart rate signal:

The largest variations in the signal are mostly given by the heart beat (typically between 20-40%). The shape of the heartbeat signal is usually very regular and can therefore be removed from the data. Note that the amplitude in the awake experiments was usually smaller and the signal to noise ratio was significantly worse, which makes the processing less reliable. This is also true for the intensity data which shows smaller oscillation with heart beat. Nevertheless the same kind of processing has been applied. Figure 4.13 shows a schematic of the processing steps, which are described in more detail in the following:

- First the dominant frequency f_{HR} in the range of normal heart beat frequencies (60bpm-300bpm - 1-5Hz[2]) is identified. Therefore first the power spectrum (fast Fourier transform (FFT) of the autocorrelation (Wiener-Khinchin theorem)) is calculated. In order to facilitate the peak finder routine a flat spectrum is computed by subtracting a noise model which corrects for the

---

[2] with ketamine/xylazine an extreme bradycardia (about 60bpm) has been observed. Therefore the frequency range has been adjusted to $0.6f_{HR}$ if this is smaller than 60bpm.

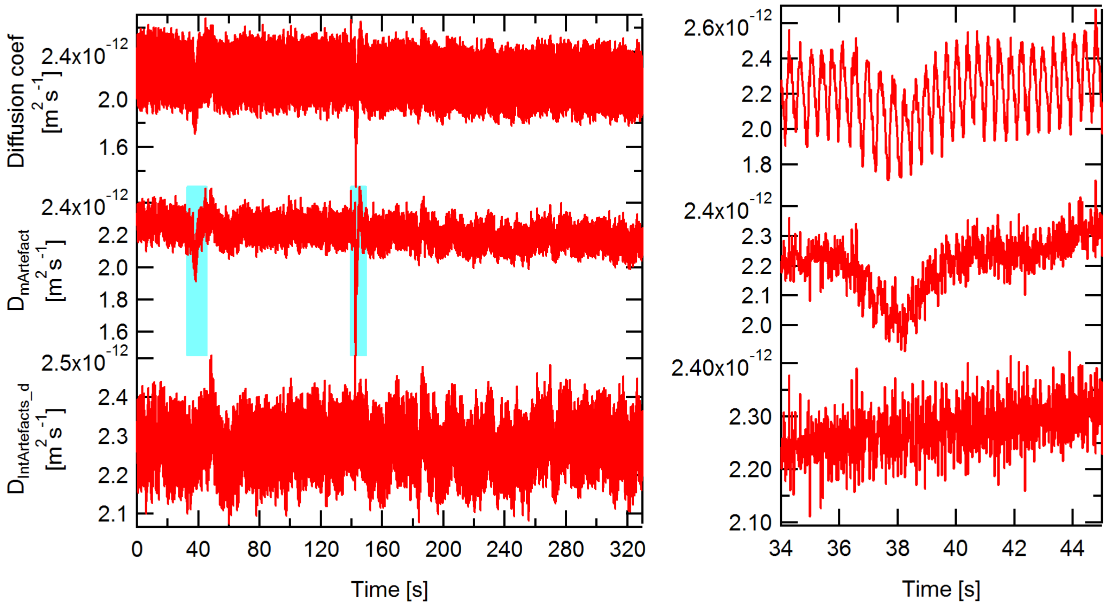

Figure 4.11: A typical measurement with various sources of periodic and non periodic noise is shown. The top curve shows the fitted diffusion coefficient without any further processing, the middle curve shows the diffusion coefficient after removal of periodic noise and the bottom curve shows diffusion coefficient after additional removal of non-periodic noise (highlighted in blue). The right figure shows an enlarged view of the same data in order to see the effects more clearly.

observed pink noise (1/f-noise) which reaches a constant level (fit log-log plot with $f(x) = Y_n + (a + b \cdot x) \cdot (x < \frac{-a}{b})$ see dashed black line in figure 4.12). Then the highest peak in the corrected spectrum is identified.

- An acausal bandpass filter in the range $[0.6 f_{HR}, 1.4 f_{HR}]$ is applied to the data. The frequency range has been chosen to allow for large heart beat variations which have been observed in extreme cases but do not include any higher harmonics to facilitate the algorithm for peak detection.
- A custom written peak finder is used to find positive peaks in the bandpass filtered data.
- It has been observed that the heart beat amplitude scales with the average diffusion coefficient. Therefore slow variations are compensated by dividing the wave by the mean of 10s multiplied by the wave average.
- Acausal bandpass filter the wave in the heart beat frequency range [1,10]Hz. The larger frequency range is used since higher harmonics have been observed up to the 6th order and one has to include the high frequency signal to accurately model the heart beat signal.

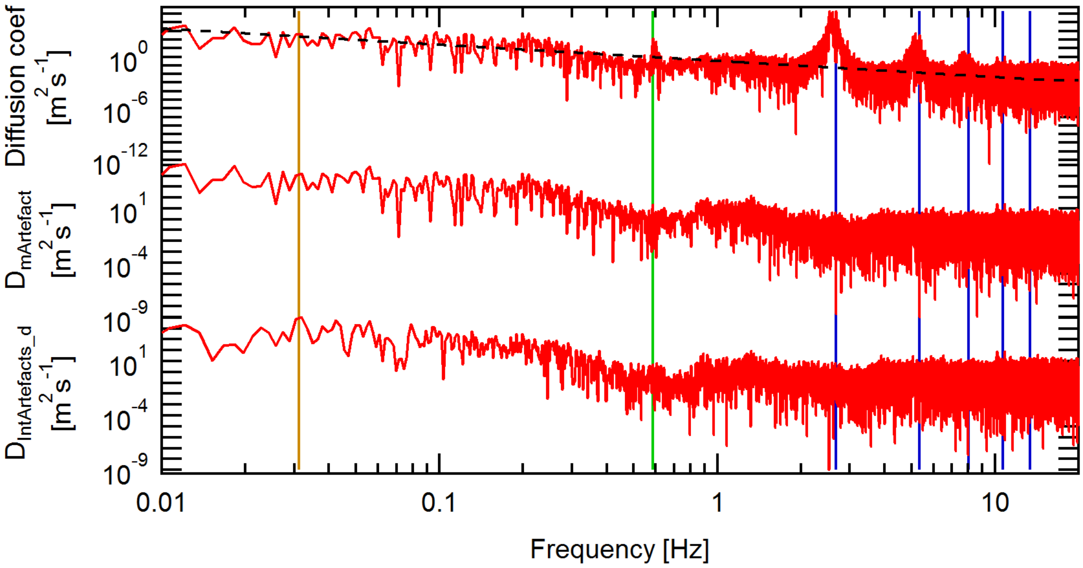

Figure 4.12: Power spectrum of the original wave (top), after removal of heart beat and breathing artifact (middle) and after artifact removal. As a guide to the eye the position of the heart rate with higher harmonics (dark blue), breathing (green) and stimulation frequency (orange) are shown. The dashed black line indicates the noise model (pink noise (1/f-noise) up to a constant noise level around 15.7 Hz) which has been subtracted before identifying the peaks in the spectrum (see text for details).

- The average heart beat length is calculated from the peak positions and all segments between peaks are stretched and compressed to the average length.
- A time-invariant signature of the cardiac pulsations is calculated by averaging over all segments. In some cases the Y value of the start and end point do not perfectly match. In these cases the waveform is corrected for the slope of a line through these points.
- The wave segments are compressed/stretched back to the original length.
- The amplitude of the heart beat waveform is scaled back to its original height.
- The residual after removing of the artifact is calculated.

After this procedure it has been observed that in some cases there is still some peak in the power spectrum at the second harmonic of the heart beat. Therefore the same procedure is run a second time if the dominant frequency of the residual wave after artifact removal is larger than the dominant frequency of the original wave. The shape of the heart beat artifact has a typical shape shown in figure 4.14 left, which shows only small variations in different experiments. The minimum in the waveform is in the diastole with minimum blood flow and the maximum is at

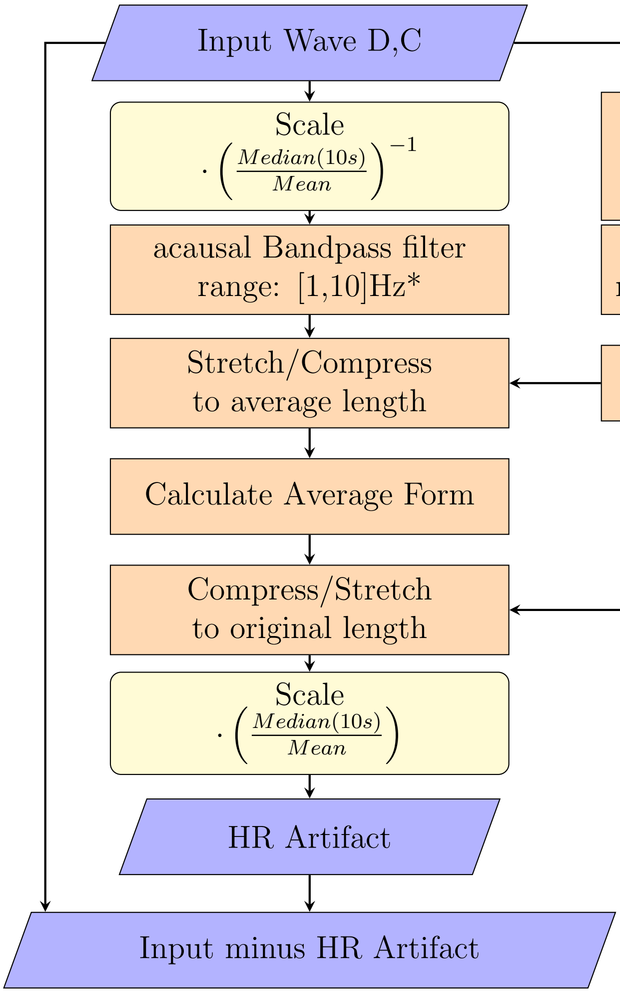

Figure 4.13: Schematic of the processing to remove the average heart beat signal. See text for a detailed description.

the systole, when the blood flow reaches its maximum.
The intensity shows in contrast a maximum at the diastole due to a smaller absorption owing to a smaller blood volume and a minimum in systole because of a larger blood volume. In addition, the relative change due to cardiac pulsations is usually small and there is a greater variability in the average shape. Note that the peak due to systole in countrate has a small delay.

Removal of breathing signal:
Variations due to breathing are less pronounced, but are repeatedly observed, particular in the case of breathing arrhythmia. Therefore after heart beat removal the same procedure is used to remove the breathing rate except that no scaling is applied (yellow procedure steps in figure 4.13) and that the frequency range is set

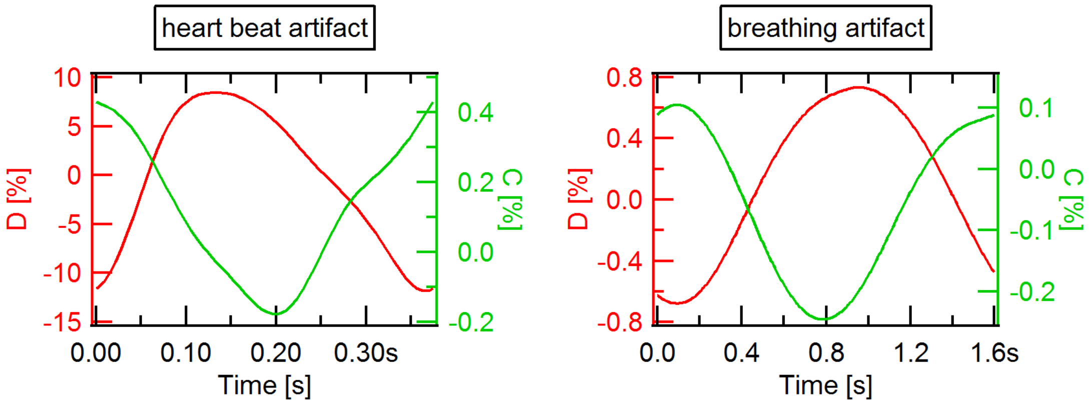

Figure 4.14: Typical shape of the dynamic data of the heart beat (left) and breathing (right) of the diffusion coefficient (left axis, red) and the countrate (right axis, green) scaled relative to the average over the whole measurement.

to 0.2-1Hz (12-60bpm). A typical representation of a breathing artifact is shown in figure 4.14 right. Note that the amplitude is about an order of magnitude smaller than the heart beat signal and there is a greater variability in the shape of the breathing artifact particularly if the variations are very small.

In contrast, in the countrate, the breathing artifact has about the same magnitude, in some cases even larger than the heart rate artifact. The delay is smaller and reversed. With experience from many experiments I speculate that (except for breathing arrhythmia) the effect in countrate is dominated by optical coupling rather than blood volume changes. Additional evidence for this hypothesis comes from the fact that the short time diffusion coefficient (long path) shows a larger change (23.0% vs 18.6%) for the heart beat artifact and a smaller change (1.7% vs 1.8%) for the breathing artifact in comparison to the long time diffusion coefficient (short path) (values for the same experiment as in 4.14).

A summary of the amplitudes of heart beat artifact and the breathing artifact over experiments with inhalation anesthesia (n=283) are reported in table 4.2.

Table 4.2: Amplitudes of periodic physiology artifacts of experiments with the pigeon in an inhalation anesthesia (n=283). The values reported are the average change relative to baseline level and standard deviation. All values are statistically significantly different (paired Student's t-test) ($p < 0.001$ except breathing artifact D_s, D_l $p = 0.017$).

	heart beat artifact %	breathing artifact %
D	27.1 ± 6.7	3.4 ± 5.0
$\mathbf{D_s}$	27.7 ± 6.7	3.6 ± 5.3
$\mathbf{D_l}$	26.3 ± 6.7	4.0 ± 5.6
C	0.79 ± 0.38	0.68 ± 0.67

Mayer waves

Mayer waves, which are oscillations in the arterial blood pressure due to oscillation of the sympathetic vasomotor tone[472] (for a review of causes see[472]), are often also compensated in neurophysiological studies. However in literature there is no information about the frequency range of mayer waves for pigeons. For rats, which have about the same weight but about double the physiological frequencies for heart and breathing rate, a frequency of 0.4Hz for the mayer waves is given[472]. Despite the peak from breathing no additional peak can be clearly identified around the frequency range 0.2 to 0.4Hz. In addition the removal of the breathing artifact is applied to the frequency range of 0.2-1Hz. Therefore the effect might already be partly compensated by the former procedure. No additional correction for the mayer waves is performed.

Remove nonperiodic artifacts

Despite physiological variations a variety of other artifacts have been observed. First a list of the most common artifacts is given and subsequently a description how they are handled.

- The most prominent artifact in awake measurements is the motion artifact due to movements as well as muscle motion during eye lid closure.
- Sharp spikes, which only rarely occur and are most likely due to experimental problems.
- During anesthesia a variety of arrhythmia has been observed including ventricular extrasystole (VES) with compensatory pause, breathing arrhythmia and arrhythmia absoluta[3].

Figure 4.15 shows the typical shape of an artifact where one heart beat has been skipped (most likely a ventricular extrasytole with compensatory pause). As will be discussed in more detail in section 4.1.6 there is a strong linear correlation between variations in heart rate and cerebral blood flow. Therefore an attempt is made to eliminate these variations in the data. First a custom written peak finder is used to obtain the heart beat. The diffusion coefficient is then averaged over one heart beat at a time (D_{HR}). To determine a delayed response in blood flow the autocorrelation between heart rate and D_{HR} is calculated and the data is shifted by the position of the peak in the autocorrelation curve. The dependence is then calculated by a linear fit between the two. From the linear dependence a correction for the heart rate is calculated. Between the heart beats the correction is linearly interpolated to the sampling frequency

---

[3] The classification has been performed by analyzing the optical data because ecg has not been routinely measured therefore no definite diagnosis can be assigned.

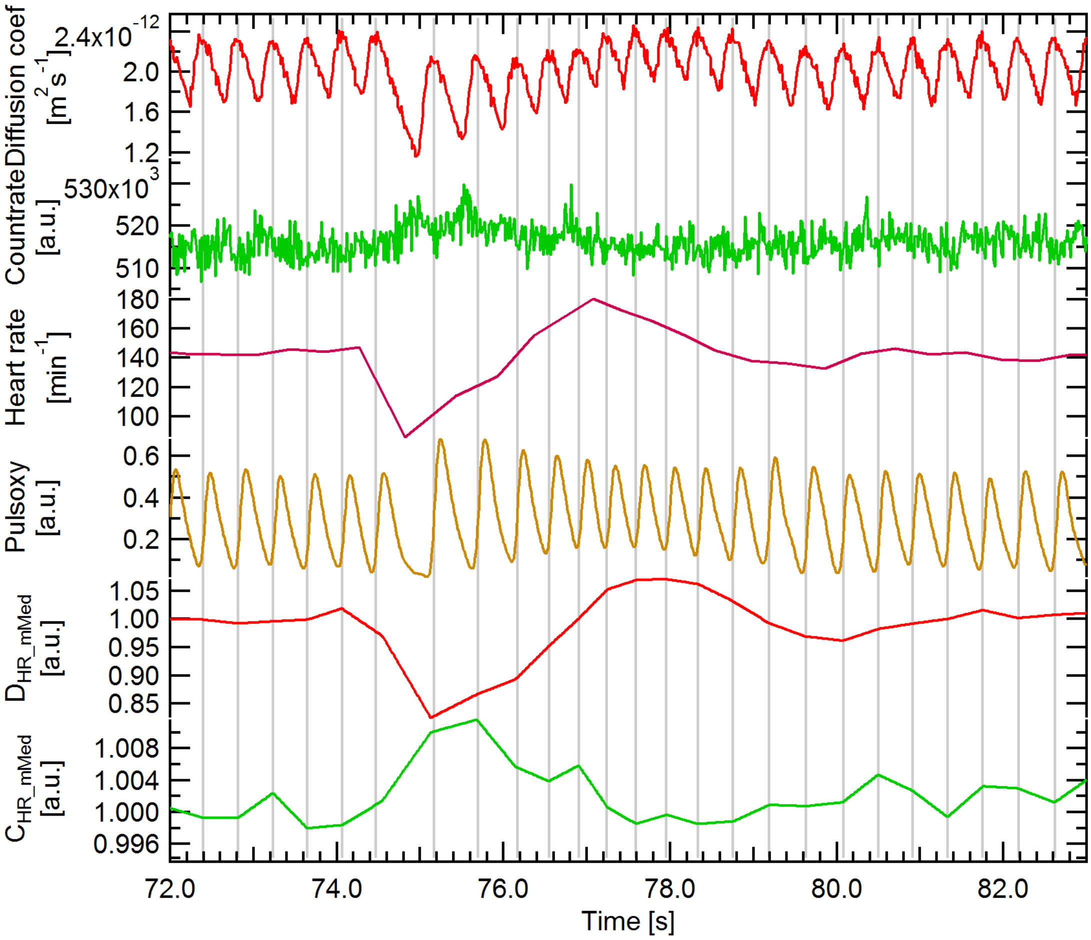

Figure 4.15: Typical time curves during an omitted heart beat (probably due to a ventricular extrasystole with a compensatory pause). The Diffusion Coef is approximately proportional to blood flow signal, the countrate is approximately inversely proportional to blood volume. Pulse oximeter data was measured at the heel of the left leg. Grey lines are the positions of peak blood flow in the brain. The phase lag between head and leg can nicely be seen. Note that the blood flow is reduced by about 15% whereas blood volume is only decreased by about 0.8%. Furthermore a hyperaemia with an increased blood flow of about 5% can be seen.

of the optical data. Exemplary data is shown in section 4.15 in figure 4.26 and 4.27.

It has been observed that the diffusion coefficient shows large spikes which show a characteristic shape of muscle motion (compare Belau et al.[420]). In order to verify this type of artifacts two cameras are used to monitor any motion of the pigeons eyes. Furthermore the pupillary response is an indicator for physiological responses (e.g dilation as reaction to sympathomimetics (fight-or-flight response)) and therefore can also be used as an indicator if the pigeon is detecting certain stimuli. In addition, rhythmic eye motion might be an indicator for the perception of certain moving stimuli.

Figure 4.16 shows exemplary images of the cameras with the eyes manually selected as region of interest. The right image shows the steps which are used to identify the eye area and the center of the pupil. The results of the analysis is shown in figure 4.17.

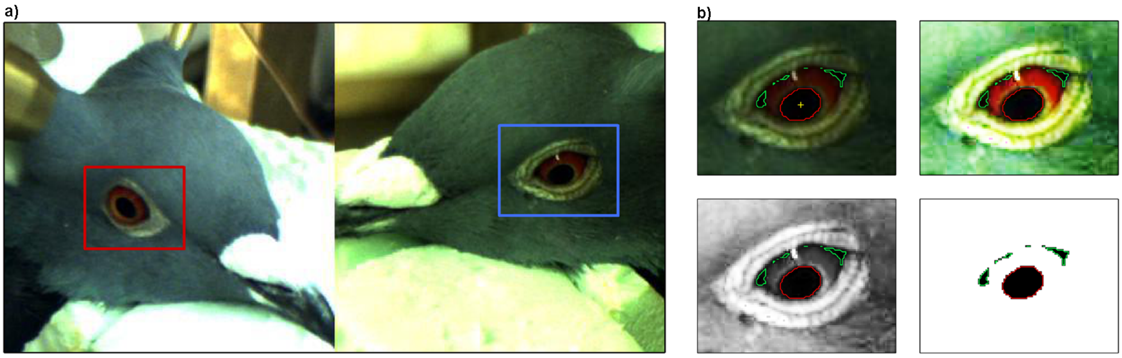

Figure 4.16: a) Combined images of the two cameras of the pigeons head with user defined area for eye movement analysis (red: right eye; blue: left eye).
b) Top left: Cutout of the left eye for the eye motion analysis overlayed with the detected area (red) and the center of the area (yellow cross); Top right: Contrast equalization; Bottom left: Converted to greyscale; Bottom right: Binarized image.

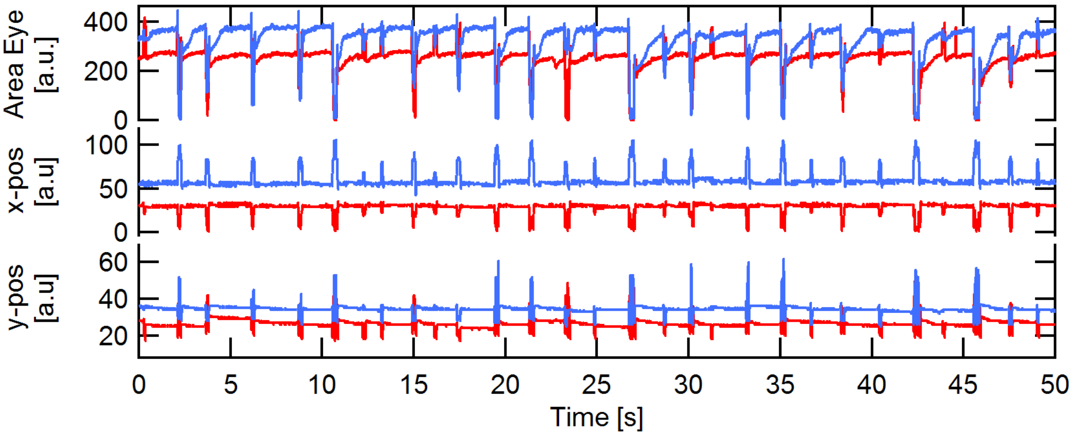

Figure 4.17: Detected eye area and position of the left eye (blue) and the right eye (red). Note that during closure of the eye (sharp spike) not the pupil but rather the complete area of the eye is detected.

There are two strategies to deal with that kind of artifacts. As explained below one can either remove them completely from the data or try to interpolate them in some way. It has been shown that the hemodynamic response function can be recovered better by interpolating the artifacts.

Therefore an algorithm which removes all kind of non-periodic artifacts has been developed.
First sharp spikes lasting only a few data points are removed by using a median averaging with 0.4s where outliers are replaced by the median if they are larger than 2.5 times the standard deviation of the wave divided by a 10s median.
This is followed by a procedure which aims in removing motion artifacts. The procedure of detection and cancellation largely follows the ideas developed by Fekete et al.[470] for NIRS imaging. In order to detect the artifact with its start and end the data is preprocessed as following:

- Acausal highpass filter with 0.01Hz
- Z-transformed (remove time series mean and divide by its standard deviation)
- Find points which are larger than 4 standard deviations
- Find artifact onset and end:
  - Find extremum of artifact interval
  - Find opposite extremum left and right of main extremum and add 40 data points to the position
  - Use bottom up segmentation of the left and right part with 3 segments each[473]
- If two artifacts overlap they are combined to one artifact

After identifying the artifacts are canceled. Therefore the artifact is interpolated by calculating the linear interpolation of the average 40 data points (0.526s) before and after the artifact plus the difference between the wave and binominal smoothed wave of the order 40 (Igor Pro). This procedure preserves the high frequency information while removing the large deviations due to motion. See figure 4.11 right for exemplary data. This procedure works very well if there are not too many of these artifacts. If too many artifacts occur close to each other the procedure might not be able to reliable cancel all artifacts. These measurements have been discarded from further analysis.

First some effects of anesthesia on cerebral blood flow which have been found by chance will be described. This is followed by functional measurments with visual and magnetic stimulation.

4.1.4 Isoflurane

The adequate perfusion of the brain is of utmost importance to avoid damage of the brain. However, the cerebral blood flow is currently not routinely monitored during general anesthesia.

Also it might be inferred from peripheral measurements such as the blood pressure from the relationship following Ohm's law (see appendix 8.3 and[474] for more details):

$$CBF = \frac{CPP}{CVR} \qquad \text{with } CPP = MAP - ICP \tag{4.55}$$

with CBF: cerebral blood flow; CPP: cerebral perfusion pressure; CVR: cerebrovascular resistance; MAP: mean arterial pressure; ICP: intracranial pressure. However, this relies on the assumption that ICP and CVR are not changed. While the former is usually valid in healthy people, the latter is not fulfilled during intact cerebral autoregulation. Both CVR and ICP can not be accessed on a routine basis.

In addition CBF, CVR and ICP may be influenced by effects of anesthetics and other drugs but also due to medical history and individual effects. Especially in critical ill patients it may not be sufficient to estimate cerebral blood flow.

Monitoring of blood flow is currently only performed during specific surgical conditions, such as surgery of carotid artery stenosis. The “gold standard” is transcranial Doppler (TCD) ultrasonography which however is limited to large arteries and the so called “ultrasonic windows” where the ultrasound can reach large cerebral arteries (for a review see[475]).

In contrast, DWS measures the local micro circulation and can be applied throughout the head. Furthermore, it is relatively inexpensive, fast and portable and might greatly improve anesthetic management as well as chronic monitoring during or after events with disturbed perfusion such as stroke.

The experiments presented in this section were not optimized to investigate the above mentioned effects, but it was rather tried to optimize the narcotic setting in respect to neurovascular coupling, but the results are still very interesting such that they are worthwhile to be presented.

4.1.4.1 Experiments

Anesthesia was performed with isoflurane as a single agent, except for two cases, in which buprenorphine (0.5mg/KG) was preemptively administered (see section 3.2.2 for details). Usually, first functional stimuli where applied and then the isoflurane concentration was either increased or decreased by 0.5% during the measurements.

Figure 4.18 shows the diffusion coefficient (cerebral blood flow) in a pilot experiment where the isoflurane concentration has been decreased at 50s from its

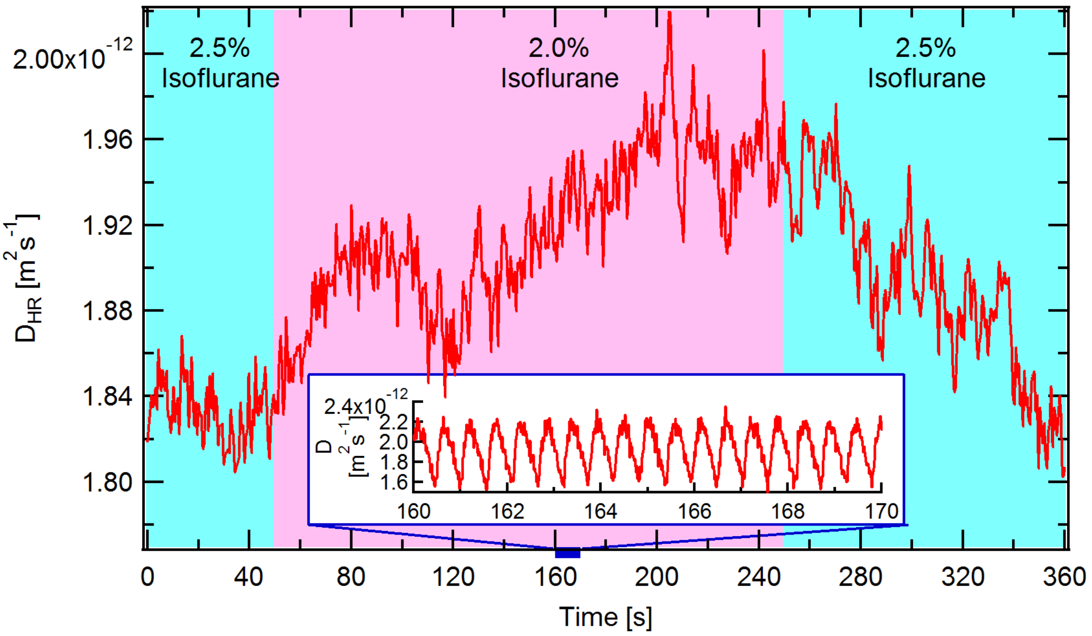

Figure 4.18: Change in the diffusion coefficient averaged over heart rate D_{HR} (cerebral blood flow) due to a variation in the isoflurane concentration. The inset shows the non-averaged diffusion coefficient.

maintenance dose of 2.5% to 2.0% followed by an increase back to 2.5% at 250s. It can nicely be seen that the diffusion coefficient, which was averaged over the heartbeat, is increased by about 8%. The inset shows the unaveraged diffusion coefficient showing the perfusion during systole and diastole. Note the that the amplitude due to variations from heartbeat is considerable larger (about 40%).

In order to better understand this effect both a decrease and increase of the isoflurane concentration was performed in two pigeons (figure 4.19). In order to show the effects more clearly the data has been smoothed (10s median) and normalized to the average value of the interval 40-50s. Both pigeons have been in narcosis for about 40-45min, the maintenance dose has been 2.5% and the concentration has first been decreased and than increased. It can be nicely seen that a decrease of isoflurane concentration leads to an increase of cerebral blood flow, whereas an increase of isoflurane concentration leads to a decrease of cerebral blood flow.

In order to analyze if this is a general effect and to estimate the magnitude of the effect, the average over all measurements where the isoflurane concentration has been changed during the measurement, has been performed. Group averages of physiological and measurement data are shown in table 4.3. Only the average body temperature is slightly lower in the group where the isoflurane concentration

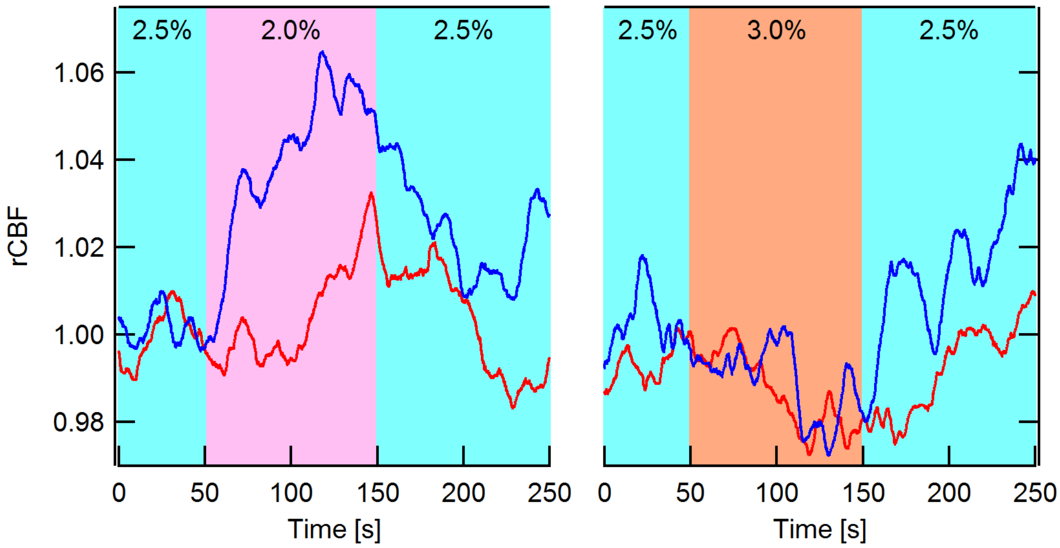

Figure 4.19: The figure exemplary displays the effect of a change in isoflurane concentration to cerebral blood in two pigeons (red and blue). To make the data more clear the 10s median of the artifact corrected diffusion coefficient normalized to the mean of 10s before the change of isoflurane concentration is shown. The maintenance dose was 2.5% (blue area) and has been decreased to 2.0% at 50s (pink area) and back to 2.5% at 150s followed by a measurement where the concentration has been increased to 3.0% at 50s (orange area) and back to 2.5% at 150s.

has been decreased. All other values are not statistically significant different. Note however that the group where isoflurane has been increased is considerable smaller.

As a first indication of the average behavior in the two groups, the average and extrema of the CBF are analyzed (see table 4.4) in the time following a change in concentration (either up to the next change or the end of the measurement). In almost all cases (decrease: 11/15, increase: 4/4, see figure 4.20 top) the CBF shows an increase/decrease after a decrease/increase of the isoflurane concentration. Note that the amplitude of the change and the time of the change shows a considerable variance which on average is about 6% and is located at about 90s. The final level of CBF cannot be accessed from the measurements since the measurement was not long enough. The average behavior indicates an approximately linear behavior in the first 150s after a change (see figure 4.20), where however individual curves show a strongly nonlinear behavior. Note, that there is a considerable variance in peak height, however the average direction is observed in nearly all cases (see figure 4.20 top).
The average values of the peaks of all data from the interval after the change (either up to the next change or till the end of the measurement) are given in the table 4.4. It can be seen that the average values show a significant difference, where the

Table 4.3: Group averages of physiological data from the measurements where isoflurane concentration has either been increased or decreased by 0.5%. Statistical analysis was performed with Student's t-test and Wilcoxon-Mann-Whitney test. ns: not significant in both tests. *: $p < 0.05$ Student's t-test. $^+$: $p < 0.05$ Wilcoxon-Mann-Whitney test.

	decrease	increase	significant
Number of Experiments	15	4	
Buprenorphin	2	0	
Isoflurane Concentration [%]	2.63 ± 0.3	2.75 ± 0.5	ns
Time in Narcosis [min]	45 ± 9	39 ± 8	ns
SpO2 [%]	91 ± 4	92 ± 4	ns
Heart rate [bpm]	126 ± 19	131 ± 18	ns
breathing rate [bpm]	26 ± 5	23 ± 4	ns
Weight [g]	464 ± 65	495 ± 80	ns
Temperature [°C]	40.8 ± 1.0	41.7 ± 0.3	*
Source Detector Separation [mm]	15 ± 3	17 ± 2	ns

CBF is increased during decreased concentration and decreased during increased concentration.

Table 4.4: Group average values of CBF data after a change in isoflurane concentration. Note that the values are from a 10s median. The reported peak values are therefore slightly smaller than the absolute extremum in the measurement. Statistical analysis was performed with Student's t-test and Wilcoxon-Mann-Whitney test. ns: not significant in both tests. *: $p < 0.05$ Students t-test; $^+$: $p < 0.05$ Wilcoxon-Mann-Whitney test

	decrease	increase	significant
Average value [%]	1.6 ± 5.3	-2.2 ± 1.6	*+
Amplitude maximum [%]	6.9 ± 9.9	1.1 ± 1.6	*
Amplitude minimum [%]	-3.1 ± 5.3	-5.2 ± 3.5	ns
Location maximum [s]	93 ± 51	40 ± 25	*
Location minimum [s]	47 ± 63	73 ± 36	ns
Extremum location [s]	100 ± 50	73 ± 36	ns
Average measurement time after change [s]	144 ± 60	138 ± 43	ns

An attempt was made to investigate if the change in blood flow is more likely induced by a change in resistance or in blood pressure. Therefore it was tried to get an estimate of cerebrovascular resistance (CVR) and mean arterial blood pressure (MAP) from the optical data.
In literature the pulsatility index (PI) or resistive index (RI) is sometimes used to reflect CVR[476–478][4]. It is usually determined by transcranial ultrasound imaging

---

[4] Note that there is not a strict relationship between the two quantities and that there are

and is defined as:

$$\begin{aligned} PI &= \frac{v_{systole} - v_{diastole}}{v_{mean}} && \text{Gosling pulsatility index} \\ RI &= \frac{v_{systole} - v_{diastole}}{v_{systole}} && \text{Pourcelot resistive index} \end{aligned} \tag{4.56}$$

Here we use the effective diffusion coefficient to determine a DWS pulsatility index in a similar manner:

$$PI = \frac{CBF_{systole} - CBF_{diastole}}{CBF_{mean}} \qquad \text{DWS pulsatility index} \tag{4.57}$$

It has to be noted that the determined value will most likely be different from the pulsatility index determined from ultrasound measurement since even without any flow the effective diffusion coefficient will not be zero. However, both pulsatility indices should be proportional to each other. Therefore the pulsatility index determined by DWS should also approximately reflect cerebrovascular resistance and the cerebral perfusion pressure can be estimated. Assuming that the intracranial pressure (ICP) is approximately constant and considerably smaller than MAP we can estimate the change in MAP:

$$MAP \approx \frac{CVR_{mean}}{PI_{mean}} \cdot PI \cdot CBF + ICP \tag{4.58}$$

$$MAP \propto PI * CBF \tag{4.59}$$

Figure 4.20 shows the summary over all data where the isoflurane concentration has been changed during the measurement. The percentage change of the normalized cerebral blood flow (rCBF), the pulsatility index (rPI) and the estimated mean arterial blood pressure (rMAP) are shown. Solid lines show the average over all measurements, light dashed lines show individual measurements. It can be nicely seen that a decrease in isoflurane concentration leads on average to an increase in CBF and an increase of isoflurane to a decrease. It has to be noted that the data shows a great variability both in amplitude and time and even reverse effects can be seen in some instances. Nevertheless the difference is highly significant ($p < 0.001$) (Student's t-test, Wilcoxon-Mann-Whitney test).

In contrast the pulsatility index is nearly constant over time. Some stronger variation can be seen in the case of decrease which are due to additional artifacts in

---

situations where CVR and PI show inverse behavior (e.g. neurally mediated syncope[479]). For a current discussion see[474,480] where a formula based on a simple model is given: $PI = \frac{AMP_{ABP}}{CPP}\sqrt{(CVR\ C_a\ HR\ 2\pi)^2+1}$ with AMP_{ABP}: amplitude of arterial blood pressure; C_a: cerebral arterial compliance; HR: heart rate. This shows in agreement with experimental findings that regardless of the direction of change in nearly all cases there is a correlation between PI and CVR.

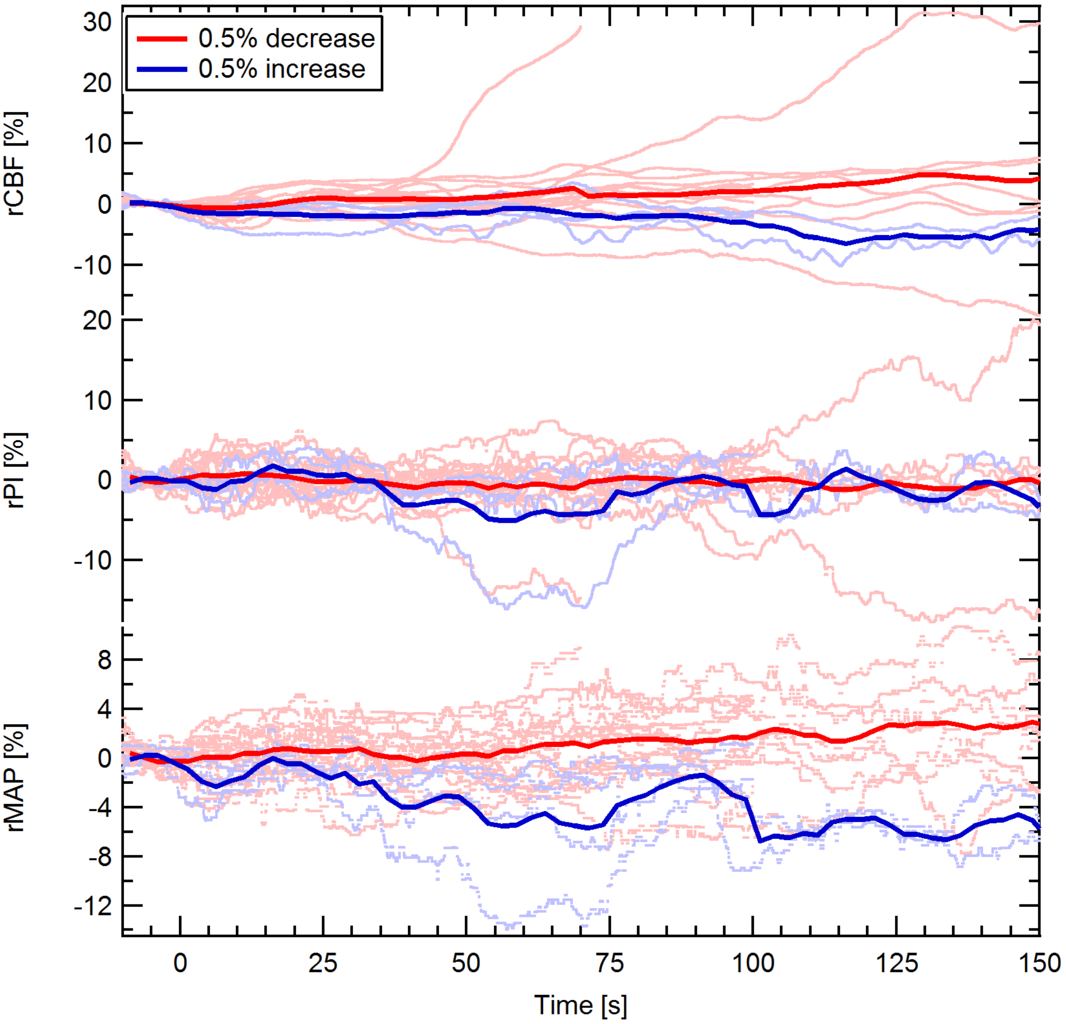

Figure 4.20: Average over all data where the isoflurane concentration has been decreased by 0.5% (red) and increased by 0.5% (blue) at 0s from the maintenance dose (average 2.66%. (2.0%(1), 2.5%(12), 3.0%(5), 3.5%(1))). The solid lines indicate the average over all measurements and the light dotted lines show all data which were used for the averages. All data has been normalized to the average value in the range -10s to 0s. rCBF denotes the percentage change in cerebral blood flow, rPI the change in the pulsatility index, rMAP the estimated change in mean arterial blood pressure (see text for details).

the data (e.g. ventricular extrasystole with compensatory pause which could not be fully compensated in data analysis). This results in some errors in the determination of the pulsatility index and the smaller number of experimental data (n=15 decrease; n=4 increase) does not fully average out this effect.

The change in the estimated mean arterial blood pressure shows a similar behavior to cerebral blood flow, although the increase in MAP during decreased isoflurane concentration is smaller and the decrease during increased isoflurane concentration is larger compared to the change in CBF. The difference between increased and decreased data is however approximately constant in both MAP and CBF.

4.1.4.2 Discussion

The observed response to a change in isoflurane concentration is somehow surprising since it is reported in literature that an increase in isoflurane concentration is associated with a cerebral vasodilation which results in an increase of blood flow[481–483]. However this response is reported for doses usually used in humans which are considerably lower than the concentrations used in pigeons. A likely explanation is that at the high concentrations used in pigeons the cerebral autoregulation might already be disturbed. In this regime the dominant effect is a change in mean arterial blood pressure which shows an increase during decreased isoflurane concentration and vice versa. Additional proof for this hypothesis is given by the fact that the pulsatility is nearly unaffected by changes of isoflurane concentration indicating that cerebrovascular resistance is constant in the range of the applied changes.

It has to be noted that these findings have been more accidental and a thorough study has not been performed. Therefore there are certainly some limitations, which restrict the conclusions drawn from the results. First, many important physiological parameters such as blood pressure, end expiratory CO_2 concentration, end tidal isoflurane concentration, narcotic depth (from electroencephalography or bispectral index), metabolic rate, ecg etc. have not been measured. In particular CO_2 and in a smaller amount O_2 also influence the vascular diameter and thereby the blood flow. In order to fully assign the effect to the concentration of the inhalation anesthetic, the other gas concentrations should be kept constant. Monitoring of the end tidal isoflurane concentration would allow to monitor the wash-in and wash-out times and identify the time when equilibrium is reached. Monitoring of blood pressure could confirm the assumed relationship and would allow for a more thorough analysis. In addition monitoring the pulsatility index both with DWS and TCD would allow to provide a quantitative relationship between both modalities. Second, one should use a standardized study protocol with equal group sizes to infer more meaningful quantitative values.

Nevertheless this preliminary work already demonstrates the great potential of DWS in anesthetic monitoring and anesthesia research. In particular it shows that, even though average values might be similar, the monitoring of each individual is very important because of the great variability in the response to a change in isoflurane concentration.

4.1.5 Temperature effect

The control of the body temperature during anesthesia is of great interest since a loss of temperature is associated with a larger number of critical incidences. For neuroimaging studies a maybe even more important effect of the body temperature is that the metabolic rate and thereby the blood flow is affected, which results in changes in the baseline of the measurement. Furthermore the solubility of isoflurane is also affected by a change in temperature.

During induction of anesthesia one often observes an initial drop in temperature, which is due to a reduction in metabolism and thereby a lowering of heat production (by about 30% in humans)[301]. In addition a redistribution of blood from the warmer body core to the colder periphery due to vasodilation of peripheral vessels results in an additional drop of the core body temperature[301].

In a post hoc analysis of the experimental data the effect on cerebral blood flow has been investigated.

4.1.5.1 Results

The analysis revealed a small but noticeable effect of temperature. Figure 4.21

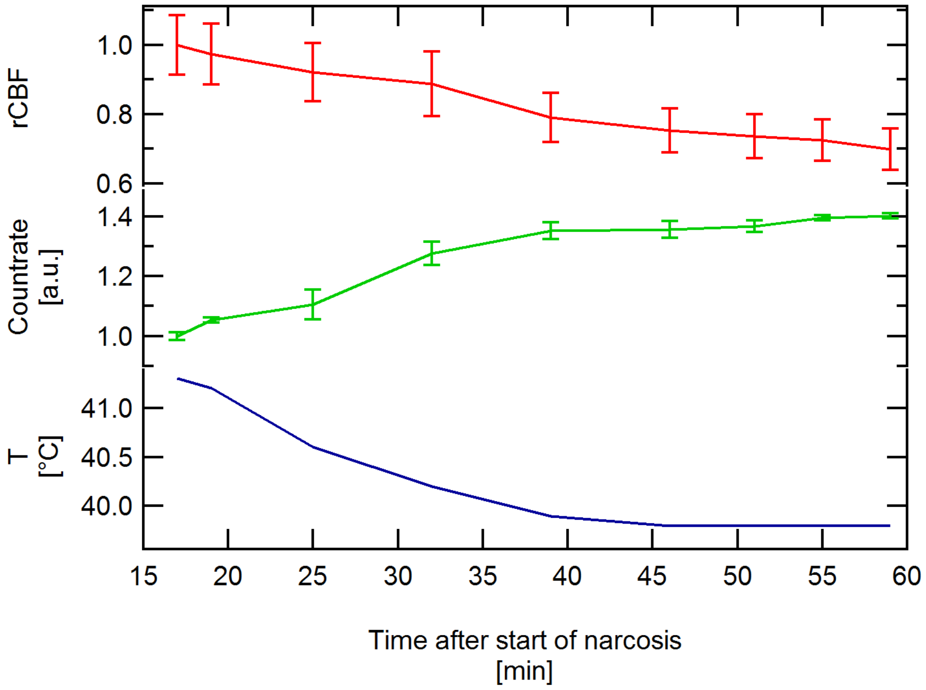

Figure 4.21: The figure shows the relative cerebral blood flow (rCBF) (diffusion coefficient normalized to first measurement point), the normalized countrate and the temperature as function of time in narcosis. The correlation coefficient of the (rCBF) and the countrate with temperature is 0.95 and -0.98, respectively.

shows an example of a DWS measurement where a large drop of temperature occurred. The relative cerebral blood flow (rCBF), the relative countrate (approximately inversely proportional to blood volume) and the body temperature as function of time in narcosis are shown. The countrate and rCBF have been normalized to the first measurement. It can be nicely seen that both the cerebral blood flow as well as the countrate are correlated with the temperature and show a decrease of 30% and an increase of 40%, respectively. This behavior has been observed for rCBF in nearly all of the measurements and in a less consistent way for the countrate.

Figure 4.22 left shows the data from all measurements with isoflurane as a single agent against temperature difference relative to the first measured temperature. One finds on average that the rCBF is reduced by about 5% per °C of decreased temperature (n=168, $r = 0.178$, $p < 0.021$). In addition figure 4.22 right shows that the first measured temperature had some predictive power for the maintenance dose of isoflurane (n=31, $r = 0.203$, p=0.27 not significant). No correlation can be found with weight (n=31, r=-0.085, not significant) and age (n=31,r=-0.089, not significant).

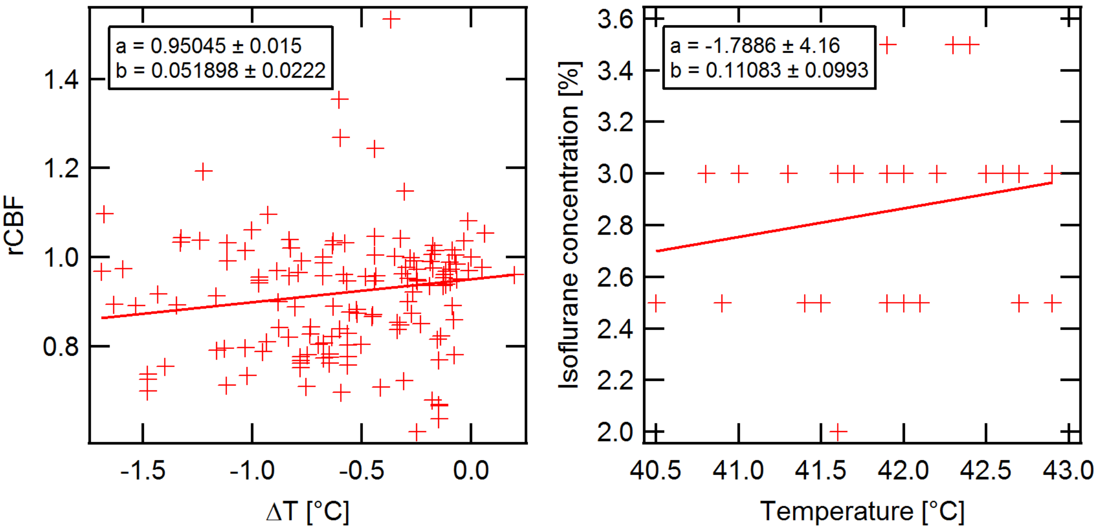

Figure 4.22: Left figure shows relative diffusion coefficient normalized to the time when the first temperature was measured versus the temperature difference relative to the first measured temperature. The right figure shows the maintenance dose of isoflurane versus the first measured temperature. The straight line represents a linear regression of the data with a slope of 0.05 ± 0.02 and $0.11 \pm 0.10\%$ per °C for the left and right figure, respectively.

The effect on the countrate can not be analyzed thoroughly. This is due to the fact that in some measurements the laser power had to be adjusted while the continuous measurement of the laser power has not been implemented yet. If one manually corrects these data points to get a smooth connection between consecutive measurement and performs the same analysis as for rCBF one finds that the countrate is on average reduced with decreasing temperature (linear fit f(x)=a+bx: a =1.018 ± 0.0151 and b =0.042315 ± 0.0224, n=168, r = 0.145, not significant).

4.1.5.2 Discussion

It has to be noted that the experiments have not specifically been designed to investigate the effect of temperature on cerebral blood flow. Notably stimulation, mostly with light, but even short changes in isoflurane concentration were performed during the measurements. In particular changes in isoflurane lead to some deviations which could be seen in the detailed analysis of single measurements. Even with these changes, which increase the variability in the data a clear correlation between cerebral blood flow and temperature can be seen. In addition one finds that the maintenance dose, which can only be set up coarsely in steps of 0.5% and where the focus in the experiments has not been set on employing the minimal required concentration, also shows a tendency to require higher concentrations of isoflurane if the first measured body temperature was higher. Note that no correlation with body weight and age of the pigeons have been found.

One explanation might be that the increased body temperature leads to higher metabolism and therefore requires a higher isoflurane concentration. The increased metabolism will certainly have an effect, but the data can nearly completely be explained with the temperature solubility of isoflurane. Lockwood et al.[385] reported that the solubility increases by 5.4% (compared to the value at 37°C) for each degree that equilibration temperature was reduced. Note that no data is available for temperatures above 40°C. Also for a larger temperature range the relation is rather logarithmic than linear[386,484,485].

Nevertheless reported changes are in good agreement with the observed data with a slope of 5 ± 2% per °C of the relative blood flow and a change relative to 2.5% isoflurane of 4±4% per °C. This is also in good agreement with data of Liu et al.[486] who investigated the effect of hypothermia on the MAC in children and found a reduction of 5.1% per °C reduced body temperature.

4.1.6 Arrhythmia

Different types of arrhythmia have been observed during anesthesia. In this section artifacts with a delayed cardiac output will be analyzed. The most likely electrophysiological reasons are extrasystoles (most likely ventricular) with compensatory pause, but may also be due to a sinuatrial or atrioventricular block. A definitive assignment is not possible since no ecg has been recorded.

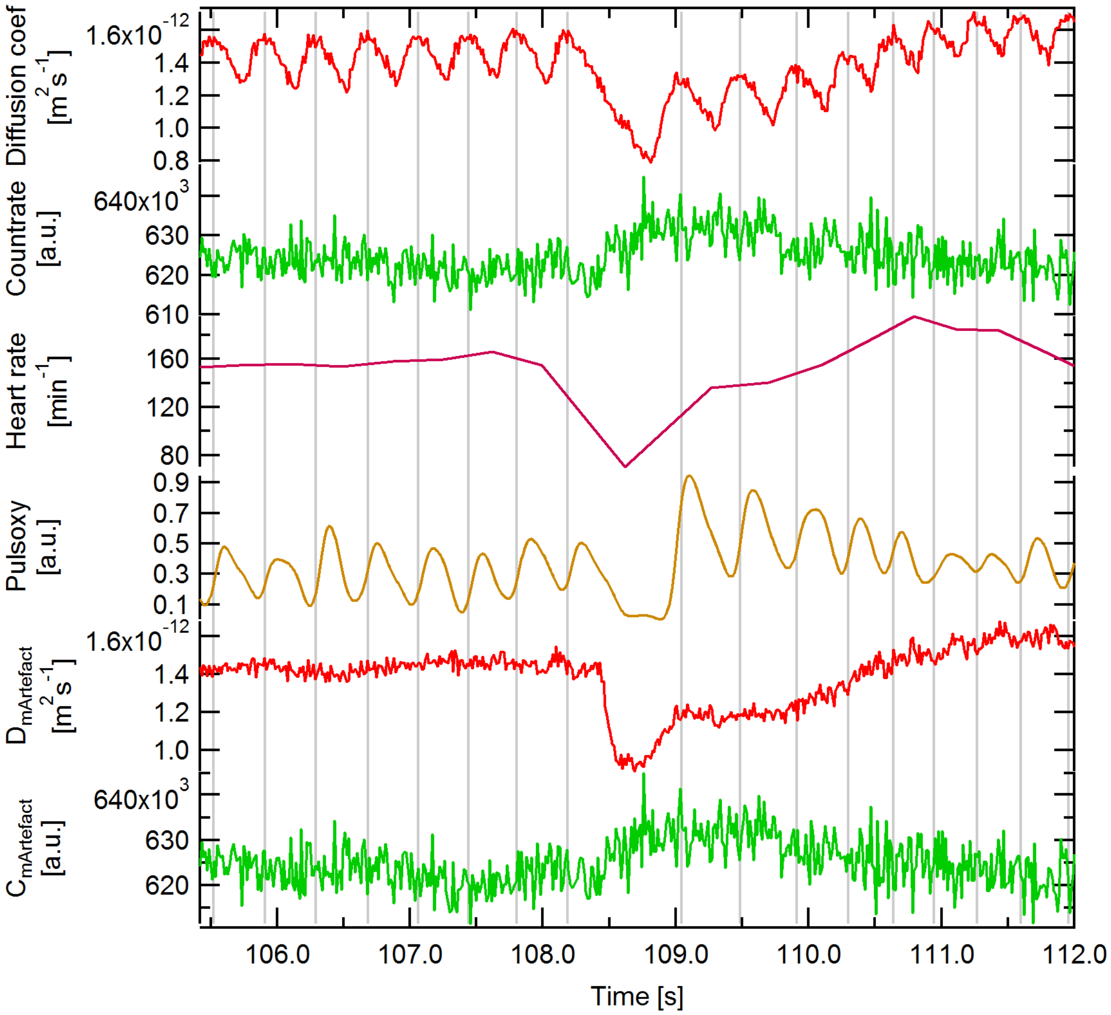

Figure 4.23: The figure shows a typical example for an arrhythmia where one heart beat has produced no cardiac output. The top graph represents the diffusion coefficient which is approximately proportional to cerebral blood flow, the countrate is approximately inversely proportional to blood volume. Heart beat has been determined from the peaks in the diffusion coefficient and are additionally indicated by gray vertical lines. The pulsoxy signal is measured at the heel and is shown in dark yellow. The lower two curve are the diffusion coefficient and the countrate after removal of variations due to heart beat and breathing (see section 4.1.3.1 for details).

An example of such an arrhythmia is shown in figure 4.23. The diffusion coefficient is approximately proportional to cerebral blood flow whereas the countrate is roughly inversely proportional to blood volume. The heart rate is determined by the maxima in the diffusion coefficient and highlighted in gray. The pulse oximeter measures the absorption at the left heel of the pigeon. It can be nicely seen that there is a delay between the signal at the foot and at the brain. Furthermore it demonstrates that really one heart beat has produced no (or almost no) cardiac output. $D_{mArtefact}$ and $C_{mArtefact}$ are the diffusion coefficient and the countrate after removal of variations due to heart beat and breathing (see section 4.1.3.1 for details). In the following curves the diffusion coefficient will be named cerebral blood flow. It can be seen that the cerebral blood flow is dramatically reduced when one heart beat does not produce an cardiac output whereas the blood volume is only slightly changed. The curves have been temporally aligned to the minimum of the diffusion coefficient and normalized to the first heart beat value and the first 11 points in the case of correlator data (Diffusion coef, Countrate, $D_{mArtefact}$, $C_{mArtefact}$). A compilation of the arrhythmia is shown in figure 4.24. The average of all data is shown, although it has to be noted that the temporal evolution is expected to be different depending on the delay of the cardiac output.

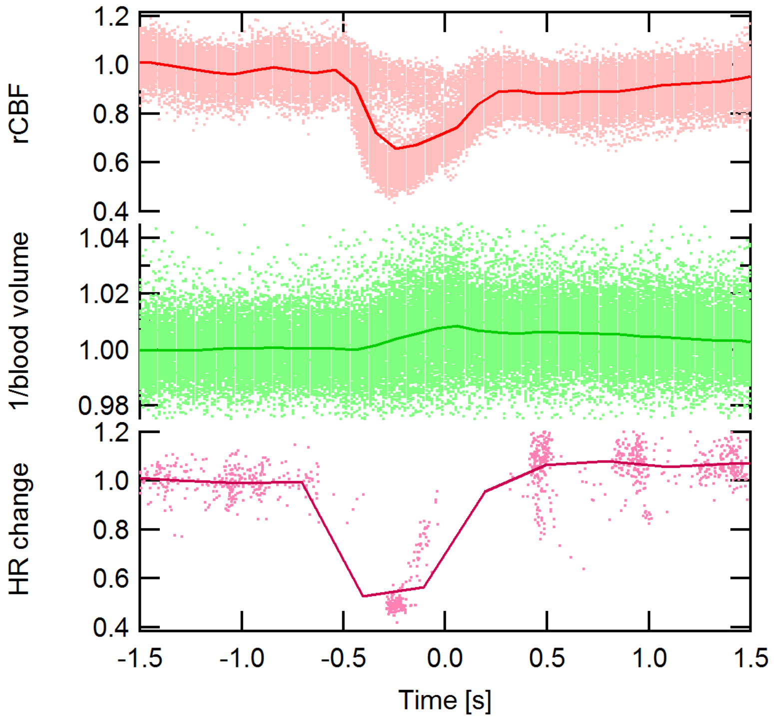

Figure 4.24: Data of all events (N=201) with a delayed heart beat with an temporal alignment to the minimum in the diffusion coefficient. Top: relative cerebral blood flow (rCBF) from $D_{mArtefact}$; Middle: countrate which is approximately proportional to blood volume; Bottom: heart rate from peaks in the diffusion coefficient. Light dottet points are data from all experiments and solid lines are temporal averages of the data with an average of 0.1s for rCBF, blood volume and and 0.3s for heart rate.

To access this in a bit more detail the dependence on relative delay time of the heart beat is analyzed (figure 4.25). Therefore the data has been normalized to the baseline value before the artifact and the amplitude of the artifact has been accessed by the minimum cerebral blood flow and heart rate. The results for N=201 events are shown in figure 4.25 left. A linear relation is found between the two (slope: 0.964 ± 0.033, offset: 0.072 ± 0.018). The Pearson correlation coefficient is 0.900, $p < 10^{-10}$.

The peak in the countrate is less pronounced and the data is noisier. Therefore an additional box smoothing over 20 points has been applied before finding the maximum. The data has also been normalized to the baseline value. Note that the countrate shows a larger variability, but also a linear relation has been found: slope: $= -0.024 \pm 0.007$; offset:$= 1.0246 \pm 0.004$ with a correlation coefficient of -0.248, $p < 0.0005$ (figure 4.25 right).

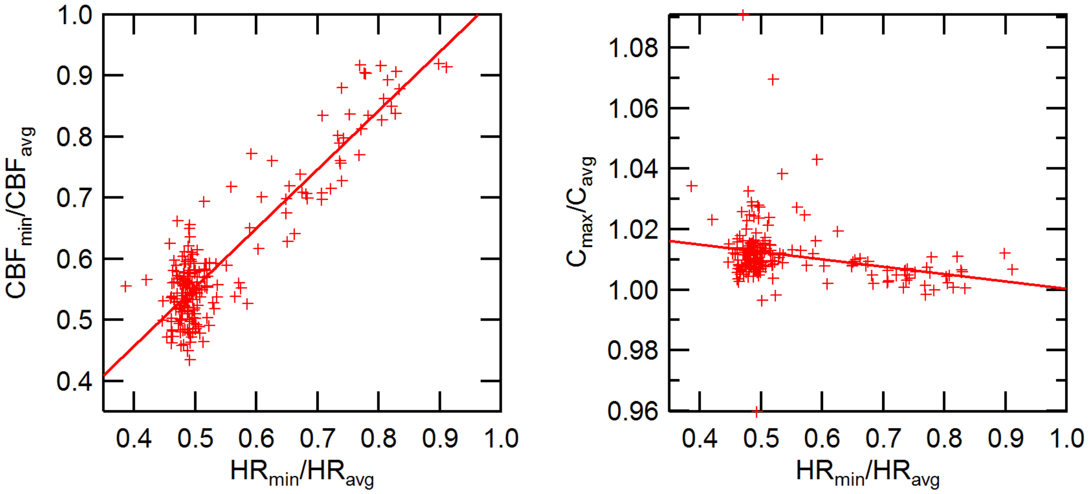

Figure 4.25: Left: The relative cerebral blood flow as a function of delay of heart beat is shown (cross). A linear fit f(x)=a+bx with a = 0.072 ± 0.018 and b = 0.964 ± 0.033 demonstrates the linear relation between the two r=0.900, $p < 10^{-10}$.
Right: Relative countrate smoothed vs relative heart rate. A linear fit f(x)=a+bx gives a =1.025 ± 0.004 b =-0.024 ± 0.007. Correlation coefficient -0.248, $p < 0.0005$

4.1.6.1 Discussion

Such types of arrhythmia are quite common in anesthesia, but also occur in healthy people, and are considered to have a weak illness value and a benign prognosis. However in situations such as during resuscitation and in critical ill patients the maintenance of circulation is of utmost importance.

Therefore the results nicely demonstrate that there is a linear relationship between the relative blood flow and the relative delay of one heart beat in the range between 20% and 120%. Malkoff et al[487] performed synchronized transcranial Doppler (TCD) measurements of the middle cerebral artery in humans with premature ventricular contractions. They found a linear decrease in blood flow when the time from the QRS complex to the systolic upstroke (measured in TCD) was increased. This is in agreement with our findings. A direct quantitative comparison is not possible because the heart rate is not reported in the paper.

Note that the blood flow is not only affected during a delayed heart beat but also during an early heart beat. Figure 4.26 shows an example of a pigeon with a strong arrhythmia. The diffusion coefficient averaged over one heart beat and the heart rate is shown. It can be nicely seen that they are strongly correlated.
For the correction of the effect due to heart rate, first the autocorrelation between the two is calculated to get any offset between the two. Then a linear fit is performed to get the linear dependence of the two (figure 4.26 right).

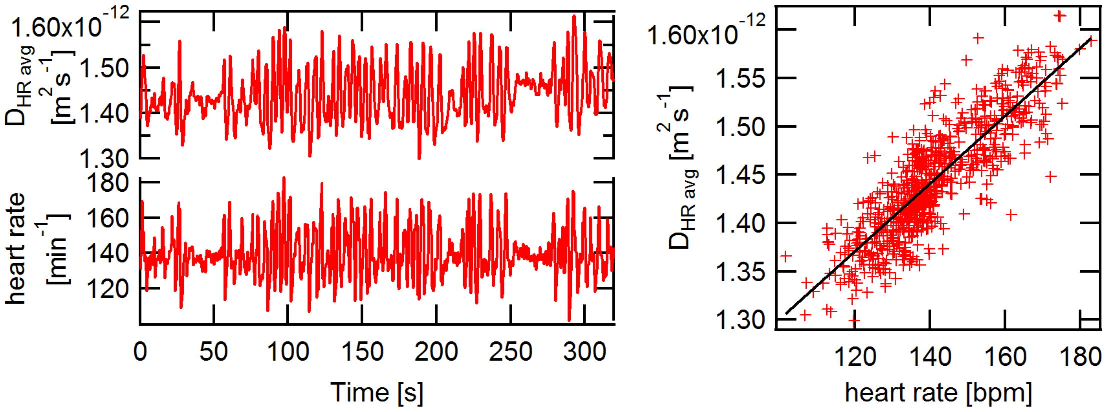

Figure 4.26: Example of strong arrhythmia. Left: Top curve shows the diffusion coefficient averaged over one heart beat and the lower curve shows the heart rate. Right: Linear dependence of the diffusion coefficient and heart rate (r=0.853, $p < 10^{-100}$)

Note that in contrast to the data shown in figure 4.25 the average blood flow rather than the peak is used for comparison. Therefore the slope is more shallow compared to the peak flow shown in the data presented in the case of delayed heart beats (figure 4.25).

From the fit a correction for the variation of heart rate is calculated and subtracted from the data (figure 4.27). Heart rate data is linearly interpolated in the range between two heart beats. This correction reduces the changes due to heart beat variability but it does not work perfectly well, because i) linear interpolation might not be optimal, ii) it does not include any prolonged effects due to reduced perfusion and iii) there is also some error in the detection of the heart rate which results in an additional error.
One also has to be careful to apply the correction to data where no arrhythmia has

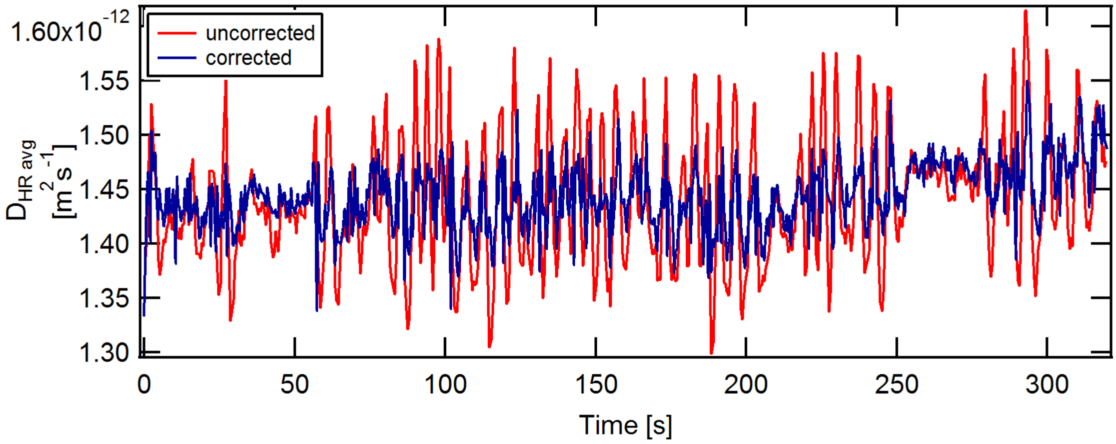

Figure 4.27: Data corrected for heart rate effect. The red curve shows the uncorrected data of a measurement where the pigeon showed a pronounced arrhythmia. The blue curve represents the data after correction for heart beat variability (see text for details).

been observed because then no correlation exists between heart rate and the diffusion coefficient. Therefore the linear fit does not yield the relation between heart rate and cerebral blood flow. Even though, due to the small heart rate variation, the errors which might be produced by the correction will be small, one should not perform the correction if no clear correlation is detected.

Nevertheless, the correction for heart rate effects allows for a significant reduction of artifacts produced by arrhythmia. This enables the analysis of data which otherwise would have to be discarded.

4.1.7 Thinned cranial window

For functional ultrasound measurements it is necessary to remove most of the bone in order to get rid of the acoustic reflexion from bone/air interfaces (see section 4.2.3.2 for details). Therefore, some pigeons underwent a surgery where the skull is thinned such that only a very thin layer of bone remains and a chronic PVC window for imaging access is installed. After complete curing of the wound DWS measurements were performed on those pigeons. This might be beneficial because one only gets a contribution from the brain and not from the skin.

Therefore, first measurements were performed with both, the laser and the detector positioned on top of the PVC window (see inset top right in figure 4.28). A typical autocorrelation function and a monoexponential fit with diffusive motion for a semi-infinite model is shown in figure 4.28.

It is evident that the decay is not monoexponential. This is most likely due to direct reflections from the PVC window and the skull which are not due to blood flow. This can be seen at the second decay at longer times which corresponds to

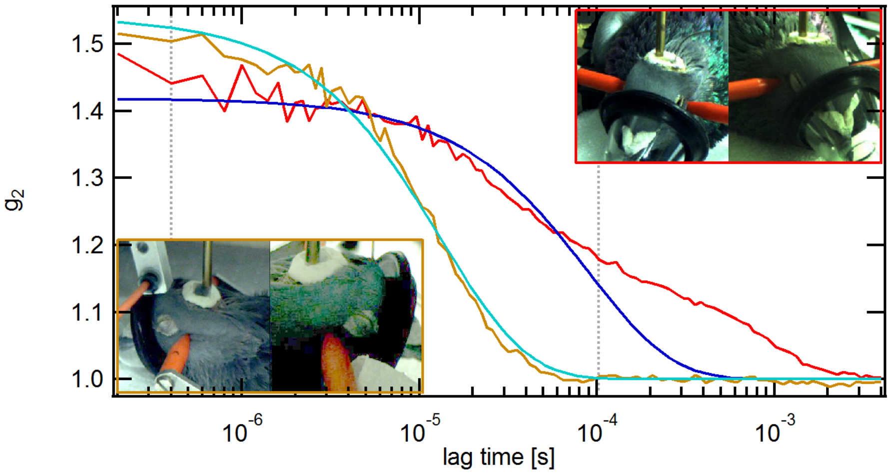

Figure 4.28: Representative intensity autocorrelation function (red) and monoexponential fit (blue) of a DWS measurement with both the laser and detector positioned on top of the "cortical window" (see inset on right top (red)) and with the detector placed on top of the "cortical window" and the laser in front of the window on the skin (see inset on left bottom (yellow)). The autocorrelation function and the fit of the second geometry is shown in yellow and light blue, respectively.

shorter path. In addition there have been normalization problems due to the fact that the integration time is too short for the very slow second decay.
The contribution from direct reflections can be minimized by using polarizers with orthogonal orientation in front of the laser and detector. However this approach has not been pursued further.

Instead, only the detector has been placed over the window and the laser has been placed beneath the window on the skin (see inset bottom left in figure 4.28). In this case a single monoexponetial decay can be observed. In these measurements there are still some contributions from superficial layers (mostly skin perfusion) but the signal is dominated by contributions from deeper regions. Therefore this geometry has been used for all measurements with pigeons with a "cortical window".

4.1.8 Visual

DWS is increasingly used to monitor changes in blood flow in a variety of conditions. However only a limited number of studies used DWS to monitor neural activity due to the more challenging detection of the small changes which are observed in this case. Visual stimulation in awake humans have previously been measured with DWS[398,448,449] but until now no measurements have been performed on pigeons. Therefore measurements with visual stimulation are performed as a control exper-

iment in order to validate DWS as a neuro-imaging tool in pigeons as well as to optimize signal analysis for the detection of neuronal activity.
The visual pathways of pigeons are described in greater detail in section 2.4.2. We used two structures which can be easily reached with DWS, namely the optical tectum of the tectofugal pathway and the visual wulst of the thalamofugal pathway.
The presented results are from different stages of the experiment and follow a similar, however not identical experimental protocol. This will be described in more detail below.
Briefly, LEDs positioned left and right of the pigeon at an angle of about 90° were periodically turned on and off.

One of the experiments was performed at the top of the head, roughly over the right visual wulst at the position described in the study of Ng et al.[245], the other two were performed over the left optical tectum. The latter is divided in two parts, one with some problems with the narcosis which resulted in a weak anesthesia, but a more pronounced signal and the other present results with normal anesthesia. These three experiments are also in chronological order.

The data was analyzed as described previously (see section 4.1.3.1).

4.1.8.1 Visual wulst

Experiments were performed on pigeons which underwent surgery for a thinned cranial window for functional ultrasound imaging (for details see next chapter 4.2.3.2). All presented results are from measurements where the surgery is more than three weeks ago and the wound has cured completely.

Figure 4.29: Measurement positions: left: ketanest/xylazine; right: isoflurane

The measurement position and study protocol was chosen according to the study protocol of De Groof et al[255] who used fMRI to study the visual system in awake pigeons trained to keep still. For stimulation they used a green LED (dominant wavelength 569nm) which were blinking with a frequency of 5Hz (100ms on, 100ms off) during on blocks of 16s followed by a 16s off block without stimulation. Note that the LEDs were positioned in front of the pigeon in these experiments.

In our experiments we used a LED with a peak wavelength of 590nm and a full width at half maximum of 28nm which were directed on the left eye. We used block lengths of 8s and 16s. Only results for block length of 8s are reported due to experimental difficulties with the 16s script (the script stopped working and the LED stayed on). Note that the data for 16s showed qualitatively the same result, namely an increase in the dynamics as observed in the 8s script but no averaging over multiple stimuli was possible. The 8s stimulation also used a slower frequency of flickering with 2.5Hz (200ms on, 200ms off) instead of the 5Hz of the 16s script. Each measurements consists of 10 stimulation blocks.
The laser and detector were positioned on the right hemisphere such that at least a part of the photons should go through the region which was reported in the study of De Groof et al.[255] and Ng et al.[245]. The detailed measurement position is shown in figure 4.29.

The results are from the same pigeon in which the measurement was performed once with ketanest (25mg/kg) and xylazine (5mg/kg) and the second time with isoflurane (2.5%) and buprenorphine (0.5mg/kg) injected about 60min before induction of narcosis. The two different anesthesia regimes were chosen in order to investigate if one shows a stronger neural response during functional activation. Note that one limitation is that the light from the LED was partly shadowed by the respiratory mask in the case of isoflurane.
The DWS signal is analyzed as described in section 4.1.3.1: The autocorrelation function is fitted with a semi-infinite model, the signal has been corrected for heart beat and breathing as well as spikes. Baseline variation has been corrected by dividing with the 50s median times the mean of the complete measurement.

Figure 4.30 shows the average response in both anesthesia regimes: A maximal increase in the average effective diffusion coefficient of about 0.251% and 0.267% is observed for isoflurane and ketanest/xylazine, respectively. Isoflurane shows a smoother increase with a peak between 6 and 8s whereas ketanest/xylazine shows a small dip at the beginning, a peak between about 3 and 7s and a decrease below baseline. Note, however, that in the case of ketanest there has been a number of sharp spikes which are most likely due to eye (muscle) motion. The analysis automatically corrects for those spikes however the analysis cannot be perfect and some small contributions may still be in the signal after averaging. Therefore one has to be cautious not to over-interpret the small difference which can be seen in the case of ketanest.

Discussion Both in isoflurane anesthesia as well as in ketanest/xylazine anesthesia a clear increase of cerebral blood flow in the area above the visual wulst has been observed during visual stimulation. It has to be noted that there is quite some variance in the single, unaveraged responses. In addition the maximum of

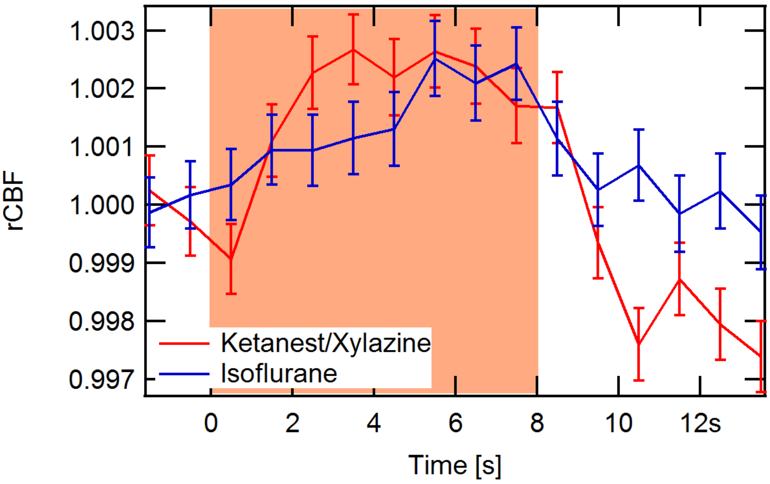

Figure 4.30: Comparison of the average response of DWS measured above the visual wulst during visual stimulation (orange area) in anesthesia with ketanest/xylazine and isoflurane/buprenorphine in a pigeon with a thinned cortical window. The average over 20 stimulations each with a temporal binning of 1s and the standard error of mean is shown.

the average change of the cerebral blood flow is only about 0.27% which is only about four times the standard error of mean. This clearly demonstrates the need to average over a large enough number of stimuli.

Within experimental resolution, no significant difference in the amplitude of the response can be observed for the two anesthesia regimes. Isoflurane has however the advantage that the anesthesia is better controlled, shows a higher reproducibility and can be maintained for a longer time. In addition physiological parameters are closer to the awake condition.

The advantageous properties of isoflurane over ketanest/xylazine led to the exclusive use of isoflurane for anesthesia.

4.1.8.2 Optical tectum

The optical tectum is a major part of the thalamofugal pathway and therefore of primary interest for the investigation of visual processing. As for the visual stimulation of the visual wulst LEDs with 590nm were positioned in front of the right and left eye. Each stimulation consisted of 10 cycles on/off where the LED was turned on for 16s followed by 16s darkness (see blue (off) and orange (on) colors in figure 4.31). First, measurements of two days where narcosis problems occurred and only the right eye was stimulated are presented. Followed by a larger number of measurements where both the right and left eye has been stimulated.

4.1.8.2.1 Problems with narcosis

In the beginning of April 2014 experiments with isoflurane anesthesia and measurement over the visual cortex have been performed. The anesthesia of one pigeon had to be discontinued due to the fact that the pigeon showed a pronounced excitation which could not be overcome. Despite a very high dose of isoflurane (3%) the second pigeon showed some reaction with twitching in anesthesia. In the last pigeon the narcosis had to be canceled after about 45min due to breathing problems.
The only difference between these experiments and previous measurements without problems has been that the oxygen bottle was changed before the experiment (technical oxygen). The gas was investigated with a mass spectrometer for an increased concentration of CO, CO_2 and NO which could act as vascular agent. No increase in concentration has been measured. After the experiments the oxygen were exchanged to medical oxygen (Air Liquide medicAL) and no problems have been observed anymore. The ingredients causing these problems could however not be determined. However it has to be noted that similar problems with anesthesia also occurred in two weeks in spring in the following year.

Regardless of the reason of the anesthesia problems a significant larger response to visual stimulation has been observed. Figure 4.31 shows normalized data of the temporal average of the measurements of the two pigeons. A clear decrease in the cerebral blood flow can be observed during stimulation. The average over all stimulation is shown in figure 4.32 left. The signal shows a steady decrease from signal onset to a minimum of -1.8% located at about 9.5s. This is followed by a

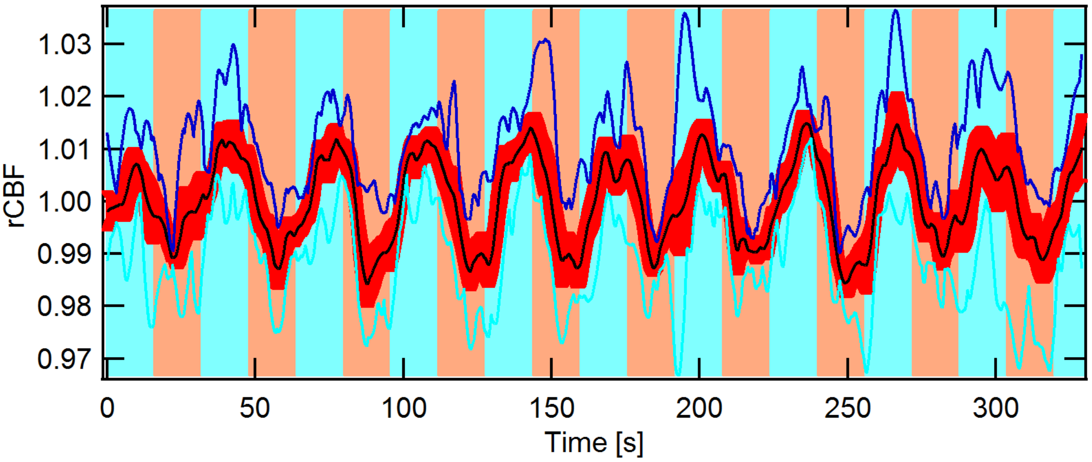

Figure 4.31: The figure shows the relative change in blood flow averaged over 6 experiments. The black line shows the average, red the standard error of mean, dark blue and light blue, the maximum and minimum respectively. Blue and orange background indicates LED off and on, respectively.

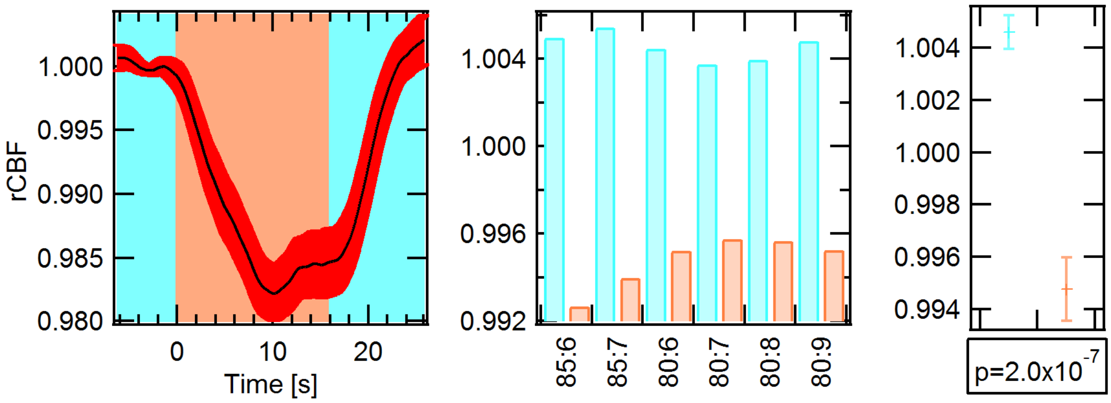

Figure 4.32: Left: Average and standard error of mean over 60 stimuli is shown. Middle: Average values over individual measurement. Light blue shows times without stimulation and orange with stimulation, respectively. Right: Average and standard deviation of all measurements. The p value is calculated by Students t-test over the 6 measurements.

slight increase to about -1.5% at the end of the stimulation period. After about 8s the signal reaches the baseline value again. Significant changes can already be observed during single measurement (figure 4.32 middle), and even during single stimulation. Students t-test shows that the result is highly significant ($p = 2 \cdot 10^{-7}$).

4.1.8.2.2 Normal measurement

The same measurements as with the narcosis problem have been performed with “normal” isoflurane anesthesia. In these measurements both the left (control) and the right eye have been stimulated. Measurements were again performed over the left visual cortex. In total 17 measurement days with 14 different pigeons (3 have been used twice) have been analyzed. Stimulations which showed a peak which was larger than 4 standard deviations have been excluded from the analysis. In total n=375 stimulations of the right eye and n=346 stimulation of the left eye could be used for the analysis.

The average over all measurements is shown in figure 4.33. The 1s average and the standard error of mean is shown by dotted lines, and the LOESS smoothed curve (Igor Pro, smoothing 0.5, robust) is shown by solid lines. For the stimulation of the right eye the relative cerebral blood flow shows a decrease of about 0.37% which is peaked at about 16s whereas the control measurement of the left eye only has a small dip at around 8s. A significant ($p < 0.0052$) difference is found by the paired Students t-test. The countrate shows a very small (about 0.1%) increase for the stimulation of the right eye but no change for the left eye. The higher countrate is due to a smaller absorption, which is found during vasoconstriction. This is in agreement with the smaller blood flow which has been observed.

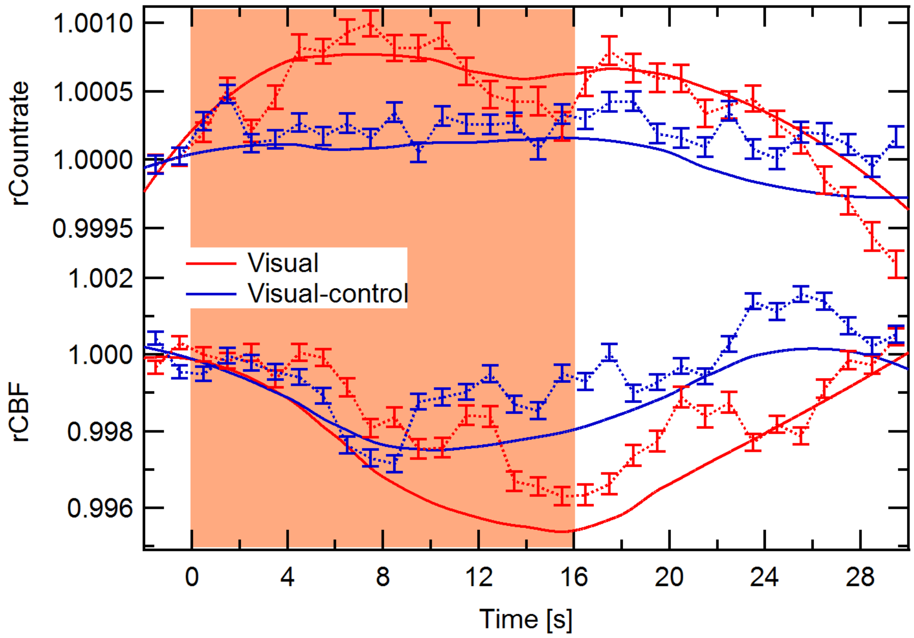

Figure 4.33: DWS measurement of the left optical tectum with stimulation of the right (visual) and left (visual-control) eye. The dotted line shows the 1s average and standard error of mean. Solid lines shows a LOESS smoothing of 0.5 (Igor Pro).

Discussion A significant decrease of the cerebral blood flow is found in the left visual cortex during visual stimulation of the right eye whereas only a small dip is observed for the stimulation of the ipsilateral side. It is not obvious if this small dip is a remnant of an artifact which has not been removed completely from the data set or if it is due to an indirect activation. There is nevertheless a significant difference between the two measurements. It is not clear why the activation leads to a decrease in cerebral blood flow. The usual response to stimulation is an increase in blood flow to fill the higher need for oxygen. One possible explanation for such a negative response is that the measurement was not performed over the activated brain region but besides and the signal is due to a “stealing” of blood from this regions. However repeated measurements with varying positions over the visual cortex all showed a decrease in blood flow which makes this explanation not very likely. At the moment it is not clear if the negative response only occurs during narcosis or if it is always found. Until now no definite explanation for the reduction in cerebral blood flow can be given.

Another interesting point to mention is the about 5 fold higher response during the measurement with narcosis problem. One explanation might be that the pigeon was presumable only lightly anesthetized where the cerebral autoregulation was fully working. Another possibility is that the vascular tone was influenced by some chemical so that the change resulted in a stronger relative response. The exact nature of the effect could not be determined. The observed effect emphasizes the need for an optimal anesthesia regime. If such an anesthesia regime can be realized no averaging has to be applied and the signal can be analyzed at a single trial level.

4.1.9 Magnetoreception

The optimal stimulation pattern for the analysis of magnetoreception is not straight forward because there is a very large parameter range. A good starting point is given by previous experiments as discussed in chapter 2. In addition the time scale of the hemodynamic response has to be considered.

4.1.9.1 Awake

In a first attempt, a large number of different stimuli have been applied to the awake pigeon in order to find the optimal stimulus for further analysis. Pigeons were placed in tights, where a hole has been cut in the toe to make room for the head. Adhesive tape was additionally placed around the legs and head motion was restricted by foam material (see figure 4.6). Movement artifacts however precluded a systematic analysis of the stimulation and lead to a poor reproducibility and a bad signal quality. Nevertheless some of the experiments showed changes associated with changes of the magnetic field (exemplary data is shown in figure 4.34).

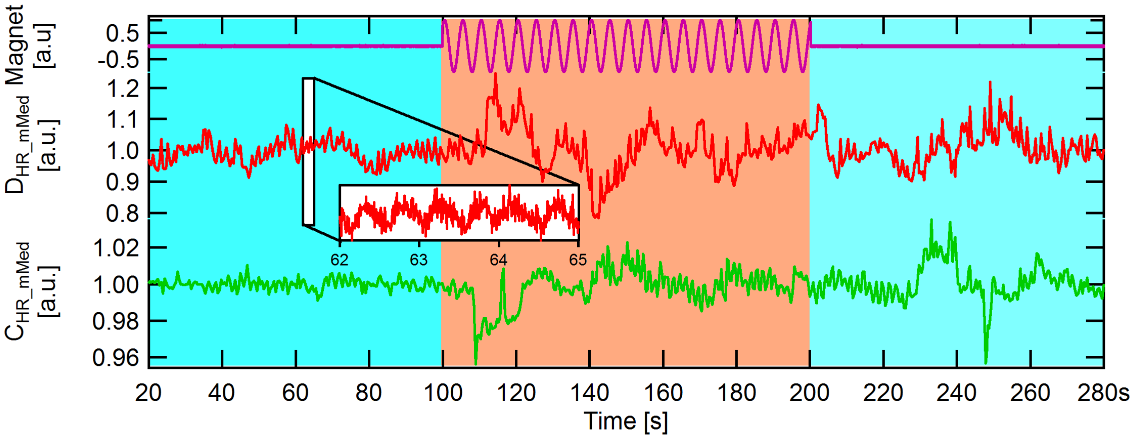

Figure 4.34: Measurement with an early setup with only one pair of coils positioned in a vertical alignment. The maximum and minimum during stimulation corresponds to roughly 10 times the earth's magnetic field. The measurement was performed in an awake pigeon. The stimulation is highlighted in orange.

However since there are only single measurements no statistical analysis could be performed. For this reason these measurements are not discussed in more details. However see[488] for some more detail.

4.1.9.2 Anesthesia

After validating, that DWS can measure changes in blood flow associated with visual stimulation, a more systematic analysis of magnetic stimulation has been performed with pigeons under anesthesia. Inhalation anesthesia was performed with isoflurane and midazolam (5mg/kg i.m.) which was administered about 30 min before induction of anesthesia (see section 3.2.2 for details). Magnetic stimulation was performed with the 3D-Merritt 4 coil system and the magnetic field was measured with the 3 axis fluxgate magnetometer. Measurements were performed over the left optic tectum and the left visual wulst where already visual data was available. Usually the room light and a small light in the experiment box was turned on. In some cases the closed eyes were additionally illuminated by LEDs or all lights were turned off. It is not discriminated between the different illuminations, except noted in the text.

4.1.9.2.1 Optic tectum

First measurements have been performed on the left optic tectum in nine pigeons. The magnetic stimulation consisted of five stimulations with a sudden change followed by stimulation with a horizontally rotating magnetic field. The sudden changes were applied by manually entering the new values for the magnetic field. Therefore the length of the stimulation block has been longer than 50s in two cases (Stim4 V1), the onset of the stimulation is always determined exactly. After about half of the measurements the position of the cameras has been changed which lead to a change in the laboratory field (field at the head of the pigeon). The script of the magnetic changes was however not changed. As a result the stimulation is slightly different. The two different stimulation are labeled V1 and V2, respectively. The magnetic stimulation paradigm is described in the following:
Four different magnetic field changes were used for the changed magnetic field:
Stim1: change of B_y and B_z with the total field constant (change of inclination)
Stim2: exchange of B_x and B_y (change of horizontal angle)
Stim3: increase total field by 20% without changing the direction of the field
Stim4: compensate external field to get a zerofield.
Note that due to changes in the laboratory field and changes in the setup the intended changes where only approximately fulfilled, however real changes are shown in figure 4.36.
After those stimulations the magnetic field vector was rotated horizontally to the tail of the pigeon (B_x-Axis) with an approximate constant total field (Stim 5). This

is followed by a measurement where the magnetic field is horizontally rotated in a counter-clockwise direction with a full rotation duration of 10s followed by a 10s period without stimulation. Five stimulations of this kind have been applied in one measurement. In some cases the same stimulation with a stimulation period of 16s has also been applied. The cross talk was not perfectly compensated, therefore also a change of the vertical component with a peak to peak amplitude of 10 µT which mimic the temporal change of the B_x-axis, was observed in the measurements. The timing of the stimulation is schematically shown in figure 4.35.

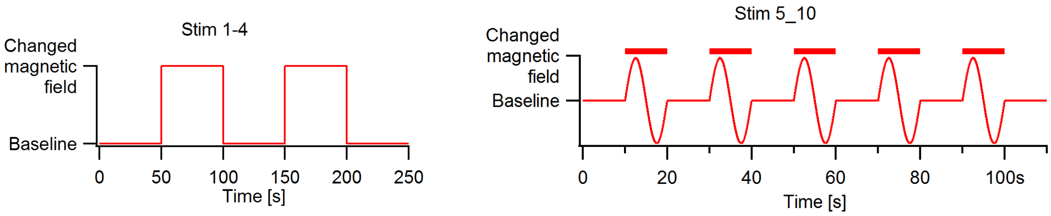

Figure 4.35: Left: Timing of Stimulation 1 to 4. Right: Timing of Stimulation 5-10

Results Figure 4.36 shows the average over all stimulation from Stim 1-4. The relative diffusion coefficient with the standard error of mean is shown in red - left axis. The average magnetic field B_x (light blue), B_y (pink), B_z (orange) are shown on the right axis. The difference vector between baseline magnetic field and the field during magnetic stimulation is shown on top. Note that the steps in Stim 4 V1 at about 55s and about 70s are due to a delayed change of the magnetic field back to the baseline value.

Small variations of about 1-2% of the baseline value are observed in the average diffusion coefficient during stimulation. Even though these changes only show a small deviation there is a tendency with a response opposite to the B_y change. It has to be noted that the response is not simply a smooth on, off type of response, but has additional features in some of the measurements. The effect is not so clear for Stim 1, but one increasingly finds a clear response for Stim 2 to Stim 4. Note that the stimuli has been applied in chronological order from Stim 1 to Stim 4.

In order to quantify the proposed correlation with the B_y-field the average response as function of the magnetic field change is plotted in figure 4.37. Both the short time response (between 8.5s and 11.5s - top) and the average over the complete stimulation period (0.5s-47s - bottom) are shown. In addition the data was linearly fitted to reveal if there is a linear dependence with the applied field changes. It can be nicely seen that the response is anti-correlated with the change in the B_y component of the magnetic field whereas no clear effect with either B_x or B_z can be observed. The fit values and the linear correlation coefficient are given in table 4.5. Only the anti-correlation with the B_y change is statistical significant for the

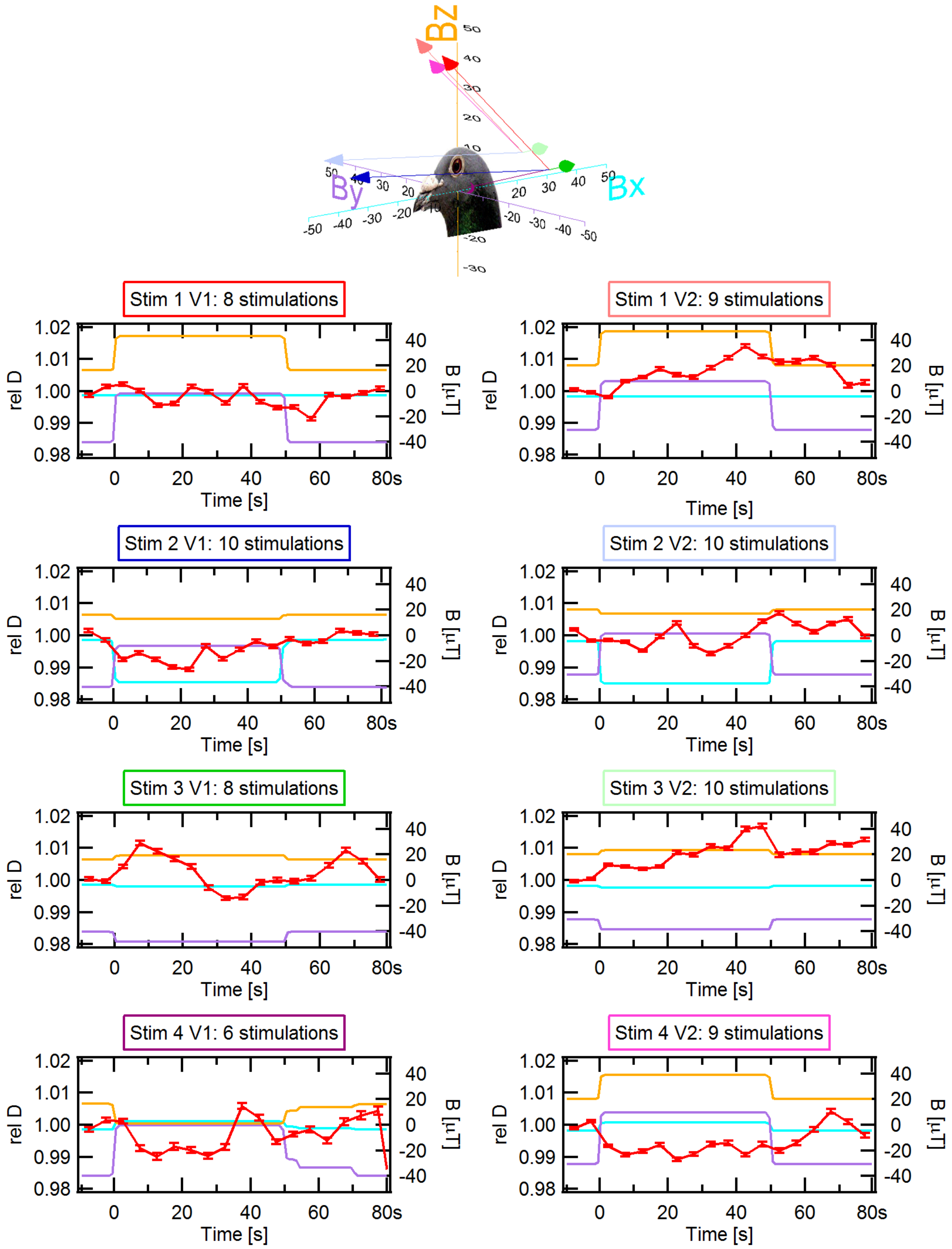

Figure 4.36: The top image illustrates the orientation of the magnetic axis and shows the vectors of the change applied from the baseline to the stimulation field. The average result of the average diffusion coefficient (red - left axis) for stimulation 1 to 4 averaged over 5s with the standard error of mean are shown. The average magnetic field (right axis) during stimulation for B_x (light blue), B_y (pink), B_z (orange) are shown. It can be seen that response of the cerebral blood flow on average shows a tendency opposite to the y-axis of the magnetic field.

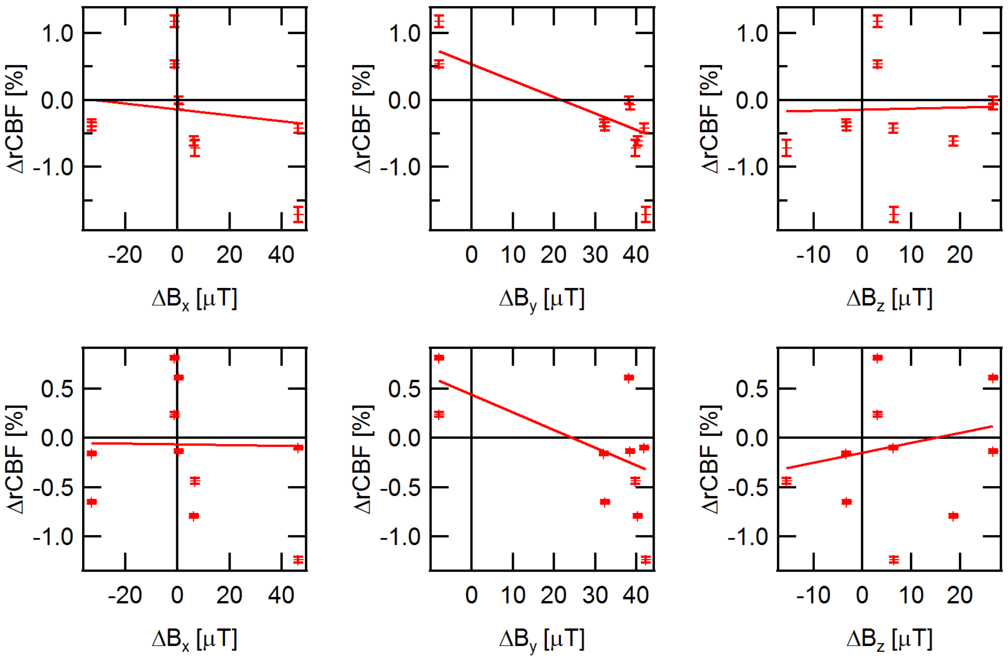

Figure 4.37: Average value and sem of the change in cerebral blood flow in response to a sudden change in the magnetic field and a linear fit thereof. The top row shows the short time response in the range 8.5 to 11.5 s and the bottom row the average response of the complete stimulation period (0.5s to 47s). As a guide to the eye the zero position is marked.

short time response and nearly significant ($p = 0.06$) for the average response over the full stimulation time.

Table 4.5: Linear fit (a+bx) to the average response of the relative cerebral blood flow in the short time range 8.5s-11.5s and over the range of the complete stimulation (0.5-47s) to Stim 1 to 5. The linear correlation coefficient (r) is also given. All correlations without an indicator are statistical not significant. $^+$: $p = 0.06$ (not significant). *: $p = 0.005$ (significant).

	short time [8.5s-11.5s]			long time [0.5s-47s]		
	a [‰]	b [‰/µT]	r	a [‰]	b [‰/µT]	r
$\mathbf{B_x}$	-1.39 ± 0.22	-0.043 ± 0.009	-0.41	-0.62 ± 0.06	-0.004 ± 0.002	-0.25
$\mathbf{B_y}$	5.33 ± 0.38	-0.244 ± 0.011	-0.80^*	4.43 ± 0.11	-0.180 ± 0.003	-0.61^+
$\mathbf{B_z}$	-1.43 ± 0.26	0.018 ± 0.017	0.10	-1.47 ± 0.07	0.101 ± 0.005	0.19

The oscillating magnetic field also shows an anti-correlation with the B_y-component of the magnetic field (see figure 4.38) where the change can be clearly seen in the stimulation with a period of 10s. It has to be noted that in the case of stimulation Stim 5-10 V2 there is also some additional oscillation when the mag-

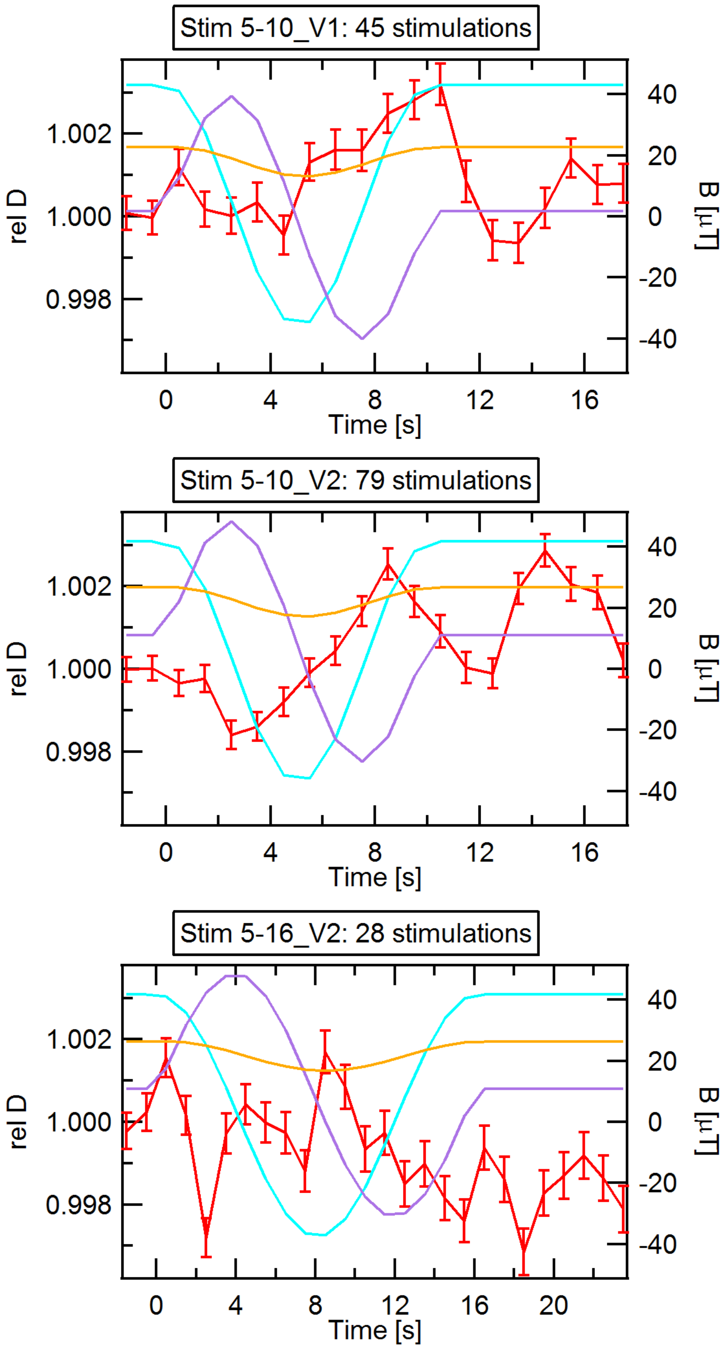

Figure 4.38: Average response of the relative diffusion coefficient (red) to a horizontally rotating magnetic field. The magnetic field components B_x (light blue), B_y (pink), B_z (orange) are plotted on the right axis. The top and middle figure show the response to a rotation with a 10s period and the bottom to a rotation with 16s. Note that a periodic stimulation is applied with 10s (top, middle) and 16s (bottom) pause between two stimulations. Therefore the figures should also be viewed as periodic, so that e.g. in the top graph the times 10-18s are identical to the times -10 to -2s.

netic stimulation has stopped. The addition oscillation might be due to adaptive effects which might build up after several stimulation.
In Stim 5-16 V2 the effect is not so clear showing only a negative peak at the beginning and a positive peak at the turning point but no smooth oscillation. The amplitude of the oscillation is about 2‰ in all cases. The linear correlation coefficient between the 1s average of the relative diffusion coefficient and the average of the B_y component in the interval 2s before stimulation and 8 s after stimulation has been calculated. One finds correlation coefficients of $r = -0.522$ ($p < 0.0182$), $r = -0.586$ ($p = 0.0066$) and $r = 0.0739$ (not significant) for Stim 5-10 V1, Stim 5-10 V2 and Stim 5-16 V2, respectively.
For stimulation Stim5-10 V2 there were also measurements where in addition to room light measurements two LEDs were used to illuminate the eyes as well as measurements where all lights have been turned off (note that there were only a few minutes between turning the lights off and the measurements). A clear anti-correlation is found for the average over all measurements with room light turned on. A nearly significant anti-correlation with room light turned on is found if one analyses only the experimental days where also a test with LEDs and no light has been performed. No significant correlation is found for the other light conditions.

Table 4.6: Linear correlation coefficient of the relative cerebral blood flow and the B_y field for Stim5-10 V2. N indicates the number of stimulation over which the data has been averaged. ns: not significant

Condition	Correlation	p-value
room light - all (N=50)	-0.710	0.00045
room light - two days (N=15)	-0.443402	0.05021 (ns)
room light and orange LED (N=10)	-0.0182947	ns
room light and white LED (N=10)	0.244871	ns
Without light (N=9)	0.107484	ns

4.1.9.2.2 Visual wulst

In the next step, it should be investigated if the oscillating magnetic field also shows an effect in the left visual wulst. In addition both a left and a right rotation of the same stimulus has been applied to verify a correlation with the magnetic y-axis and to exclude any unspecific cues, such as e.g. noise from the power supply driving the magnetic field, as origin of the observed changes in the cerebral blood flow. The stimulation is similar to Stim 5-10 except that in addition an oscillation with a peak to peak amplitude of 10µT was also applied to the B_z-Axis and 15 stimulations were applied per measurement. This has been applied because in the former measurements also a small variation in the B_z magnetic field has been observed. Also, due to the fact that the optimal magnetic stimulus is not known, it enhances the chance that one is in the correct parameter range for detectable magnetic activation. In order to evaluate if the response can be enhanced the same stimulation with twice the magnetic field has also been applied in two pigeons.

Results Figure 4.39 shows the response of the relative diffusion coefficient averaged over all stimuli with a clockwise and counter clockwise rotation of the horizontal component of the magnetic field. In contrast to the biphasic response to the oscillating field measured at the left optic tectum one observes a M-shaped response for Horizontal 1 and a W-shaped response for Horizontal 2. One has to note that some of the pigeons showed a pronounced arrhythmia as previously described (see section 4.1.6) which increases the noise in the signal. Nevertheless the observed change is again about 2‰.

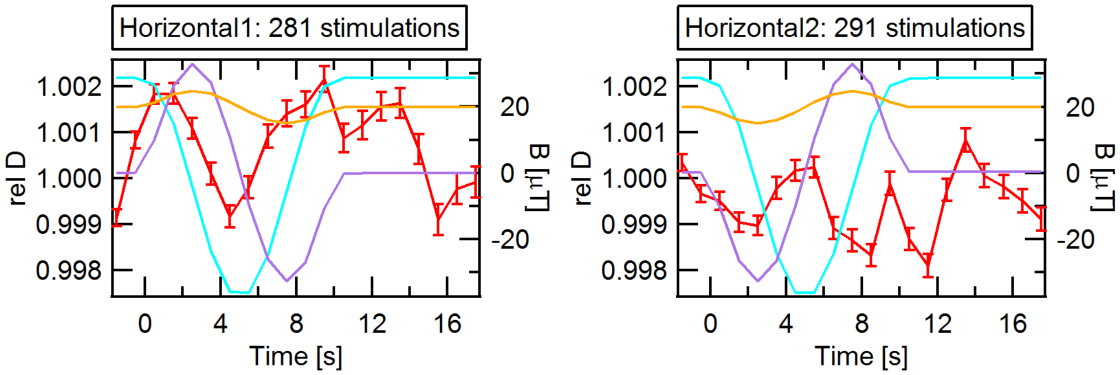

Figure 4.39: The figure shows the average response of the relative diffusion coefficient (left axis - red) to an counterclockwise (Horizontal 1) and clockwise (Horizontal 2) rotated magnetic field. The right axis indicate the average magnetic field during stimulation with B_x (light blue), B_y (pink) and B_z (orange).

Figure 4.40 shows the results of the measurement with double the magnetic field strength. Therefore before the measurement the magnetic field strength has been doubled while keeping the direction of the magnetic field vector constant. In the measurement the magnetic field is then again horizontally rotated, but in this case no modulation of the horizontal component was applied. The magnetic stimulation has been applied directly after the change to double the magnetic field so that there has been no time for adapting to the magnetic field. One observes a slope which has a slightly negative tendency and does not show a clear correlation with the magnetic field. For Horizontal1-2Labfield a small negative dip is observed between about 0 and 7 s followed by a second dip after about 8s. For Horizontal2-2Labfield also a negative dip from 0 to about 10s is observed also followed by a second negative dip. Note that the number of stimulation is

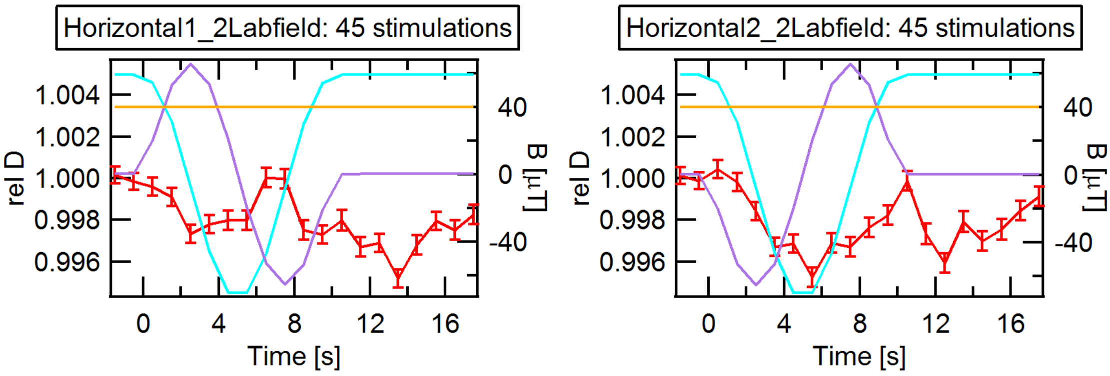

Figure 4.40: Average response of the relative diffusion coefficient (red - left axis) to a rotating magnetic field with a field strength of double the ambient field. Horizontal 1-2Labfield and Horizontal 2-2Labfield corresponds to a counterclockwise and clockwise rotation, respectively. The average magnetic field components B_x (light blue), B_y (pink), B_z (orange) are shown on the right axis.

significantly smaller than for the rotation with fields with an amplitude of the ambient magnetic field.

In order to see if the number of stimulation is sufficient to see a clear response the average response to Horizontal 1 and Horizontal 2 has been calculated only for the measurement days where also double the magnetic field has been applied. In this case (figure 4.41) a response which is similar to the response which has been observed over the optic tectum with the stimulation Stim5-10 can be seen.

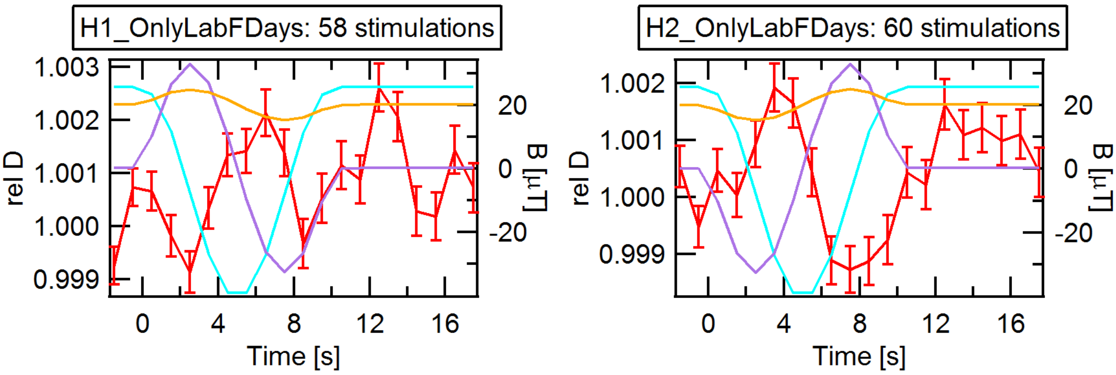

Figure 4.41: Response of the relative diffusion coefficient (red - left axis) to magnetic stimulation with Horizontal 1 (left) and Horizontal 2 (right) on the days where also double the magnetic field has been applied. The average magnetic field is shown on the right axis with B_x, B_y and B_z are colored light blue, pink and orange, respectively.

4.1.10 Discussion

The cerebral blood flow of pigeons has been measured with diffusing wave spectroscopy. Changes during functional activation due to magnetic stimulation have been measured over the left optic tectum and the visual wulst. A small, but significant change in the average relative cerebral blood flow, which on average is opposite to the B_y-axis (interaural axis), has been observed over the left optic tectum after a sudden change in the magnetic field. The response is however not always monotonic and shows a considerable variation between different measurements and different individuals. For a rotating horizontal field with field strength of the ambient magnetic field also a statistical relevant anti-correlation with the B_y-axis has been observed. In measurements over the left visual wulst a M and W shaped response to a counterclockwise and clockwise rotation with a magnetic field at ambient field strength is observed for the grand average. However if only a part of the data is analyzed a similar response as for the optic tectum is found. The stimulation with double the magnetic field did not show a clear effect, at least none which is simply stronger than at ambient field strength. The measurements over the visual wulst contain a particular high number of measurements with a pronounced arrhythmia. Therefore one should be particular careful with interpreting these results.

The observed variability in the response is quite common in functional studies[317] (also see section 3.1.6 for a more detailed discussion). In the following some of the factors which contribute to the variability in this study should be discussed.

Lee at al.[410] also reported a complex response to trials with 15s song playback which show a biphasic response in total hemoglobin content. Furthermore they reported that the absorption spectra of zebra finches is different from the one observed in humans (figure 4.1), which might complicate the signal by influences of the oxidation state.

The signal is furthermore particularly influenced by the depth of anesthesia as well as the isoflurane concentration which is required to maintain anesthesia in this regime. Also small variations in the measured brain volume due to different laser and detector positions as well as differences in the shape of the head of different pigeons might contribute to these variability. Furthermore a very small signal to noise ratio is observed which even in the case of averaging still might have contribution from large noise artifacts such as arrhythmia.

Also the brain regions which detect and process changes in the magnetic field as well as the optimal stimulation are not definitely known. Since the DWS signal measures the average dynamics in the sample volume the effect might by diminished if only a part of the sample area is activated or if the activation might even occur outside of the sample area and only the indirect response of “stealing” blood from this area is observed. It is currently not possible to discriminate between the two possibilities due to the fact that even though the blood flow is usually increased during functional activation, an inverse response has been observed for optical stimulation in the optical tectum. Furthermore negative responses have been observed in other studies (in particular in anesthesia) and in addition it is not definitely known if the activation is excitatory or inhibitory in this area (but see section 2.3.3 for electrophysiological measurements).

One also has to mention that during deep anesthesia brain regions which are not directly stimulated also show a response[378]. Therefore the spatial resolution might even be worse than the volume probed by the photon cloud itself.

The fact that there was no clear response observed when the field was doubled might be explained by the fact that the birds did not have a sufficient time to adjust to the new magnetic field intensity. For European robins it is reported that changes larger than 25-30% lead to disorientation but with a sufficient adaption time they can orient again[190]. In the experiments there were only a few minutes between doubling the field and the measurements.

Measurements with an enhanced light level and no light both showed no clear correlation with the magnetic field. However one has to note that measurements with room light turned on also only showed significant results if the number of stimulation were large enough. Due to the fact that the number of stimulation with changed light condition was ≤ 10 for each condition one should be careful to draw reliable conclusions from the results. The finding nevertheless hints to the fact that a correlation of the relative diffusion coefficient only exists during the room light conditions (at least if there is not sufficient time to adjust to other light levels). In future measurements the number of stimulation in each condition should be increased. Furthermore one should allow for a sufficient long time to adjust to the new light level. In particular for the dark condition more than 30min are required that all of the semiquione $FADH^{\bullet}$ is photoreduced[166,190].

4.2 Functional Ultrasound

4.2.1 Motivation

Ultrasound imaging is a well established clinical method with a very good spatial resolution which also allows for the measurement of blood flow velocities. However for a large field of few (centimeters) conventional ultrasound has lacked the temporal resolution which is required for functional neuroimaging studies. In 2011, Mace et al.[489] published a paper which describes a new method based on plane wave imaging which significantly reduces the time required to scan a 2d slice and thereby achieves a temporal resolution sufficient for functional studies. They demonstrated the feasibility of functional measurements during whisker stimulation and an epileptic seizure. When I was reading the paper it was immediately clear to me that this could complement diffusing wave spectroscopy with its high sensitivity and temporal resolution but with a low spatial resolution. Therefore we tried to implement the method for pigeons.

Because of our long-standing contact with the group of Prof. Fink at Institut Langevin, ESPCI Paristech, we attempted to built up a collaboration. Test measurements with a system (Aixplorer®, SuperSonic Imagine) borrowed from the group showed that it should be possible to do functional studies with pigeons, as the vascular system of the pigeons brain could be clearly resolved. However after almost two years of negotiation, it turned out, that it was not possible to buy a suitable ultrasound device from SuperSonic Imagine. Therefore we decided to implement plane wave imaging in the *Vevo*® 2100 system in collaboration with Visual Sonics. After about two years it turned out, that Visual Sonics was not able to implement plane wave imaging with a sufficient data rate in the current imaging system (for details see master's thesis of Julia Sester[490] and Richard Rau[491]). Therefore we decided to implement plane wave imaging on our own in the system of Verasonics which only recently came to market and has full programming access. First test measurements at the Erasmus MC in Rotterdam showed that plane wave imaging can easily be implemented in the US device from Verasonics. However due to delays in obtaining the ultrasound device the implementation is still in progress and only a limited number of images from non-functional tests are available. Therefore the idea of plane wave ultrasound imaging will only be briefly described and the details of ultrasound imaging will not be discussed in detail.

The focus will be set on the steps which are necessary for transcranial ultrasound imaging on the pigeon. This includes a stable narcosis as well as the thinning of the skull to remove reflexions from the air filled cavities in the bone (see figure 4.42 for an illustration of the spongy structures). Furthermore the implementation of a cortical window for chronic imaging is described. To the best of the authors knowledge this has not been previously described in the literature.

4.2.2 Principle of functional plane wave imaging

Conventional ultrasound uses a focused beam to scan the image line by line. This process is however too slow to measure blood dynamics from microvasculature in a large field of view. Therefore small regions have to be scanned successively. In contrast the idea of functional ultrasound is to let all piezos emit a plane wave through the medium and detect the backscattered signal with all transducers. A single plane wave emission for a large field image takes the same acquisition time as one focused ultrasound. In order to improve resolution and avoid artifactual signals several tilted plane waves are coherently summed to build a so called compound image. Such a compound image has better resolution, lower noise with a kilohertz frame rate[492,493]. The summing of the different angles can be viewed as having a focus at each image point.

Mace et al.[489] first applied this concept of functional ultrasound imaging (fUS)

Figure 4.42: The figure shows the 3 dimensional reconstruction from 400 slices of the micro CT (see section 4.3) showing the osseous structures in the skull of pigeons. The air filled inclusion which are distracting for functional ultrasound can nicely be seen.

to study the hemodynamic response to whisker stimulation in the brain of a rat. Figure 4.43 shows modified images from[489] which nicely explain the principle of fUS imaging and demonstrate imaging capabilities.

4.2.3 Experiments

Birds have developed a sponge like bone structure at the skull which is very robust, but still lightweight (see images 4.42). Ultrasound is strongly scattered at interfaces with a large impedance mismatch in sound velocity, which is particularly true for the air - bone interfaces in the skull, where the sound velocity changes by an order of magnitude. In order to perform functional ultrasound measurements it is therefore necessary to thin or remove the skull. The complete procedure will be discussed in quite some detail since to the best of the authors knowledge the procedure has not been described for pigeons before.
First the drug therapy is shortly described. Followed by a detailed description of the surgery. All experiments have been approved by the german regional commission (35-9185.81 G-12 54).

4.2.3.1 Anesthesia

The pigeon is fasted for about 12h prior to the procedure. At least 30 minutes before the surgical operation the pigeon is injected with 0.5mg/kg BW buprenorphine (Temgesic 0.3mg/ml) i.m. in the M. supracoracoideus as a preemptive analgesic. The pigeon is placed on a water perfused heat blanket. An isoflurane narcosis is then performed (typically about 2-3%). When the surgical plane is reached (intended

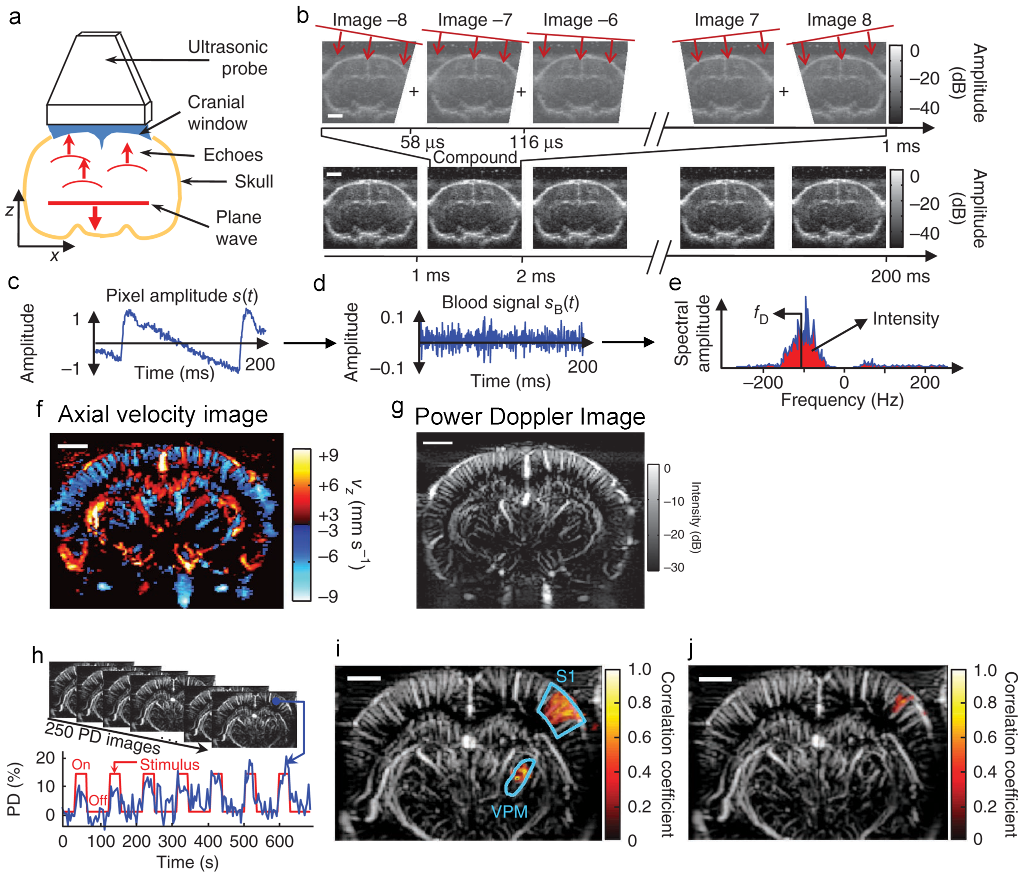

Figure 4.43: The principle of functional ultrasound (fUS) is presented. a) Schematic setup showing the ultrasound probe on the cortical window. The principle of plane wave ultrasound is depicted. b) fUS with the emission of tilted plane waves which are combined to a compound image of 2cm x 2cm. c) Temporal variation of the backscattered ultrasound signal of one pixel which is highpass filtered to obtain the blood signal shown in d). e) Frequency spectrum of the blood signal. The central frequency f_D which is proportional to axial blood velocity with respect to z axis and the intensity (power Doppler) which is proportional to blood volume are shown. f) Axial velocity map and g) power Doppler map. h) Changes during a functional stimulation task with whisker stimulation. i) Activation map showing the correlation of the power Doppler signal and the stimulus patter during left whisker stimulation. j) Activation map during stimulation of a single whisker. Modified images from[489].

reflex score: 3 after Korbel et al.[294]). The pigeon is fixated in a stereotactic device. The heart beat and oxygen saturation is measured by a pulse oximeter on the M. gastrocnemius. The temperature is measured rectally with a digital thermometer. Furthermore are the eyes regularly moistened with Thilo Tears®. For the postoperative analgesia 0.5mg/kg BW buprenorphine i.m. is administered every 12h for at least 3 days as well as three injections of meloxicam (Metacam®

2mg/ml) 0.5mg/kg BW every 4h. In addition one can supply the pigeon once daily with 20-30ml/kg BW s.c. of a mix of Ringer's- and 5% glucose solution (50:50).

4.2.3.2 Thinned skull cortical window

An about 15mm long medial skin incision is performed from rostral to caudal in the area of the regio frontalis. In the area where the bone should be thinned the periosteum is removed. The bone is slowly[5] removed with a drill until only a very thin layer of bone remains (figure 4.44 left). When the procedure is finished a "pool" of dental cement (Havard Cement) is build around the area of thinned skull (figure 4.44 middle). The pool is filled with hand-warm agarose (about 1 weight percent) which is mixed with an antibiotic (ampicillin). The agarose bath is closed with a PVC plate. This construction will be called cortical window in the following. The skin is attached with dental cement to the cortical window.

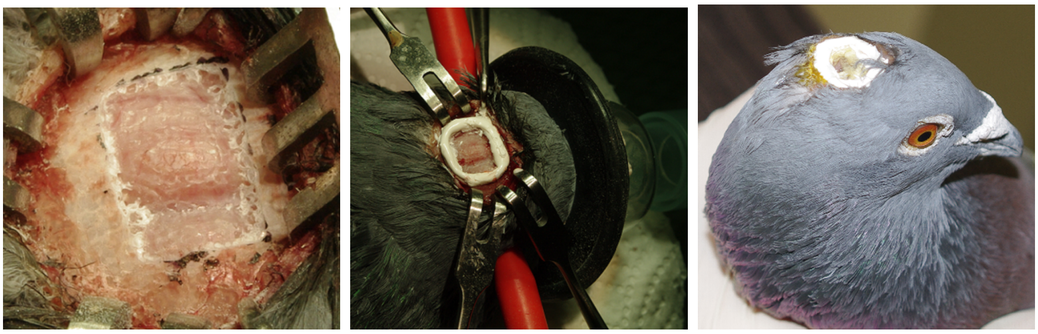

Figure 4.44: Left: The thinned cranial window with only a thin layer of bone is shown. Middle: The head of the pigeon after building a "pool" of dental cement which is filled with agarose. Right: The awake pigeon with the fully implemented cortical window.

Three pigeons have been operated so far. It was observed that the pigeons recovered quickly from the surgery and did not show any signs of discomfort after a few days. One pigeon developed a local inflammation which could be treated by removing the pus-filled area and flushing the area. Furthermore the wound was treated with anti-inflammatory ointment. With this treatment no further inflammation occurred. Therefore the administration of the analgesic could be discontinued after about 3 days. The pigeons were held in separated cages in the animal facility. After a few days to a week the agarose (or at least the water) was absorbed and the chamber was filled with air.

After about 1-2 month the cortical window self-loosened and was falling off. It can then be either reinstalled or removed and the skin is sutured. If one reinstalls

---

[5] Note that if the bone is removed too fast some areas of the brain might be denatured due to the heat produced by grinding.

the window one observes an increased bleeding due to stronger vascularization of the healing tissue. Furthermore one could observe that the osseous structure also recovered. This requires that the scull is thinned again before reinstalling the window. Nevertheless neither the bleeding nor the second thinning of the scull affected the recovery of the pigeon. A quantitative measurement of the recovery of the osseous thickness was not possible due to the lack of the continuous availability of an ultrasound device.
All pigeons fully recovered and can be kept with the other pigeons in the loft without any restrictions.

4.2.3.3 Ultrasound measurements

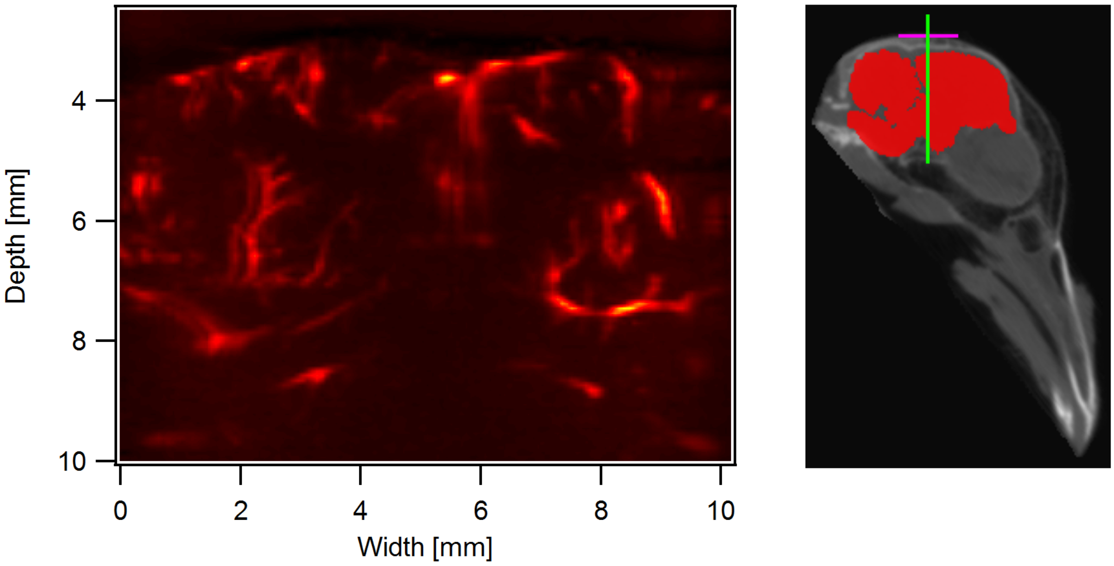

Figure 4.45: A post processed Power Doppler map of the pigeon brain acquired with the Supersonic Aixplorer is shown on the left. Vasculature with vessels as small as about 100µm can be resolved. The right image shows a CT image of a pigeon overlayed with the brain surface (data from [231]). The approximate position of the ultrasound slice (green) and the approximate position of the osteotomy (pink) are highlighted in the image.

First proof of principle experiments in collaboration with the Group of Prof. Fink were performed with the Aixplorer from Supersonic, which is the ultrasound device used in the work of Mace et al.[489]. Measurements were first performed without an osteotomy but it turned out that the attenuation due to scattering was too high to resolve the vascular structure in the brain. After thinning of the skull one could nicely measure the vascular structure and the blood flow. Figure 4.45 left shows a post processed power Doppler map of a slice of the pigeon brain.

Even though the osteotomy was not perfect vessel sizes as low as 100µm could be resolved. The transducer frequency was 15MHz with a spatial resolution of 80µm. The ultrasound device used angled ultrafast plane wave imaging with 17 angles between -8° to +8° (in 1° steps) with an ensemble number of 500 frames which results in an acquisition time of 500ms. With the ultrafast ultrasound imaging the feasibility of functional measurement could be accessed. Therefore the angles were reduced to [-3° 0° +3°] with 8 repetitions each. A simple stimulation with one Helmholtz coil was used, where the horizontal component of the magnetic field could be changed. Magnetic stimulation consisted of 60s baseline, 10s where the horizontal component has been set to approximately zero, followed by 110s after the stimulation. First a measurement over the same time, but without magnetic stimulation was performed to check the stability of physiological parameters and the system. The temporal evolution of the region of interest (green rectangle in figure 4.46 a) is shown in figure 4.46 b. It can be nicely seen that no change in the baseline measurement is observed. The change from the baseline (0-60s) is also shown for the complete field of view for the intervals 60-70s, 70-125 and 125-180s (figure 4.46 c-e). Only very small changes can be observed in the images which shows that the system is very stable. In contrast the cerebral blood volume is increased in the region of interest during stimulation and stays at this higher level over the rest of the measurement (figure 4.46 f-h). The same effect in the same region has been observed in a second measurement with a smaller field of view and a higher temporal resolution(figure 4.46 i-j).
However this was a one time test experiment which could not be repeated due to problems in obtaining our own ultrasound device from SuperSonic Imagine. Therefore one has to be careful to draw any general conclusions from these measurements. Nevertheless the measurements indicate that the system and the physiology is sufficiently stable to perform functional ultrasound imaging in the pigeon. Also one might already have detected a change of cerebral blood volume associated with magnetic stimulation. Future measurements will show the reproducibility of this signal.

Additional measurements were performed with the ultrasound device *Vevo*® 2100 from Visual Sonics in conventional ultrasound mode with a 32MHz transducer. Even though the pixel size was only about half of the size of the Aixplorer only larger vessels could be detected (see figure 4.47 left). This is however crucial, because in particular the microvasculature is of interest for functional imaging. In principle one could increase the ensemble average, which were held quite low at $N_e = 14$, but already with these imaging parameters the acquisition time for one image was 2.73s. This emphasizes the need to implement angled plane wave imaging for functional ultrasound imaging in a large field of view.

With repeated measurements it was nevertheless possible to generate a 3-dimensional image of the vascular system of the pigeon (see figure 4.47 right).

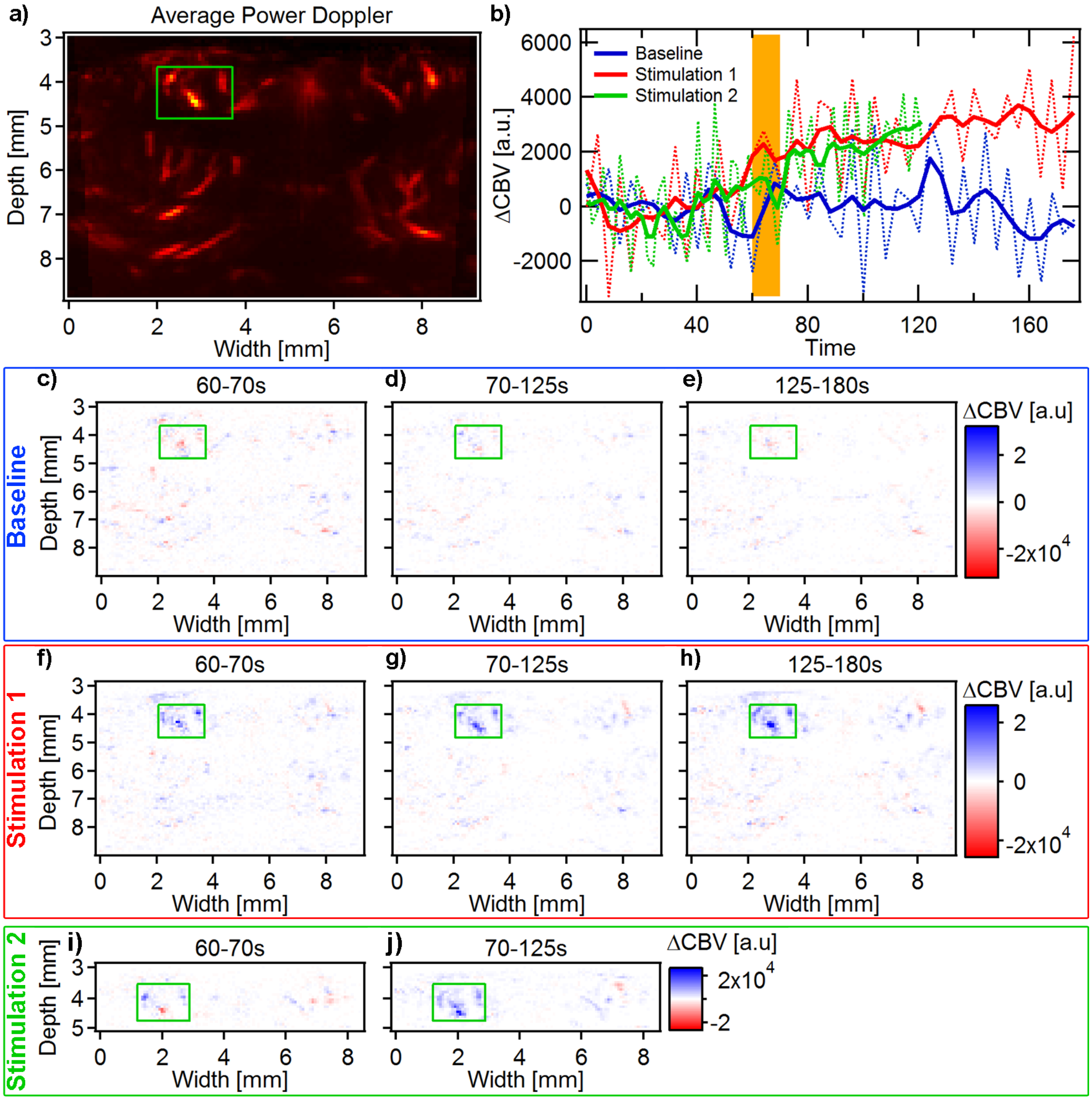

Figure 4.46: Functional ultrasound imaging in the pigeon. a) shows the average of the power Doppler map during the measurement. The green rectangle highlights the area with the largest change during magnetic stimulation. b) shows the temporal evolution of the signal in the green area. The dotted lines show the original data, solid lines show smoothed curves (Binominal smoothing: Baseline and Stimulation 1 (1 pass), Stimulation 2 (2 passes)). The orange area shows the time where the magnetic field was changed. An increase in cerebral blood volume during and after stimulation can be observed in two repeated measurements. No change is observed if no stimulation is applied (Baseline - blue). c)-e) Baseline measurement where no stimulation has been applied. The images show the average over the indicated times subtracted by the baseline signal. f)-h) Measurement where the horizontal magnetic component has been compensated (Stimulation 1). i)-j) same stimulation with an increased temporal resolution and a smaller field of view (note that the region of interest is slightly moved).

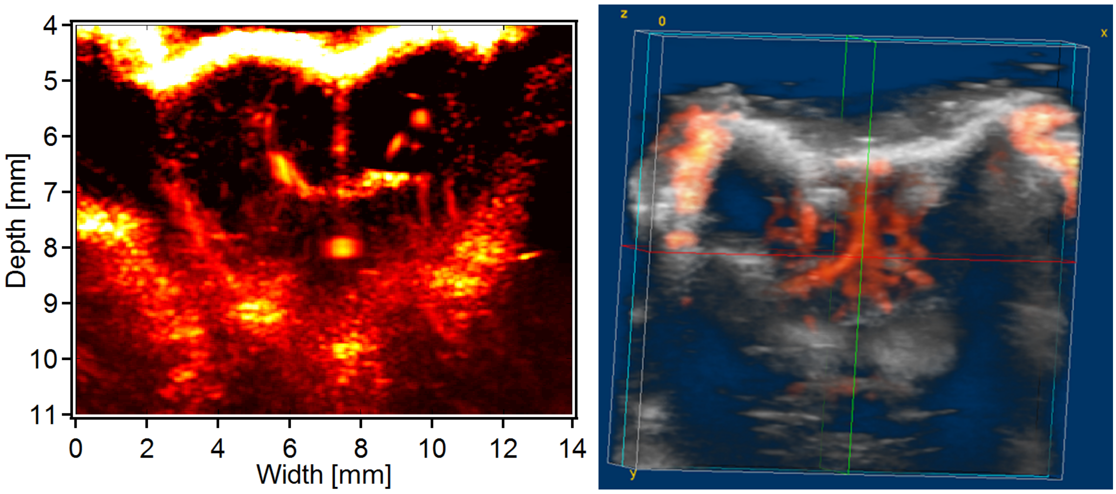

Figure 4.47: Left: The image shows a post processed Power Doppler map of the pigeon brain acquired with the Visual Sonics *Vevo*® 2100. The post processing included a clutter filter at 70Hz, lateral and axial autocorrelation of 5 pixel averaged to one and persistence filtering over $N_f = 80$ frames. Image from [491].
Right: 3-dimensional reconstruction of the vascular structure (red) and anatomical data (grey) measured with the *Vevo* ® 2100 from Visualsonics on a pigeon with a thinned skull.

To the best of the authors knowledge this is the first time that the vascular system has been measured with ultrasound in a pigeon.
Measurements were also performed with the PVC window installed on the pigeon. While quite large reflexes prevent high quality images the ease to remove and reattach the PVC window allows for repeated measurements. In the future a plug-in connection for the top cover will be used which will make imaging even more convenient.

4.2.4 Discussion

Ultrasound imaging is a well established method to measure blood flow and blood volume. With conventional ultrasound the temporal resolution in the measurement of blood flow is only sufficient to measure small region of interest. Recently Mace et al.[489] introduced ultrafast plane wave imaging for functional imaging with a high sensitivity and a large field of view. For high resolution ultrasound measurements one has to get rid of the reflexes from the spongy bone structure of the pigeon skull. Therefore the procedure of thinning the skull of a pigeon has been implemented which allows for high quality repeated ultrasound measurement. Thinning the skull and installing a “cortical window” instead of performing a craniotomy is both beneficial for scientific as well as animal welfare reasons: it allows for repeated measurements on the same animal, the brain is not injured and the meninges are not irritated. Furthermore one can apply an anesthesia regime which is optimized for neuroimaging rather than surgery. In addition the repeated use of the same animal allows for a reduction in animal numbers. The PVC plate, which has been used as top cover, successfully prevents the head from injury and inflammation, but produces strong reflexions which precludes imaging of smaller vessels. This requires the removal of the PVC plate before each imaging session. Therefore in future experiments a removable window with a plug-in connection will make the removal faster and more convenient.

One limitation of the thinned-skull is the regrowing of osseous structures which requires repeated thinning of the skull. A quantitative analysis of the renewal of the bone will be performed in future experiments. Additionally one might try to optimize the time till self loosening of the cortical window by using other dental cements.

With the thinned skull successful measurements of the microvasculature with vessels with diameters as small as 100µm have been performed. A 3-dimensional map of the vascular structure have been generated from repeated measurements of adjacent slices. Furthermore a first functional experiment with magnetic stimulation showed the feasibility of functional ultrasound imaging in the pigeon brain. The implementation of ultrafast plane wave imaging in the Vantage 128 from Verasonics is currently underway so that it should be possible to repeat and extend the functional imaging in the near future.

4.3 Magnetic resonance imaging and computed tomography

Magnetic resonance imaging (MRI) is a widely used non-invasive imaging technique which is mostly used to view soft tissue as well as to extract hemodynamic changes to perform functional studies.

There has been a limited number of MRI measurements on pigeons which have focused on the analysis of the anatomy in order to build a pigeon brain atlas[231] as well as one functional study with an awake pigeon during visual stimulation[255]. However no study focusing on the detection of magnetic material in the head of the pigeon has been performed with MRI so far.

As already discussed in section 2.2.2 there is a controversy in literature if there are magnetic particles in the pigeon beak[108] or if the iron containing structures are just macrophages[141]. In addition, magnetic particles have been suggested to be located in other places such as the ear[114,145,148]. In fact magnetic particles have been claimed to be found in many animals (e.g. honeybees[494]). However in many cases it turned out that the magnetic particles were just contaminations from the environment which were accumulated during the preparation of the specimen.

The main problem with earlier studies is that they have all been invasive (cutting the sample with a microtome) and therefore might be contaminated by e.g. dust, which may lead to false positive results. Alternatively the slicing is done too sparse and magnetic particles might have been overlooked which might result in false negative findings.

Therefore we had the idea to apply high resolution magnetic resonance imaging (MRI) to investigate the pigeon's head for magnetic particles. Magnetic particles lead to a change in the local magnetic field which results in an image artifact due to a spin dephasing (shortening of T_2^*) and consequently a signal drop as well as a spatial mismapping[495]. Even though the particles themselves are most likely smaller than the voxel size of the MRI image, they might still be detected due to the large distortion of the local B-field.
Susceptibility changes do not only produce artifacts but are the contrast mechanism for functional studies (blood oxygen-level dependent) and are as well used in the imaging of brain iron and its role in brain function and disease[496–498].

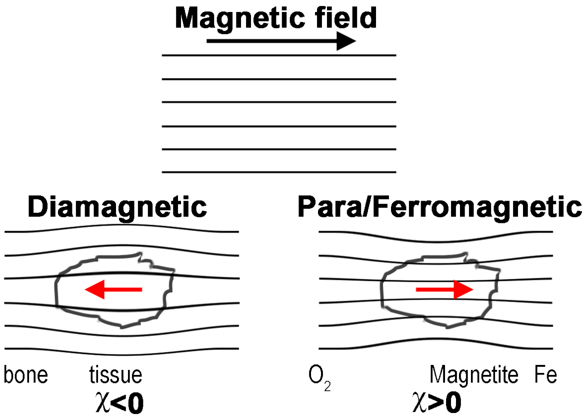

Figure 4.48: Schematic depicting the effect of field disturbance by other material. The material of interest are shown ordered from diamagnetic (left) to para- and ferromagnetic (right).

If the susceptibility changes are however large, the signal is saturated and appears as dark or bright spots in the image. This is not only caused by magnetic particles but also by tissue-air (paramagnetic O_2) and tissue-bone (diamagnetic) surfaces.
No extended discussion about MRI theory will be given, but the basic principles which are most relevant for the contrast produced by magnetic material will be given. These effects are nicely covered in the review[495].
For $\chi \ll 1$ an intuitive understanding of the susceptibility can be developed by considering the induced field, when the object is placed in a homogenous field B_0. Only ΔB_z, the component parallel to B_0 is relevant for magnetic resonance. In the region of the magnetized object ΔB_z takes on both positive and negative values: The induced field is strongest inside the object and at the surface and although it depends on the samples shape, it is always[495]: $-\chi B_0 < \Delta B_z < \chi B_0$. The maximum field perturbation ΔB_{max} can be related to χ: $\Delta B_{max} \approx \chi B_0$.

Table 4.7: Volume susceptibility (χ) values of material relevant for MRI image artifacts in SI Units ($B = \mu_0 (H + M)$ and volume susceptibility $\chi = M/H$) are given. Density (ρ) and atomic/molecular weight (MW) is given to facilitate the calculation of molar ($\chi_M = \chi MW/\rho$)) and mass ($\chi_g = \chi/\rho$)) susceptibility . Values (except O_2) are copied from[495]. *The diamagnetic properties of cortical bone are due to the composition of hydroxyapatite (a calcium phoshate hydroxylate), calcium carbonate, and other calcium salts.

Material	Density [10^3kg/m^3]	Atomic/ Molecular weight [a.u.]	Susceptibility
Cortical bone*			(-12.82 to -8.86) $\cdot 10^{-6}$
Water (37°C)	0.933	18.015	-9.05 $\cdot 10^{-6}$
Human Tissues	1.00-1.05		(-11 to -7) $\cdot 10^{-6}$
Whole blood (deoxygenated)	1.057		-7.9 $\cdot 10^{-6}$
Red blood cell (deoxygenated)	1.093		-6.52 $\cdot 10^{-6}$
Hemoglobin molecule (deoxygenated)	1.335	64650	0.15 $\cdot 10^{-6}$
Air	0.00129	28.97	0.36 $\cdot 10^{-6}$
O_2 (20°C; 0.209atm)	0.278	31.99	0.37 $\cdot 10^{-6}$
Calcium	1.55	40.078	21.7 $\cdot 10^{-6}$
α-Fe_2O_3 (hematite)	5.277	159.70	1.46 $\cdot 10^{-3}$
α-FeOOH (goethite)	4.28	88.85	2.65 $\cdot 10^{-3}$
Fe_3O_4 (magnetite)	5.18	231.54	70
Iron	7.874	55.847	$200 \cdot 10^3$

Therefore χ is a rough measure of the degree to which an object can perturb an applied field[495].

In a standard MRI an intense static magnetic field B_0 in the z direction, a radio frequency field B_1 perpendicular to z and three gradient fields are used to create image information[495]. The gradient fields ($G_x(t), G_y(t), G_z(t)$) are used to manipulate the frequency and phase of the processing spins as a function of position. The frequency ($\omega = -\gamma B_z$) of the NMR signal arising from a given point is proportional to the z component of the magnetic field at that point. With a perturbation due to a susceptibility mismatch the z component of the total field is given by

$$B_z = B_0 + G_x(t)x + G_y(t)y + G_z(t)z + \Delta B_z(x, y, z) \tag{4.60}$$

Therefore a positional error is observed due to the field perturbation.

Based on the numbers given in the paper of Fleissner et al.[108] one dendrite with magnetic particles contains 35pg of Iron with about 15% Magnetite and 85%

Maghemite. This is equivalent to a mass of about 7.3pg Magnetite (Fe_3O_4) and 42.5pg Maghemite (γ-Fe_2O_3) and a volume of 1.4µm^3 and 8.1µm^3, respectively. For a rough estimate if one can measure the effect in a MRI measurement the volume averaged susceptibility for one voxel is calculated by taking the values from table 4.7 and assuming that the rest of the voxel has a susceptibility of tissue ($-9 \cdot 10^{-6}$). Since no reliable values for the susceptibility from maghemite has been found in literature, as a lower boundary only magnetite is considered and as a upper boundary the susceptibility of maghemite is set to the same value as magnetite. This gives a susceptibility of about $1.39 \cdot 10^{-4}$ to $1.06 \cdot 10^{-3}$. This results in an upper limit for the field perturbation of $\Delta B_{max} \approx \chi B_0 = 1.31\text{mT}-10.0\text{mT}$. Note that this is only a very rough estimate because it does not consider the exact distribution and demagnetization due to the shape of the particles, but should provide an estimate for the magnitude of the effect.

4.3.1 Experiment

A “lucky shot” experiment was performed on a pigeon that died a natural death. The pigeon was found shortly after death. The head was cut off and fixated for 3 days with 4% paraformaldehyde (PFA) in 0.1M sodium phosphate (NaPi) buffer (solution renewed after 1 day). The head was then washed with phosphate buffered saline (PBS) and stored on ice.

The MRI scan was performed in the group of Prof. Faber at the University of Münster on a Bruker BioSpin MRI GmbH BioSpec94/21 at 9.4T with a spatial resolution of 77.8µm x 78.1µm x 109.4µm (Voxel Volume $664.6 \cdot 10^3$µm^3). The imaging sequence was a fast spin echo sequence with the following measurement parameters:

Scanning Sequence:	RM
Sequence Variant:	NONE
Scan Options:	
MR Acquisition Type:	3D
Sequence Name:	RARE (pvm)
Slice Thickness:	0.109375
Repetition Time:	500 ms
Echo Time:	48 ms
Number of Averages:	16
Imaging Frequency:	400.3129209 MHz
Imaged Nucleus:	1H
Spacing Between Slices:	0.109375mm
Number of Phase Encoding Steps:	360
Echo Train Length:	12
Percent Phase Field of View:	160.7142857

Pixel Bandwidth:	125.2003205
Software Versions(s):	ParaVision Acquisition 5.1 ParaVision 5.1
Protocol Name:	TurboRARE-3D 18
Acquisition Matrix:	0 360 576 0
Phase Encoding Direction:	ROW
Flip Angle:	270

A first measurement was performed directly on the fixated head and a second measurement was performed after outgassing the head for about two weeks and substitute the surrounding tissue by a contrast agent (2% Magnevist). The reported results are from the second measurement which has a smaller number of artifacts from air and a better image contrast.

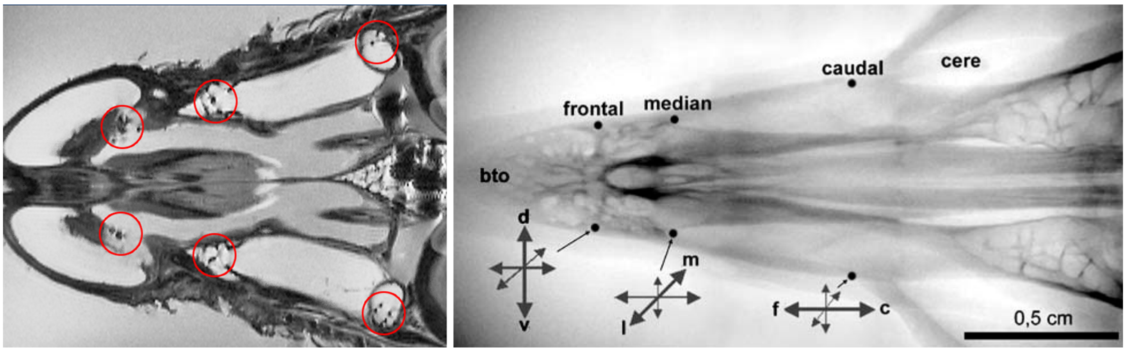

Figure 4.49: Left: Preliminary results from high resolution MRI data of the beak of a fixated pigeon. The light blurring in the image is due to alpha transparency of consecutive slices for better visualization of image artifacts (in our case signal). The dark points (highlighted with red circles) are symmetrically positioned at roughly the location described for magnetic particles in [108]. Right: For comparison figure from [108] showing a x-ray image of the upper beak and its six iron-containing areas with the prevailing orientation of their dendritic fields.

Several artifacts have been found. In particular six artifacts which roughly fit to the description of Fleissner et al. are shown in figure 4.49. Such type of artifact is typically due to either magnetic material, air, (blood) or bones.

In addition very large artifacts were present in some areas, such as in the brain and the inner ear (see figure 4.50). These large artifacts are most likely due to air or an incomplete fixation of the tissue. This precludes any meaningful analysis of these areas.

In order to narrow down the different types of artifacts, a micro-CT scan was performed on the SkyScan1176 (Bruker) which has an isotropic 3D spatial resolution of 8.52µm.

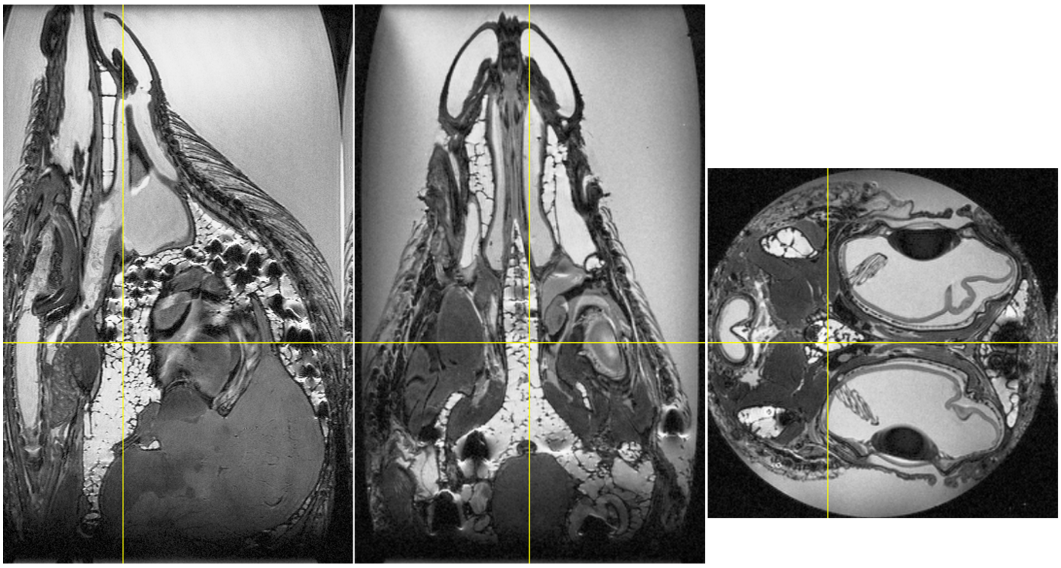

Figure 4.50: The images shows three orthogonal slices of a MRI image of the head of a pigeon. Dark spots in the brain are artifacts which are most likely due to air or an incomplete fixation of the tissue.

The scanning details, which were used, are as follows: a 0.5mmAl-Filter corresponding to 50kV was used. Exposure time was 1000ms. Exposure with 10 averages and 0.3° rotation per step. The field of view scan is in z-direction over a length of 35mm (scanning was performed in two overlapping blocks). This results in an image with 3312 x 3312 x 4311 pixel corresponding to a volume of 28.22mm x 28.22mm x 36.73mm and about 90GB data. CT and MRI data were manually co-registered with 3DSlicer. An adjustment of the x-ray energy to optimize the contrast for the discrimination of air and dense structures (such as bone or magnetic material) was not possible.

Regions where artifacts have been identified in the MRI image have been investigated in the CT. Four of the six artifacts have been identified as osseous structures (see figure 4.51). The remaining two structures do not show any contrast in the CT. The bright spots surrounding the dark spots are however typical for artifacts from air bubbles. Other regions which are most likely also filled with air also show no contrast in CT.

4.3.2 Discussion

A number of artifacts have been found in the MRI images of the head of the pigeon. In particular six artifacts roughly at the positions described by Fleissner et al.[108] have been identified. Four of these dark spots also show a strong contrast

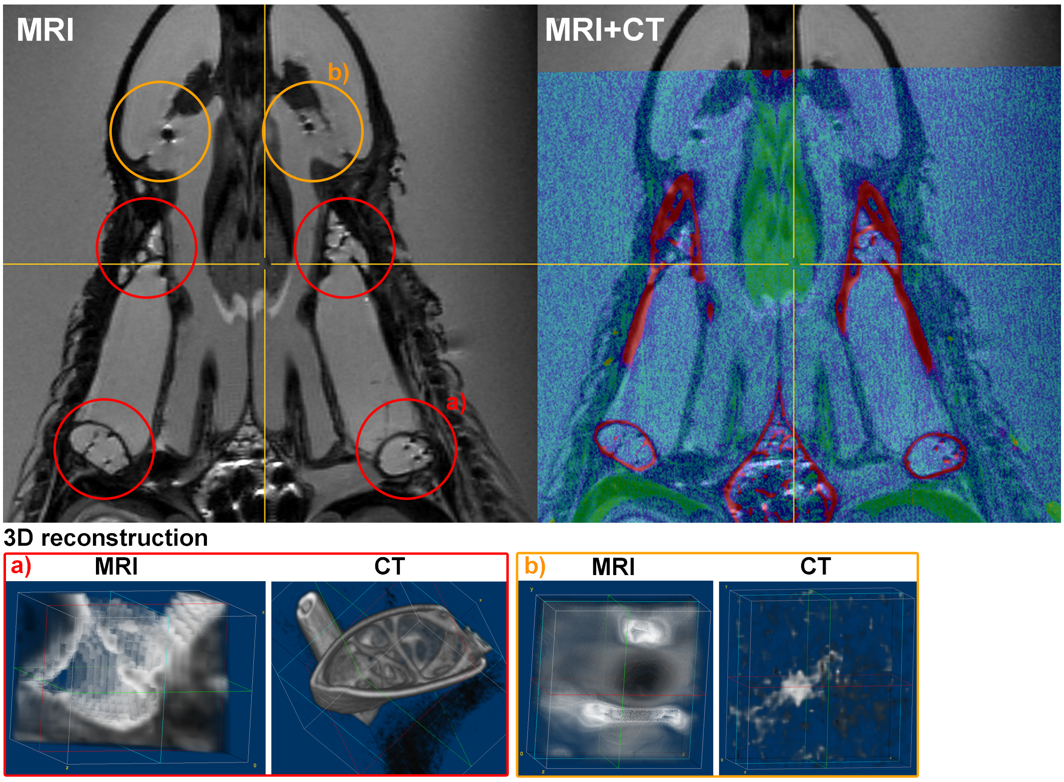

Figure 4.51: left: MRI image (gray) and right: overlay of MRI (gray) and CT (color) data of a slice through the beak of a pigeon. The dark spots in the region with red circle have been identified as osseous structures (see exemplary data of a 3d reconstruction of region a)). The upper two regions show no contrast in the CT data (see reconstruction in b)). The bright spots surrounding the dark spots are however typical for artifacts produced by air bubbles (see text for more details).

in micro-CT data and could by identified as bony structures. However, this does not exclude that despite the bones there are also magnetic particles. In particular Williams et al.[132] noted that the location of iron-containing (PB-positive) cells is arranged in an oval, sac-like structure with a diameter of about 0.5mm which is embedded in the bone caudo ventral to the concha. Additionally they found that the distribution was similar, but by no means identical in the six pigeons, but always showed a bilateral distribution.

However with the current measurement it is not possible to discriminate between bone and magnetic particles embedded in the bone. One possibility might be to use quantitative susceptibility mapping[498] to discriminate between bone (more diamagnetic than tissue) and magnetic particles. In addition other imaging sequences optimized to increase the contrast for superparamagnetic iron oxide nanoparticles (SPIONs) such as e.g off-resonance imaging might be used (for a current review see[499]).

The other two structures show no contrast in the CT images. It has been suggested that these structures are air bubbles due to the fact that they show a typical signature (bright spots around the artifact) which have often been observed in the presence of air. It is usually possible to adjust the energy of the CT in order to improve the contrast from air, however for the high resolution CT this is not possible in routine operation and could thus not be performed.

Signals from the ear of the pigeon could not be analyzed in detail due to artifacts precluding further analysis. These artifacts are most likely due an incomplete fixation of the tissue. This can be optimized by perfusing the pigeon with paraformaldehyde instead of only passively placing the head in the solution.

In order to get an improved image quality measurements with a perfused pigeon are planned. This excludes blood as a possible source of artifact, improves tissue fixation and might also allow to remove even more air from the birds head. In addition measurements with magnetic bacteria as well with known amounts of magnetic particles (both magnetite and maghemite) are planned in order to experimentally measure the sensitivity of the MRI scanner and give an upper limit for the maximum number of magnetic material which could be in the head.

5 Summary & Outlook

Despite more than 50 years of research the mechanism of magnetoreception in birds is still not fully resolved. The aim of this study was therefore to advance the field by applying novel methods for the investigation of magnetoreception in pigeons. Two different approaches were applied.

The first relies on the detection of hemodynamic changes in the pigeons brain during functional stimulation. In this work, two different methods were implemented for this purpose. First a non-invasive optical imaging method, diffusing wave spectroscopy (DWS), which extracts changes in cerebral blood flow from temporal intensity fluctuations of the interference pattern of multiple scattered light. Second, an advanced ultrasound imaging technique, functional ultrasound (fUS)[489], which relies on the implementation of ultrafast angled plane wave imaging and allows for fast Doppler ultrasound measurements of the pigeons microvaculatur in a large field of view with a high signal to noise ratio, enabling functional measurements.

For both methods working anesthesia regimes for surgery and optimized for neuroimaging have been implemented.

With DWS there were a number of interesting findings during narcosis:
First it is shown that the average cerebral blood flow shows a linear increase/decrease by about 4% after 150s when the isoflurane concentration is decreased/increased by 0.5%. With a simple model it could be shown that the changes are most likely due to changes in the mean arterial blood pressure. However strong variations in individual responses have been observed which highlight the need for a routine monitoring of cerebral blood flow in anesthesia. DWS is an ideal candidate for this purpose, because in contrast to conventional transcranial ultrasound it measures the microvasculatur, is non-invasive, fast, portable and relative inexpensive. Therefore a more thorough investigation of this effect with a sound study design should be performed on humans.
Second, the cerebral blood flow is significantly reduced by 5 ± 2% per °C of reduced body temperature. The change is in agreement with literature values of an increased solubility of isoflurane with decreasing temperature resulting in a deeper anesthesia. Furthermore the body temperature has been established as predictive factor for the maintenance dose of isoflurane.

Third, during arrhythmia with a delayed or skipped heart beat, a linear dependence of the relative cerebral blood flow on the delay has been found. The linear relation holds for both the delayed as well as shortened heart beats. Furthermore it can be used to correct the cerebral blood flow data for those artifacts if the effect of arrhythmia is disruptive for the purpose of the measurement.

In addition, an advanced signal processing, which removes periodic physiological artifacts, such as heart beating and breathing, as well as non periodic artifacts (e.g. motion) and baseline variations from the data, has been developed. The data processing enabled, for the first time, successful functional neuro-imaging measurements with DWS in a pigeon. Validation experiments have been performed with visual stimulation. An average increase of 2.7‰ and a decrease of 3.7‰ of the cerebral blood flow has been found for the right visual wulst and the left optic tectum, receptively. Furthermore, a significant difference between contralateral and ipsilateral stimulation has been found.

Measurements over the optic tectum, during magnetic stimulation with a sudden change and a horizontally rotating magnetic field, revealed a significant correlation of changes in cerebral blood flow with magnetic field changes along the interaural axis. Experiments under different light conditions hint at a possible effect of light, but too small group sizes preclude a meaningful conclusion.

Measurements over the left visual wulst, with horizontal rotating magnetic fields with opposite directions, showed a W and M shaped response for clockwise and counterclockwise rotation, respectively. However pronounced artifacts due to arrhythmia lead to a large variance between the measurements so that the results should be treated with care.

Future experiments with an equal number of control measurements without stimulation as well as magnetic stimulation, where the field is rotated horizontally in both a clockwise and counterclockwise direction, will be performed to reproduce the current findings. This will serve as a final proof that DWS can detect changes in cerebral blood flow due to magnetic stimulation. After establishing the typical response to this stimulus, predictions from theory, such as effects due to wavelength, rf-fields, etc., can be tested. In addition a mapping of the response as a function of the probed brain region will be performed.

First ultrasound measurements showed that reflexions from the sponge like skull with multiple bone, air interfaces preclude high quality imaging. Therefore a procedure of thinning the skull and installing a “cortical” window which allows for chronic access for ultrasound measurements have been implemented. After installation, the window adheres for about 1-2 month to the skull. After self-loosening, the window can either be reattached or the skin is sutured. So far, the surgery has been performed in three pigeons which all fully recovered without any signs of discomfort. With the thinned skull 3-dimensional measurements of the vascular structure have been performed. Furthermore, first proof of principle

functional measurements with magnetic stimulation have been performed.
The next steps for the ultrasound measurements are the implementation of ultrafast angled plane wave imaging in the ultrasound device of Verasonics. Then a systematic study, with magnetic stimulation similar to the one used with DWS, will be performed to refine the brain regions which are involved in detecting and processing magnetic fields. Furthermore an absolute quantification of the blood flow changes will be possible.

The second approach tries to detect the presence or absence of magnetic particles, which have been suggested to be involved in magnetoreception, in the pigeons' head. Therefore high field magnetic resonance imaging (MRI) and mirco-computed tomography (μ-CT) are used. The idea of the approach is to identify image artifacts in the MRI images, which are produced by magnetic particles. μ-CT measures the electron density and can therefore be used to discriminate between other origins of the artifacts, such as bone or air. In contrast to previous attempts both methods are non-destructive and therefore cannot be contaminated by particles from the laboratory environment.
A first investigation was performed on a pigeon which died a natural death and was posthumous fixated in 4% paraformaldehyde. The MRI images showed six artifacts, bilaterally located in the beak, roughly at the positions described by Fleissner et al.[108]. With CT data, four of the six artifacts could be identified as osseous structures. The remaining two artifacts in the MRI image show a signature which is typically observed for air artifacts. The CT measurement do not show any contrast at the position. However at other positions, where air bubbles are expected, also no contrast could be seen with the x-ray energies used in this measurement. The inner ear, which also has been suggested for magnetic particles, could not be analyzed due to a large image artifact which probably resulted from an incomplete tissue fixation.
In order to get an optimal tissue fixation, perfused pigeons will be used in future measurements. Furthermore, an even greater effort to remove all of the air in the pigeon's head will be made. In addition a μ-CT which allows for the adjustment of the x-ray energy, and therefore for the definite identification of air, might be useful. Moreover magnetic bacteria will be used as a control to establish a lower detection limit of the MRI-scanner.

In summary, this thesis was devoted to developing, implementing and validating a novel methodology which allows for measuring magnetic field dependent changes in neural hemodynamics of the pigeon. While this long and cumbersome task has been finally successful, the original question, which of the models of magnetoreception is correct, has not yet been answered. However with everything in place we will hopefully be able to give an answer in the near future.

6 Zusammenfassung

Das Heimfindevermögen von Tauben fasziniert Menschen schon mehr als 2000 Jahre. Es ist bekannt, dass sie viele verschiedene Quellen wie Landmarken, die Sonne, Gerüche und viele mehr zur Orientierung benutzen. Durch Manipulation des Magnetfeldes am Kopf der Taube konnte aber insbesondere gezeigt werden, dass sie auch das Erdmagnetfeld zur Orientierung nutzen[8,9]. Aber nicht nur Tauben benutzen das Magnetfeld der Erde, sondern viele weitere Vogelarten (z.B. Rotkehlchen[7], Gartengrasmücke[47], Trauerschnäpper[51]), sowie auch Tiere anderer Spezies wie Reptilien (z.B. Schildkröten[500]), Fische (z.B. Lachse[25]), wirbellose Tiere (z.B. Salamander[36]), Bakterien (z.B. Magnetotaktische Bakterien[11]) und Säugetiere (z.B. Fledermäuse[54]).
Der genaue Mechanismus der Magnetorezeption ist trotz der Vielzahl von Tieren welche das Magnetfeld nutzen und mehr als 50 Jahren Forschung auf dem Gebiet immer noch nicht vollständig entschlüsselt. Für Vögel werden im Moment im Wesentlichen zwei Theorien diskutiert.
Die erste beruht auf eisenhaltigen magnetischen Teilchen welche sich entweder im oberen Schnabel[108–110] oder in der Lagena, einem Teil des Gleichgewichtsorgans im Innenohr[114,144,145,148], befinden. Es wird angenommen, dass die Teilchen an Rezeptoren oder Ionenkanäle in der Zellmembran koppeln und so magnetfeldabhängig die Aktivierung der Nerves modulieren. Evidenz für den Schnabel kommt aus Messungen, die die Beteiligung des Nervus ophthalmicus, einen Ast des Nervus trigeminus, der den oberen Schnabel innerviert, zeigen[111,122,128]. Der überzeugendste Hinweis kam aber von anatomischen Messungen von Fleissner et al.[108–110], die sechs längliche, eisenhaltige Strukturen (Magnetite, Maghemite) welche sich symmetrisch, beidseitig angeordnet im oberen Schnabel einer Taube finden, zeigen konnten. Das Untersuchungsergebnis wurde aber durch eine Studie von Treiber et al.[140] infrage gestellt, bei dem sie nahelegen, dass es sich bei den eisenhaltigen Zellen eher um Makrophagen als um magneto-sensitive Zellen handelt. Anhaltspunkte für die Lagena kommen von eisenhaltigen Organellen in den Haarzellen von Vögeln[148] und der magnetischen Aktivierung von Gehirnregionen, welchen mit dem Innenohr assoziert sind[114,145].
Die zweite Theorie, das Radikal-Paar Modell[153,154], basiert auf der Bildung eines Radikal-Paares, welches durch einen lichtaktivierten Elektronentransfer zwischen einem Donor und Akzeptormolekül gebildet wird. Das Radikal-Paar kann sich entweder zwischen dem Singulett und Triplett Zustand umwandeln oder in Endprodukte zerfallen. Die Umwandlung zwischen Singulett und Triplett Zus-

tand wird magnetfeldabhängig durch die Hyperfein- und Zeemanwechselwirkung beeinflusst und hängt sowohl von dem internen (z.B. Wasserstoff, Stickstoff), als auch von dem externen (geomagnetisches) Magnetfeldern ab. Daher sind auch die Endprodukte magnetfeldabhängig. Es wurde zusätzlich vorgeschlagen, dass die Endprodukte die Sicht der Vögel beeinflussen und sie somit buchstäblich das Magnetfeld sehen können. Als Kandidat für das Radikal-Paar wurde Cryptochrome, ein blauer Photorezeptor, vorgeschlagen[154]. Experimentelle Hinweise für die Theorie kommen von Funden, dass es sich um einen Inklinationskompass handelt[7], die Orientierung Wellenlängen abhängig ist[42,48,92,175–179] und durch ein radio-frequenz Magnetfeld bei der Lamorfrequenz eines freien Elektrons zerstört werden kann[50,180–182]. Außerdem wurde Cryptochrome in den äußeren Segmenten der ultravioletten/violetten Zapfen der Netzhaut gefunden[164].
Obwohl eine Vielzahl von Experimenten gewisse Aspekte von Vorhersagen der Theorien zeigen konnten, ist der Mechanismus der Magnetorezeption weit davon entfernt vollständig verstanden zu sein. Dies liegt insbesondere auch daran, dass viele Schlüsselexperimente nicht unabhängig reproduziert wurden bzw. widersprüchliche Ergebnisse geliefert haben.

Die Idee dieser Studie ist daher die Anwendung von neu entwickelten Methoden, welche unter kontrollierten Laborbedingungen angewendet werden können und somit zur Entschlüsselung der Magnetorezeption beitragen. Es wurden hier zwei unterschiedliche Herangehensweisen gewählt.
Der erste Ansatz beruht auf der Detektion von hämodynamischen Änderungen im Gehirn. Eine etablierte Methode hierfür ist die funktionelle Magnetresonanztomographie (fMRI), welche aufgrund der hohen Magnetfelder die hierfür nötig sind, in diesem Fall aber nicht angewendet werden kann. Es wird daher eine nicht-invasive optische Methode, Diffusing Wave Spectroscopy (DWS), welche aus Intensitätsfluktuationen in dem Interferenzmuster von vielfach gestreuten kohärenten Licht Informationen über den zerebralen Blutfluss extrahiert, verwendet. Des Weiteren wird eine Weiterentwicklung von Ultraschall, funktioneller Ultraschall (fUS)[489], welcher im Gegensatz zu konventionellen Ultraschall das Bild nicht Punkt für Punkt abrastert, sondern ebene Wellen unter verschiedenen Winkeln in das Gewebe schickt und das Bild aus der kohärente Überlagerung der reflektierten Signale generiert, benutzt. Dies erlaubt, in einem großen Bildfeld, die schnelle Messung des Doppler Ultraschall Signals (Blutfluss, Blutvolumen) der Mikrozirkulation und ermöglicht damit funktionelle Messungen. Die Methoden komplementieren sich gegenseitig, da Ultraschall eine sehr hohe örtliche Auflösung hat und DWS sehr sensitiv auf kleinste Bewegungen ist sowie eine hohe zeitliche Auflösung hat.

Es hat sich herausgestellt, dass sowohl für Diffusing Wave Spectroscopy, als auch für Ultraschall Messungen eine stabile Narkose nötig ist. Hierfür wurden zwei

Narkoseregimes etabliert. Das Erste ist für chirurgische Eingriff, wie das dünner Schleifen der Schädeldecke um Ultraschall Reflexionen zu vermeiden, optimiert. Das Zweite wurde für funktionelle Messungen optimiert. Hierbei wird zusätzlich zur Isoflurannarkose 5mg/kg Midazolam i.m. appliziert, um die Erhaltungsdosis von Isofluran herabzusetzen und damit die neurovaskuläre Kopplung möglichst wenig zu stören.

Bei DWS Messungen in Narkose wurden einige interessante Effekte beobachtet:
1. Der mittlere zerebrale Blutfluss zeigt einen linearen Anstieg/Abfall von ca. 4% nach 150s, wenn die Isoflurankonzentration um 0.5% herab/herauf gesetzt wird. Mit Hilfe eines einfachen Modells konnte gezeigt werden, dass die Änderungen des Blutflusses wahrscheinlich durch Änderungen im mittleren arteriellen Blutdruck verursacht wurden. Man muss aber beachten, dass es große Unterschiede in den individuellen Antworten auf die Konzentrationsänderung gab. Das zeigt, dass man die Reaktion auf eine Konzentrationsänderung nicht von Populationsmittelwerten ableiten sollte, sondern routinemäßig den zerebralen Blutfluss messen sollte. Aktuell wird der zerebrale Blutfluss nur bei speziellen Eingriffen in großen Gefäßen mit Ultraschall gemessen. DWS ist ein idealer Kandidat für Routinemessungen, da es die Mikrozirkulation nicht-invasiv, schnell und relativ kostengünstig messen kann. Es wäre daher sinnvoll, den Effekt in einer sauber designten Studie am Menschen näher zu untersuchen. DWS kann ähnlich wie die Pulsoxymetrie, welche die Sauerstoffsättigung misst und inzwischen Standard geworden ist, helfen, die Anästhesie noch ein Stück sicherer zu machen.
2. Für jedes °C reduzierte Körperkerntemperatur wird der zerebrale Blutfluss um $5 \pm 2\%$ reduziert. Die Änderung ist in Übereinstimmung mit Literaturwerten von einer erhöhten Löslichkeit von Isofluran bei niedrigeren Temperaturen und einer damit einhergehend tieferen Narkose. In Übereinstimmung mit oben beschriebenen Messungen führt die tiefere Narkose zu einer Reduktion im Blutfluss. Es konnte zusätzlich gezeigt werden, dass die erste gemessene Temperatur ein vorraussagender Faktor für die Erhaltungsdosis ist.
3. Während Herzrhythmusstörungen mit einem verspäteten oder ausgelassenen Herzschlag findet man einen linearen Zusammenhang zwischen dem relativen zerebralen Blutfluss und der Verzögerung des Herzschlags. Diese lineare Beziehung ist sowohl für einen verzögerten als auch für einen vorzeitigen Herzschlag gültig. Für den Fall, dass die Blutflussändungen aufgrund der Arrhythmie störend für eine Fragestellung sind, kann man daher die lineare Beziehung verwenden, um die Daten von dem Effekt zu bereinigen.
Zusätzlich wurde eine hochentwickelte Datenanalyse entwickelt, welche das Signal von periodischen physiologischen Artifakten, wie Herzschlag und Atmung, sowie nicht-periodischen Artifakten (z.B. Bewegung) und Schwankungen in der Baseline bereinigt. Durch die Datenprozessierung konnten zum ersten Mal erfolgreich funktionale Messungen in einer Taube mit DWS durchgeführt werden. Zur Bestätigung

wurden funktionale Messungen mit visueller Stimulation durchgeführt. Es wurde ein mittlerer Anstieg von 2.7‰ für eine Messung über dem rechten visuellen Wulst und ein Abfall von 3.7‰ über dem linken optischen Tectum beobachtet. Es wurde zusätzlich ein signifikanter Unterschied zwischen kontralateraler und ipsilateraler Stimulation gefunden.
Messungen über dem optischen Tectum, bei denen eine magnetische Stimulation mit plötzlichen Änderungen im Magnetfeld und einem horizontal rotierenden Magnetfeld verwendet wurde, haben eine signifikate Korrelation zwischen der Änderung des zerebralen Blutflusses und der Änderung der Magnetfeldkomponente, welche entlang der Ohr-Achse liegt, gezeigt. Experimente unter verschiedenen Lichtbedingungen deuten auf einen möglichen Effekt des Lichts hin, die Gruppengrößen waren aber zu klein um definitive Aussagen zu treffen.
Messungen über dem linken visuellen Wulst mit linksherum und rechtsherum rotierenden horizontalen Magnetfeld haben eine M bzw. W förmige Antwort gezeigt. Man sollte bei der Interpretation dieser Ergebnisse allerdings vorsichtig sein, da bei einigen der Messungen eine ausgeprägte Arrhythmie vorhanden war, welche möglicherweise nicht völlig herausgerechnet werden konnte.
Zukünftige Messungen mit gleich großen Gruppen von Kontrollmessungen und Messungen mit links und rechts Drehung sollen die Ergebnisse reproduzieren und als finaler Beweis für die Detektion von durch das Magnetfeld ausgelösten Änderungen des zerebralen Blutfluss mit DWS dienen. Wenn die typische Antwort auf das Magnetfeld etabliert ist, können Vorhersagen der Theorien, wie z.B. die Wellenlängenabhängigkeit, der Effekt von radio-frequenz magnetischen Feldern und weitere überprüft werden. Zusätzlich können durch eine systematische Positionierung des Lasers und Detektors die Gehirnregionen welche in die Prozessierung der Magnetfelddetektion involviert sind bestimmt werden.

Erste Ultraschallmessungen an Tauben haben gezeigt, dass aufgrunder der Reflexionen von dem schwammartigen Schädel mit vielen Knochen/Luft Grenzflächen keine hochaufgelösten Bilder möglich sind. Aus diesem Grund wurde eine Prozedur etabliert, bei der der Knochen bis auf eine dünne Knochenschicht herunter geschliffen und dann ein Fenster für wiederholte Ultraschallmessungen installiert wird. Typischerweise ein bis zwei Monate nach der Installation löst sich das Fenster vom Knochen. Man kann es dann entweder erneut anbringen oder die Kopfhaut zunähen. Bisher wurden drei Tauben auf diese Weise operiert und alle haben sich vollständig von der Operation erholt und können jetzt ohne Einschränkung mit ihren Artgenossen leben.
Bei Tauben mit dem dünner geschliffenen Schädel konnten 3-dimensionale Aufnahmen der Gefäßstruktur durchgeführt werden. Zusätzlich konnte die Machbarkeit der Methode mit ersten funktionellen magnetischen Messungen gezeigt werden.
Im Moment wird die Methode der ultraschnellen Ultraschallmessungen mit unter verschiedenen Winkeln ausgesendeten ebenen Wellen in das Gerät der Firma

Verasonics implementiert. Danach wird eine systematische Studie mit der selben magnetischen Stimulation, wie in den DWS Untersuchungen, durchgeführt. Hierbei sollen die Gehirnregionen, welche in die Magnetorezeption involviert sind genauer eingegrenzt werden, sowie die absolute Änderung des Blutflusses bestimmt werden.

Der zweite Ansatz verwendet Magnetresonanztomography (MRI) und Röntgen-Mikrocomputertomographie (μ-CT), um das Vorhandensein bzw. die Abwesenheit von magnetischen Teilchen im Kopf der Taube zu detektieren. Die Idee bei dem Ansatz ist, dass auch wenn die magnetischen Teilchen wahrscheinlich kleiner als die Voxel Größe sind, die Änderung im lokalen Magnetfeld so groß ist, dass sie im MRI Bild Artefakte erzeugen. Durch Messung der Elektronendichte mithilfe von μ-CT kann man zwischen Artefakten mit anderer Ursache, wie Knochen oder Luft, unterscheiden. Der Vorteil dieser Herangehensweise ist, dass im Gegensatz zu früheren Messungen, die Methoden nicht destruktiv sind und die Probe somit nicht mit Teilchen aus der Laborumgebung verunreinigt werden kann.
Erste Messungen wurden an einer natürlich gestorbenen Taube, welche nach dem Tod mit 4% Paraformaldehyd fixiert wurde, durchgeführt. Das MRI zeigt sechs Artefakte, welche beidseitig, symmetrisch, ungefähr an den Positionen, welche in Fleissner et al.[108] beschrieben wurden, liegen. Vier der sechs Artefakte konnten mit den CT Daten als knöcherne Strukturen identifiztiert werden. Die anderen zwei Artefakte zeigen eine MRI-Signatur, wie sie typischerweise bei Luft detektiert wird. In den CT Messungen findet sich an dieser Stelle kein Kontrast, aber auch nicht an anderen Stellen an denen Luft sehr wahrscheinlich ist.
Das Innenohr konnte aufgrund eines sehr großen Artefakts, welches vermutlich durch eine inkomplette Fixierung entstanden ist, nicht analysiert werden.
Um eine optimale Gewebe Fixierung zu erreichen, werden zukünftige Messungen mit perfundierten Tauben durchgeführt. Es werden zusätzlich noch stärkere Anstrengungen unternommen alle Luft aus dem Kopf zu eliminieren. Ergänzend könnten μ-CT Messungen sinnvoll sein, bei denen sich die Röntgenenergie anpassen lässt und Luft damit eindeutig identifiziert werden kann. Zusätzlich sollen Kontrollmessungen mit magnetotaktischen Bakterien durchgeführt werden, um ein unteres Detektionslimit des MRI-Scanners zu etablieren.

Zusammenfassend wurde diese Doktorarbeit der Entwicklung, Implementierung und Validierung einer neuen Methodik, welche magnetfeldabhängige Änderungen der neuronalen Hämodynamik der Brieftaube messen kann, gewidmet. Auch wenn diese langwierige und mühsame Aufgabe schlussendlich erfolgreich war, konnte die ursprüngliche Frage, welches Modell der Magnetorezeption korrekt ist, noch nicht beantwortet werden. Mit allen gemachten Vorarbeiten erwarten wir aber, dass wir in naher Zukunft Antworten auf diese Frage geben können.

7 Acknowledgment

First of all I want to thank Prof. Maret for giving me the opportunity to work on the fascinating and challenging topic magnetoreception. I especially appreciated that one always had the possibility to take an equal part in decision making, realize one's own ideas, as well as the ongoing support. His pleasant manner resulted in a good and supportive atmosphere in the whole group. Furthermore I want to highlight the group excursions which always were great fun and I will especially keep exceptional experiences, such as camping in the snow, in good memories. Also many anecdotes from his far-reaching experience as well as scientific discussion were both entertaining and instructive to gain an deeper insight in many topics.

I also want to thank the people in magnetoreception group for the good working environment. It was always great fun to work together. I also want to thank all the bachelor/ master/ diploma students, namely Wolfgang Scheffer, Annika Schoe, Julian Ströbele, Maike Vennekel, Moritz Schlötter, Clara Engesser, Julia Sester and Richard Rau who get involved in this challenging topic and got the persistence to go through hard times where there were difficulties with collaborations/companies and the project only progressed slowly. A special thanks go to Wolfgang Scheffer who started his diploma thesis together with my PhD and continuously accompanied the project with me. In particular he took care of the full development of the measurement software and equally contributed to building up the set-up. Furthermore all diffusing wave spectroscopy and ultrasound measurements were performed together. I also want to highlight Wolfgang Scheffer and Richard Rau for thoroughly correcting this thesis and many helpful discussions about ultrasound.

Furthermore I enjoyed the good and cooperative atmosphere in the whole group where everyone supported each other. In particular I want to mention the early eating group where we had both very interesting scientific as well as entertaining private discussions which often led to new ideas in experiments. Here I particularly want to mention Markus Ninck, Nathan Isert, Wolfgang Bührer, Tilo Sperling and Lukas Schertel.

In addition I want to thank Bruno-Felix Osmanski and Michael Tanter who helped in performing the functional ultrasound measurements and pre-processed the ultrasound data. Furthermore I want to thank Prof. Faber and Nina Nagelmann for performing the MRI and CT measurements.

I also want to thank the employes of the TFA for continuous support. Especially I want to thank Dr. Mende for the confidence and support during the project. I always greatly appreciated his helpful advices. Furthermore I want to thank Melanie Schauber for keeping care of the pigeon and her great commitment for the project. But I don't want to forget all the others who were always supportive and helped out when it was needed.
Moreover I highly appreciated the helpful advices of Prof. Korbel, Prof. Haberstroh, Dr. Julia Henke and Dr. Ludger Kamphausen on how to best perform anesthesia in pigeons.

I also want to highlight our secretaries Sabine Lucas and Doris Drexler. Especially Sabine was always a great support for any administrative problem and helped to keep the chair alive.
Also I want to mention the scientific workshop which helped in building much of the equipment which was needed for the investigations.

Finally I want to thank my family for continuous support during the complete work. I always felt lucky to have such a great family which is always there if I needed them. Last I want to thank my girlfriend Julia for being always understanding if I had to work late hours or if we had to arrange our weekends and evenings according to the experiments.

8 Appendix

8.1 Korbel Reflex score

A reflex score to access the optimal anesthetic depth for surgery in birds was developed by Korbel et al.[294]. A score between 0 and 29 points can be reached. For the surgical plane an intended reflex score of 3 has been suggested by[294] (see table 8.2).

Table 8.1: Reflexscore developed by Korbel et al.[294].

Relexstatus (Score)	Auslösung und Bewertung von Reflexen
1. Lidschluss	
0 = Lidspalte geschlossen	Beurteilt wird der Zustand der Lidspalte. Mit zunehmender Narkosetiefe wird von einem Schluß der Lidspalte ausgegangen.
1 = Lidspalte halb geöffnet	
2 = Lidspalte geöffnet	
2. Palpebralreflex	
0 = Reflex erloschen	Die Refelexauslösung erfolgt mit einem angefeuchteten Wattetupfer durch Berühren des Lidrandes im medialen Augenwinkel.
1 = Auslösbar mit Lidbewegung	
2 = Auslösbar; mit Kopfbewegung	
3. Pupillenöffnung	
0 = Mydriasis	Beurteilt wird die relative Öffnung der Pupille. Mit zunehmender Narkosetiefe wird eine größere Pupillenöffnung erwertet.
1 = Pupillenöffnung 50 - 75 %	
2 = Miosis	
4. Pupillarreflex	
0 = Reflex erloschen	Beurteilt wird die Geschwindigkeit und das Ausmaß der Pupillenreaktion nach Beleuchten des Augens (Diaskleralkegel, Distanz 0.5cm).
1 = Refex verzögert	
2 = Reflex physiologisch	
5. Kornealreflex	
0 = Reflex erloschen	Die geschlossene Lidspalte wird geöffnet. Beurteilt wird die Reaktion der Nickhaut nach dezentraler Berührung der Hornhaut mit einem angefeuchteten, sterilen Tupfer. Für die Gewichtung des Reflexes ist die Bewegungsgeschwindigkeit der Nickhaut und die Vollständigkeit des Reflexablaufes maßgeblich.
1 = Verzögert auslösbar; langsames, unvollst. Vorziehen der Nickhaut	
2 = Verzögert auslösbar; langsames vollständiges Vorzeichen der Nickhaut	
3 = Reflex physiologisch	
6. Kopflage	
0 = Schlaff herabhängend	Beurteilt wird die Tiefensensibilität durch Lage des herabhängenden Kopfes ohne Einwirken eines speziellen Stimulus.
1 = Leichtes Anheben	
2 = Deutliches Anheben	

7. Nackentonus		
0 =	Nicht vorhanden	Beurteilung der Tiefensensibilität anhand des Muskeltonus durch vorsichtiges Bewegen des Kopfes.
1 =	Vorhanden	
8. Beintonus		
0 =	Nicht vorhanden	Beurteilt wird die Tiefensensibilität anhand des Muskeltonus und von Reaktionen nach passiver Streckung der Gliedmaße (aktives Zurückziehen des Ständers), Maximalreaktion durch zusätzliches Abwehrbewegungen (Flügelschlagen) gekennzeichnet.
1 =	Geringer Tonus	
2 =	Kontraktion	
3 =	Kontraktion & Abwehrbewegung	
9. Pektoralisreflex		
0 =	Reflex erloschen	Beurteilt werden Reaktionen nach Kneifen der Haut zwischen den Ossa pubis mit einem einheitlichen Druch (Spez. Kneifzange) von 0.9 kp/0.5 cm2. Geringgradige Reaktionen sind durch Flügelzittern gekennzeichnet, stärkere Reaktionen durch uneinheitliche Bewegung verschiedener Körperteile,
1 =	Geringe Flügelbewegung	
2 =	Anziehen einzelner Körperteile, Kopfbewegung, ggf. Öffnung der Lider	
3 =	Massive Abwehrbewegungen	
10. Propatagiumreflex		
0 =	Spannhautreflex erloschen	Beurteilt werden Reaktionen nach Kneifen der Flügelspannhaut. Beurteilungskriterien s.o.
1 =	Geringe Flügelbewegungen	
2 =	Anziehen v. Extremitäten, Lidöffnung	
3 =	Massive Abwehrbewegungen	
11. Interphalangealreflex		
0 =	Reflex erloschen	Beurteilt werden Reaktionen nach Kneifen der Zwischenzehenhaut. Beurteilungskriterien s.o.
1 =	Geringes Anziehen der Beine	
2 =	Deutl. Anziehen d. Beine, Lidöffnung	
3 =	Massive Abwehrbewegungen	
12. Kloakalreflex		
0 =	Reflex erloschen	Beurteilt werden Reaktionen nach Kneifen der Perikloakalen Haut. Beurteilungskriterien s.o.
1 =	Kontraktion des Sphinkters, geringgradiges Anziehen der Beine	
2 =	Anziehen einzelner Körperteile, Kopfbewegung, ggf. Öffnung der Lider	
3 =	Massive Abwehrbewegungen	

8.2 Pigeon blood

Summary of hematological data from pigeons is shown in table 8.3. Note that in contrast to human erythrocytes avian red blood cells have a nucleus and are considerably larger.

Table 8.2: Goal reflex score to go for in a surgical tolarance stage in bird anesthesia. Copied and translated from[294]

Parameter	assessment	intended score
1. Lidschluss	0 to 2	0
2. Palpebralreflex	0 to 2	0
3. Pupillenöffnung	0 to 2	1
4. Pupillarreflex	0 to 2	0
5. Kornealreflex	0 to 3	2
6. Kopflage	0 to 2	0
7. Nackentonus	0 to 2	0
8. Beintonus	0 to 2	0
9. Pektoralisreflex	0 to 3	0
10. Propatagiumreflex	0 to 3	0
11. Interphalangealreflex	0 to 3	0
12. Kolakalreflex	0 to 3	0
Sum of reflex scores	0 to 29	3

Table 8.3: Pigeon hematological parameters. Data from[501–503]. Hb: Haemoglobin; HcT: Haematocrit; RBC: red blood cell; WBC: white blood cell; MCV: mean corpuscular volume; MCH: mean corpuscular haemoglobin concentration; RCV: red cell volume

Parameter	Value	Literature
Hb (g/100ml blood)	17.3 ± 2.5	[501,502]
HcT (%)	48.4 ± 5.4	[501,502]
RBC $10^6/\mu$**l blood**	4.1 ± 0.8	[501,502]
WBC $10^6/\mu$**l blood**	4.1 ± 0.8	[501,502]
blood volume (ml/100g bw)	15.7 ± 3.1	[502,503]
total blood volume (ml)	46.9 ± 12.8	[502]
MCV (fl)	201 ± 7	[503]
MCH (pg)	61.1 ± 2	[503]
MCHC (%)	38.5 ± 2.3	[501,503]
RBC cytosome length (µm)	11.7 ± 0.4	[503]
RBC cytosome width (µm)	6.6 ± 0.0	[503]
RBC nucleus length (µm)	6.8 ± 0.3	[503]
RBC nucleus width (µm)	3.3 ± 0.0	[503]
pH of arterial blood	7.43 ± 0.02	[504]
pH of mixed venous blood	7.36 ± 0.01	[504]

8.3 Circulatory hemodynamics

The chapter closely follows[225,505].

The circulatory systems consists of three major constituents: 1) the arteries and distributing vessels, 2) the capillaries and exchange vessels, 3) the veins, which are storage vessels. The arterioles and venules are muscular vessels which control the blood flow distribution. The major arteries bifurcate many times before the capillaries. At each bifurcation vascular resistance is increased. In steady state the volume flow in parent and daughter vessels remains the same, but flow velocity in daughter vessels is about 80% of the parent vessel. The sum of the cross sectional areas of both daughter vessels is therefore increased by about 25%.

The pressure is generated by the cardiac contraction drives blood flow. In steady flow one can relate the volume flow ($\dot{Q}$) to the pressure drop ($P_1 - P_2$) along a tube of radius r and length L:

$$\dot{Q} = (P_1 - P_2)\,\frac{\pi r^4}{8\mu L} = \frac{P_1 - P_2}{R} \tag{8.1}$$

where η is blood viscosity and $R = \frac{8\mu L}{\pi r^4}$ the vascular resistance.

For the whole body this can be expressed as:

$$CO = \frac{MAP - MVP}{TPR} \tag{8.2}$$

with CO: cardiac output, MAP: mean arterial blood pressure, MVP: mean venous pressure and TRP: total peripheral resistance.

The same relation can be applied for cerebral blood flow (CBF):

$$CBF = \frac{CPP}{CVR} = \frac{MAP - ICP}{CVR} \tag{8.3}$$

where the pressure difference CPP (cerebral perfusion pressure) is calculated by the difference between either ICP (intracranial pressure) or JVP (jungular venous pressure) whichever is higher and CVR is the cerebrovascular resistance. For humans CBF is about 15% of CO.

Note that Poiseuille flow is steady state and at least for major arteries the flow is highly pulsatile. Due to inertia of blood flow and high heartbeat frequencies flow amplitude may no longer vary linearly with the pressure gradient in pulsatile flow. The extend of the deviation of poiseuille law to pulsatile flow can be accessed by the dimensionless Womersley number:

$$\alpha = r\sqrt{\frac{2\pi f \rho}{\mu}} \tag{8.4}$$

with r: radius, f: frequency, ρ: blood density and μ: blood viscosity. The phase lag is negligible and the flow agrees approximately with Posiseille's flow when $\alpha < 0.5$

for the fundamental frequency (i.e. heartbeat). Due to the dependence of r this is certainly fulfilled for for smaller arteries. Note that in small capillaries the viscosity cannot be assumed constant anymore.

8.4 Calibration of magnetic field

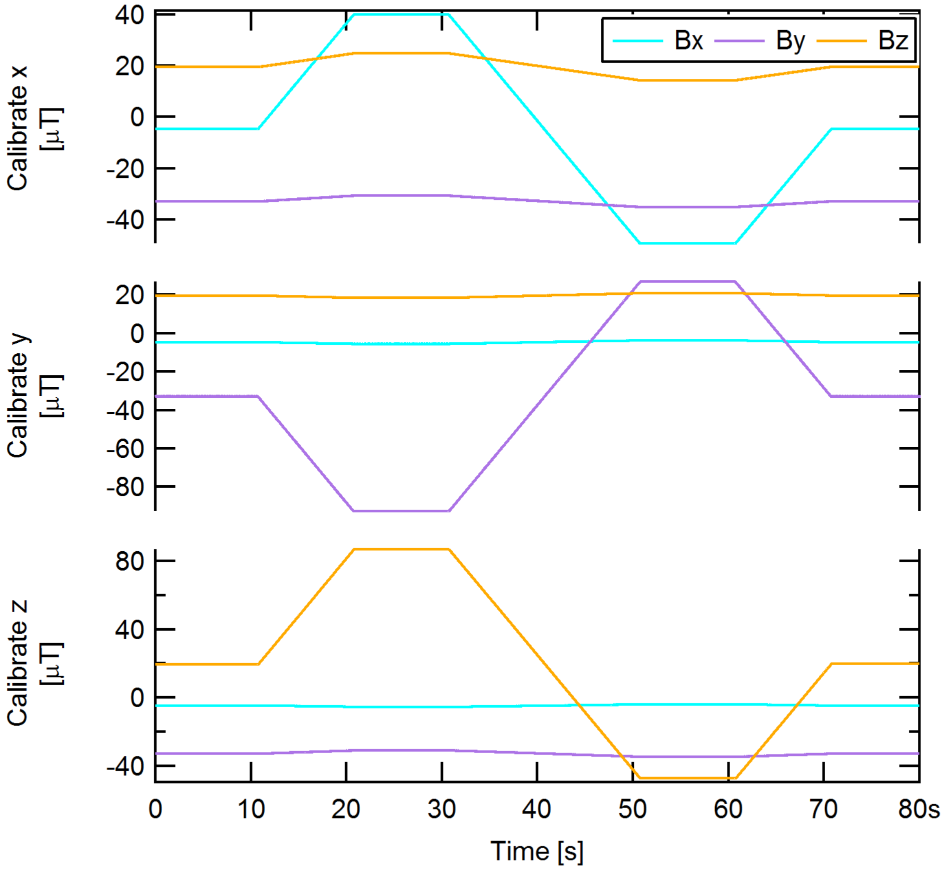

Figure 8.1: Calibration of the magnetic field generated by the 3 Merritt 4 coil system to a change of $\pm 3V$ applied to each axis.

The Calibration for the magnetic field is applied on a regular basis. For the calibration a voltage of $\pm 3V$ is applied to each axis and the response of the axis and the cross talk of the other axis is calculated. From the measurement one can calculate the cross talk matrix to compensate the cross talk. For the calibration shown in figure 8.1 one gets:

$$\begin{pmatrix} 14.848\mu T/V & -0.30037\mu T/V & -0.24725\mu T/V \\ 0.73611\mu T/V & -19.88\mu T/V & 0.62077\mu T/V \\ 1.7515\mu T/V & -0.39321\mu T/V & 22.349\mu T/V \end{pmatrix} \quad (8.5)$$

Note that there is a small hysteresis which can be observed at the end of the measurement.

$$\begin{pmatrix} -0.026159\mu T & 0.011025\mu T & -0.029959\mu T \\ 0.030583\mu T & -0.0036374\mu T & 0.0058482\mu T \\ 0.065922\mu T & 0.020453\mu T & 0.20106\mu T \end{pmatrix} \tag{8.6}$$

Labfield:

$$\begin{pmatrix} -4.7168\mu T \\ -32.894\mu T \\ 19.7\mu T \end{pmatrix} \tag{8.7}$$

8.5 Case report arrhythmia

In one experiment a strange, yet unexplained behavior has been observed. Anesthesia was performed as described in section 3.2.2 with 5mg/kg BW midazolam and isoflurane (maintenance dose: 2.0%). An oscillation in the heart rate

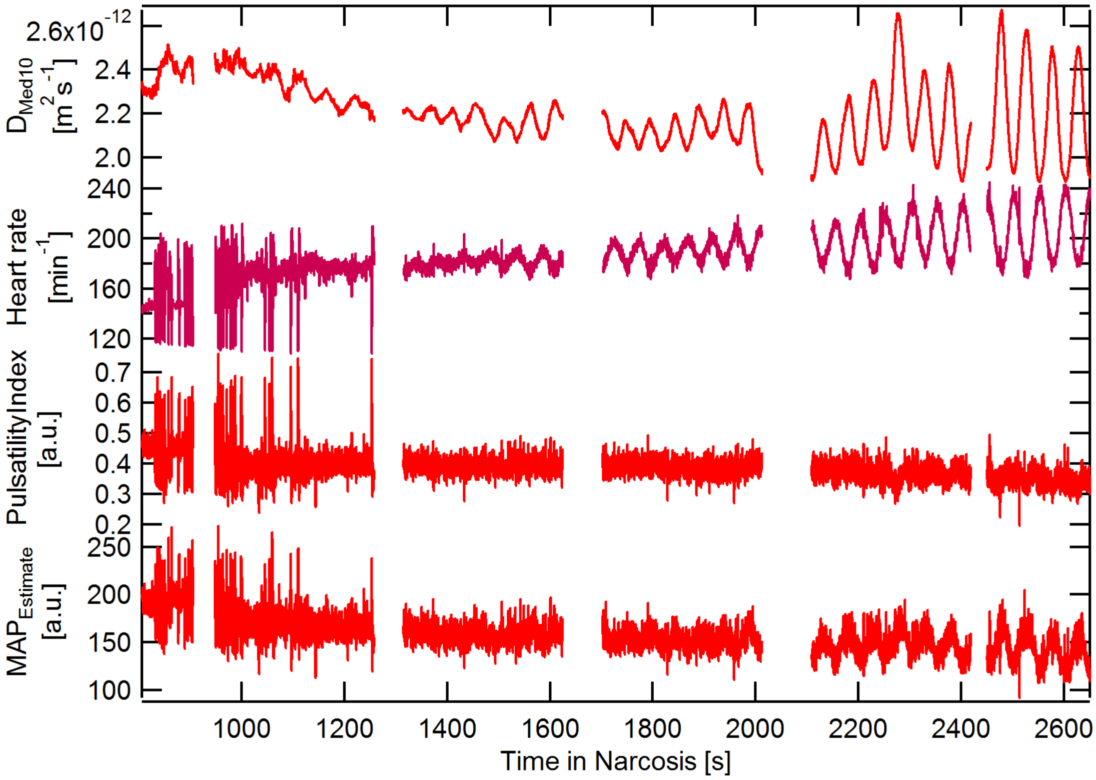

Figure 8.2: The temporal evolution of D_{Med10} (cerebral blood flow), heart rate, DWS Pulsatility Index, and estimate of mean arterial blood pressure are shown. Artifacts with one heart beat is skipped can be seen in the first 300s. This is followed by an oscillation of both the heart rate and the cerebral blood flow with a period of about 50s.

with an increasing amplitude has been observed. In the beginning a “typical” arrhythmia (one heart beat skipped) as described in section 4.1.6 has been observed. After some time an oscillation of the heart rate with a period of about 50s started to show up with an increasing amplitude (see figure 8.2). Note that the period is significantly longer than the breathing rate. No changes in saturation and temperature has been observed.
The 10s median of the cerebral blood flow (D_{Med10}) first shows a correlated behavior with heart rate during the time of the ’typical’ arrhythmia (up to about 1100s), but an anti-correlated behavior during the oscillating heart rate (see figure 8.3).
The DWS pulsatility index (see equation 4.57) is also shown. From the cerebral blood flow and the pulsatility index the mean arterial blood pressure is estimated from equation 4.58. Note that it is not completely clear if the estimate of the MAP is valid under this conditions.

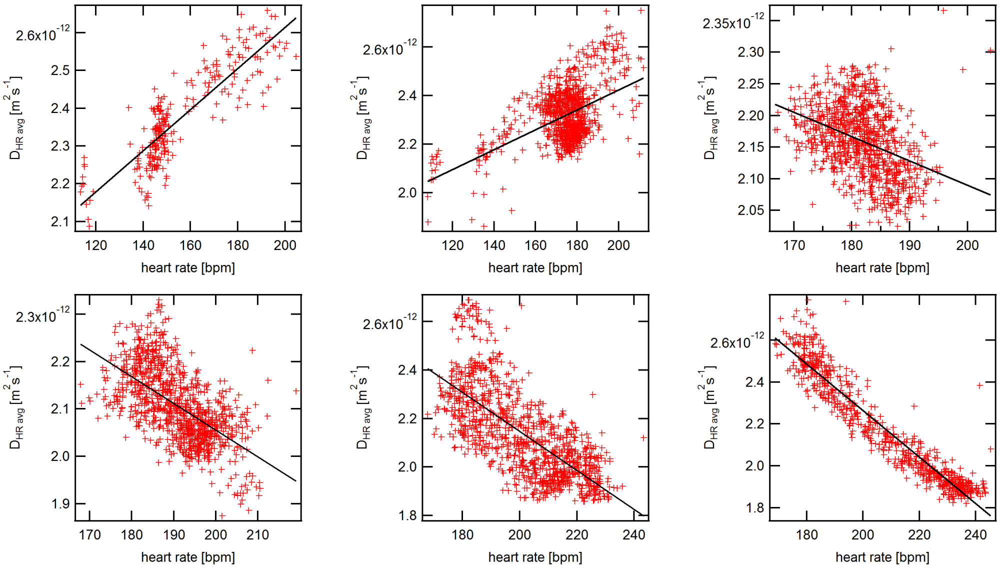

Figure 8.3: The plots show the correlation between heart rate and diffusion coefficient of consecutive measurements from left top to right bottom.
Left top: Correlation: 0.86591; slope: 0.35782; HR is delayed by 0 points
Middle top: Correlation: 0.50872; slope: 0.30755; HR is delayed by 0 points
Right top: Correlation: -0.37693; slope: -0.32397; HR is delayed by 3 points
Left bottom: Correlation: -0.60931; slope: -0.51271; HR is delayed by 3 points
Middle bottom : Correlation: -0.69959; slope: -0.76008; HR is delayed by 3 points
Right bottom: Correlation: -0.95097; slope: -1.0626; HR is delayed by 2 points

If the assumption is true it might give some hint about the origin of the signal: It might be some feedback signal of the blood pressure regulation which resulted in an overshooting reaction. No reference of such an arrhythmia have been found in literature. A definite assignment is not possible without additional measurements of e.g. the blood pressure, ecg, etc. One has to note that this behavior has only been detected once. Therefore the details could not be investigated in more detail.

Nomenclature

μ-XANES	micro-synchrotron x-ray absorption-near-edge-structure spectroscopy
AMPA	α-amino-3-hydroxy-5-methyl-4-isoxazolepropionic acid
AOS	accessory optic system
APD	avalanche photo diode
API	active pharmaceutical ingredient
ASL	arterial spin labeling
BOLD	blood oxygenation level dependent
bpm	beats per minute
bpm	breath per minute
CBF	cerebral blood flow
Cry	cryptochrome
CT	cloacal temperature
DCS	diffuse correlation spectroscopy
DWS	diffusing wave spectroscopy
FAD	flavin adenine dinucleotide
fUS	functional ultrasound
GABA	γ-aminobutyric acid
HA	hyperstriatum accesorium/ hyperpallium apicale
HCN	hyperpolarization-activated cyclic nucleotide-gated
HD	hyperstriatum dorsale/ hyperpallium densocellulare
HIRF	hemodynamic response function
HIS	hypertriatium intercalatus superior/ hyperpallium intercalatum
i.m.	intramuscular
i.n.	intranasal
i.o.	intraosseous
i.p.	intraperitoneal

i.v.	intravenous
IHA	intercalated nucleus of the hyperstriatum/ nucleus interstitialis hyperpallii apicale
Imc	magnocellular nucleus isthmi
Ipc	parvocellular nucleus isthmi
LASCA	laser speckle contrast analysis
LSCI	laser speckle contrast imaging
MAC	minimal alveolar concentration
MAP	mean arterial blood pressure
mg/kg BW	mg per kilogram body weight
MHC II	major histocompatibility complex class II
MRI	magnetic resonance imaging
MSD	mean square displacement
MSPF	mean square phase fluctuations
NaPi	sodium phosphate
NFC	nuclear fast red - used to identify nuclei
NIR	near infrared
NIRS	near infrared spectroscopy
NMDA	N-methyl-D-aspartate
nRt	nucleus rotundus
PB	Prussion blue - labels ferric (Fe^{3+}) iron
PBS	phosphate buffered saline
PFA	paraformaldehyde
SAED	selected area electron diffraction
sc	subcutaneous injection
SLu	nucleus semilunaris
TB	Turnbull's blue - labels ferrous (Fe^{2+}) iron
TEM	transmission electron microscopy
TeO	optic tectum
Trp	tryptophan
VES	ventricular extrasystole
ZENK	acronym for zif268, Egr-1, NGF-1A, Krox-24. ZENK is an immediate early gene which expression is driven by neuronal activity.

Bibliography

[1] Michael D. Shapiro and Eric T. Domyan. Domestic pigeons. *Current Biology*, 23(8):R302–R303, April 2013.

[2] Ilia A Solov'yov. *Magnetoreception mechanisms in birds–towards the discovery of the sixth sense*. PhD thesis, Dissertation, Johann-Wolfgang Goethe Universität Frankfurt am Main, Germany, 2008.

[3] H. L. Yeagley. A preliminary study of a physical basis of bird navigation. *Journal of Applied Physics*, 18(12):1035–1063, 1947.

[4] FW Merkel and W Wiltschko. Magnetismus und Richtungsfinden zugunruhiger Rotkehlchen (Erithacus rubecula). *Vogelwarte*, 23:71–77, 1965.

[5] Wolfgang Wiltschko and Friedrich W Merkel. Orientierung zugunruhiger Rotkehlchen im statischen Magnetfeld. *Verhandlungen der Deutschen Zoologischen Gesellschaft*, 59 (362.367), 1966.

[6] W. Wiltschko. Über den Einfluß statischer Magnetfelder auf die Zugorientierung der Rotkehlchen (Erithacus rubecula). *Zeitschrift fur Tierpsychologie*, 25(5):537–58, August 1968.

[7] W. Wiltschko and R. Wiltschko. Magnetic compass of european robins. *Science*, 176(4030): 62–64, 1972.

[8] W. T. Keeton. Magnetics interfere with pigeon homing. *Proceedings of the National Academy of Sciences of the United States of America*, 68(1):102–106, 1971.

[9] Charles Walcott and R. P. Green. Orientation of homing pigeons altered by a change in direction of an applied magnetic-field. *Science*, 184(4133):180–182, 1974.

[10] Vlastimil Hart, Erich Pascal Malkemper, Tomas Kusta, Sabine Begall, Petra Novakova, Vladimir Hanzal, Lukas Pleskac, Milos Jezek, Richard Policht, Vaclav Husinec, Jaroslav Cerveny, and Hynek Burda. Directional compass preference for landing in water birds. *Frontiers In Zoology*, 10(1):38, July 2013.

[11] R Blakemore. Magnetotactic bacteria. *Science*, 190(4212):377–379, 1975.

[12] Dirk Schueler. Formation of magnetosomes in magnetotactic bacteria. *Journal of Molecular Microbiology and Biotechnology*, 1(1):79–86, 1999.

[13] Dennis A. Bazylinski and Richard B. Frankel. Magnetosome formation in prokaryotes. *Nat Rev Micro*, 2(3):217–230, March 2004.

[14] Dirk Schüler. *Magnetoreception and magnetosomes in bacteria*, volume 3. Springer Science & Business Media, 2006.

[15] Damien Faivre and Dirk Schueler. Magnetotactic bacteria and magnetosomes. *Chemical Reviews*, 108(11):4875–4898, November 2008.

[16] Lei Yan, Shuang Zhang, Peng Chen, Hetao Liu, Huanhuan Yin, and Hongyu Li. Magnetotactic bacteria, magnetosomes and their application. *Microbiological Research*, 167(9):507 – 519, 2012.

[17] Kenneth J. Lohmann, Catherine M. F. Lohmann, Llewellyn M. Ehrhart, Dean A. Bagley, and Timothy Swing. Animal behaviour: Geomagnetic map used in sea-turtle navigation. *Nature*, 428(6986):909–910, April 2004.

[18] Kenneth J. Lohmann, Catherine M. F. Lohmann, and Nathan F. Putman. Magnetic maps in animals: nature's gps. *Journal of Experimental Biology*, 210(21):3697–3705, November 2007.

[19] Nathan F. Putman and Kenneth J. Lohmann. Compatibility of magnetic imprinting and secular variation. *Current Biology*, 18(14):R596–R597, July 2008.

[20] N. F. Putman and K. J. Lohmann. Loggerhead sea turtle migrations and secular variation: Navigating through an ever-changing geomagnetic environment. *Integrative and Comparative Biology*, 51:E113–E113, March 2011.

[21] K. J. Lohmann, N. F. Putman, and C. M. F. Lohmann. Navigating the atlantic ocean with geomagnetic markers: An inherited magnetic map in hatchling loggerhead sea turtles. *Integrative and Comparative Biology*, 52:E108–E108, April 2012.

[22] Kenneth J. Lohmann, Nathan F. Putman, and Catherine M. F. Lohmann. The magnetic map of hatchling loggerhead sea turtles. *Current Opinion In Neurobiology*, 22(2):336–342, April 2012.

[23] J Roger Brothers and Kenneth J Lohmann. Evidence for geomagnetic imprinting and magnetic navigation in the natal homing of sea turtles. *Current Biology*, 25(3):392–396, February 2015.

[24] N. F. Putman, P. Verley, C. S. Endres, and K. J. Lohmann. Magnetic navigation behavior and the oceanic ecology of young loggerhead sea turtles. *Journal of Experimental Biology*, 218(7):1044–1050, April 2015.

[25] Nathan F. Putman, Michelle M. Scanlan, Eric J. Billman, Joseph P. O'Neil, Ryan B. Couture, Thomas P. Quinn, Kenneth J. Lohmann, and David L. G. Noakes. An inherited magnetic map guides ocean navigation in juvenile pacific salmon. *Current Biology*, 24(4): 446–450, February 2014.

[26] Chin-Yuan Hsu, Fu-Yao Ko, Chia-Wei Li, Kuni Fann, and Juh-Tzeng Lue. Magnetoreception system in honeybees (apis mellifera). *Plos One*, 2(4):e395, April 2007.

[27] Martin Vacha. Laboratory behavioural assay of insect magnetoreception: magnetosensitivity of periplaneta americana. *Journal of Experimental Biology*, 209(19):3882–3886, October 2006.

[28] Martin Vacha, Tereza Puzova, and Dana Drstkova. Effect of light wavelength spectrum on magnetic compass orientation in tenebrio molitor. *Journal of Comparative Physiology A-neuroethology Sensory Neural and Behavioral Physiology*, 194(10):853–859, October 2008.

[29] Martin Vacha, Tereza Puzova, and Marketa Kvicalova. Radio frequency magnetic fields disrupt magnetoreception in american cockroach. *Journal of Experimental Biology*, 212 (21):3473–3477, November 2009.

[30] L. C. Boles and K. J. Lohmann. True navigation and magnetic maps in spiny lobsters. *Nature*, 421(6918):60–63, January 2003.

[31] J. H. Wang, S. D. Cain, and K. J. Lohmann. Identifiable neurons inhibited by earth-strength magnetic stimuli in the mollusc tritonia diomedea. *Journal of Experimental Biology*, 207 (6):1043–1049, February 2004.

[32] SD Cain, LC Boles, JH Wang, and KJ Lohmann. Magnetic orientation and navigation in marine turtles, lobsters, and molluscs: Concepts and conundrums. *Integrative and Comparative Biology*, 45(3):539–546, June 2005.

[33] MJ Freake and JB Phillips. Light-dependent shift in bullfrog tadpole magnetic compass orientation: Evidence for a common magnetoreception mechanism in anuran and urodele amphibians. *Ethology*, 111(3):241–254, March 2005.

[34] Francisco J.Javier Diego-Rasilla, Rosa Milagros Luengo, and John B. Phillips. Light-dependent magnetic compass in iberian green frog tadpoles. *Naturwissenschaften*, 97(12): 1077–1088, 2010.

[35] Francisco J. Diego-Rasilla, Rosa M. Luengo, and John B. Phillips. Use of a light-dependent magnetic compass for y-axis orientation in european common frog (rana temporaria) tadpoles. *Journal of Comparative Physiology A-neuroethology Sensory Neural and Behavioral Physiology*, 199(7):619–628, July 2013.

[36] J. B. Phillips. Two magnetoreception pathways in a migratory salamander. *Science*, 233 (4765):765–767, August 1986.

[37] Robert J. Gegear, Amy Casselman, Scott Waddell, and Steven M. Reppert. Cryptochrome mediates light-dependent magnetosensitivity in drosophila. *Nature*, 454(7207):1014–1018, August 2008.

[38] Robert J. Gegear, Lauren E. Foley, Amy Casselman, and Steven M. Reppert. Animal cryptochromes mediate magnetoreception by an unconventional photochemical mechanism. *Nature*, 463(7282):804–807, February 2010.

[39] Andrés Vidal-Gadea, Kristi Ward, Celia Beron, Navid Ghorashian, Sertan Gokce, Joshua Russell, Nicholas Truong, Adhishri Parikh, Otilia Gadea, Adela Ben-Yakar, and Jonathan Pierce-Shimomura. Magnetosensitive neurons mediate geomagnetic orientation in caenorhabditis elegans. *eLife*, 2015.

[40] Patrick A Guerra, Robert J Gegear, and Steven M Reppert. A magnetic compass aids monarch butterfly migration. *Nat Commun*, 5, June 2014.

[41] W Wiltschko and R Wiltschko. Magnetic orientation and magnetoreception in birds and other animals. *Journal of Comparative Physiology A-neuroethology Sensory Neural and Behavioral Physiology*, 191(8):675–693, August 2005.

[42] W Wiltschko, U Munro, H Ford, and R Wiltschko. Red-light disrupts magnetic orientation of migratory birds. *Nature*, 364(6437):525–527, August 1993.

[43] W Wiltschko, U Munro, H Ford, and R Wiltschko. Effect of a magnetic pulse on the orientation of silvereyes, zosterops-l-lateralis, during spring migration. *Journal of Experimental Biology*, 201(23):3257–3261, December 1998.

[44] W Wiltschko, R Wiltschko, and U Munro. Light dependent magnetoreception in birds: the effect of intensity of 565-nm green light. *Naturwissenschaften*, 87(8):366–369, August 2000.

[45] W. Wiltschko, U. Munro, R. Wiltschko, and J. L. Kirschvink. Magnetite-based magnetoreception in birds: the effect of a biasing field and a pulse on migratory behavior. *Journal of Experimental Biology*, 205(19):3031–3037, October 2002.

[46] Wolfgang Wiltschko, Ursula Munro, Hugh Ford, and Roswitha Wiltschko. Avian orientation: the pulse effect is mediated by the magnetite receptors in the upper beak. *Proceedings of the Royal Society B-biological Sciences*, 276(1665):2227–2232, June 2009.

[47] W. Wiltschko and R. Wiltschko. Migratory orientation - magnetic compass orientation of garden warblers (sylvia-borin) after a simulated crossing of the magnetic equator. *Ethology*, 91(1):70–74, May 1992.

[48] R Rappl, R Wiltschko, P Weindler, P Berthold, and W Wiltschko. Orientation behavior of garden warblers (sylvia borin) under monochromatic light of various wavelengths. *Auk*, 117(1):256–260, January 2000.

[49] Christine Maira Hein, Manuela Zapka, Dominik Heyers, Sandra Kutzschbauch, Nils-Lasse Schneider, and Henrik Mouritsen. Night-migratory garden warblers can orient with their magnetic compass using the left, the right or both eyes. *Journal of The Royal Society Interface*, 7(Suppl. 2):S227–S233, April 2010.

[50] Kirill Kavokin, Nikita Chernetsov, Alexander Pakhomov, Julia Bojarinova, Dmitry Kobylkov, and Barot Namozov. Magnetic orientation of garden warblers (sylvia borin) under 1.4 mhz radiofrequency magnetic field. *Journal of the Royal Society Interface*, 11 (97):20140451, August 2014.

[51] W Beck and W Wiltschko. Magnetic factors control the migratory direction of pied flycatchers (ficedula hypoleuca pallas). *Acta XIX Congr. Intern. Ornithol*, 2:1955–1962, 1988.

[52] Sabine Begall, Hynek Burda, and Pascal Malkemper. Magnetoreception in mammals. *Advances in the study of behavior*, 46:45–88, 2014.

[53] S. Marhold, W. Wiltschko, and H. Burda. A magnetic polarity compass for direction finding in a subterranean mammal. *Naturwissenschaften*, 84(9):421–423, September 1997.

[54] Richard A. Holland, Kasper Thorup, Maarten J. Vonhof, William W. Cochran, and Martin Wikelski. Navigation - bat orientation using earth's magnetic field. *Nature*, 444(7120): 702–702, December 2006.

[55] Richard A. Holland. Orientation and navigation in bats: known unknowns or unknown unknowns? *Behavioral Ecology and Sociobiology*, 61(5):653–660, March 2007.

[56] Sabine Begall, Jaroslav Cerveny, Julia Neef, Oldrich Vojtech, and Hynek Burda. Magnetic alignment in grazing and resting cattle and deer. *Proceedings of the National Academy of Sciences of the United States of America*, 105(36):13451–13455, September 2008.

[57] P. Slaby, K. Tomanova, and M. Vacha. Cattle on pastures do align along the north-south axis, but the alignment depends on herd density. *Journal of Comparative Physiology A-neuroethology Sensory Neural and Behavioral Physiology*, 199(8):695–701, August 2013.

[58] Jaroslav Cerveny, Sabine Begall, Petr Koubek, Petra Novakova, and Hynek Burda. Directional preference may enhance hunting accuracy in foraging foxes. *Biology Letters*, 7(3): 355–357, June 2011.

[59] Dorothee Kremers, Juliana Lopez Marulanda, Martine Hausberger, and Alban Lemasson. Behavioural evidence of magnetoreception in dolphins: detection of experimental magnetic fields. *Naturwissenschaften*, 101(11):907–911, 2014.

[60] R. R. Baker. Human navigation and magnetoreception - the manchester experiments do replicate. *Animal Behaviour*, 35:691–704, June 1987.

[61] R. R. Baker. Human magnetoreception for navigation. *Progress in clinical and biological research*, 257:63–80, 1988.

[62] R. R. Baker. Human navigation influence of blindfolds on involvement of magnetoreception. *Lieth, H. (ed.). Progress In Biometeorology, Vol. 8. Effects of Atmospheric and Geophysical Variables In Biology and Medicine; International Symposium, Stockholm, Sweden, May 31-june 3, 1989. Vii+141p. Spb Academic Publishing: the Hague, Netherlands. Illus. Paper*, pages 67–79, 1991.

[63] F Thoss, B Bartsch, B Fritzsche, D Tellschaft, and M Thoss. The magnetic field sensitivity of the human visual system shows resonance and compass characteristic. *Journal of Comparative Physiology A-sensory Neural and Behavioral Physiology*, 186(10):1007–1010, October 2000.

[64] F Thoss, B Bartsch, D Tellschaft, and M Thoss. The light sensitivity of the human visual system depends on the direction of view. *Journal of Comparative Physiology A-neuroethology Sensory Neural and Behavioral Physiology*, 188(3):235–237, April 2002.

[65] F Thoss and B Bartsch. The human visual threshold depends on direction and strength of a weak magnetic field. *Journal of Comparative Physiology A-neuroethology Sensory Neural and Behavioral Physiology*, 189(10):777–779, October 2003.

[66] S. Carrubba, II Frilot, C., Jr. Chesson, A. L., and A. A. Marino. Evidence of a nonlinear human magnetic sense. *Neuroscience*, 144(1):356–367, January 2007.

[67] Gustav Kramer. Wird die Sonnenhöhe bei der Heimfindeorientierung verwertet? *Journal of Ornithology*, 94(3):201–219, 1953.

[68] Gustav Kramer. Experiments on bird orientation and their interpretation. *Ibis*, 99(2): 196–227, 1957.

[69] R. A. Holland. True navigation in birds: from quantum physics to global migration. *Journal of Zoology*, 293(1):1–15, May 2014.

[70] G Kramer. Die sonnenorientierung der vögel. *Verh Dtsch Zool Ges*, 1:77–84, 1952.

[71] Tim Guilford and Dora Biro. Route following and the pigeon's familiar area map. *Journal of Experimental Biology*, 217(2):169–179, January 2014.

[72] Klaus Schmidt-König. Experimentelle Einflußnahme auf die 24-Stunden-Periodik bei Brieftauben und deren Auswirkungen unter besonderer Berücksichtigung des Heimfindevermögens. *Zeitschrift für Tierpsychologie*, 15(3):301–331, 1958.

[73] Klaus Schmidt-König. Sun azimuth compass - one factor in the orientation of homing pigeons. *Science*, 131(3403):826–828, 1960.

[74] Klaus Schmidt-König, J. U. Ganzhorn, and R. Ranvaud. Orientation in birds. the sun compass. *Experientia Supplementum*, 60:1–15, 1991.

[75] S. T. Emlen. Celestial rotation - its importance in development of migratory orientation. *Science*, 170(3963):1198–1201, 1970.

[76] J. T. Hagstrum. Infrasound and the avian navigational map. *Journal of Experimental Biology*, 203(7):1103–1111, April 2000.

[77] J. T. Hagstrum. Infrasound and the avian navigational map. *Journal of Navigation*, 54(3): 377–391, September 2001.

[78] Jonathan T. Hagstrum. Atmospheric propagation modeling indicates homing pigeons use loft-specific infrasonic 'map' cues. *Journal of Experimental Biology*, 216(4):687–699, February 2013.

[79] HP Lipp, AL Vyssotski, DP Wolfer, S Renaudineau, M Savini, G Troster, and G Dell'Omo. Pigeon homing along highways and exits. *Current Biology*, 14(14):1239–1249, July 2004.

[80] F Papi, L Fiore, V Fiaschi, and S Benvenuti. Olfaction and homing in pigeons. *Monitore Zoologico Italiano*, 6(1):85–95, 1972.

[81] HG Wallraff. Avian olfactory navigation: its empirical foundation and conceptual state. *Animal Behaviour*, 67(Part 2):189–204, February 2004.

[82] H. G. Wallraff. Beyond familiar landmarks and integrated routes: goal-oriented navigation by birds. *Connection Science*, 17(1-2):91–106, 2005.

[83] H. G. Wallraff. Ratios among atmospheric trace gases together with winds imply exploitable information for bird navigation: a model elucidating experimental results. *Biogeosciences*, 10(11):6929–6943, 2013.

[84] Anna Gagliardo. Forty years of olfactory navigation in birds. *Journal of Experimental Biology*, 216(12):2165–2171, June 2013.

[85] Hans G. Wallraff. Do olfactory stimuli provide positional information for home-oriented avian navigation? *Animal Behaviour*, 90:E1–E6, April 2014.

[86] Hans G. Wallraff. An amazing discovery: bird navigation based on olfaction. *Journal of Experimental Biology*, 218(10):1464–1466, May 2015.

[87] Paulo E. Jorge, Alice E. Marques, and John B. Phillips. Activational rather than navigational effects of odors on homing of young pigeons. *Current Biology*, 19(8):650–654, April 2009.

[88] Paulo E. Jorge, Paulo A. M. Marques, and John B. Phillips. Activational effects of odours on avian navigation. *Proceedings of the Royal Society B-biological Sciences*, 277(1678):45–49, January 2010.

[89] K. Dornfeldt. Pigeon homing in relation to geomagnetic, gravitational, topographical, and meteorological conditions. *Behavioral Ecology and Sociobiology*, 28(2):107–123, 1991.

[90] Nicole Blaser, Sergei I. Guskov, Virginia Meskenaite, Valerii A. Kanevskyi, and Hans-Peter Lipp. Altered orientation and flight paths of pigeons reared on gravity anomalies: A gps tracking study. *Plos One*, 8(10):e77102, October 2013.

[91] Nicole Blaser, Sergei I Guskov, Vladimir A Entin, David P Wolfer, Valeryi A Kanevskyi, and Hans-Peter Lipp. Gravity anomalies without geomagnetic disturbances interfere with pigeon homing–a gps tracking study. *The Journal of experimental biology*, 217(22):4057–4067, 2014.

[92] Wolfgang Wiltschko and Roswitha Wiltschko. Magnetoreception in birds: two receptors for two different tasks. *Journal of Ornithology*, 148(Suppl. 1):S61–S76, December 2007.

[93] A. Chulliat, S. Macmillan, P. Alken, C. Beggan, M. Nair, B. Hamilton, A. Woods, V. Ridley, S. Maus, and A. Thomson. The us/uk world magnetic model for 2015-2020, 2014.

[94] Gerta Fleissner, Guenther Fleissner, Branko Stahl, and Gerald Falkenberg. Iron-mineral-based magnetoreception in birds: the stimulus conducting system. *Journal of Ornithology*, 148:S643–S648, December 2007.

[95] Roswitha Wiltschko and Wolfgang Wiltschko. Sensing magnetic directions in birds: radical pair processes involving cryptochrome. *Biosensors*, 4(3):221–242, 2014.

[96] W Wiltschko and R Wiltschko. Magnetic orientation in birds. *Journal of Experimental Biology*, 199(1):29–38, January 1996.

[97] Nele Lefeldt, David Dreyer, Nils-Lasse Schneider, Friederike Steenken, and Henrik Mouritsen. Migratory blackcaps tested in emlen funnels can orient at 85 degrees but not at 88 degrees magnetic inclination. *Journal of Experimental Biology*, 218(2):206–211, January 2015.

[98] S. Akesson, J. Morin, R. Muheim, and U. Ottosson. Avian orientation at steep angles of inclination: experiments with migratory white-crowned sparrows at the magnetic north pole. *Proceedings of the Royal Society B-biological Sciences*, 268(1479):1907–1913, September 2001.

[99] Charles Walcott, J. L. Gould, and J. L. Kirschvink. Pigeons have magnets. *Science*, 205 (4410):1027–1029, 1979.

[100] JL Kirschvink. The horizontal magnetic dance of the honeybee is compatible with a single-domain ferromagnetic magnetoreceptor. *Biosystems*, 14(2):193–203, 1981.

[101] JL Kirschvink, MM Walker, and CE Diebel. Magnetite-based magnetoreception. *Current Opinion in Neurobiology*, 11(4):462–467, August 2001.

[102] RC Beason. Mechanisms of magnetic orientation in birds. *Integrative and Comparative Biology*, 45(3):565–573, June 2005.

[103] Ilia A. Solov'yov and Walter Greiner. Micromagnetic insight into a magnetoreceptor in birds: Existence of magnetic field amplifiers in the beak. *Physical Review E*, 80(4, Part 1), October 2009.

[104] Michael Winklhofer and Joseph L. Kirschvink. A quantitative assessment of torque-transducer models for magnetoreception. *Journal of The Royal Society Interface*, 7(Suppl. 2):S273–S289, April 2010.

[105] Valera P. Shcherbakov and Michael Winklhofer. Theoretical analysis of flux amplification by soft magnetic material in a putative biological magnetic-field receptor. *Physical Review E*, 81(3, Part 1), March 2010.

[106] Herve Cadiou and Peter A. McNaughton. Avian magnetite-based magnetoreception: a physiologist's perspective. *Journal of The Royal Society Interface*, 7(Suppl. 2):S193–S205, April 2010.

[107] R. Wiltschko and W. Wiltschko. The magnetite-based receptors in the beak of birds and their role in avian navigation. *Journal of Comparative Physiology A-neuroethology Sensory Neural and Behavioral Physiology*, 199(2):89–98, February 2013.

[108] Gerta Fleissner, Branko Stahl, Peter Thalau, Gerald Falkenberg, and Guenther Fleissner. A novel concept of fe-mineral-based magnetoreception: histological and physicochemical data from the upper beak of homing pigeons. *Naturwissenschaften*, 94(8):631–642, August 2007.

[109] Gerald Falkenberg, Gerta Fleissner, Kirsten Schuchardt, Markus Kuehbacher, Peter Thalau, Henrik Mouritsen, Dominik Heyers, Gerd Wellenreuther, and Guenther Fleissner. Avian magnetoreception: Elaborate iron mineral containing dendrites in the upper beak seem to be a common feature of birds. *Plos One*, 5(2), February 2010.

[110] G Fleissner, E Holtkamp-Rotzler, M Hanzlik, M Winklhofer, G Fleissner, N Petersen, and W Wiltschko. Ultrastructural analysis of a putative magnetoreceptor in the beak of homing pigeons. *Journal of Comparative Neurology*, 458(4):350–360, April 2003.

[111] P Semm and RC Beason. Responses to small magnetic variations by the trigeminal system of the bobolink. *Brain Research Bulletin*, 25(5):735–740, November 1990.

[112] RC Beason and P Semm. Magnetic responses of the trigeminal nerve system of the bobolink (dolichonyx-oryzivorus). *NEUROSCIENCE LETTERS*, 80(2):229–234, September 1987.

[113] P Semm and RC Beason. Sensory basis of bird orientation. *Experientia*, 46(4):372–378, April 1990.

[114] Le-Qing Wu and J. David Dickman. Neural correlates of a magnetic sense. *Science*, 336 (6084):1054–1057, May 2012.

[115] Henrik Mouritsen and P. J. Hore. The magnetic retina: light-dependent and trigeminal magnetoreception in migratory birds. *Current Opinion In Neurobiology*, 22(2):343–352, April 2012.

[116] Manuela Zapka, Dominik Heyers, Christine M. Hein, Svenja Engels, Nils-Lasse Schneider, Joerg Hans, Simon Weiler, David Dreyer, Dmitry Kishkinev, J. Martin Wild, and Henrik Mouritsen. Visual but not trigeminal mediation of magnetic compass information in a migratory bird. *Nature*, 461(7268):1274–U108, October 2009.

[117] RC Beason and P Semm. Does the avian ophthalmic nerve carry magnetic navigational information? *Journal of Experimental Biology*, 199(5):1241–1244, May 1996.

[118] Dmitry Kishkinev, Nikita Chernetsov, Dominik Heyers, and Henrik Mouritsen. Migratory reed warblers need intact trigeminal nerves to correct for a 1,000 km eastward displacement. *Plos One*, 8(6):e65847, June 2013.

[119] A. Gagliardo, P. Ioale, M. Savini, and J. M. Wild. Having the nerve to home: trigeminal magnetoreceptor versus olfactory mediation of homing in pigeons. *Journal of Experimental Biology*, 209(15):2888–2892, August 2006.

[120] Anna Gagliardo, Paolo Ioale, Maria Savini, and Martin Wild. Navigational abilities of homing pigeons deprived of olfactory or trigeminally mediated magnetic information when young. *Journal of Experimental Biology*, 211(13):2046–2051, July 2008.

[121] Anna Gagliardo, Paolo Ioale, Maria Savini, and Martin Wild. Navigational abilities of adult and experienced homing pigeons deprived of olfactory or trigeminally mediated magnetic information. *Journal of Experimental Biology*, 212(19):3119–3124, October 2009.

[122] CV Mora, M Davison, JM Wild, and MM Walker. Magnetoreception and its trigeminal mediation in the homing pigeon. *Nature*, 432(7016):508–511, November 25 2004.

[123] Cordula V. Mora and Verner P. Bingman. Detection of magnetic field intensity gradient by homing pigeons (columba livia) in a novel ”virtual magnetic map” conditioning paradigm. *Plos One*, 8(9):e72869, September 2013.

[124] C. V. Mora, M. L. Acerbi, and V. P. Bingman. Conditioned discrimination of magnetic inclination in a spatial-orientation arena task by homing pigeons (columba livia). *Journal of Experimental Biology*, 217(23):4123–4131, December 2014.

[125] Peter Thalau, Elke Holtkamp-Roetzler, Gerta Fleissner, and Wolfgang Wiltschko. Homing pigeons (columba livia f. domestica) can use magnetic cues for locating food. *Naturwissenschaften*, 94(10):813–819, October 2007.

[126] R Wiltschko and W Wiltschko. Magnetoreception: Why is conditioning so seldom successful? *Naturwissenschaften*, 83(6):241–247, June 1996.

[127] D. Kishkinev, H. Mouritsen, and C. V. Mora. An attempt to develop an operant conditioning paradigm to test for magnetic discrimination behavior in a migratory songbird. *Journal of Ornithology*, 153(4):1165–1177, October 2012.

[128] Dominik Heyers, Manuela Zapka, Mara Hoffmeister, John Martin Wild, and Henrik Mouritsen. Magnetic field changes activate the trigeminal brainstem complex in a migratory bird. *Proceedings of the National Academy of Sciences of the United States of America*, 107(20): 9394–9399, May 2010.

[129] Nele Lefeldt, Dominik Heyers, Nils-Lasse Schneider, Svenja Engels, Dana Elbers, and Henrik Mouritsen. Magnetic field-driven induction of zenk in the trigeminal system of pigeons (columba livia). *Journal of the Royal Society, Interface / the Royal Society*, 11(100), November 2014.

[130] R. C. Beason and J. E. Nichols. Magnetic orientation and magnetically sensitive material in a transequatorial migratory bird. *Nature*, 309(5964):151–153, 1984.

[131] RC Beason and WJ Brennan. Natural and induced magnetization in the bobolink, dolichonyx-oryzivorus (aves, icteridae). *Journal of Experimental Biology*, 125:49–56, September 1986.

[132] M. N. Williams and J. M. Wild. Trigeminally innervated iron-containing structures in the beak of homing pigeons, and other birds. *Brain Research*, 889(1-2):243–246, January 2001.

[133] Lanxiang Tian, Bo Xiao, Wei Lin, Shuyi Zhang, Rixiang Zhu, and Yongxin Pan. Testing for the presence of magnetite in the upper-beak skin of homing pigeons. *Biometals*, 20(2): 197–203, April 2007.

[134] E Holtkamp-Rötzler, G Fleissner, M Hanzlik, W Wiltschko, and N Petersen. Mechanoreceptors in the upper beak of homing pigeons (columba livia) as putative structural candidates for magnetoreception. *Verh. dt. zool. Ges*, 90:290, 1997.

[135] M. Hanzlik, C. Heunemann, E. Holtkamp-Rotzler, M. Winklhofer, N. Petersen, and G. Fleissner. Superparamagnetic magnetite in the upper beak tissue of homing pigeons. *Biometals*, 13(4):325–331, December 2000.

[136] M Winklhofer, E Holtkamp-Rotzler, M Hanzlik, G Fleissner, and N Petersen. Clusters of superparamagnetic magnetite particles in the upper-beak skin of homing pigeons: evidence of a magnetoreceptor? *European Journal of Mineralogy*, 13(4):659–669, July-August 2001.

[137] AF Davila, G Fleissner, M Winklhofer, and N Petersen. A new model for a magnetoreceptor in homing pigeons based on interacting clusters of superparamagnetic magnetite. *Physics and Chemistry of the Earth*, 28(16-19):647–652, 2003.

[138] Branko Stahl, Gerta Fleissner, Gunther Fleissner, and Elisabeth Holub-Krappe. Micromagnetic aspects of magnetoreception of homing pigeons based on iron minerals. *X-Ray Absorption Fine Structure–XAFS 13*, 882:755–757, 2007.

[139] Michael Winklhofer and Joseph L Kirschvink. Does avian magnetoreception rely on both magnetite and maghemite? *arXiv preprint arXiv:0805.2249*, 2008.

[140] Christoph Daniel Treiber, Marion Claudia Salzer, Johannes Riegler, Nathaniel Edelman, Cristina Sugar, Martin Breuss, Paul Pichler, Herve Cadiou, Martin Saunders, Mark Lythgoe, Jeremy Shaw, and David Anthony Keays. Clusters of iron-rich cells in the upper beak of pigeons are macrophages not magnetosensitive neurons. *Nature*, 484(7394):367–U102, April 2012.

[141] Christoph Daniel Treiber, Marion Salzer, Martin Breuss, Lyubov Ushakova, Mattias Lauwers, Nathaniel Edelman, and David Anthony Keays. High resolution anatomical mapping confirms the absence of a magnetic sense system in the rostral upper beak of pigeons. *Communicative & integrative biology*, 6(4):e24859–e24859, July 2013.

[142] Henrik Mouritsen. Sensory biology search for the compass needles. *Nature*, 484(7394): 320–321, April 2012.

[143] Christine Nießner. *Feinstrukturelle und immunhistologische Charakterisierung potenzieller Rezeptoren der Magnetsinnesorgane von Vögeln.* PhD thesis, Univ.-Bibliothek, 2013.

[144] Y. Harada, M. Taniguchi, H. Namatame, and A. Iida. Magnetic materials in otoliths of bird and fish lagena and their function. *Acta Oto-laryngologica*, 121(5):590–595, July 2001.

[145] Le-Qing Wu and J. David Dickman. Magnetoreception in an avian brain in part mediated by inner ear lagena. *Current Biology*, 21(5):418–423, March 2011.

[146] Yasuo Harada. The relation between the migration function of birds and fishes and their lagenal function. *Acta Oto-laryngologica*, 128(4):432–439, 2008.

[147] Ying Zhao, Yi-Na Huang, Lv Shi, and Lin Chen. Analysis of magnetic elements in otoliths of the macula lagena in homing pigeons with inductively coupled plasma mass spectrometry. *Neuroscience bulletin*, 25(3):101–108, 2009.

[148] Mattias Lauwers, Paul Pichler, Nathaniel Bernard Edelman, Guenter Paul Resch, Lyubov Ushakova, Marion Claudia Salzer, Dominik Heyers, Martin Saunders, Jeremy Shaw, and David Anthony Keays. An iron-rich organelle in the cuticular plate of avian hair cells. *Current Biology*, 23(10):924–929, May 2013.

[149] Nathaniel B. Edelman, Tanja Fritz, Simon Nimpf, Paul Pichler, Mattias Lauwers, Robert W. Hickman, Artemis Papadaki-Anastasopoulou, Lyubov Ushakova, Thomas Heuser, Guenter P. Resch, Martin Saunders, Jeremy A. Shaw, and David A. Keays. No evidence for intracellular magnetite in putative vertebrate magnetoreceptors identified by magnetic screening. *Proceedings of the National Academy of Sciences*, 2014.

[150] Stephan H. K. Eder, Herve Cadiou, Airina Muhamad, Peter A. McNaughton, Joseph L. Kirschvink, and Michael Winklhofer. Magnetic characterization of isolated candidate vertebrate magnetoreceptor cells. *Proceedings of the National Academy of Sciences of the United States of America*, 109(30):12022–12027, July 2012.

[151] J David Dickman and Qian Fang. Differential central projections of vestibular afferents in pigeons. *The Journal of comparative neurology*, 367(1):110–131, 1996.

[152] Dale C. Roberts, Vincenzo Marcelli, Joseph S. Gillen, John P. Carey, Charles C. Della Santina, and David S. Zee. Mri magnetic field stimulates rotational sensors of the brain. *Current Biology*, 21(19):1635–1640, October 2011.

[153] K. Schulten, C. E. Swedberg, and A. Weller. Biomagnetic sensory mechanism based on magnetic-field modulated coherent electron-spin motion. *Zeitschrift Fur Physikalische Chemie-frankfurt*, 111(1):1–5, 1978.

[154] T Ritz, S Adem, and K Schulten. A model for photoreceptor-based magnetoreception in birds. *Biophysical Journal*, 78(2):707–718, February 2000.

[155] Thorsten Ritz. Quantum effects in biology: bird navigation. *Procedia Chemistry*, 3(1): 262–275, 2011.

[156] Bao-Ming Xu, Jian Zou, Jun-Gang Li, and Bin Shao. Estimating the hyperfine coupling parameters of the avian compass by comprehensively considering the available experimental results. *Physical Review E*, 88(3):032703, September 2013.

[157] Christopher T. Rodgers and P. J. Hore. Chemical magnetoreception in birds: The radical pair mechanism. *Proceedings of the National Academy of Sciences of the United States of America*, 106(2):353–360, January 2009.

[158] Ilia A. Solov'yov, Henrik Mouritsen, and Klaus Schulten. Acuity of a cryptochrome and vision-based magnetoreception system in birds. *Biophysical Journal*, 99(1):40–49, July 2010.

[159] Jason C. S. Lau, Nicola Wagner-Rundell, Christopher T. Rodgers, Nicholas J. B. Green, and P. J. Hore. Effects of disorder and motion in a radical pair magnetoreceptor. *Journal of The Royal Society Interface*, 7(Suppl. 2):S257–S264, April 2010.

[160] Erin Hill and Thorsten Ritz. Can disordered radical pair systems provide a basis for a magnetic compass in animals? *Journal of The Royal Society Interface*, 7(Suppl. 2):S265–S271, April 2010.

[161] Jason C. S. Lau, Christopher T. Rodgers, and P. J. Hore. Compass magnetoreception in birds arising from photo-induced radical pairs in rotationally disordered cryptochromes. *Journal of the Royal Society Interface*, 9(77):3329–3337, December 2012.

[162] H Mouritsen, U Janssen-Bienhold, M Liedvogel, G Feenders, J Stalleicken, P Dirks, and R Weiler. Cryptochromes and neuronal-activity markers colocalize in the retina of migratory birds during magnetic orientation. *Proceedings of the National Academy of Sciences of the United States of America*, 101(39):14294–14299, September 2004.

[163] A Moller, S Sagasser, W Wiltschko, and B Schierwater. Retinal cryptochrome in a migratory passerine bird: a possible transducer for the avian magnetic compass. *Naturwissenschaften*, 91(12):585–588, December 2004.

[164] Christine Nießner, Susanne Denzau, Julia Christina Gross, Leo Peichl, Hans-Joachim Bischof, Gerta Fleissner, Wolfgang Wiltschko, and Roswitha Wiltschko. Avian ultraviolet/violet cones identified as probable magnetoreceptors. *Plos One*, 6(5):e20091, May 2011.

[165] Christine Nießner, Susanne Denzau, Katrin Stapput, Margaret Ahmad, Leo Peichl, Wolfgang Wiltschko, and Roswitha Wiltschko. Magnetoreception: activated cryptochrome 1a concurs with magnetic orientation in birds. *Journal of the Royal Society, Interface / the Royal Society*, 10(88):20130638–20130638, August 2013.

[166] Christine Nießner, Susanne Denzau, Leo Peichl, Wolfgang Wiltschko, and Roswitha Wiltschko. Magnetoreception in birds: I. immunohistochemical studies concerning the cryptochrome cycle. *Journal of Experimental Biology*, 217(23):4221–4224, December 2014.

[167] Miriam Liedvogel and Henrik Mouritsen. Cryptochromes-a potential magnetoreceptor: what do we know and what do we want to know? *Journal of The Royal Society Interface*, 7(Suppl. 2):S147–S162, April 2010.

[168] Ines Chaves, Richard Pokorny, Martin Byrdin, Nathalie Hoang, Thorsten Ritz, Klaus Brettel, Lars-Oliver Essen, Gijsbertus T. J. van der Horst, Alfred Batschauer, and Margaret Ahmad. The cryptochromes: Blue light photoreceptors in plants and animals. *Annual Review of Plant Biology, Vol 62*, 62:335–364, 2011.

[169] Pavel Mueller and Margaret Ahmad. Light-activated cryptochrome reacts with molecular oxygen to form a flavin-superoxide radical pair consistent with magnetoreception. *Journal of Biological Chemistry*, 286(24):21033–21040, June 2011.

[170] J. Wang, X. L. Du, W. S. Pan, X. J. Wang, and W. J. Wu. Photoactivation of the cryptochrome/photolyase superfamily. *Journal of Photochemistry and Photobiology C-photochemistry Reviews*, 22:84–102, March 2015.

[171] Till Biskup, Erik Schleicher, Asako Okafuji, Gerhard Link, Kenichi Hitomi, Elizabeth D. Getzoff, and Stefan Weber. Direct observation of a photoinduced radical pair in a cryptochrome blue-light photoreceptor. *Angewandte Chemie-international Edition*, 48(2):404–407, 2009.

[172] Till Biskup. Time-resolved epr of radical pair intermediates in cryptochromes. *Molecular Physics*, 111(24):3698–3703, December 2013.

[173] T Ritz. Disrupting magnetic compass orientation with radio frequency oscillating fields. *Orientation and navigation—birds, humans and other animals*, 2001.

[174] KB Henbest, P Kukura, CT Rodgers, PJ Hore, and CR Timmel. Radio frequency magnetic field effects on a radical recombination reaction: A diagnostic test for the radical pair mechanism. *Journal of the American Chemical Society*, 126(26):8102–8103, July 2004.

[175] Wolfgang Wiltschko, Roswitha Wiltschko, and Thorsten Ritz. The mechanism of the avian magnetic compass. *Procedia Chemistry*, 3(1):276–284, 2011.

[176] R. Wiltschko and W. Wiltschko. Pigeon homing: Effect of various wavelengths of light during displacement. *Naturwissenschaften*, 85(4):164–167, April 1998.

[177] R Muheim, J Backman, and S Akesson. Magnetic compass orientation in european robins is dependent on both wavelength and intensity of light. *Journal of Experimental Biology*, 205(24):3845–3856, December 2002.

[178] Wolfgang Wiltschko, Rafael Freire, Ursula Munro, Thorsten Ritz, Lesley Rogers, Peter Thalau, and Roswitha Wiltschko. The magnetic compass of domestic chickens, gallus gallus. *Journal of Experimental Biology*, 210(13):2300–2310, July 2007.

[179] Roswitha Wiltschko, Katrin Stapput, Peter Thalau, and Wolfgang Wiltschko. Directional orientation of birds by the magnetic field under different light conditions. *Journal of The Royal Society Interface*, 7(Suppl. 2):S163–S177, April 2010.

[180] T Ritz, P Thalau, JB Phillips, R Wiltschko, and W Wiltschko. Resonance effects indicate a radical-pair mechanism for avian magnetic compass. *Nature*, 429(6988):177–180, May 2004.

[181] Thorsten Ritz, Roswitha Wiltschko, P. J. Hore, Christopher T. Rodgers, Katrin Stapput, Peter Thalau, Christiane R. Timmel, and Wolfgang Wiltschko. Magnetic compass of birds is based on a molecule with optimal directional sensitivity. *Biophysical Journal*, 96(8): 3451–3457, April 2009.

[182] Nina Keary, Tim Ruploh, Joe Voss, Peter Thalau, Roswitha Wiltschko, Wolfgang Wiltschko, and Hans-Joachim Bischof. Oscillating magnetic field disrupts magnetic orientation in zebra finches, taeniopygia guttata. *Frontiers In Zoology*, 6:25, October 2009.

[183] P Thalau, T Ritz, K Stapput, R Wiltschko, and W Wiltschko. Magnetic compass orientation of migratory birds in the presence of a 1.315 mhz oscillating field. *Naturwissenschaften*, 92 (2):86–90, February 2005.

[184] Roswitha Wiltschko, Peter Thalau, Dennis Gehring, Christine Nießner, Thorsten Ritz, and Wolfgang Wiltschko. Magnetoreception in birds: the effect of radio-frequency fields. *Journal of The Royal Society Interface*, 12(103), 2014.

[185] Svenja Engels, Nils-Lasse Schneider, Nele Lefeldt, Christine Maira Hein, Manuela Zapka, Andreas Michalik, Dana Elbers, Achim Kittel, P. J. Hore, and Henrik Mouritsen. Anthropogenic electromagnetic noise disrupts magnetic compass orientation in a migratory bird. *Nature*, 509(7500):353–356, May 2014.

[186] Thorsten Ritz, Margaret Ahmad, Henrik Mouritsen, Roswitha Wiltschko, and Wolfgang Wiltschko. Photoreceptor-based magnetoreception: optimal design of receptor molecules, cells, and neuronal processing. *Journal of The Royal Society Interface*, 7(Suppl. 2):S135–S146, April 2010.

[187] W Wiltschko and R Wiltschko. Theoretical-model for migratory orientation and homing in birds. *OIKOS*, 30(2):177–187, 1978.

[188] Wolfgang Wiltschko, Katrin Stapput, Peter Thalau, and Roswitha Wiltschko. Avian magnetic compass: fast adjustment to intensities outside the normal functional window. *Naturwissenschaften*, 93(6):300–304, June 2006.

[189] Michael Winklhofer, Evelyn Dylda, Peter Thalau, Wolfgang Wiltschko, and Roswitha Wiltschko. Avian magnetic compass can be tuned to anomalously low magnetic intensities. *Proceedings of the Royal Society B-biological Sciences*, 280(1763):UNSP 20130853, July 2013.

[190] Roswitha Wiltschko, Dennis Gehring, Susanne Denzau, Christine Nießner, and Wolfgang Wiltschko. Magnetoreception in birds: II. behavioural experiments concerning the cryptochrome cycle. *Journal of Experimental Biology*, 217(23):4225–4228, December 2014.

[191] Bao-Ming Xu, Jian Zou, Hai Li, Jun-Gang Li, and Bin Shao. Effect of radio frequency fields on the radical pair magnetoreception model. *Physical Review E*, 90(4):042711, October 2014.

[192] Erik M. Gauger, Elisabeth Rieper, John J. L. Morton, Simon C. Benjamin, and Vlatko Vedral. Sustained quantum coherence and entanglement in the avian compass. *Physical Review Letters*, 106(4):040503, January 2011.

[193] Erik M. Gauger and Simon C. Benjamin. Comment on "quantum coherence and sensitivity of avian magnetoreception". *Physical Review Letters*, 110(17):178901, April 2013.

[194] Li-Ping Yang, Qing Ai, and C. P. Sun. Generalized holstein model for spin-dependent electron-transfer reactions. *Physical Review A*, 85(3):032707, March 2012.

[195] Jayendra N. Bandyopadhyay, Tomasz Paterek, and Dagomir Kaszlikowski. Quantum coherence and sensitivity of avian magnetoreception. *Physical Review Letters*, 109(11):110502, September 2012.

[196] Jayendra N. Bandyopadhyay, Tomasz Paterek, and Dagomir Kaszlikowski. Comment on "quantum coherence and sensitivity of avian magnetoreception" reply. *Physical Review Letters*, 110(17):178902, April 2013.

[197] B. Giovani, M. Byrdin, M. Ahmad, and K. Brettel. Light-induced electron transfer in a cryptochrome blue-light photoreceptor. *Nature Structural Biology*, 10(6):489–490, June 2003.

[198] Miriam Liedvogel, Kiminori Maeda, Kevin Henbest, Erik Schleicher, Thomas Simon, Christiane R. Timmel, P. J. Hore, and Henrik Mouritsen. Chemical magnetoreception: Bird cryptochrome 1a is excited by blue light and forms long-lived radical-pairs. *Plos One*, 2 (10), October 2007.

[199] Kevin B. Henbest, Kiminori Maeda, P. J. Hore, Monika Joshi, Adelbert Bacher, Robert Bittl, Stefan Weber, Christiane R. Timmel, and Erik Schleicher. Magnetic-field effect on the photoactivation reaction of escherichia coli dna photolyase. *Proceedings of the National Academy of Sciences of the United States of America*, 105(38):14395–14399, September 2008.

[200] Kiminori Maeda, Simon R. T. Neil, Kevin B. Henbest, Stefan Weber, Erik Schleicher, P. J. Hore, Stuart R. Mackenzie, and Christiane R. Timmel. Following radical pair reactions in solution: A step change in sensitivity using cavity ring-down detection. *Journal of the American Chemical Society*, 133(44):17807–17815, November 2011.

[201] Stefan Weber, Till Biskup, Asako Okafuji, Anthony R. Marino, Thomas Berthold, Gerhard Link, Kenichi Hitomi, Elizabeth D. Getzoff, Erik Schleicher, and James R. Norris, Jr. Origin of light-induced spin-correlated radical pairs in cryptochrome. *The Journal of Physical Chemistry B*, 114(45):14745–14754, November 2010.

[202] Kiminori Maeda, Kevin B. Henbest, Filippo Cintolesi, Ilya Kuprov, Christopher T. Rodgers, Paul A. Liddell, Devens Gust, Christiane R. Timmel, and P. J. Hore. Chemical compass model of avian magnetoreception. *Nature*, 453(7193):387–U38, May 2008.

[203] Kiminori Maeda, Jonathan G. Storey, Paul A. Liddell, Devens Gust, P. J. Hore, C. J. Wedge, and Christiane R. Timmel. Probing a chemical compass: novel variants of low-frequency reaction yield detected magnetic resonance. *Physical Chemistry Chemical Physics*, 17(5): 3550–3559, 2015.

[204] Kiminori Maeda, Alexander J. Robinson, Kevin B. Henbest, Hannah J. Hogben, Till Biskup, Margaret Ahmad, Erik Schleicher, Stefan Weber, Christiane R. Timmel, and P. J. Hore. Magnetically sensitive light-induced reactions in cryptochrome are consistent with its proposed role as a magnetoreceptor. *Proceedings of the National Academy of Sciences of the United States of America*, 109(13):4774–4779, March 2012.

[205] Margaret Ahmad, Paul Galland, Thorsten Ritz, Roswitha Wiltschko, and Wolfgang Wiltschko. Magnetic intensity affects cryptochrome-dependent responses in arabidopsis thaliana. *PLANTA*, 225(3):615–624, February 2007.

[206] Sue-Re Harris, Kevin B. Henbest, Kiminori Maeda, John R. Pannell, Christiane R. Timmel, P. J. Hore, and Haruko Okamoto. Effect of magnetic fields on cryptochrome-dependent responses in arabidopsis thaliana. *Journal of The Royal Society Interface*, 6(41):1193–1205, December 2009.

[207] P Semm, D Nohr, C Demaine, and W Wiltschko. Neural basis of the magnetic compass - interactions of visual, magnetic and vestibular inputs in the pigeons brain. *Journal of Comparative Physiology*, 155(3):283–288, 1984.

[208] P Semm and C Demaine. Neurophysiological properties of magnetic cells in the pigeons visual-system. *Journal of Comparative Physiology A-sensory Neural and Behavioral Physiology*, 159(5):619–625, 1986.

[209] Edgardo Ramirez, Gonzalo Marin, Jorge Mpodozis, and Juan-Carlos Letelier. Extracellular recordings reveal absence of magneto sensitive units in the avian optic tectum. *Journal of Comparative Physiology A-neuroethology Sensory Neural and Behavioral Physiology*, 200 (12):983–996, December 2014.

[210] Ingo Schiffner, Johann Baumeister, and Roswitha Wiltschko. Mathematical analysis of the navigational process in homing pigeons. *Journal of Theoretical Biology*, 291:42–46, December 2011.

[211] S. T. Emlen and J. T. Emlen. A technique for recording migratory orientation of captive birds. *Auk*, 83(3):361–367, 1966.

[212] AL Vyssotski, AN Serkov, PM Itskov, G Dell'Omo, AV Latanov, DP Wolfer, and HP Lipp. Miniature neurologgers for flying pigeons: Multichannel eeg and action and field potentials in combination with gps recording. *Journal of Neurophysiology*, 95(2):1263–1273, February 2006.

[213] Alexei L. Vyssotski, Giacomo Dell'Omo, Gaia Dell'Ariccia, Andrei N. Abramchuk, Andrei N. Serkov, Alexander V. Latanov, Alberto Loizzo, David P. Wolfer, and Hans-Peter Lipp. Eeg responses to visual landmarks in flying pigeons. *Current Biology*, 19(14, Sp. Iss. SI):1159–1166, July 2009.

[214] Juan Pedro Vargas, Jennifer J. Siegel, and Verner P. Bingman. The effects of a changing ambient magnetic field on single-unit activity in the homing pigeon hippocampus. *Brain Research Bulletin*, 70(2):158–164, June 2006.

[215] M. A. Bookman. Sensitivity of homing pigeon to an earth-strength magnetic-field. *Nature*, 267(5609):340–342, 1977.

[216] Christiane Wilzeck, Wolfgang Wiltschko, Onur Guentuerkuen, Jens-Uwe Buschmann, Roswitha Wiltschko, and Helmut Prior. Learning of magnetic compass directions in pigeons. *Animal Cognition*, 13(3):443–451, May 2010.

[217] Rafael Freire, Ursula H Munro, Lesley J Rogers, Roswitha Wiltschko, and Wolfgang Wiltschko. Chickens orient using a magnetic compass. *Current Biology*, 15(16):R620–R621, 2005.

[218] Susanne Denzau, Dany Kuriakose, Rafael Freire, Ursula Munro, and Wolfgang Wiltschko. Conditioning domestic chickens to a magnetic anomaly. *Journal of Comparative Physiology A-neuroethology Sensory Neural and Behavioral Physiology*, 197(12):1137–1141, December 2011.

[219] Joe Voss, Nina Keary, and Hans-Joachim Bischof. The use of the geomagnetic field for short distance orientation in zebra finches. *Neuroreport*, 18(10):1053–1057, July 2007.

[220] Rafael Freire and Tessa E. Birch. Conditioning to magnetic direction in the pekin duck (anas platyrhynchos domestica). *Journal of Experimental Biology*, 213(20):3423–3426, October 2010.

[221] Rafael Freire, Emma Dunston, Emmalee M. Fowler, Gary L. McKenzie, Christopher T. Quinn, and Jacob Michelsen. Conditioned response to a magnetic anomaly in the pekin duck (anas platyrhynchos domestica) involves the trigeminal nerve. *Journal of Experimental Biology*, 215(14):2399–2404, July 2012.

[222] G. J. Carman, M. M. Walker, and A. K. Lee. Attempts to demonstrate magnetic discrimination by homing pigeons in flight. *Animal Learning & Behavior*, 15(2):124–129, May 1987.

[223] H Mouritsen, G Feenders, M Liedvogel, K Wada, and ED Jarvis. Night-vision brain area in migratory songbirds. *Proceedings of the National Academy of Sciences of the United States of America*, 102(23):8339–8344, June 2005.

[224] G Causey Whittow. *Sturkie's avian physiology*. Academic press, 1999.

[225] Colin G Scanes. *Sturkie's avian physiology*. Elsevier, 2014.

[226] Dominik Heyers, Martina Manns, Harald Luksch, Onur Guentuerkuen, and Henrik Mouritsen. A visual pathway links brain structures active during magnetic compass orientation in migratory birds. *Plos One*, 2(9):e937, September 2007.

[227] Manuela Zapka, Dominik Heyers, Miriam Liedvogel, Erich D. Jarvis, and Henrik Mouritsen. Night-time neuronal activation of cluster n in a day- and night-migrating songbird. *European Journal of Neuroscience*, 32(4):619–624, August 2010.

[228] Miriam Liedvogel, Gesa Feenders, Kazuhiro Wada, Nikolaus F. Troje, Erich D. Jarvis, and Henrik Mouritsen. Lateralized activation of cluster n in the brains of migratory songbirds. *European Journal of Neuroscience*, 25(4):1166–1173, February 2007.

[229] Nina Keary and Hans-Joachim Bischof. Activation changes in zebra finch (taeniopygia guttata) brain areas evoked by alterations of the earth magnetic field. *Plos One*, 7(6): e38697, June 2012.

[230] Harvey J Karten and William Hodos. *A Stereotaxic Atlas of the Brain of the Pigeon:(Columba Livia)*, volume 696. Citeseer, 1967.

[231] Onur Guentuerkuen, Marleen Verhoye, Geert De Groof, and Annemie Van der Linden. A 3-dimensional digital atlas of the ascending sensory and the descending motor systems in the pigeon brain. *Brain Structure & Function*, 218(1):269–281, January 2013.

[232] Horst Erich König and Hermann Bragulla. *Anatomie der Vögel: Klinische Aspekte und Propädeutik; Zier-, Greif-, Zoo-, Wildvögel und Wirtschaftsgeflügel*. Schattauer, 2008.

[233] E Jarvis, O Gunturkun, L Bruce, A Csillag, H Karten, W Kuenzel, L Medina, G Paxinos, DJ Perkel, T Shimizu, G Striedter, JM Wild, GF Ball, J Dugas-Ford, SE Durand, GE Hough, S Husband, L Kubikova, DW Lee, CV Mello, A Powers, C Siang, TV Smulders, K Wada, SA White, K Yamamoto, J Yu, A Reiner, AB Butler, and Avian Brain Nomenclature Consorti. Avian brains and a new understanding of vertebrate brain evolution. *Nature Reviews Neuroscience*, 6(2):151–159, February 2005.

[234] E.D. Jarvis. Bird brain: Evolution. In Larry R. Squire, editor, *Encyclopedia of Neuroscience*, pages 209 – 215. Academic Press, Oxford, 2009.

[235] A Reiner, DJ Perkel, LL Bruce, AB Butler, A Csillag, W Kuenzel, L Medina, G Paxinos, T Shimizu, G Striedter, M Wild, GF Ball, S Durand, O Gunturkun, DW Lee, CV Mello, A Powers, SA White, G Hough, L Kubikova, TV Smulders, K Wada, J Dugas-Ford, S Husband, K Yamamoto, J Yu, C Siang, and ED Jarvis. Revised nomenclature for avian telencephalon and some related brainstem nuclei. *Journal of Comparative Neurology*, 473(3): 377–414, May 2004.

[236] Anton Reiner, Kei Yamamoto, and Harvey J Karten. Organization and evolution of the avian forebrain. *The Anatomical Record Part A: Discoveries in Molecular, Cellular, and Evolutionary Biology*, 287(1):1080–1102, 2005.

[237] Anton Reiner. Avian evolution: from darwin's finches to a new way of thinking about avian forebrain organization and behavioural capabilities. *Biology letters*, 5(1):122–124, 2009.

[238] Gesa Feenders, Miriam Liedvogel, Miriam Rivas, Manuela Zapka, Haruhito Horita, Erina Hara, Kazuhiro Wada, Henrik Mouritsen, and Erich D. Jarvis. Molecular mapping of movement-associated areas in the avian brain: A motor theory for vocal learning origin. *Plos One*, 3(3), March 2008.

[239] P Semm and C Demaine. Electrical responses to direct and indirect photic-stimulation of the pineal-gland in the pigeon. *Journal of Neural Transmission*, 58(3-4):281–289, 1983.

[240] Jonas Rose. The neural basis of avian magnetic orientation. Master thesis, University of Otago (New Zeland), 2005.

[241] Edgardo Ramirez. Is there a photo-dependent magneto-reception mechanism in the pigeon's optic tectum? Master thesis, University of Chile (Chile), 2011.

[242] H Mouritsen and T Ritz. Magnetoreception and its use in bird navigation. *Current Opinion in Neurobiology*, 15(4):406–414, August 2005.

[243] Henrik Mouritsen. The magnetic senses. In *Neurosciences-From Molecule to Behavior: a university textbook*, pages 427–443. Springer, 2013.

[244] D. R. W. Wylie, C. Gutierrez-Ibanez, J. M. P. Pakan, and A. N. Iwaniuk. The optic tectum of birds: Mapping our way to understanding visual processing. *Canadian Journal of Experimental Psychology-revue Canadienne De Psychologie Experimentale*, 63(4):328–338, 2009.

[245] B. S. W. Ng, A. Grabska-Barwinska, O. Gunturkun, and D. Jancke. Dominant vertical orientation processing without clustered maps: Early visual brain dynamics imaged with voltage-sensitive dye in the pigeon visual wulst. *Journal of Neuroscience*, 30(19):6713–6725, 2010.

[246] D. M. Kelly, W. F. Bischof, D. R. Wong-Wylie, and M. L. Spetch. Detection of glass patterns by pigeons and humans: Implications for differences in higher-level processing. *Psychological Science*, 12(4):338–342, July 2001.

[247] Shigeru Watanabe and Nikolaus F. Troje. Towards a "virtual pigeon": A new technique for investigating avian social perception. *Animal Cognition*, 9(4):271–279, October 2006.

[248] B.J. Frost, D.R. Wylie, and Y.C. Wang. The analysis of motion in the visual systems of birds. In MarkN.O. Davies and PatrickR. Green, editors, *Perception and Motor Control in Birds*, pages 248–269. Springer Berlin Heidelberg, 1994.

[249] H. J. Sun and B. J. Frost. Computation of different optical variables of looming objects in pigeon nucleus rotundus neurons. *Nature Neuroscience*, 1(4):296–303, August 1998.

[250] A. G. Palacios and F. J. Varela. Color mixing in the pigeon (columba-livia) .2. a psychophysical determination in the middle, short and near-uv wavelength range. *Vision Research*, 32 (10):1947–1953, October 1992.

[251] M. Remy and J. Emmerton. Behavioral spectral sensitivities of different retinal areas in pigeons. *Behavioral Neuroscience*, 103(1):170–177, February 1989.

[252] J. J. Vos Hzn, M. A. J. M. Coemans, and J. F. W. Nuboer. The photopic sensitivity of the yellow field of the pigeon's retina to ultraviolet light. *Vision Research*, 34(11):1419–1425, 1994.

[253] S. A. McFadden and J. M. Wild. Binocular depth-perception in the pigeon. *Journal of the Experimental Analysis of Behavior*, 45(2):149–160, March 1986.

[254] A. D. Milner and M. A. Goodale. Two visual systems re-viewed. *Neuropsychologia*, 46(3): 774–785, 2008.

[255] Geert De Groof, Elisabeth Jonckers, Onur Guentuerkuen, Petra Denolf, Johan Van Auderkerke, and Annemie Van der Linden. Functional mri and functional connectivity of the visual system of awake pigeons. *Behavioural Brain Research*, 239:43–50, February 2013.

[256] J. I. McGill, T. P. S. Powell, and W. M. Cowan. Retinal representation upon optic tectum and isthom-optic nucleus in pigeon. *Journal of Anatomy*, 100:5–33, 1966.

[257] P. G. H. Clarke and D. Whitteridge. Projection of retina, including red area, on to optic tectum of pigeon. *Quarterly Journal of Experimental Physiology and Cognate Medical Sciences*, 61(4):351–358, 1976.

[258] L. I. Benowitz and H. J. Karten. Organization of tectofugal visual pathway in pigeon - retrograde transport study. *Journal of Comparative Neurology*, 167(4):503–520, 1976.

[259] Martina Manns and Felix Stroeckens. Functional and structural comparison of visual lateralization in birds - similar but still different. *Frontiers In Psychology*, 5, March 2014.

[260] O. Gunturkun, B. Hellmann, G. Melsbach, and H. Prior. Asymmetries of representation in the visual system of pigeons. *Neuroreport*, 9(18):4127–4130, December 1998.

[261] Felix Stroeckens, Nadja Freund, Martina Manns, Sebastian Ocklenburg, and Onur Guentuerkuen. Visual asymmetries and the ascending thalamofugal pathway in pigeons. *Brain Structure & Function*, 218(5):1197–1209, September 2013.

[262] N. Brecha, H. J. Karten, and S. P. Hunt. Projections of the nucleus of the basal optic root in the pigeon - an autoradiographic and horseradish-peroxidase study. *Journal of Comparative Neurology*, 189(4):615–670, 1980.

[263] P. D. R. Gamlin and D. H. Cohen. Projections of the retinorecipient pretectal nuclei in the pigeon (columba-livia). *Journal of Comparative Neurology*, 269(1):18–46, March 1988.

[264] K. L. Lau, R. G. Glover, B. Linkenhoker, and D. R. W. Wylie. Topographical organization of inferior olive cells projecting to translation and rotation zones in the vestibulocerebellum of pigeons. *Neuroscience*, 85(2):605–614, July 1998.

[265] Janelle M. P. Pakan and Douglas R. W. Wylie. Two optic flow pathways from the pretectal nucleus lentiformis mesencephali to the cerebellum in pigeons (columba livia). *Journal of Comparative Neurology*, 499(5):732–744, December 2006.

[266] D. R. W. Wylie. Projections from the nucleus of the basal optic root and nucleus lentiformis mesencephali to the inferior olive in pigeons (columba livia). *Journal of Comparative Neurology*, 429(3):502–513, 2001.

[267] H. J. Bischof and S. Watanabe. On the structure and function of the tectofugal visual pathway in laterally eyed birds. *European Journal of Morphology*, 35(4):246–254, October 1997.

[268] M. Remy and O. Gunturkun. Retinal afferents to the tectum-opticum and the nucleus-opticus-principalis thalami in the pigeon. *Journal of Comparative Neurology*, 305(1):57–70, March 1991.

[269] Reza Khanbabaie, Alireza S. Mahani, and Ralf Wessel. Contextual interaction of gabaergic circuitry with dynamic synapses. *Journal of Neurophysiology*, 97(4):2802–2811, April 2007.

[270] J. C. Letelier, J. Mpodozis, G. Marin, D. Morales, C. Rozas, C. Madrid, and M. Velasco. Spatiotemporal profile of synaptic activation produced by the electrical and visual stimulation of retinal inputs to the optic tectum: a current source density analysis in the pigeon (columba livia). *European Journal of Neuroscience*, 12(1):47–57, January 2000.

[271] H. Luksch. Cytoarchitecture of the avian optic tectum: Neuronal substrate for cellular computation. *Reviews In the Neurosciences*, 14(1-2):European Network Neuoinformat, 2003.

[272] M. Metzger, L. R. G. Britto, and C. A. B. Toledo. Monoaminergic markers in the optic tectum of the domestic chick. *Neuroscience*, 141(4):1747–1760, 2006.

[273] T. Sebesteny, D. C. Davies, N. Zayats, A. Nemeth, and T. Tombol. The ramification and connections of retinal fibres in layer 7 of the domestic chick optic tectum: a golgi impregnation, anterograde tracer and gaba-immunogold study. *Journal of Anatomy*, 200 (2):169–183, February 2002.

[274] Y. Wang, H. Luksch, N. C. Brecha, and H. J. Karten. Columnar projections from the cholinergic nucleus isthmi to the optic tectum in chicks (gallus gallus): A possible substrate for synchronizing tectal channels. *Journal of Comparative Neurology*, 494(1):7–35, January 2006.

[275] Y. C. Wang and B. J. Frost. Visual response characteristics of neurons in the nucleus isthmi magnocellularis and nucleus isthmi parvocellularis of pigeons. *Experimental Brain Research*, 87(3):624–633, 1991.

[276] Y. Wang, D. E. Major, and H. J. Karten. Morphology and connections of nucleus isthmi pars magnocellularis in chicks (gallus gallus). *Journal of Comparative Neurology*, 469(2): 275–297, February 2004.

[277] Y. C. Wang, S. Y. Jiang, and B. J. Frost. Visual processing in pigeon nucleus rotundus - luminance, color, motion, and looming subdivisions. *Visual Neuroscience*, 10(1):21–30, January 1993.

[278] Ludger Kamphausen. inquiry narcosis. personal communication, November 2012. E-Mail.

[279] Julia Henke. inquiry narcosis. personal communication, July 2012. Phone call.

[280] V. M. Lukasik and R. J. Gillies. Animal anaesthesia for in vivo magnetic resonance. *Nmr In Biomedicine*, 16(8):459–467, December 2003.

[281] V-S Eckle, C Hucklenbruch, and SM Todorovic. Was wissen wir über narkosemechanismen? *Der Anaesthesist*, 58(11):1144–1149, 2009.

[282] H. C. Hemmings, M. H. Akabas, P. A. Goldstein, J. R. Trudell, B. A. Orser, and N. L. Harrison. Emerging molecular mechanisms of general anesthetic action. *Trends In Pharmacological Sciences*, 26(10):503–510, October 2005.

[283] N. P. Franks. Molecular targets underlying general anaesthesia. *British Journal of Pharmacology*, 147:S72–S81, January 2006.

[284] Andrew Jenkins, Ingrid A. Lobo, Diane Gong, James R. Trudell, Ken Solt, R. Adron Harris, and II Eger, Edmond I. General anesthetics have additive actions on three ligand gated ion channels. *Anesthesia and Analgesia*, 107(2):486–493, August 2008.

[285] Jr. Hemmings, H. C. Sodium channels and the synaptic mechanisms of inhaled anaesthetics. *British Journal of Anaesthesia*, 103(1):61–69, July 2009.

[286] J. J. Carmody. Some scientific reflections on possible mechanisms of general anaesthesia. *Anaesthesia and Intensive Care*, 37(2):Australian & New Zealand Coll Anaesthet, March 2009.

[287] L. Uhrig, S. Dehaene, and B. Jarraya. Cerebral mechanisms of general anesthesia. *Annales Francaises D Anesthesie Et De Reanimation*, 33(2):72–82, February 2014.

[288] Yong Son. Molecular mechanisms of general anesthesia. *Korean journal of anesthesiology*, 59(1):3–8, July 2010.

[289] Christian Grasshoff, Uwe Rudolph, and Bernd Antkowiak. Molecular and systemic mechanisms of general anaesthesia: the 'multi-site and multiple mechanisms' concept. *Current opinion in anaesthesiology*, 18(4):386–91, August 2005.

[290] Ken Solt and Stuart A. Forman. Correlating the clinical actions and molecular mechanisms of general anesthetics. *Current opinion in anaesthesiology*, 20(4):300–6, August 2007.

[291] Wikipedia. Guedel's classification, 05 2015.

[292] L Arnall. Anaesthesia and surgery in cage and aviary birds. *Veterinary Record*, 73:139–142, 1961.

[293] Michael Lierz and Ruediger Korbel. Anesthesia and analgesia in birds. *Journal of Exotic Pet Medicine*, 21(1):44–58, January 2012.

[294] R. Korbel. Comparative investigations on inhalation anaesthesia with isoflurane (forene (r)) and sevoflurane (sevorane (r)) in racing pigeons (columba livia gmel., 1789, var. domestica) and presentation of a reference anaesthesia protocol for birds. *Tierarztliche Praxis Ausgabe Kleintiere Heimtiere*, 26(3):211–223, May 1998.

[295] R. Korbel. An anaesthetic procedure for surgery in the head area and for ophthalmoscopy in birds-a practical guideline. *Vet Observ*, November 1998.

[296] Wolf Erhardt, Julia Henke, Jörg Haberstroh, Christine Baumgartner, and Sabine Tacke, editors. *Anästhesie und Analgesie beim Klein- und Heimtier mit Exoten, Labortieren, Vögeln, Reptilien, Amphibien und Fischen.* Schattauer; Auflage: 2., Auflage., 2012.

[297] Uzma F. Durrani, Muhammad Ashraf, and Muhammad A. Khan. A comparison of the clinical effects associated with xylazine, ketamine, and a xylazine-ketamine cocktail in pigeons (columba livia). *Turkish Journal of Veterinary & Animal Sciences*, 33(5):413–417, 2009.

[298] Aidin Azizpour and Yashar Hassani. Clinical evaluation of general anaesthesia in pigeons using a combination of ketamine and diazepam. *Journal of the South African Veterinary Association*, 83(1):24–28, 2012.

[299] Anke Weiske. *Untersuchungen zu einer Injektionsnarkose bei der Taube (Columba livia, var. dom., Gmel. 1789) mit Medetomidin, Midazolam und Fentanyl und ihrer vollständigen Antagonisierung mit Atipamezol, Sarmazenil und Naloxon.* PhD thesis, Tierärztliche Fakultät der Ludwig-Maximilians-Universität, 2001.

[300] Klaus Aktories, Ulrich Förstermann, Bernhard Hofmann, and Klaus Starke, editors. *Allgemeine und spezielle Pharmakologie und Toxikologie.* Elsevier, Urban & Fischer, 11. Auflage, 2013.

[301] Hans Walter Striebel. *Die Anästhesie.* Schattauer, 3. Auflage, 2014.

[302] J Smith, DE Masson, and WW Muir. The influence of midazolam on the minimum anesthetic concentration of isoflurane in racing pigeons. *Veterinary Surgery*, 22:546–547, 1993.

[303] G Fitzgerald and D Blais. Effect of nitrous oxide on the minimal anaesthetic dose of isoflurane in pigeons and red-tailed hawks. *Veterinary Anaesthesia and Analgesia*, 18(s1): 111–115, 1991.

[304] J Smith and WW Muir. Cardiopulmonary effects of midazolam and flumazenil in racing pigeons. *Veterinary Surgery*, 21:499, 1992.

[305] B. Drexler, C. Grasshoff, U. Rudolph, K. Unertl, and B. Antkowiak. The gaba(a) receptor family. possibilities for the development of better anesthetics. *Anaesthesist*, 55(3):287–295, March 2006.

[306] Jörg Haberstroh. inquiry narcosis. personal communication, November 2014. E-Mail.

[307] Bettina Gaggermeier. *Untersuchung zur Schmerzausschaltung unter Buprenorphin und Butorphanol bei der Taube (Columba livia, Gmel., 1789, var. domestica).* PhD thesis, Tierärztliche Fakultät der Ludwig-Maximilians-Universität München, 2001.

[308] G. C. Whittow. *Comparative Physiology of Thermoregulation*, volume 1. Academic Press, 1970.

[309] BM Freeman, DJ Bell, and BM Freeman. Body temperature and thermoregulation in the physiology and biochemistry of the domestic fowl. *Vol. I.(Ed.: BELL, DJ)*, 1971.

[310] C Vogel, H Gerlach, and M Loffler. Columbiformes. *Avian Medicine: Principles and Application. Lake Worth, FL, Wingers Publishing*, pages 1200–1217, 1994.

[311] J. S. Hart and O. Z. Roy. Respiratory and cardiac responses to flight in pigeons. *Physiological Zoology*, 39(4):291–306, 1966.

[312] K. Bucher and P. Baettig. Special respiratory effects of co2 in pigeons. *Agents and Actions*, 5(4):378–382, 1975.

[313] P. Bouverot and P. Sebert. O2-chemoreflex drive of ventilation in awake birds at rest. *Respiration Physiology*, 37(2):201–218, 1979.

[314] R. M. Smith. Circulation, respiratory volumes and temperature regulation of pigeon in dry and humid heat. *Comparative Biochemistry and Physiology*, 43(3):477–490, 1972.

[315] B. R. Grubb. Cardiac-output and stroke volume in exercising ducks and pigeons. *Journal of Applied Physiology*, 53(1):207–211, 1982.

[316] P. Bouverot, G. Hildewein, and P. Oulhen. Ventilatory and circulatory o2 convection at 4000 m in pigeon at neutral or cold temperature. *Respiration Physiology*, 28(3):371–385, 1976.

[317] Chris Martin. Contributions and complexities from the use of in vivo animal models to improve understanding of human neuroimaging signals. *Frontiers in neuroscience*, 8, 2014.

[318] Lun-De Liao, Vassiliy Tsytsarev, Ignacio Delgado-Martinez, Meng-Lin Li, Reha Erzurumlu, Ashwati Vipin, Josue Orellana, Yan-Ren Lin, Hsin-Yi Lai, You-Yin Chen, and Nitish V. Thakor. Neurovascular coupling: in vivo optical techniques for functional brain imaging. *Biomedical Engineering Online*, 12:38, April 2013.

[319] Anna Devor, Sava Sakadžić, Vivek J Srinivasan, Mohammad A Yaseen, Krystal Nizar, Payam A Saisan, Peifang Tian, Anders M Dale, Sergei A Vinogradov, Maria Angela Franceschini, et al. Frontiers in optical imaging of cerebral blood flow and metabolism. *Journal of Cerebral Blood Flow & Metabolism*, 32(7):1259–1276, 2012.

[320] Elizabeth MC Hillman. Coupling mechanism and significance of the bold signal: A status report. *Annual Review of Neuroscience*, 37(1), 2014.

[321] A. Villringer. Understanding functional neuroimaging methods based on neurovascular coupling. *Optical Imaging of Brain Function and Metabolism 2: Physiological Basis and Comparison To Other Functional Neuroimaging Methods*, 413:177–193, 1997.

[322] N. K. Logothetis and B. A. Wandell. Interpreting the bold signal. *Annual Review of Physiology*, 66:735–769, 2004.

[323] Nikos K. Logothetis. What we can do and what we cannot do with fmri. *Nature*, 453(7197): 869–878, June 2008.

[324] David Attwell, Alastair M Buchan, Serge Charpak, Martin Lauritzen, Brian A MacVicar, and Eric A Newman. Glial and neuronal control of brain blood flow. *Nature*, 468(7321): 232–243, 2010.

[325] Giorgio Carmignoto and Marta Gomez-Gonzalo. The contribution of astrocyte signalling to neurovascular coupling. *Brain research reviews*, 63(1):138–148, 2010.

[326] Bruno Cauli and Edith Hamel. Revisiting the role of neurons in neurovascular coupling. *Frontiers in neuroenergetics*, 2, 2010.

[327] Richard B. Buxton. Dynamic models of bold contrast. *Neuroimage*, 62(2):953–961, August 2012.

[328] Aaron B. Simon and Richard B. Buxton. Understanding the dynamic relationship between cerebral blood flow and the bold signal: Implications for quantitative functional mri. *Neuroimage*, 116:158–167, August 2015.

[329] Yoshiyuki Hirano, Bojana Stefanovic, and Afonso C. Silva. Spatiotemporal evolution of the functional magnetic resonance imaging response to ultrashort stimuli. *Journal of Neuroscience*, 31(4):1440–1447, January 2011.

[330] J. Martindale, J. Mayhew, J. Berwick, M. Jones, C. Martin, D. Johnston, P. Redgrave, and Y. Zheng. The hemodynamic impulse response to a single neural event. *Journal of Cerebral Blood Flow and Metabolism*, 23(5):546–555, May 2003.

[331] Daniel A. Handwerker, Javier Gonzalez-Castillo, Mark D'Esposito, and Peter A. Bandettini. The continuing challenge of understanding and modeling hemodynamic variation in fmri. *Neuroimage*, 62(2):1017–1023, August 2012.

[332] N. K. Logothetis, J. Pauls, M. Augath, T. Trinath, and A. Oeltermann. Neurophysiological investigation of the basis of the fmri signal. *Nature*, 412(6843):150–157, July 2001.

[333] Ahalya Viswanathan and Ralph D. Freeman. Neurometabolic coupling in cerebral cortex reflects synaptic more than spiking activity. *Nature Neuroscience*, 10(10):1308–1312, October 2007.

[334] M. Jones, N. Hewson-Stoate, J. Martindale, P. Redgrave, and J. Mayhew. Nonlinear coupling of neural activity and cbf in rodent barrel cortex. *Neuroimage*, 22(2):956–965, June 2004.

[335] K. Caesar, K. Thomsen, and M. Lauritzen. Dissociation of spikes, synaptic activity, and activity-dependent increments in rat cerebellar blood flow by tonic synaptic inhibition. *Proceedings of the National Academy of Sciences of the United States of America*, 100(26): 16000–16005, December 2003.

[336] K. Thomsen, N. Offenhauser, and M. Lauritzen. Principal neuron spiking: neither necessary nor sufficient for cerebral blood flow in rat cerebellum. *Journal of Physiology-london*, 560 (1):181–189, October 2004.

[337] Alexander Rauch, Gregor Rainer, and Nikos K. Logothetis. The effect of a serotonin-induced dissociation between spiking and perisynaptic activity on bold functional mri. *Proceedings of the National Academy of Sciences of the United States of America*, 105(18):6759–6764, May 2008.

[338] Myles Jones, Ian M. Devonshire, Jason Berwick, Chris Martin, Peter Redgrave, and John Mayhew. Altered neurovascular coupling during information-processing states. *European Journal of Neuroscience*, 27(10):2758–2772, May 2008.

[339] S. A. Sheth, M. Nemoto, M. Guiou, M. Walker, N. Pouratian, and A. W. Toga. Linear and nonlinear relationships between neuronal activity, oxygen metabolism, and hemodynamic responses. *Neuron*, 42(2):347–355, April 2004.

[340] N. Hewson-Stoate, M. Jones, J. Martindale, J. Berwick, and J. Mayhew. Further nonlinearities in neurovascular coupling in rodent barrel cortex. *Neuroimage*, 24(2):565–574, January 2005.

[341] Chris Martin, John Martindale, Jason Berwick, and John Mayhew. Investigating neural–hemodynamic coupling and the hemodynamic response function in the awake rat. *Neuroimage*, 32(1):33–48, 2006.

[342] Henrik W. Hoffmeyer, Pia Enager, Kirsten J. Thomsen, and Martin J. Lauritzen. Nonlinear neurovascular coupling in rat sensory cortex by activation of transcallosal fibers. *Journal of Cerebral Blood Flow and Metabolism*, 27(3):575–587, March 2007.

[343] Nanyin Zhang, Essa Yacoub, Xiao-Hong Zhu, Kamil Ugurbil, and Wei Chen. Linearity of blood-oxygenation-level dependent signal at microvasculature. *Neuroimage*, 48(2):313–318, November 2009.

[344] Zhongming Liu, Cristina Rios, Nanyin Zhang, Lin Yang, Wei Chen, and Bin He. Linear and nonlinear relationships between visual stimuli, eeg and bold fmri signals. *Neuroimage*, 50(3):1054–1066, April 2010.

[345] Cesare Magri, Nikos K. Logothetis, and Stefano Panzeri. Investigating static nonlinearities in neurovascular coupling. *Magnetic Resonance Imaging*, 29(10):1358–1364, December 2011.

[346] H. L. Sloan, V. C. Austin, A. M. Blamire, J. W. H. Schnupp, A. S. Lowe, K. A. Allers, P. M. Matthews, and N. R. Sibson. Regional differences in neurovascular coupling in rat brain as determined by fmri and electrophysiology. *Neuroimage*, 53(2):399–411, November 2010.

[347] Ian M. Devonshire, Nikos G. Papadakis, Michael Port, Jason Berwick, Aneurin J. Kennerley, John E. W. Mayhew, and Paul G. Overton. Neurovascular coupling is brain region-dependent. *Neuroimage*, 59(3):1997–2006, February 2012.

[348] Jozien Goense, Hellmut Merkle, and Nikos K. Logothetis. High-resolution fmri reveals laminar differences in neurovascular coupling between positive and negative bold responses. *Neuron*, 76(3):629–639, November 2012.

[349] Anna Devor, Peifang Tian, Nozomi Nishimura, Ivan C Teng, Elizabeth MC Hillman, SN Narayanan, Istvan Ulbert, David A Boas, David Kleinfeld, and Anders M Dale. Suppressed neuronal activity and concurrent arteriolar vasoconstriction may explain negative blood oxygenation level-dependent signal. *The Journal of neuroscience*, 27(16):4452–4459, 2007.

[350] Luke Boorman, Aneurin J Kennerley, David Johnston, Myles Jones, Ying Zheng, Peter Redgrave, and Jason Berwick. Negative blood oxygen level dependence in the rat: a model for investigating the role of suppression in neurovascular coupling. *The Journal of Neuroscience*, 30(12):4285–4294, 2010.

[351] Chris Martin, Ying Zheng, Nicola R Sibson, John EW Mayhew, and Jason Berwick. Complex spatiotemporal haemodynamic response following sensory stimulation in the awake rat. *Neuroimage*, 66:1–8, 2013.

[352] Chris J. Martin, Aneurin J. Kennerley, Jason Berwick, Michael Port, and John E. W. Mayhew. Functional mri in conscious rats using a chronically implanted surface coil. *Journal of Magnetic Resonance Imaging*, 38(3):739–744, September 2013.

[353] R. B. Buxton, E. C. Wong, and L. R. Frank. Dynamics of blood flow and oxygenation changes during brain activation: The balloon model. *Magnetic Resonance In Medicine*, 39 (6):855–864, June 1998.

[354] A. T. Smith, A. L. Williams, and K. D. Singh. Negative bold in the visual cortex: Evidence against blood stealing. *Human Brain Mapping*, 21(4):213–220, April 2004.

[355] Aneurin J Kennerley, John E Mayhew, Luke Boorman, Ying Zheng, and Jason Berwick. Is optical imaging spectroscopy a viable measurement technique for the investigation of the negative bold phenomenon? a concurrent optical imaging spectroscopy and fmri study at high field (7t). *Neuroimage*, 61(1):10–20, 2012.

[356] K. M. Aquino, P. A. Robinson, and P. M. Drysdale. Spatiotemporal hemodynamic response functions derived from physiology. *Journal of Theoretical Biology*, 347:118–136, April 2014.

[357] Aileen Schroeter, Felix Schlegel, Aline Seuwen, Joanes Grandjean, and Markus Rudin. Specificity of stimulus-evoked fmri responses in the mouse: The influence of systemic physiological changes associated with innocuous stimulation under four different anesthetics. *Neuroimage*, 94:372–384, July 2014.

[358] K. M. Lahti, C. F. Ferris, F. H. Li, C. H. Sotak, and J. A. King. Comparison of evoked cortical activity in conscious and propofol-anesthetized rats using functional mri. *Magnetic Resonance In Medicine*, 41(2):412–416, 1999.

[359] Y. Nakao, Y. Itoh, T. Y. Kuang, M. Cook, J. Jehle, and L. Sokoloff. Effects of anesthesia on functional activation of cerebral blood flow and metabolism. *Proceedings of the National Academy of Sciences of the United States of America*, 98(13):7593–7598, June 2001.

[360] M. E. Brevard, T. Q. Duong, J. A. King, and C. F. Ferris. Changes in mri signal intensity during hypercapnic challenge under conscious and anesthetized conditions. *Magnetic Resonance Imaging*, 21(9):995–1001, November 2003.

[361] K. Sicard, Q. Shen, M. E. Brevard, R. Sullivan, C. F. Ferris, J. A. King, and T. Q. Duong. Regional cerebral blood flow and bold responses in conscious and anesthetized rats under basal and hypercapnic conditions: Implications for functional mri studies. *Journal of Cerebral Blood Flow and Metabolism*, 23(4):472–481, April 2003.

[362] Feng Luo, Zhixin Li, Steven N. Treistman, Young Ro Kim, Jean A. King, Gerard B. Fox, and Craig F. Ferris. Confounding effects of volatile anesthesia on cbv assessment in rodent forebrain following ethanol challenge. *Journal of Magnetic Resonance Imaging*, 26(3):557–563, September 2007.

[363] T. Tsurugizawa, A. Uematsu, H. Uneyama, and K. Torii. Effects of isoflurane and alpha-chloralose anesthesia on bold fmri responses to ingested l-glutamate in rats. *Neuroscience*, 165(1):244–251, January 2010.

[364] Mitsuhiro Fukuda, Alberto L. Vazquez, Xiaopeng Zong, and Seong-Gi Kim. Effects of the a2-adrenergic receptor agonist dexmedetomidine on neural, vascular and bold fmri responses in the somatosensory cortex. *European Journal of Neuroscience*, 37(1):80–95, January 2013.

[365] M Andrea Pisauro, Neel T Dhruv, Matteo Carandini, and Andrea Benucci. Fast hemodynamic responses in the visual cortex of the awake mouse. *The Journal of Neuroscience*, 33 (46):18343–18351, 2013.

[366] R. G. Shulman, D. L. Rothman, and F. Hyder. Stimulated changes in localized cerebral energy consumption under anesthesia. *Proceedings of the National Academy of Sciences of the United States of America*, 96(6):3245–3250, March 1999.

[367] F. Hyder, D. L. Rothman, and R. G. Shulman. Total neuroenergetics support localized brain activity: Implications for the interpretation of fmri. *Proceedings of the National Academy of Sciences of the United States of America*, 99(16):10771–10776, August 2002.

[368] Kristin Engelhard and Christian Werner. Inhalational or intravenous anesthetics for craniotomies? pro inhalational. *Current opinion in anaesthesiology*, 19(5):504–8, October 2006.

[369] W. E. Hoffman, G. Edelman, E. Kochs, C. Werner, L. Segil, and R. F. Albrecht. Cerebral autoregulation in awake versus isoflurane-anesthetized rats. *Anesthesia and Analgesia*, 73 (6):753–757, December 1991.

[370] S. Strebel, A. M. Lam, B. Matta, T. S. Mayberg, R. Aaslid, and D. W. Newell. Dynamic and static cerebral autoregulation during isoflurane, desflurane, and propofol anesthesia. *Anesthesiology*, 83(1):66–76, July 1995.

[371] K. S. Hendrich, P. M. Kochanek, J. A. Melick, J. K. Schiding, K. D. Statler, D. S. Williams, D. W. Marion, and C. Ho. Cerebral perfusion during anesthesia with fentanyl, isoflurane, or pentobarbital in normal rats studied by arterial spin-labeled mri. *Magnetic Resonance In Medicine*, 46(1):202–206, July 2001.

[372] J. Vanhemelrijck, M. Verhaegen, and H. Vanaken. Cerebral effects of inhalational anesthetics. *Baillieres Clinical Anaesthesiology*, 7(4):1035–1055, December 1993.

[373] Joanna K. Huttunen, Olli Groehn, and Markku Penttonen. Coupling between simultaneously recorded bold response and neuronal activity in the rat somatosensory cortex. *Neuroimage*, 39(2):775–785, January 2008.

[374] Maria Angela Franceschini, Harsha Radhakrishnan, Kiran Thakur, Weicheng Wu, Svetlana Ruvinskaya, Stefan Carp, and David A Boas. The effect of different anesthetics on neurovascular coupling. *Neuroimage*, 51(4):1367–1377, 2010.

[375] M. Fukuda, U. M. Rajagopalan, R. Homma, M. Matsumoto, M. Nishizaki, and M. Tanifuji. Localization of activity-dependent changes in blood volume to submillimeter-scale functional domains in cat visual cortex. *Cerebral Cortex*, 15(6):823–833, June 2005.

[376] Kazuto Masamoto, Mitsuhiro Fukuda, Alberto Vazquez, and Seong-Gi Kim. Dose-dependent effect of isoflurane on neurovascular coupling in rat cerebral cortex. *European Journal of Neuroscience*, 30(2):242–250, 2009.

[377] Kazuto Masamoto and Iwao Kanno. Anesthesia and the quantitative evaluation of neurovascular coupling. *Journal of Cerebral Blood Flow & Metabolism*, 32(7):1233–1247, 2012.

[378] Ruediger Land, Gerhard Engler, Andrej Kral, and Andreas K. Engel. Auditory evoked bursts in mouse visual cortex during isoflurane anesthesia. *Plos One*, 7(11):e49855, November 2012.

[379] Gernot G. Supp, Markus Siegel, Joerg F. Hipp, and Andreas K. Engel. Cortical hypersynchrony predicts breakdown of sensory processing during loss of consciousness. *Current Biology*, 21(23):1988–1993, December 2011.

[380] Stéphane Mottin, Bruno Montcel, Hugues Guillet De Chatellus, and Stéphane Ramstein. Functional white-laser imaging to study brain oxygen uncoupling/recoupling in songbirds. *Journal of Cerebral Blood Flow & Metabolism*, 31(2):393–400, 2011.

[381] Paul Flecknell. *Laboratory Animal Anaesthesia.* Elsevier, 3rd Edition, 2009.

[382] Rüdiger Korbel. inquiry analgesia. personal communication, May 2012. E-Mail.

[383] V. Ramachandra, C. Moore, N. Kaur, and F. Carli. Effect of halothane, enflurane and isoflurane on body-temperature during and after surgery. *British Journal of Anaesthesia*, 62(4):409–414, April 1989.

[384] Maike Albrecht, Julia Henke, Sabine Tacke, Michael Markert, and Brian Guth. Effects of isoflurane, ketamine-xylazine and a combination of medetomidine, midazolam and fentanyl on physiological variables continuously measured by telemetry in wistar rats. *Bmc Veterinary Research*, 10:198, August 2014.

[385] G. G. Lockwood, S. M. SapsedByrne, and M. A. Smith. Effect of temperature on the solubility of desflurane, sevoflurane, enflurane and halothane in blood. *British Journal of Anaesthesia*, 79(4):517–520, October 1997.

[386] N. C. Yang, H. F. Wang, K. L. Hwang, and W. M. Ho. A novel method for determining the blood/gas partition coefficients of inhalation anesthetics to calculate the percentage of loss at different temperatures. *Journal of Analytical Toxicology*, 28(2):122–127, March 2004.

[387] Jihwan Myung, Sungho Hong, Daniel DeWoskin, Erik De Schutter, Daniel B. Forger, and Toru Takumi. Gaba-mediated repulsive coupling between circadian clock neurons in the scn encodes seasonal time. *Proceedings of the National Academy of Sciences of the United States of America*, 112(29):E3920–E3929, July 2015.

[388] Daniel DeWoskin, Jihwan Myung, Mino D. C. Belle, Hugh D. Piggins, Toru Takumi, and Daniel B. Forger. Distinct roles for gaba across multiple timescales in mammalian circadian timekeeping. *Proceedings of the National Academy of Sciences of the United States of America*, 112(29):E3911–E3919, July 2015.

[389] G. Maret and P. E. Wolf. Multiple light-scattering from disordered media - the effect of brownian-motion of scatterers. *Zeitschrift für Physik B-Condensed Matter*, 65(4):409–413, 1987.

[390] D. J. Pine, D. A. Weitz, P. M. Chaikin, and E. Herbolzheimer. Diffusing-wave spectroscopy. *Physical Review Letters*, 60(12):1134–1137, Mar 1988.

[391] N. Isert, G. Maret, and C. M. Aegerter. Coarsening dynamics of three-dimensional levitated foams: From wet to dry. *Eur Phys J E Soft Matter*, 36(10):116, Oct 2013.

[392] Nathan Isert, Georg Maret, and Christof M. Aegerter. Studying foam dynamics in levitated, dry and wet foams using diffusing wave spectroscopy. *Colloids and Surfaces A-physicochemical and Engineering Aspects*, 473:40–45, May 2015.

[393] D. A. Boas, L. E. Campbell, and A. G. Yodh. Scattering and imaging with diffusing temporal field correlations. *Physical Review Letters*, 75(9):1855–1858, 1995.

[394] M. Heckmeier and G. Maret. Visualization of flow in multiple-scattering liquids. *Europhysics Letters*, 34(4):257–262, 1996.

[395] M. Heckmeier, S. E. Skipetrov, G. Maret, and R. Maynard. Imaging of dynamic heterogeneities in multiple-scattering media. *Journal of the Optical Society of America A-optics Image Science and Vision*, 14(1):185–191, 1997.

[396] D. A. Boas. *Diffuse photon probes of structural and dynamical properties of turbid media: Theory and biomedical applications.* PhD thesis, University of Pennsylvania, 1996.

[397] T. Durduran, R. Choe, W. B. Baker, and A. G. Yodh. Diffuse optics for tissue monitoring and tomography. *Reports On Progress In Physics*, 73(7):076701, July 2010.

[398] T. Durduran and A. G. Yodh. Diffuse correlation spectroscopy for non-invasive, microvascular cerebral blood flow measurement. *Neuroimage*, 85 Pt 1:51–63, 2014.

[399] Rickson C. Mesquita, Turgut Durduran, Guoqiang Yu, Erin M. Buckley, Meeri N. Kim, Chao Zhou, Regine Choe, Ulas Sunar, and Arjun G. Yodh. Direct measurement of tissue blood flow and metabolism with diffuse optics. *Philos Trans A Math Phys Eng Sci*, 369 (1955):4390–4406, Nov 2011.

[400] Guoqiang Yu. Diffuse correlation spectroscopy (dcs): A diagnostic tool for assessing tissue blood flow in vascular-related diseases and therapies. *Current Medical Imaging Reviews*, 8 (3):194–210, August 2012.

[401] David A. Boas, Constantinos Pitris, and Nimmi Ramanujam, editors. *Handbook of Biomedical Optics.* CRC Press, 2011.

[402] Erin M. Buckley, Ashwin B. Parthasarathy, P. Ellen Grant, Arjun G. Yodh, and Maria Angela Franceschini. Diffuse correlation spectroscopy for measurement of cerebral blood flow: future prospects. *Neurophotonics*, 1(1):011009, 2014.

[403] T. Vo-Dinh. *Biomedical Photonics Handbook.* CRC Press, 2003.

[404] W. Brown. *Dynamic light scattering the method and some applications.* Clarendon Press, 1993.

[405] G. Dietsche. *Optische Abbildung von Gehirnfunktionen mit vielfach gestreutem Licht.* PhD thesis, Universität Konstanz, 2007.

[406] G. Mie. Articles on the optical characteristics of turbid tubes, especially colloidal metal solutions. *Annalen der Physik*, 25(3):377–445, 1908.

[407] L. H. Kou, D. Labrie, and P. Chylek. Refractive-indexes of water and ice in the 0.65 μm to 2.5 μm spectral range. *Applied Optics*, 32(19):3531–3540, 1993.

[408] W. B. Gratzer. Tabulated molar extinction coefficient for hemoglobin in water. Technical report, Med. Res. Council Labs, Holly Hill, London, 1998.

[409] N. Kollias. Tabulated molar extinction coefficient for hemoglobin in water. Technical report, Wellman Laboratories, Harvard Medical School, Boston, 1998.

[410] James V. Lee, Edward L. Maclin, Kathy A. Low, Gabriele Gratton, Monica Fabiani, and David F. Clayton. Noninvasive diffusive optical imaging of the auditory response to birdsong in the zebra finch. *Journal of Comparative Physiology A-neuroethology Sensory Neural and Behavioral Physiology*, 199(3):227–238, March 2013.

[411] D. A. Boas and A. G. Yodh. Spatially varying dynamical properties of turbid media probed with diffusing temporal light correlation. *Journal of the Optical Society of America A-Optics Image Science and Vision*, 14(1):192–215, 1997.

[412] T. Gisler, H. Ruger, S. U. Egelhaaf, J. Tschumi, P. Schurtenberger, and J. Ricka. Mode-selective dynamic light-scattering - theory versus experimental realization. *Applied Optics*, 34(18):3546–3553, 1995.

[413] P. N. Pusey, J. M. Vaughan, and D. V. Willetts. Effect of spatial incoherence of the laser in photon-correlation spectroscopy. *Journal of the Optical Society of America*, 73(8):1012–1017, 1983.

[414] T. Bellini, M. A. Glaser, N. A. Clark, and V. Degiorgio. Effects of finite laser coherence in quasi-elastic multiple-scattering. *Physical Review A*, 44(8):5215–5223, 1991.

[415] I. Flammer and J. Ricka. Dynamic light scattering with single-mode receivers: partial heterodyning regime. *Applied Optics*, 36(30):7508–7517, 1997.

[416] I. Flammer, G. Bucher, and J. Ricka. Diffusive wave illumination: light-scattering study of colloidal dynamics in opaque media. *Journal of the Optical Society of America A-Optics Image Science and Vision*, 15(8):2066–2077, 1998.

[417] D. A. Boas, I. V. Meglinsky, L. Zemany, L. E. Campbell, B. Chance, and A. G. Yodh. Diffusion of temporal field correlation with selected applications. *SPIE Proceedings*, 2732: 34–46, 1996.

[418] X. L. Wu, D. J. Pine, P. M. Chaikin, J. S. Huang, and D. A. Weitz. Diffusing-wave spectroscopy in a shear-flow. *Journal of the Optical Society of America B-Optical Physics*, 7(1):15–20, 1990.

[419] D. Bicout and R. Maynard. Diffusing wave spectroscopy in inhomogeneous flows. *Physica A*, 199(3-4):387–411, 1993.

[420] Markus Belau, Markus Ninck, Gernot Hering, Lorenzo Spinelli, Davide Contini, Alessandro Torricelli, and Thomas Gisler. Noninvasive observation of skeletal muscle contraction using near-infrared time-resolved reflectance and diffusing-wave spectroscopy. *Journal of Biomedical Optics*, 15(5):057007, 2010.

[421] B. J. Ackerson, R. L. Dougherty, N. M. Reguigui, and U. Nobbmann. Correlation transfer - application of radiative transfer solution methods to photon correlation problems. *Journal of Thermophysics and Heat Transfer*, 6(4):577–588, 1992.

[422] R. L. Dougherty, B. J. Ackerson, N. M. Reguigui, F. Dorrinowkoorani, and U. Nobbmann. Correlation transfer - development and application. *Journal of Quantitative Spectroscopy & Radiative Transfer*, 52(6):713–727, 1994.

[423] R. C. Haskell, L. O. Svaasand, T. T. Tsay, T. C. Feng, M. S. McAdams, and B. J. Tromberg. Boundary-conditions for the diffusion equation in radiative-transfer. *Journal of the Optical Society of America A-Optics Image Science and Vision*, 11(10):2727–2741, 1994.

[424] D. J. Pine, D. A. Weitz, J. X. Zhu, and E. Herbolzheimer. Diffusing-wave spectroscopy - dynamic light-scattering in the multiple-scattering limit. *Journal de Physique*, 51(18): 2101–2127, 1990.

[425] S. C. Feng, F. A. Zeng, and B. Chance. Photon migration in the presence of a single defect - a perturbation analysis. *Applied Optics*, 34(19):3826–3837, 1995.

[426] Guoqiang Yu, Turgut Durduran, Chao Zhou, Hsing-Wen Wang, Mary E. Putt, H Mark Saunders, Chandra M. Sehgal, Eli Glatstein, Arjun G. Yodh, and Theresa M. Busch. Noninvasive monitoring of murine tumor blood flow during and after photodynamic therapy provides early assessment of therapeutic efficacy. *Clin Cancer Res*, 11(9):3543–3552, May 2005.

[427] E. M. Buckley, N. M. Cook, T. Durduran, M. N. Kim, C. Zhou, R. Choe, G. Q. Yu, S. Shultz, C. M. Sehgal, D. J. Licht, P. H. Arger, M. E. Putt, H. Hurt, and A. G. Yodh. Cerebral hemodynamics in preterm infants during positional intervention measured with diffuse correlation spectroscopy and transcranial doppler ultrasound. *Optics Express*, 17 (15):12571–12581, 2009.

[428] Nadege Roche-Labarbe, Stefan A. Carp, Andrea Surova, Megha Patel, David A. Boas, R. Ellen Grant, and Maria Angela Franceschini. Noninvasive optical measures of cbv, sto(2), cbf index, and rcmro(2) in human premature neonates' brains in the first six weeks of life. *Human Brain Mapping*, 31(3):341–352, March 2010.

[429] C. Menon, G. M. Polin, I. Prabakaran, A. Hsi, C. Cheung, J. P. Culver, J. F. Pingpank, C. S. Sehgal, A. G. Yodh, D. G. Buerk, and D. L. Fraker. An integrated approach to measuring tumor oxygen status using human melanoma xenografts as a model. *Cancer Research*, 63(21):7232–7240, November 2003.

[430] Peyman Zirak, Raquel Delgado-Mederos, Joan Marti-Fabregas, and Turgut Durduran. Effects of acetazolamide on the micro- and macro-vascular cerebral hemodynamics: a diffuse optical and transcranial doppler ultrasound study. *Biomed Optics Express*, 1(5):1443–1459, 2010.

[431] Ulas Sunar, Sosina Makonnen, Chao Zhou, Turgut Durduran, Guoqiang Yu, Hsing-Wen Wang, William M. F. Lee, and Arjun G. Yodh. Hemodynamic responses to antivascular therapy and ionizing radiation assessed by diffuse optical spectroscopies. *Optics Express*, 15(23):15507–15516, November 2007.

[432] Turgut Durduran. *Non-invasive measurements of tissue hemodynamics with hybrid diffuse optical methods*. PhD thesis, University of Pennsylvania, 2004.

[433] Yu Shang, Lei Chen, Michal Toborek, and Guoqiang Yu. Diffuse optical monitoring of repeated cerebral ischemia in mice. *Optics Express*, 19(21):20301–20315, Oct 2011.

[434] Rickson C. Mesquita, Nicolas Skuli, Meeri N. Kim, Jiaming Liang, Steve Schenkel, Amar J. Majmundar, M Celeste Simon, and Arjun G. Yodh. Hemodynamic and metabolic diffuse optical monitoring in a mouse model of hindlimb ischemia. *Biomed Optics Express*, 1(4): 1173–1187, 2010.

[435] Meeri N. Kim, Turgut Durduran, Suzanne Frangos, Brian L. Edlow, Erin M. Buckley, Heather E. Moss, Chao Zhou, Guoqiang Yu, Regine Choe, Eileen Maloney-Wilensky, Ronald L. Wolf, M Sean Grady, Joel H. Greenberg, Joshua M. Levine, Arjun G. Yodh, John A. Detre, and W Andrew Kofke. Noninvasive measurement of cerebral blood flow and blood oxygenation using near-infrared and diffuse correlation spectroscopies in critically brain-injured adults. *Neurocrit Care*, 12(2):173–180, Apr 2010.

[436] Chao Zhou, Stephanie A. Eucker, Turgut Durduran, Guoqiang Yu, Jill Ralston, Stuart H. Friess, Rebecca N. Ichord, Susan S. Margulies, and Arjun G. Yodh. Diffuse optical monitoring of hemodynamic changes in piglet brain with closed head injury. *Journal of Biomedical Optics*, 14(3):Article No.: 034015, 2009.

[437] G. Q. Yu, T. F. Floyd, T. Durduran, C. Zhou, J. J. Wang, J. A. Detre, and A. G. Yodh. Validation of diffuse correlation spectroscopy for muscle blood flow with concurrent arterial spin labeled perfusion MRI. *Optics Express*, 15(3):1064–1075, 2007.

[438] T. Durduran, G. Q. Yu, M. G. Burnett, J. A. Detre, J. H. Greenberg, J. J. Wang, C. Zhou, and A. G. Yodh. Diffuse optical measurement of blood flow, blood oxygenation, and metabolism in a human brain during sensorimotor cortex activation. *Optics Letters*, 29 (15):1766–1768, August 2004.

[439] S. A. Carp, G. P. Dai, D. A. Boas, M. A. Franceschini, and Y. R. Kim. Validation of diffuse correlation spectroscopy measurements of rodent cerebral blood flow with simultaneous arterial spin labeling mri; towards mri-optical continuous cerebral metabolic monitoring. *Biomed Optics Express*, 1(2):553–565, 2010.

[440] Turgut Durduran, Chao Zhou, Erin M. Buckley, Meeri N. Kim, Guoqiang Yu, Regine Choe, J William Gaynor, Thomas L. Spray, Suzanne M. Durning, Stefanie E. Mason, Lisa M. Montenegro, Susan C. Nicolson, Robert A. Zimmerman, Mary E. Putt, Jiongjiong Wang, Joel H. Greenberg, John A. Detre, Arjun G. Yodh, and Daniel J. Licht. Optical measurement of cerebral hemodynamics and oxygen metabolism in neonates with congenital heart defects. *Journal of Biomedical Optics*, 15(3):037004, 2010.

[441] G. Q. Yu, T. Durduran, G. Lech, C. Zhou, B. Chance, E. R. Mohler, and A. G. Yodh. Time-dependent blood flow and oxygenation in human skeletal muscles measured with noninvasive near-infrared diffuse optical spectroscopies. *Journal of Biomedical Optics*, 10(2), 2005.

[442] C. Cheung, J. P. Culver, K. Takahashi, J. H. Greenberg, and A. G. Yodh. In vivo cerebrovascular measurement combining diffuse near-infrared absorption and correlation spectroscopies. *Physics In Medicine and Biology*, 46(8):2053–2065, 2001.

[443] Markus Ninck, Markus Untenberger, and Thomas Gisler. Diffusing-wave spectroscopy with dynamic contrast variation: disentangling the effects of blood flow and extravascular tissue shearing on signals from deep tissue. *Biomed Optics Express*, 1(5):1502–1513, 2010.

[444] J. Li, G. Dietsche, D. Iftime, S. E. Skipetrov, G. Maret, T. Elbert, B. Rockstroh, and T. Gisler. Noninvasive detection of functional brain activity with near-infrared diffusing-wave spectroscopy. *Journal of Biomedical Optics*, 10(4), 2005.

[445] Nadege Roche-Labarbe, Angela Fenoglio, Harsha Radhakrishnan, Marcia Kocienski-Filip, Stefan A. Carp, Jay Dubb, David A. Boas, P. Ellen Grant, and Maria Angela Franceschini. Somatosensory evoked changes in cerebral oxygen consumption measured non-invasively in premature neonates. *Neuroimage*, 85:279–286, January 2014.

[446] T. Durduran, C. Zhou, G. Yu, A. M. Hoang, K. Z. Tang, J. A. Detre, J. H. Greenberg, and A. G. Yodh. Diffuse optical measurement of local cerebral blood flow, blood oxygenation and metabolism during cognitive tasks. In *12th Annual Meeting of the Organization for Human Brain Mapping*, Florence, Italy, 2006.

[447] Glen M. Tellis, Rickson C. Mesquita, and A. G. Yodh. Use of diffuse correlation spectroscopy to measure brain blood flow differences during speaking and nonspeaking tasks for fluent speakers and persons who stutter. *SIG 4 Perspectives on Fluency and Fluency Disorders*, 21(3):96–106, 2011.

[448] F. Jaillon, J. Li, G. Dietsche, T. Elbert, and T. Gisler. Activity of the human visual cortex measured non-invasively by diffusing-wave spectroscopy. *Optics Express*, 15(11):6643–6650, 2007.

[449] J. Li, M. Ninck, L. Koban, T. Elbert, J. Kissler, and T. Gisler. Transient functional blood flow change in the human brain measured noninvasively by diffusing-wave spectroscopy. *Optics Letters*, 33(19):2233–2235, 2008.

[450] F. Jaillon, S. E. Skipetrov, J. Li, G. Dietsche, G. Maret, and T. Gisler. Diffusing-wave spectroscopy from head-like tissue phantoms: influence of a non-scattering layer. *Optics Express*, 14(22):10181–10194, 2006.

[451] Louis Gagnon, Michele Desjardins, Julien Jehanne-Lacasse, Louis Bherer, and Frederic Lesage. Investigation of diffuse correlation spectroscopy in multi-layered media including the human head. *Optics Express*, 16(20):15514–15530, September 2008.

[452] Markus Belau, Markus Ninck, Gernot Hering, and Thomas Gisler. Non-invasive measurement of skeletal muscle contraction with time-resolved diffusing-wave spectroscopy. In *Biomedical Optics*, page BSuD70. Optical Society of America, 2010.

[453] E. C. Eckstein, D. G. Bailey, and A. H. Shapiro. Self-diffusion of particles in shear-flow of a suspension. *Journal of Fluid Mechanics*, 79(1):191–208, January 1977.

[454] D. Leighton and A. Acrivos. Measurement of shear-induced self-diffusion in concentrated suspensions of spheres. *Journal of Fluid Mechanics*, 177:109–131, April 1987.

[455] Laurens Victor Adriaan Breedveld. *Shear-induced self-diffusion in concentrated suspensions*. PhD thesis, Universiteit Twente, 2000.

[456] DK Hill. The volume change resulting from stimulation of a giant nerve fibre. *Journal of Physiology-London*, 111(3-4):304–327, 1950.

[457] D. K. Hill and R. D. Keynes. Opacity changes in stimulated nerve. *Journal of Physiology-London*, 108(3):278–281, 1949.

[458] G. Gratton, P. M. Ccorballis, E. H. Cho, M. Fabiani, and D. C. Hood. Shades of gray-matter - noninvasive optical-images of human brain responses during visual-stimulation. *Psychophysiology*, 32(5):505–509, 1995.

[459] G. Gratton and P. M. Corballis. Removing the heart from the brain - compensation for the pulse artifact in the photon migration signal. *Psychophysiology*, 32(3):292–299, 1995.

[460] J. Steinbrink, F. C. D. Kempf, A. Villringer, and H. Obrig. The fast optical signal-robust or elusive when non-invasively measured in the human adult? *Neuroimage*, 26(4):996–1008, July 2005.

[461] H. Radhakrishnan, W. Vanduffel, H. P. Deng, L. Ekstrom, D. A. Boas, and M. A. Franceschini. Fast optical signal not detected in awake behaving monkeys. *Neuroimage*, 45(2): 410–419, April 2009.

[462] Julian Ströbele. Dynamische Lichtstreuung an elektrisch stimulierten Nervenzellen. Diploma thesis, Universität Konstanz, 2012.

[463] Maike Vennekel. Dynamische Lichtstreuung an Erythrozyten. Bachelor thesis, Universität Konstanz, 2012.

[464] Moritz Schlötter. Dynamische Lichtstreuung an natürlichen und künstlichen Erythrozyten in Suspension. Diploma thesis, Universität Konstanz, 2013.

[465] Clara Engesser. Dynamische Lichtstreuung an Erythrozyten in Suspension. Master thesis, Universität Konstanz, 2014.

[466] Maxim A. Yurkin and Alfons G. Hoekstra. The discrete-dipole-approximation code adda: Capabilities and known limitations. *Journal of Quantitative Spectroscopy & Radiative Transfer*, 112(13):2234–2247, September 2011.

[467] G. Dietsche, M. Ninck, C. Ortolf, J. Li, F. Jaillon, and T. Gisler. Fiber-based multispeckle detection for time-resolved diffusing-wave spectroscopy: characterization and application to blood flow detection in deep tissue. *Applied Optics*, 46(35):8506–8514, 2007.

[468] R. Merritt, C. Purcell, and G. Stroink. Uniform magnetic-field produced by 3-square, 4-square, and 5-square coils. *Review of Scientific Instruments*, 54(7):879–882, 1983.

[469] JL Kirschvink. Uniform magnetic-fields and double-wrapped coil systems - improved techniques for the design of bioelectromagnetic experiments. *Bioelectromagnetics*, 13(5):401–411, 1992.

[470] Tomer Fekete, Denis Rubin, Joshua M. Carlson, and Lilianne R. Mujica-Parodi. The nirs analysis package: Noise reduction and statistical inference. *Plos One*, 6(9):e24322, September 2011.

[471] Juliette Selb, David A Boas, Suk-Tak Chan, Karleyton C Evans, Erin M Buckley, and Stefan A Carp. Sensitivity of near-infrared spectroscopy and diffuse correlation spectroscopy to brain hemodynamics: simulations and experimental findings during hypercapnia. *Neurophotonics*, 1(1):015005–015005, 2014.

[472] C. Julien. The enigma of mayer waves: Facts and models. *Cardiovascular Research*, 70(1): 12–21, April 2006.

[473] Eamonn Keogh, Selina Chu, David Hart, and Michael Pazzani. An online algorithm for segmenting time series. In *Data Mining, 2001. ICDM 2001, Proceedings IEEE International Conference on*, pages 289–296. IEEE, 2001.

[474] Georgios V. Varsos, Magdalena Kasprowicz, Peter Smielewski, and Marek Czosnyka. Model-based indices describing cerebrovascular dynamics. *Neurocritical Care*, 20(1):142–157, February 2014.

[475] V. Fodale, D. Schifilliti, A. Conti, T. Lucanto, G. Pino, and L. B. Santamaria. Transcranial doppler and anesthetics. *Acta Anaesthesiol Scand*, 51(7):839–847, 2007.

[476] R. G. Gosling, G. Dunbar, D. H. King, D. L. Newman, C. D. Side, J. P. Woodcock, D.E. Fitzgerald, J. S. Keates, and D. MacMillan. Quantitative analysis of occlusive peripheral arterial disease by a non-intrusive ultrasonic technique. *Angiology*, 22(1):52–55, 1971.

[477] R. G. Gosling and D. H. King. Arterial assessment by doppler-shift ultrasound. *Proceedings of the Royal Society of Medicine-london*, 67(6):447–449, 1974.

[478] Arenda H. E. A. van Beek, Jurgen A. H. R. Claassen, Marcel G. M. Olde Rikkert, and Rene W. M. M. Jansen. Cerebral autoregulation: an overview of current concepts and methodology with special focus on the elderly. *Journal of Cerebral Blood Flow and Metabolism*, 28 (6):1071–1085, June 2008.

[479] R. Schondorf, J. Benoit, and T. Wein. Cerebrovascular and cardiovascular measurements during neurally mediated syncope induced by head-up tilt. *Stroke*, 28(8):1564–1568, August 1997.

[480] Nicolas de Riva, Karol P. Budohoski, Peter Smielewski, Magdalena Kasprowicz, Christian Zweifel, Luzius A. Steiner, Matthias Reinhard, Neus Fabregas, John D. Pickard, and Marek Czosnyka. Transcranial doppler pulsatility index: What it is and what it isn't. *Neurocritical Care*, 17(1):58–66, August 2012.

[481] B. F. Matta, T. S. Mayberg, and A. M. Lam. Direct cerebrovasodilatory effects of halothane, isoflurane, and desflurane during propofol-induced isoelectric electroencephalogram in humans. *Anesthesiology*, 83(5):980–985, November 1995.

[482] B. F. Matta, K. J. Heath, K. Tipping, and A. C. Summors. Direct cerebral vasodilatory effects of sevoflurane and isoflurane. *Anesthesiology*, 91(3):Amer Soc Anesthesiologists, September 1999.

[483] Chun-Xia Li, Sudeep Patel, Danny J. J. Wang, and Xiaodong Zhang. Effect of high dose isoflurane on cerebral blood flow in macaque monkeys. *Magnetic Resonance Imaging*, 32 (7):956–960, September 2014.

[484] J. X. Zhou and J. Liu. The effect of temperature on solubility of volatile anesthetics in human tissues. *Anesthesia and Analgesia*, 93(1):234–238, July 2001.

[485] A. Bergadano, R. Lauber, A. Zbinden, U. Schatzmann, and Y. Moens. Blood/gas partition coefficients of halothane, isoflurane and sevoflurane in horse blood. *British Journal of Anaesthesia*, 91(2):276–278, August 2003.

[486] M. Z. Liu, X. Q. Hu, and J. Liu. The effect of hypothermia on isoflurane mac in children. *Anesthesiology*, 94(3):429–432, March 2001.

[487] M. D. Malkoff, C. R. Gomez, G. Myles, and S. CruzFlores. Cerebrovascular hemodynamic inefficiency of premature ventricular contractions. *Angiology*, 47(1):51–56, January 1996.

[488] Wolfgang Scheffer. Lichtstreuexperimente am Taubenkopf zur Untersuchung der Magnetorezeption. Master thesis, Universität Konstanz, 2011.

[489] Emilie Mace, Gabriel Montaldo, Ivan Cohen, Michel Baulac, Mathias Fink, and Mickael Tanter. Functional ultrasound imaging of the brain. *Nature Methods*, 8(8):662–664, August 2011.

[490] Julia Sester. Funktioneller Ultraschall zur Detektion der Magnetrezeption an Brieftauben. Master thesis, Universität Konstanz, Fachbereich Physik, 2012.

[491] Richard Rau. A preliminary study on the utilization of functional ultrasound imaging of homing pigeons. Master thesis, University of Konstanz, Department of Physics, 2013.

[492] G. Montaldo, M. Tanter, J. Bercoff, N. Benech, and M. Fink. Coherent plane-wave compounding for very high frame rate ultrasonography and transient elastography. *Ieee Transactions On Ultrasonics Ferroelectrics and Frequency Control*, 56(3):489–506, 2009.

[493] J. Bercoff, G. Montaldo, T. Loupas, D. Savery, F. Meziere, M. Fink, and M. Tanter. Ultrafast compound doppler imaging: Providing full blood flow characterization. *Ieee Transactions On Ultrasonics Ferroelectrics and Frequency Control*, 58(1):134–147, 2011.

[494] C. Y. Hsu and C. W. Li. Magnetoreception in honeybees. *Science*, 265(5168):95–97, July 1994.

[495] J. F. Schenck. The role of magnetic susceptibility in magnetic resonance imaging: Mri magnetic compatibility of the first and second kinds. *Medical Physics*, 23(6):815–850, June 1996.

[496] J. F. Schenck and E. A. Zimmerman. High-field magnetic resonance imaging of brain iron: birth of a biomarker? *Nmr In Biomedicine*, 17(7):433–445, November 2004.

[497] E. M. Haacke, N. Y. C. Chengb, M. J. House, Q. Liu, J. Neelavalli, R. J. Ogg, A. Khan, M. Ayaz, W. Kirsch, and A. Obenaus. Imaging iron stores in the brain using magnetic resonance imaging. *Magnetic Resonance Imaging*, 23(1):1–25, January 2005.

[498] E. Mark Haacke, Saifeng Liu, Sagar Buch, Weili Zheng, Dongmei Wu, and Yongquan Ye. Quantitative susceptibility mapping: current status and future directions. *Magnetic Resonance Imaging*, 33(1):1–25, January 2015.

[499] Zachary R. Stephen, Forrest M. Kievit, and Miqin Zhang. Magnetite nanoparticles for medical mr imaging. *Materials Today*, 14(7-8):330–338, July 2011.

[500] K. J. Lohmann. Magnetic orientation by hatchling loggerhead sea turtles (caretta caretta). *Journal of Experimental Biology*, 155:37–49, January 1991.

[501] M. Kalomenopoulou and G. Koliakos. Total-body hematocrit iron kinetics and erythrocyte life-span in pigeons (columba-livia). *Comparative Biochemistry and Physiology A-physiology*, 92(2):215–218, 1989.

[502] J. Ramis and J. Planas. Iron-metabolism in pigeons. *Quarterly Journal of Experimental Physiology and Cognate Medical Sciences*, 63(4):383–393, 1978.

[503] K. L. Gayathri, K. B. Shenoy, and S. N. Hegde. Blood profile of pigeons (columba livia) during growth and breeding. *Comparative Biochemistry and Physiology A-molecular & Integrative Physiology*, 138(2):187–192, June 2004.

[504] P. J. Butler, N. H. West, and D. R. Jones. Respiratory and cardiovascular-responses of pigeon to sustained, level flight in a wind-tunnel. *Journal of Experimental Biology*, 71 (DEC):7–26, 1977.

[505] Wilmer Nichols, Michael O'Rourke, and Charalambos Vlachopoulos. *McDonald's blood flow in arteries: theoretical, experimental and clinical principles.* CRC Press, 2011.